GEERT JAN BESJES

PUSHING SUSY'S BOUNDARIES

SEARCHES AND PROSPECTS FOR STRONGLY-PRODUCED SUPERSYMMETRY AT THE LHC WITH THE ATLAS DETECTOR

PUSHING SUSY'S BOUNDARIES

SEARCHES AND PROSPECTS FOR STRONGLY-PRODUCED
SUPERSYMMETRY AT THE LHC WITH THE ATLAS DETECTOR

PUSHING SUSY'S BOUNDARIES

SEARCHES AND PROSPECTS FOR STRONGLY-PRODUCED SUPERSYMMETRY AT THE LHC WITH THE ATLAS DETECTOR

PROEFSCHRIFT

ter verkrijging van de graad van doctor
aan de Radboud Universiteit Nijmegen
op gezag van de rector magnificus prof. dr. Th.L.M. Engelen,
volgens besluit van het college van decanen
in het openbaar te verdedigen op donderdag 19 maart 2015
om 14.30 uur precies

door

GEERT JAN BESJES

geboren op 29 augustus 1987
te Utrecht

PROMOTOR Prof. dr. N. de Groot
COPROMOTOR Dr. S. Caron

MANUSCRIPTCOMMISSIE Prof. dr. A. Achterberg (voorzitter)
Prof. dr. W.J.P. Beenakker (Universiteit van Amsterdam)
Prof. dr. ir. P.J. de Jong (Universiteit van Amsterdam)
Prof. dr. P.J.G. Mulders (Vrije Universiteit Amsterdam)
Dr. J. Boyd (CERN)

Pushing SUSY's boundaries – Searches and prospects for strongly-produced supersymmetry at the LHC with the ATLAS detector
Thesis, Radboud University Nijmegen
x + 214 pages; illustrated, with bibliographic references and summary in Dutch

ISBN 978 · 94 · 6259 · 545 · 3

Set in 9/12 pt using pdfLaTeX
Cover design by Buro Brouns
Printed in the Netherlands by Ipskamp Drukkers

Available online as CERN-THESIS-2014-228

This work is part of the research programme of the Stichting voor Fundamenteel Onderzoek der Materie *(FOM), which is financially supported by the* Nederlandse Organisatie voor Wetenschappelijk Onderzoek *(NWO). The author was financially supported by NWO.*

It eluded us then, but that's no matter — tomorrow we will run faster, stretch out our arms farther... And then one fine morning —

So we beat on, boats against the current, borne back ceaselessly into the past.

— F. Scott Fitzgerald, *The Great Gatsby*

Contents

CHAPTER ONE

Introduction

This thesis describes a search for new elementary particles predicted by a theory called supersymmetry, which attempts to address shortcomings in our current description of particle physics, the Standard Model.

Since ancient times, mankind has endeavoured to understand its surroundings. As early as the 5^{th} century BC, Democritus had developed a theory that the universe consists of empty space filled with indivisible particles, which he called *atoms*. Soon after the actual discovery of atoms in the early 20^{th} century, physicists were quick to realise that what they had named atoms are in fact not indivisible particles. Rather, atoms consist of a nucleus, made of protons and neutrons, surrounded by electrons. Protons and neutrons are *also* not indivisible: these consist of *quarks*.

Particle physics, or high energy physics, is the branch of science that researches these building blocks of the universe. Our current understanding is enshrined in the *Standard Model* of particle physics, developed in the 1960's and '70's. Over the course of several decades, all its predicted particles were discovered and their properties measured to astonishing precision, culminating in the discovery of the last missing link in 2012: the Higgs boson.

However, the Standard Model in its current form does not describe all observed physical effects in the universe. For one, quantum mechanics and general relativity are not unified in a single framework. Moreover, even excluding gravity, several shortcomings led physicists to develop larger, more encompassing models of particle physics. These shortcomings are both theoretical and experimental in nature and are further discussed later; among other things, the Standard Model suffers from a problem known as *fine-tuning* (or the hierarchy problem), and the cold dark matter observed in the universe cannot be explained by any of the model's particles.

This thesis presents searches for *physics beyond the Standard Model* (by looking for observations incompatible with the Standard Model alone), and prospects for future searches for such physics. Supersymmetry, or SUSY, is one of the most promising attempts to solve the Standard Model's shortcomings, out of the many that exist. It addresses mathematical issues elegantly and can provide a candidate for dark matter. Moreover, the particles that SUSY predicts may be produced in high-energy collision experiments, depending on their masses and couplings – heavier or weakly coupled particles would be produced more rarely. Chapter 2 provides an overview of the Standard Model, discusses its shortcomings, and introduces supersymmetry.

To produce heavy particles, colliders are used. The Large Hadron Collider (LHC), operated by the European Organisation for Nuclear Research CERN on the Franco-Swiss border, is such an accelerator where energetic collisions between protons take place. Specialised detectors observe the debris coming from the interactions, after which the measurements are used to reconstruct each event algorithmically. The ATLAS experiment is one of the four experiments at the LHC that is used to explore the Standard Model and what may lie beyond. Chapter 3 describes the LHC and the ATLAS detector; chapter 4 describes the event reconstruction.

Supersymmetry can manifest itself in many different ways, depending on the masses of the new particles and their interactions. In chapter 5, a search for SUSY in events with jets and missing energy is presented: the missing energy is due to the lightest SUSY particle produced, which is a candidate for dark matter, while events with jets are the most predominant at the LHC. Events with electrons or muons in them are discarded in order to provide a better ratio of signal to background: the produced particles predicted by SUSY decay into Standard Model particles, which in turn decay predominantly without electrons or muons. As a consequence, the search presented in this thesis is one of the most powerful generic searches for heavy particles at a hadron collider. No excess of events over the Standard Model expectation is observed, and the results are used to set limits on a variety of supersymmetrical models. These limits extend substantially beyond previously obtained results.

Results from the searches for supersymmetry at colliders can be used to further explore the parameter space of larger models. By combining all available experimental measurements and limits from other experiments with results from the LHC, fits to a generic supersymmetry model can be performed by exploring a large parameter space and determining which parameter values are ruled out, and which are compatible with all observations. Such fits, presented in chapter 6, lead to the current best expected values for various particle masses, and provide statements on whether these particles can be detected in future collision or dark matter detection experiments.

A combination of results based on publicly available data cannot leverage correlations of uncertainties easily, however, and is hence often conservative. Instead, limits from individual analyses within ATLAS may be combined using correlated uncertainties, leading to better exclusion limits for SUSY models. Chapter 7 presents a combination of the results of several channels with jets and missing energy, both with and without electrons or muons.

The research programme of the LHC and the ATLAS experiment has not been concluded after merely three years of data-taking. Even given the fact that SUSY particles have thus far not been observed, supersymmetry remains a viable theory. Chapter 8 presents the prospects for a search for SUSY similar to the one described earlier at the proposed high-luminosity LHC, which will operate at higher energy than the LHC has until now and record a dataset 150 times bigger than the one currently available. As a result, models currently out of reach can be probed.

Searches and measurements at particle colliders are not easily performed. Analyses in high-energy physics require complicated bookkeeping of many datasets and histograms, and rely on dedicated tools to perform all the required handling of data and computations easily and efficiently. Chapter 9 describes HistFitter, a software package developed within the SUSY working group of the ATLAS collaboration that has been used to obtain the results in several other chapters.

This thesis concludes with a short discussion on the obtained results.

CHAPTER TWO

Supersymmetry

THE FIRST HALF of the twentieth century saw the discovery of a great deal of subatomic particles. Starting from the discovery of the electron by Thomson in 1897 [1], Rutherford demonstrated in 1911 atoms consist of a nucleus surrounded with electrons [2] and by the 1930's, Anderson had shown that Dirac's proposed positron [3, 4] existed (1932) [5], Chadwick had discovered the neutron (1932) [6] and Anderson and Neddermeyer the muon (1936) [7].

In order to understand the continuous energy spectrum observed in β decay of the neutron, Pauli had in 1930 advanced the idea of a neutrino. Building on that, Fermi proposed a new *weak force* that described the decay of a neutron into a proton, an electron and a neutrino, with an interaction strength G_F much weaker than that of the electromagnetic force [8].

The period immediately after the Second World War witnessed the discovery of a plethora of strongly interacting *hadrons*. So many of them were discovered that a classification scheme was sought: Gell-Mann [9] and Zweig [10] independently postulated these hadrons consisted of *quarks*. The subsequent discovery of the Ω^- state [11] confirmed their hypothesis.

Fermi's weak force was unified with electrodynamics by Weinberg and Salam in 1968 in the *electroweak* force [12, 13], building on the theory of quantum electrodynamics (QED) developed in the 1950's by Feynman, Schwinger, Tomonaga and others [14–16], work of Glashow on electroweak unification models that predicted a neutral current [17], and the work of Anderson, Higgs, Englert, Brout, Kibble, Guralnik and Hagen [18–21]. In a hugely important theoretical milestone, 't Hooft and Veltman proved the renormalisability of the model in 1972 [22]. The W and Z bosons predicted by electroweak theory were observed at the SPS collider in 1983 by the UA1 and UA2 collaborations [23–26].

The strong interaction in its modern form is described by quantum chromodynamics (QCD), developed between 1973 and 1975 by, among others, Gell-Mann, Gross, Politzer and Wilcek [27–29]. The subsequent discovery of gluons in 1979 at PETRA [30], precision measurements at CERN's Large Electron Positron collider (LEP) and of F_2 at HERA [31] validated perturbative QCD.

These theories together form the Standard Model of particle physics. In 2012, the ATLAS and CMS collaborations announced the discovery of its last remaining ingredient, the Higgs boson [32, 33]. Its mass has since been measured to be approximately 125 GeV [34, 35]. Notwithstanding the extraordinary success it has enjoyed, the Standard Model cannot be the final theory of particle physics, let alone nature. This chapter briefly reviews the theory behind the Standard Model and discusses why the model is incomplete. Supersymmetry (SUSY) is introduced as a solution to several of the Standard Model's shortcomings and current constraints on SUSY are discussed.

The material is largely based on [36–38], with major references cited in place.

2.1 The Standard Model of particle physics

The Standard Model describes our current understanding of particle physics. It is a quantum field theory (QFT) in which each particle is described by a field in space-time. To be a viable model, the Standard Model must

- describe all of the directly observed particles and their interactions;
- be invariant under transformations of the Poincaré group; that is, invariant under Lorentz translations, rotations and boosts;
- be invariant under local transformations of the gauge group $SU(3)_C \times SU(2)_L \times U(1)_Y$;
- have an energy spectrum bounded from below;
- be renormalisable.

In order to satisfy this short list of requirements, the Standard Model relies on the entire breadth of modern physics, from special relativity [39] and quantum mechanics [40, 41] to unified electroweak theory, the Higgs mechanism, the quark model and quantum chromodynamics. However, the Standard Model's structure can seem rather ad-hoc: the choice of the gauge group and fermion masses lack any immediate theoretical motivation.

The Standard Model is described by Lagrangian densities, for brevity referred to as Lagrangians, that describe particle fields and their interactions. A simple fermionic model is

$$\mathcal{L} = \overline{\psi} i \partial\!\!\!/ \psi, \tag{2.1}$$

where ψ is a massless fermion field and $\partial\!\!\!/ = \gamma^\mu \partial_\mu$, with $\partial_\mu \equiv \partial/\partial x^\mu$ and γ^μ the Dirac matrices satisfying $\{\gamma^\mu, \gamma^\nu\} = 2g^{\mu\nu}$, where g is the metric, and a summation over the index μ (running from 0 to 3) is implied. The field ψ is a *spinor* and can be represented by a four-component vector[1].

Interactions between fields are described by gauge fields that come from requiring local gauge symmetry. All fields and particles are listed in table 2.1. In the following, QED, the electroweak force, including the Higgs mechanism, and QCD are briefly described. For a full introduction to the Standard Model, see e.g. [42–44].

2.1.1 Electrodynamics

Relativistic electrodynamics is described by quantum electrodynamics, based on the symmetry group $U(1)$. The interaction between charged particles is mediated by the neutral and massless photon. A coupling between the fermion field ψ and the photon field A^μ is introduced by incor-

[1] Alternatively, one may also describe fields through a decomposition in two components, so-called Weyl spinors. Such a description shall become useful later when discussing the electroweak force.

Table 2.1 · Field content of the Standard Model with the corresponding particles, their charge and spin, and the fields' representation. The last column indicates the weak hypercharge $Y_W = 2(Q - T_3)$.

Particle(s)	**Field(s)**	**Content**	**Charge**	**Spin**	$SU(3)_C$	$SU(2)_L$	$U(1)_Y$
Quarks	Q_i	$(u, d)_L$	(2/3, −1/3)	1/2	**3**	**2**	1/3
(Three generations)	u_{Ri}	u_R	2/3	1/2	$\bar{\mathbf{3}}$	**1**	4/3
	d_{Ri}	d_R	−1/3	1/2	$\bar{\mathbf{3}}$	**1**	−2/3
Leptons	L_i	$(\nu_e, e)_L$	(0, −1)	1/2	**1**	**2**	−1
(Three generations)	l_{Ri}	e_R	−1	1/2	**1**	**1**	−2
Gluons	G^a_μ	g	0	1	**8**	**1**	0
W bosons	$W^{1,2}_\mu$	$W^\pm$	±1	1	**1**	**3**	0
Photon, Z boson	W^3_μ, B_μ	γ, Z^0	0	1	**1**	**3**, **1**	0
Higgs boson	ϕ	H	0	0	**1**	**2**	1

porating such a symmetry in (2.1) and demanding the Lagrangian be invariant under the local gauge transformation $\psi(x) \to e^{i\alpha(x)}\psi$. In order to do so, the *covariant derivative* is defined:

$$D_\mu = \partial_\mu + igt_a A^a_\mu, \tag{2.2}$$

where g is a coupling constant, t_a the matrix representation of the group generators and A^a_μ a vector field. For quantum electrodynamics, the gauge group is $U(1)$ and the field transforms as $A_\mu \to A_\mu - \frac{1}{e}\partial\alpha(x)$. Adding a kinetic term for the photon field, the Lagrangian is given by

$$\mathcal{L}_{\text{QED}} = \overline{\psi}(i\not{D} - m)\psi - \frac{1}{4}F^{\mu\nu}F_{\mu\nu}, \tag{2.3}$$

where $F_{\mu\nu}$ is the electromagnetic field tensor defined as

$$F_{\mu\nu} = \partial_\mu A_\nu - \partial_\nu A_\mu. \tag{2.4}$$

2.1.2 Electroweak theory

Electroweak interactions arise from the $SU(2)_L \times U(1)_Y$ gauge symmetry, with the subscript L indicating the left-handed nature of the weak interaction and the subscript Y the hypercharge conservation under $U(1)$ transformations. The fermions are described by the chirality eigenstates ψ_L and ψ_R:

$$\psi = P_L\psi + P_R\psi = \psi_L + \psi_R, \tag{2.5}$$

where $P_L = \frac{1-\gamma^5}{2}$ and $P_R = \frac{1+\gamma^5}{2}$, with $\gamma^5 = i\gamma^0\gamma^1\gamma^2\gamma^3$.

In electroweak theory, left-handed fermions appear as lepton doublets $L_i = (\nu_i, l_i^-)$ and quarks doublets $Q_i = (u_{Li}, d_{Li})$, where the index i denotes the generation. The right-handed fermion fields L_{Ri} (leptons) and u_{Ri} and d_{Ri} (up- and down-type quarks) appear as singlets that have zero weak isospin and do not interact under $SU(2)$. Note that we do not discuss right-handed neutrino singlets. All these fields and their particles are shown in table 2.1.

The gauge fields corresponding to the symmetry $SU(2)\times U(1)$ are three $SU(2)$ bosons $W_\mu^{1,2,3}$ and one $U(1)$ boson B_μ. The Lagrangian can be written as

$$\mathcal{L}_{\text{EW}} = \sum_f \overline{\psi}_f i \not{D} \psi_f - \frac{1}{4} W^j_{\mu\nu} W_j^{\mu\nu} - \frac{1}{4} B_{\mu\nu} B^{\mu\nu}, \tag{2.6}$$

where the sum runs over all fermion fields and a summation over the index j is implied. Fermionic mass terms will be discussed later. The field strength tensors are given by

$$W^i_{\mu\nu} = \partial_\mu W^i_\nu - \partial_\nu W^i_\mu - g_1 \epsilon_{ijk} W^j_\mu W^k_\nu, \tag{2.7a}$$

$$B_{\mu\nu} = \partial_\mu B_\nu - \partial_\nu B_\mu, \tag{2.7b}$$

where ϵ_{ijk} is the Levi-Civita symbol. The covariant derivative is

$$D_\mu = \partial_\mu + \frac{1}{2} i g_1 \sigma^i W^i_\mu P_L + \frac{1}{2} i g_2 Y B_\mu, \tag{2.8}$$

with g_1 and g_2 the interaction strengths of the $SU(2)$ and $U(1)$ interactions. The Pauli matrices σ^i and the hypercharge Y are the generators of the respective symmetries; the projection operator P_L is added to reflect the observed left-handedness of the weak interaction.

2.1.3 Electroweak symmetry breaking

In contradiction to the observed masses of the $W^\pm$ and Z^0 bosons, the $SU(2)\times U(1)$ symmetry group leaves these particles massless. Moreover, gauge invariance prohibits the simple solution of introducing an explicit mass term for the fields. Within the Standard Model, the Higgs mechanism of electroweak symmetry breaking [18–21] solves the issue elegantly.

Symmetry breaking in the electroweak sector is a consequence of the addition of a complex scalar doublet with a non-zero vacuum expectation value and four degrees of freedom $\phi_{1,2,3,4}$. These degrees of freedom correspond to two complex scalars making up an $SU(2)_L$ doublet

$$\phi = \begin{pmatrix} \phi^+ \\ \phi^0 \end{pmatrix} = \frac{1}{\sqrt{2}} \begin{pmatrix} \phi_3 + i\phi_4 \\ \phi_1 + i\phi_2 \end{pmatrix} \tag{2.9}$$

with hypercharge $Y = 1$. The doublet is added to the Lagrangian via

$$\mathcal{L}_H = D_\mu \phi^\dagger D^\mu \phi - \mu^2 (\phi^\dagger \phi) - \lambda (\phi^\dagger \phi)^2, \tag{2.10}$$

with the covariant derivative identical to the one previously used for the electroweak Lagrangian, without the projection operator. Requiring $\mu^2 < 0$ and $\lambda > 0$, a non-zero vacuum expectation value that leads to the desired symmetry breaking is ensured. The ground state of ϕ occurs at $(\phi^\dagger\phi) = -\mu^2/(2\lambda)$. Gauge freedom hence allows the choice of the unitary gauge $\phi_{2,3,4} = 0$ and

$$\phi = \begin{pmatrix} 0 \\ v/\sqrt{2} \end{pmatrix}, \tag{2.11}$$

with $v = |\mu|/\sqrt{\lambda}$. The expansion $\phi_1 = v + h$, with h a real scalar field, around the ground state yields the Higgs potential

$$V_H = \lambda v^2 h^2 + \lambda v h^3 + \frac{\lambda}{4} h^4, \tag{2.12}$$

which has a mass term with $m_H = \sqrt{2\lambda v^2}$ and cubic and quartic self-couplings for h. For the kinetic term, the expansion gives rise to new terms for the gauge bosons, including scalar-vector couplings. The gauge bosons may be redefined to make the mass matrix diagonal:

$$W^{\pm}_\mu = \frac{1}{\sqrt{2}}(W^1_\mu \mp i W^2_\mu), \tag{2.13a}$$

$$Z^0_\mu = \frac{1}{\sqrt{g_1^2 + g_2^2}}(g_1 W^3_\mu - g_2 B_\mu), \tag{2.13b}$$

$$A_\mu = \frac{1}{\sqrt{g_1^2 + g_2^2}}(g_2 W^3_\mu + g_1 B_\mu), \tag{2.13c}$$

where the mixing is usually parametrised using the weak mixing angle θ_W:

$$\sin\theta_W = \frac{g_2}{\sqrt{g_1^2 + g_2^2}} \quad \text{and} \quad \cos\theta_W = \frac{g_1}{\sqrt{g_1^2 + g_2^2}}. \tag{2.14}$$

Re-expressing the kinetic term in these new fields, it becomes apparent that the introduction of the scalar field ϕ has resulted in a Lagrangian that contains $W^\mu W_\mu$ and $Z^\mu Z_\mu$ terms and *no* mass terms for the field A_μ. The photon therefore remains massless, while the masses of the W and Z bosons are given by $m_W = g_1 v/2 = m_Z \cos\theta_W$. The remaining degree of freedom corresponds to a new scalar particle of which the mass is a free parameter, the Higgs boson H.

Fermionic mass terms

Before symmetry breaking, mass terms of the form $\overline{\psi}_L \psi_R + \overline{\psi}_R \psi_L$ were forbidden by $SU(2)_L$ invariance. However, by virtue of the Higgs mechanism a gauge-invariant Yukawa coupling to the scalar field ϕ may be introduced:

$$\mathcal{L}_{\text{leptons}} = -\sum_i \left[y_i \left(\overline{L}_i \phi\right) l_{Ri} + \text{h.c.} \right], \tag{2.15}$$

where the index i indicates the generation and y_i the coupling constants. After symmetry breaking, this term becomes

$$\mathcal{L}_{\text{leptons}} = -\sum_i \left[\frac{v + h}{\sqrt{2}} y_i \left(\overline{l}_{Li} l_{Ri} + \overline{l}_{Ri} l_{Li} \right) \right]. \tag{2.16}$$

Here the choice of $Y = 1$ for the Higgs field becomes clear: without it, couplings to e.g. $\overline{e}_L e_R$ would be forbidden by hypercharge conservation. Similar terms may be written for the quark fields for both up- and down-type quarks. For the upper member of each quark doublet, the conjugated Higgs doublet $\phi_c = i\sigma_2\phi^*$ is constructed.[1]

Fermion masses are thus closely linked to their couplings to the Higgs boson. However, due to the couplings being arbitrary, no actual predictions for the fermion masses (nor for the Higgs mass from observed fermion masses) are obtained in this way. It must further be noted that the couplings y_i for quarks were written in a diagonal format. In reality, the mass eigenstates are not identical to the flavour eigenstates and the Cabbibo-Kobayashi-Maskawa (CKM) matrix [45, 46] is introduced to translate between the two bases. Interactions with $W^\pm$ can hence change the flavour states.

2.1.4 Quantum chromodynamics

Analogous to the construction of the QED Lagrangian (2.3), a similar term for QCD can be obtained by imposing local gauge invariance under $SU(3)_C$. Instead of A_μ, the vector field is that of the gluon G^a_μ, where $a = 1, \ldots, 8$. The covariant derivative and field strength are given by

$$D_\mu = \partial_\mu + i g_a t^a G^a_\mu, \tag{2.17a}$$

$$G^a_{\mu\nu} = \partial_\mu G^a_\nu - \partial_\nu G^a_\mu - g_s f^{abc} G^b_\mu G^c_\nu, \tag{2.17b}$$

with g_s related to the QCD coupling constant $\alpha_s = g_s^2/4\pi$.

The generators are given by the matrices t_a that satisfy $\left[t^a, t^b\right] = i f^{abc} t^c$. One possible representation is the set of Gell-Mann matrices λ_a with $\left[\lambda_a/2, \lambda_b/2\right] = i f^c_{ab} \lambda_c/2$. The structure constants are completely antisymmetric in their indices and given by

$$f^{123} = 1\,, \quad f^{147} = f^{165} = f^{246} = f^{257} = f^{345} = f^{376} = \frac{1}{2}\,, \quad f^{458} = f^{678} = \frac{\sqrt{3}}{2}, \tag{2.18}$$

with the other terms equal to 0. The Lagrangian is given by

$$\mathcal{L}_{\text{QCD}} = \sum_q \overline{\psi}_{q,i} (i \not{D}_{ij} - m_q \delta_{ij}) \psi_{q,j} - \frac{1}{4} G^a_{\mu\nu} G^{a\,\mu\nu}, \tag{2.19}$$

where the sum runs over all quark flavours q and the implicit summation in i and j sums over the three colour charges in the fundamental representation of $SU(3)$.

Gluons transform as octets under $SU(3)_C$ and as singlets under $SU(2)_L$ and $U(1)_Y$. The colour charge of gluons allows for gluon self-interactions, terms that are impossible in QED.

Although the gluons are massless, the range of the strong force is limited to nuclear length scales due to *colour confinement*, i.e. the absence of free states that are not colour singlets. Hence, quarks hadronise and form colour singlet states: quark–anti-quark pairs (mesons) or states of three quarks (baryons). Energetic quarks and gluons are thus only observed through particle jets, sprays of hadrons with sufficient lifetime to reach the detector.

The second important aspect of QCD is *asymptotic freedom* [28, 29]: the coupling constant α_s decreases with decreasing distance (or higher energies). In other words, $\alpha_s \to 0$ as $Q^2 \to \infty$,

[1] Clearly, an equivalent procedure with $Y = -1$ may be followed. Instead of ϕ generating the mass for down-type quarks, up-type quarks would acquire mass. Such fields are present in the Lagrangian for supersymmetry, as discussed later.

where Q is the energy scale of the interaction. Hence, for low energies QCD cannot be pertubatively calculated. For energies of 1 to 2 GeV and higher valid expansions can be made.

2.1.5 Particle production at hadron colliders

The proton is not an elementary particle, but rather a combination of three *valence* quarks (two u, one d), gluons, and *sea quarks* that constantly come in and out of existence through quantum fluctuations. These are called the *partons* of the proton. The cross-section of the process $pp \to X$ is thus not as neatly described as e.g. $e^+e^- \to X$, but relies on *parton distribution functions*:

$$\sigma_{pp\to X} = \sum_{ij} \int_0^1 \mathrm{d}x_1 \int_0^1 \mathrm{d}x_2\, \hat{\sigma}_{ij\to X}\, f_i(x_1, \mu_F^2)\, f_j(x_2, \mu_F^2), \tag{2.20}$$

where $f_{i,j}$ are parton distribution functions (PDFs) of the proton, $x_{1,2}$ momentum fractions of the partons and $\hat{\sigma}$ the cross-section of the underlying process. These distribution functions rely on the *factorisation scale* μ_F. The *hard cross-section* $\hat{\sigma}_{ij\to X}$ is a function of several parameters:

$$\hat{\sigma}_{ij\to X} = \hat{\sigma}_{ij\to X}\Big(x_1 p_1, x_2 p_2, \alpha_s(\mu_R^2), Q^2, \mu_F^2, \mu_R^2, \{m\}\Big), \tag{2.21}$$

where Q is the energy scale of the interaction, $x_i p_i$ the momentum carried by the particles, μ_R the *renormalisation scale* and $\{m\}$ is the set of masses of particles involved in the process. The various terms are briefly discussed below.

The PDF $f_i(x, \mu_F^2)$ is the probability of a parton i in an incoming proton having a momentum that is a fraction x of the proton's momentum at a scale μ_F. These functions are determined experimentally at a certain μ_F, through a fit to measurements of various processes [31, 47–53] and extrapolated to different values of μ_F using the DGLAP evolution equation [54–57]. Commonly used PDF sets are MSTW [58], CTEQ [59] and NNPDF [60].

The factorisation scale μ_F is the energy scale at which the PDFs are evaluated and where long and short distance effects are assumed to factorise. The renormalisation scale μ_R is the energy scale at which the strong coupling constant α_s is evaluated and is due to the renormalisation procedure used: in evaluating loop diagrams it is necessary to control integrals $\int_{-\infty}^{\infty} \mathrm{d}^4 l$ over loop momenta through a process of *regularisation* and *renormalisation*. 't Hooft and Veltman demonstrated [22] that all non-abelian gauge theories are renormalisable; Standard Model observables are independent of μ_R once an finite sum over counter-terms is performed. Each counter-term may contain loop contributions at *all* orders and can be truncated at a given order. In practice, the evaluation of a *finite* number of perturbative contributions therefore leads to an uncertainty through the choice of μ_R. The renormalisation scale is often taken to be the energy scale of the interaction to avoid large logarithms [61]. For a full discussion on regularisation and renormalisation, the reader is referred to [43, 62]. SUSY cross-sections are calculated using $\mu_R = \mu_F = Q$, with Q the average mass of the final-state particles [63].

2.2 Shortcomings of the Standard Model

The Standard Model has been phenomenally successful from a purely empirical point of view. Predictions such as the masses of the W and Z bosons agree well with the extremely precise measurements. Over orders of magnitude in energy, the Standard Model is an accurate description of (the interactions of) elementary particles. However, several fundamental issues with the model have led to searches for physics *beyond the Standard Model*. These shortcomings can broadly be grouped in two categories: theoretical and experimental considerations. We start with the experimental ones, not worrying about General Relativity and gravity:

1. observed neutrino oscillations suggest that neutrinos have mass;
2. the observation of cold dark matter in the universe (see §2.2.2);
3. the bulk of the universe's energy resides in an unknown form, described as dark energy;
4. the matter–antimatter asymmetry due to CP violation cannot be reconciled with the amount of violation in the Standard Model.

Theoretically, the Standard Model's underpinnings are oft poorly understood:

1. the masses and mixing matrices in the Standard Model are ad-hoc;
2. the choice of the gauge group lacks theoretical motivation;
3. a mechanism by which electroweak symmetry is broken needs to be inserted by hand.

With mild derision, one could in other words state that the Standard Model works, simply because it works. Nonetheless, it is a formidable theory with tremendous predictive power.

Unfortunately, the experimental shortcomings do not immediately point to an energy scale at which these issues might be addressed. However, a slightly different argument can be made that not only new physics should exist, but also that this new physics should manifest itself at the weak scale. This argument is due to the *hierarchy problem* of the Standard Model. The next sections describe several of the shortcomings in more detail.

2.2.1 The hierarchy problem

Consider the Standard Model Higgs boson, a scalar particle with mass m_H. The radiative corrections to this mass are given by one-loop bosonic and fermionic corrections to the propagator. The fermonic corrections are proportional to

$$\delta m_H^2 \propto \lambda_f^2 \int \mathrm{d}^4 k \left(\frac{1}{k^2 - m_f^2} + \frac{2m_f^2}{(k^2 - m_f^2)^2} \right), \tag{2.22}$$

where λ_f is the coupling of the fermion with mass m_f to the Higgs boson. The largest correction comes from the fermion with the largest coupling, which is the top quark. The bosonic corrections are similar, but opposite in sign. Presuming that new physics exists, the Standard Model is an effective theory up to an energy scale Λ. Using that scale as a cut-off scale, the physical Higgs mass is given by

$$m_H^2(\text{phys.}) \sim m_H^2 + \mathcal{O}(\lambda_f^2 \Lambda^2) + \mathcal{O}(\ln \Lambda). \tag{2.23}$$

However, such a procedure begs a simple question: what is the choice that is made for the cut-off scale? Assuming no new physics exists, the scale is typically taken as the GUT scale (10^{19} GeV). Unitarity requirements on the Higgs boson mass require its mass to be smaller than several hundred GeV. The consequence is that the parameter m_H^2 is severely *fine-tuned* over at least 17 orders of magnitude: not an elegant prospect for a physical theory. The large Λ^2 corrections that occur for $\Lambda \gg 1$ TeV lead to the phenomenological conclusion that new TeV-scale particles should provide additional Feynman diagrams to deal with the fine-tuning problem.

Acknowledging the use of a cut-off is problematic, one may instead suppose a new particle with mass M_χ exists and use dimensional regularisation in order to avoid a cut-off scale. However, dimensional regularisation leads to the same problem: provided that new physics with couplings to the Higgs boson exists, a mass term M_χ^2 for new particles is added to the result of the integral. This leads to similar types of fine-tuning as in the previous paragraph, with the mass of the new particles rather than the cut-off scale in the corrections to m_H^2.

One could argue that the introduction of the scale Λ presupposes that any new particles couple to the Higgs boson, and that this is not necessarily true. The Standard Model could be treated as a theory valid up to very high energy scales. A different argument for new physics processes at a certain scale may then be made, however. The Standard Model is meta-stable: the Higgs quartic coupling λ might become negative at high energy scales (see fig. 2.1). Whether this is a problem depends on the coupling's exact value: the more negative, the higher the chance of tunneling to a different minimum of the Higgs potential becomes. More precise measurements of the top mass and the Higgs mass will shed more light on λ and on whether the Standard Model is incompatible with the universe's lifetime.

In the case where the Standard Model is indeed incompatible, new processes are needed to ensure λ is increased: again an effective cut-off Λ, the energy scale of these processes, would be introduced. It must be noted that at high energy scales λ could become exactly zero: in that case the Standard Model could originate from a conformal field theory [65]; dark matter and inflation would be incorporated through 3 light (0.1–100 GeV) right-handed sterile Majorana neutrinos [66].

However, even in the scenario in which the Standard Model is valid up to high energy scales a problem remains. For the $U(1)$ coupling constant a Landau pole exists: at $\sim 10^{40}$ GeV, the coupling constant becomes infinite [67, 68]. This, again, leads to the conclusion that the Standard Model is an effective field theory, and the hierarchy problem remains. Only a solution of the Landau pole *without* any particles that couple to the Higgs boson would avoid the problem.

The conclusion that new physics should exist at the TeV scale can be avoided, however. The most obvious way is to simply accept nature that is fine-tuned. Another is that no scalar fields

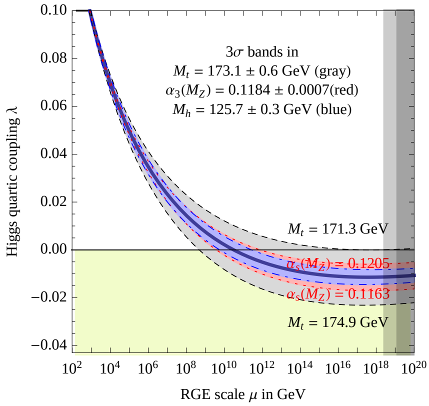

Fig. 2.1 · Stability regions of the Standard Model vacuum as a function of the top mass and the Higgs mass (left) and the Higgs potential quartic coupling as a function of the energy scale (right); from [64].

exist, and the Higgs boson in reality is a composite fermionic state (technicolour).[1] Finally, extra dimensions with strong couplings to gravity would alleviate the hierarchy problem by lowering the Planck scale. Such scenarios would lead to exotic resonances and the production of micro black holes at colliders [70]. Several other ways exist; see e.g. [36, §2.3]. We shall proceed on the assumption that the TeV scale is indeed special, and that new physics from a theory called *supersymmetry* cancels the large divergences.

2.2.2 Dark matter

Astrophysical observations provide compelling evidence that the universe consists of more than visible matter. Measurements of the orbital velocity of stars in our galaxy and galaxies in clusters cannot be explained without the presence of invisible matter acting only gravitationally in said galaxies [71–73]. This *dark matter* can not be electrically charged or carry colour charge, and can only interact via gravity and the weak nuclear force. Moreover, recent measurements from the Planck satellite of the temperature fluctuations of the cosmic microwave background indicate the universe is flat and its content is dominated by dark energy (68.3 %) and dark matter (26.8 %) [74]. A mere 4.9 % consists of ordinary matter. However, the Standard Model lacks a particle that would allow us to describe dark matter.

2.2.3 Gauge coupling unification

Throughout the history of physics, theories have often been unified in larger, more encompassing models. A relevant case in point is the combined description of electricity and magnetism. The unification of all four forces in nature (including gravity) in a Grand Unified Theory (GUT) is a holy grail that has eluded physicists over the past several decades.

[1] The technicolour approach becomes problematic when attempting to describe fermionic masses. These issues can in turn be solved by extended models, that however predict unacceptably large flavour-changing neutral currents or are in conflict with precision measurements. Technicolour is entirely outside the scope of this work; for an introduction, see [69].

A first stage in which the strong force would be unified with the electroweak force would be an encouraging first step towards such a theory. The gauge group $SU(3) \times SU(2) \times U(1)$ would be embedded in a larger group of which the symmetry is broken at a yet unknown high energy scale. However, using renormalisation group equations it can be shown that the Standard Model forces never unify. As shall become clear later supersymmetric theories do offer the possibility, depending on their exact parameters.

2.3 Supersymmetry

The fact that particle physics can be so comprehensively understood by imposing symmetry constraints on the Lagrangian raises the question whether any larger symmetries may be imposed, and what their effects would be. Coleman and Mandula showed that for *any* interacting quantum field theory with a finite number of particles the symmetry group of the Lagrangian can only be a product of an internal symmetry (e.g. the gauge group) and the Poincaré group [75].

However, the theorem assumes that all symmetries are bosonic. Haag, Łopuszański and Sohnius demonstrated that operators that transform as spinors under Lorentz transformations are exempt from these requirements [76]. Alternatively stated, space-time and internal symmetries are still independent, but transformations between the spin states are allowed. Such transformations, described by spinor operators Q_a, modify the spin of a state:

$$Q_a|J\rangle = |J \pm 1/2\rangle. \tag{2.24}$$

The operators Q generate a graded Lie algebra and are part of the *super-Poincaré algebra*:

$$[P_\mu, P_\nu] = 0 \tag{2.25a}$$

$$[M_{\mu\nu}, P_\lambda] = i(g_{\nu\lambda}P_\mu - g_{\mu\lambda}P_\nu), \tag{2.25b}$$

$$[M_{\mu\nu}, M_{\rho\sigma}] = -i(g_{\mu\rho}M_{\nu\sigma} - g_{\nu\rho}M_{\mu\sigma} - g_{\nu\sigma}M_{\mu\rho}), \tag{2.25c}$$

$$[P_\mu, Q_a] = 0, \tag{2.25d}$$

$$[M_{\mu\nu}, Q_a] = -\frac{1}{2}(\sigma_{\mu\nu})_{ab}Q_b, \tag{2.25e}$$

$$\{Q_a, \overline{Q}_b\} = 2(\gamma^\mu)_{ab}P_\mu, \tag{2.25f}$$

where $\overline{Q}_{a,b} = Q^*_{a,b}\gamma^0$ (the Dirac conjugate), P is the generator of space-time translations and $\sigma_{\mu\nu} = \frac{i}{2}[\gamma_\mu, \gamma_\nu]$. M is the generator of Lorentz transformations defined through $M_{ij} = \epsilon_{ijk}J_k$ and $M_{0i} = -K_i$, where J and K respectively are the generators of rotations and boosts.

The Wess-Zumino model

The simplest supersymmetry Lagangrian is due to Wess and Zumino [77]:

$$\mathcal{L} = \frac{1}{2}(\partial_\mu A)^2 + \frac{1}{2}(\partial_\mu B)^2 + \frac{1}{2}\overline{\psi}(i\partial\!\!\!/ - m)\psi + \frac{1}{2}\left(F^2 + G^2\right) + mFB + mGA, \tag{2.26}$$

where A and B are real scalar fields and ψ a 4-component Majorana spinor. F and G are real scalar fields with mass dimension $\dim m^2$ that have no propagator; they are *auxiliary fields*. Solving the Euler-Lagrange equation relates them to A and B through

$$F = -mB \text{ and } G = -mA. \tag{2.27}$$

Eliminating these fields from the Lagangrian results in a theory with three free fields A, B and ψ that correspond to two spin-0 particles and one spin-½ particle with equal mass. Wess and Zumino realised that under the following set of global transformations, the Lagrangian changed by a total derivative:

$$\delta A = i\bar{\alpha}\gamma_5\psi, \tag{2.28a}$$

$$\delta B = -\bar{\alpha}\psi, \tag{2.28b}$$

$$\delta\psi = -F\alpha + iG\gamma_5\alpha + \not{\partial}\gamma_5 A\alpha + i\not{\partial}B\alpha, \tag{2.28c}$$

$$\delta F = i\bar{\alpha}\not{\partial}\psi, \tag{2.28d}$$

$$\delta G = \bar{\alpha}\gamma_5\not{\partial}\psi, \tag{2.28e}$$

where α is a space-time-independent anticommuting Majorana spinor. These transformations, which mix the bosonic and fermionic fields, are the simplest supersymmetry transformations.

The Lagrangian (2.26) is readily rewritten in terms of three complex fields

$$\mathcal{S} = \frac{1}{\sqrt{2}}(A + iB), \quad \psi_L = \frac{1-\gamma_5}{2}\psi \text{ and } \mathcal{F} = \frac{1}{\sqrt{2}}(F + iG) \tag{2.29}$$

that follow the transformations

$$\delta\mathcal{S} = -i\sqrt{2}\bar{\alpha}\psi_L, \quad \delta\psi_L = -\sqrt{2}\mathcal{F}\alpha_L + \sqrt{2}\not{\partial}\mathcal{S}\alpha_R \text{ and } \delta\mathcal{F} = i\sqrt{2}\bar{\alpha}\not{\partial}\psi_L. \tag{2.30}$$

The three fields $\mathcal{S}$, ψ_L and $\mathcal{F}$ hence form a left chiral *supermultiplet* in the same way the proton and neutron form an isospin doublet. In a further analogy, the *superfield* mechanism treats all of them as a single entity $\hat{S}$. This mechanism is not described in further detail here.

In particular (2.25f) has interesting consequences: performing two SUSY transformations is equivalent to the generator of translations. Hence, space-time itself needs to be extended with fermionic degrees of freedom. It is these that Q_a operates on. To that end, space-time coordinates x^μ are complemented with a second set of coordinates θ, forming a four-component spinor whose components are Grassmann variables. Superfields are denoted $\hat{S}(x^\mu, \theta^\mu)$.

Two important observations can be made. First, Q commutes with P^2 by virtue of (2.25d): particles and their superpartners must have equal mass. Moreover, since both Q and $\overline{Q}$ commute with the generators of the gauge groups the charge, isospin and colour charge of the components of each supermultiplet must be identical.

Table 2.2 · Superfield content of the Minimal Supersymmetric Standard Model and the fields' representations in $SU(3)_C$ and $SU(2)_L$. The last column indicates the weak hypercharge. The two Higgs doublets mix with the gauginos $\tilde{W}$ and $\tilde{B}$ as described in the text.

Supermultiplet	**Bosons**	**Fermions**	$SU(3)_C$	$SU(2)_L$	$U(1)_Y$
Gauge multiplets	spin-1	spin-½			
Gluons, gluinos	g	$\tilde{g}$	**8**	**1**	0
W bosons, winos	$W^{\pm}, W^3$	$\tilde{W}^{\pm}, \tilde{W}^3$	**1**	**3**	0
Photons, Z bosons, binos	B	$\tilde{B}$	**1**	**1**	0
Matter multiplets	spin-0	spin-½			
Squarks, quarks	$(\tilde{u}_L, \tilde{d}_L)$	$(u, d)_L$	**3**	**2**	⅓
(Three generations)	$\tilde{u}_R^*$	u_R^c	$\overline{\mathbf{3}}$	**1**	−4⁄3
	$\tilde{d}_R^*$	d_R^c	$\overline{\mathbf{3}}$	**1**	⅔
Sleptons, leptons	$(\tilde{\nu}_L, \tilde{e}_L)$	$(\nu_e, e)_L$	**1**	**2**	−1
(Three generations)	$\tilde{e}_R^*$	e_R^c	**1**	**1**	2
Higgs bosons, higgsinos	H_d^j	$(\tilde{h}_d^0, \tilde{h}_d^-)_L$	**1**	**2**	−1
	H_u^j	$(\tilde{h}_u^+, \tilde{h}_u^0)_L$	**1**	**2**	1

2.3.1 The Minimal Supersymmetric Standard Model

The case of $N = 1$ supersymmetry, with just a single transformation generator, turns out to be the only possibility that permits chiral representations. [1] We shall not derive the full SUSY Lagrangian and its superpotential W, but limit ourselves to the particle content. For a full derivation, the reader is referred to e.g. [36–38].

Much like in the Wess-Zumino model, fermionic and bosonic fields are placed in supermultiplets. The gauge fields are promoted to gauge superfields; the fermion fields are promoted to chiral scalar superfields. Specifying this set superfields almost suffices to define the *Minimal Supersymmetric Standard Model* – only the Higgs sector must be carefully dealt with.

The superpartners of matter fermions are called *sfermions*. For each chiral fermion in the Standard Model, there is a sfermion pair with the same internal quantum numbers. Partners of the quarks are the *squarks* (scalar quarks); likewise, the partners of the leptons are the *selectron*, *smuon* and *stau*. The Higgs and gauge bosons have fermionic superpartners: two *Higgsinos* and *gauginos*, the bino and the winos and gluinos. Superpartners are indicated with the same symbol as Standard Model particles, with a tilde added: e.g., the left-handed up-squark is denoted $\tilde{u}_L$.

In the MSSM, the usual Higgs doublet is promoted to

$$\phi \to H_u = \begin{pmatrix} h_u^+ \\ h_u^0 \end{pmatrix}. \tag{2.31}$$

[1] In scenarios with more superpartners, the fermionic fields would also have spin-1 partners. Such gauge bosons are not chiral.

However, unlike in the Standard Model, an analogy to $\phi^c = i\sigma_2\phi^*$ cannot be made. Such a field would necessarily be the scalar component of the *right-chiral* superfield $\widehat{h}_u^{0\dagger}$, which is forbidden in the superpotential, for two reasons. First, the superpotential W is required to be a holomorphic function [37, p. 22]. Hence, it cannot depend on both a field and on its complex conjugate. Second, introducing a Higgs doublet leads to a higgsino. Any triangular anomalous terms arising as the result of the introduction of this new particle cannot be cancelled by terms involving any of the other particles. Therefore, a second higgsino with opposite hypercharge is needed and introduced through a second doublet that gives mass to the down-type quarks:

$$H_d = \begin{pmatrix} \tilde{h}_d^- \\ \tilde{h}_d^0 \end{pmatrix}. \tag{2.32}$$

After electroweak symmetry breaking five bosonic degrees of freedom are left: two neutral scalars h and H, two charged scalars $h^\pm$ and one neutral pseudoscalar A. In addition, there are four accompanying Higgsinos. The particle content of the MSSM is shown in table 2.2.

The mass of the W boson is now given by $m_W^2 = \frac{g_1^2}{4}(v_u^2 + v_d^2)$, leaving three free parameters. The usual choice for these is $\tan\beta = v_u/v_d$, the pseudoscalar mass m_A and sgn(μ): the *value* of μ must be fixed to match the observed Z boson mass, but its sign can be left free, since

$$m_Z^2 = 2\frac{m_{H_d}^2 - m_{H_u}^2 \tan^2\beta}{\tan^2\beta - 1} - 2\mu^2. \tag{2.33}$$

Mixing in the MSSM

The spontaneous breaking of $SU(2)_L \times U(1)_Y$ results not only in mixing to form the W and Z bosons, but also in the mixing of the superpartners. Combinations of the neutral Higgsinos $\tilde{h}_u^0$ and $\tilde{h}_d^0$ with the electroweak gauginos $\tilde{W}_3$ and $\tilde{B}$ result in four *neutralinos*. These are denoted as $\tilde{\chi}^0_{1,2,3,4}$, with $\tilde{\chi}^0_1$ the lightest. *Charginos* are formed by combinations of the charged higgsinos and gauginos $\tilde{h}_u^+$, $\tilde{h}_d^+$, $\tilde{W}_1$ and $\tilde{W}_2$ and are indicated $\tilde{\chi}^\pm_{1,2}$. The mixing matrices are of tremendous importance to the phenomenology of the MSSM.

Moreover, the sfermions $\tilde{f}_{L,R}$ and squarks $\tilde{q}_{L,R}$ are not mass eigenstates and can mix. Their mixing is proportional to the mass of the Standard Model partner: the largest mixing occurs for the third generation squarks.

R-parity

Within the Standard Model, lepton and baryon number conservation is automatically guaranteed by gauge invariance. However, in the superpotential terms violating L and B but consistent with $SU(3)_C \times SU(2)_L \times U(1)_Y$ are present, such as $\lambda_{ijk}\epsilon_{ab}\widehat{L}_i^a\widehat{L}_j^b\widehat{E}_k^c$, $\lambda'_{ijk}\epsilon_{ab}\widehat{L}_i^a\widehat{Q}_j^b\widehat{D}_k^c$ and $\lambda''_{ijk}\widehat{U}_i^c\widehat{D}_k^c\widehat{D}_j^c$, where ϵ_{ab} is the two-dimensional Levi-Civita symbol. The presence of such terms is preferably avoided, as the resulting B- and L-violating processes are experimentally strongly constrained. Moreover, the presence of a squark would lead to rapid proton decay through e.g. $p \to e^+\pi^0$ (via $ud \to \tilde{s}_R^* \to e^+\overline{u}$), for which the width is roughly given by [37, p. 53]

$$\Gamma \sim m_p^5 \sum_{i=2,3} |\lambda'^{11i}\lambda''^{11i}|^2/m_{\tilde{d}_i}^4, \tag{2.34}$$

where the sum runs over down-type quarks. For couplings of $\mathcal{O}(1)$ and squark masses of approximately 1 TeV, proton decay would occur in under a second, in flagrant violation of the observed lower limit of 5.9×10^{33} years [78].

The terms could simply be set to zero, with the SUSY non-renormalisation theorem [79] ensuring they are not regenerated.[1] However, non-perturbative effects break the conservation of lepton and baryon number in any case.[2] Imposing the terms do not exist would be a step backward from the Standard Model, where the conservation is not assumed but a coincidence of the fact that no renormalisable terms that violate lepton or baryon number exist.

Instead of outright forbidding them, the B- and L-violating terms can be made to never appear by requiring the superpotential to be invariant under a new type of parity

$$R = (-1)^{3(B-L)+2s}, \tag{2.35}$$

where s is the spin of the field. The scalar and fermion components of a chiral superfield have opposite R-parities. The same holds for the spinor and vector components of a gauge superfield. In other words: R-parity distinguishes between Standard Model and SUSY particles.

A consequence of R-parity conservation is that the lightest supersymmetrical particle is inherently stable. Stated differently, R-parity conserving SUSY models provide a candidate particle for cold dark matter. Usually, this is the $\tilde{\chi}_1^0$, a mixture of bino, wino and Higgsino fields.

2.3.2 Supersymmetry breaking

At this stage, the proverbial elephant in the room is the fact that SUSY particles have never been observed. Clearly, if supersymmetry exists a mechanism by which it is broken must be at work, allowing the Standard Model particles to be light and the currently undiscovered particles to be heavy. From a theoretical perspective, one expects the breaking to occur spontaneously, similar to electroweak symmetry breaking in the Standard Model. The Lagrangian is then invariant under supersymmetry, but the vacuum is not.

Many mechanisms by which supersymmetry is spontaneously broken have been proposed. These include gravity-mediated breaking [80], gauge-mediated SUSY breaking (GMSB) [81] and anomaly-mediated SUSY breaking (AMSB) [82]. A common feature of these mechanisms is that they extend the MSSM to include new particles and interactions at very high mass scales.[3]

Lacking any consensus on the SUSY breaking, the breaking terms are added explicitly in the MSSM. In other words, we profess our ignorance of the breaking mechanism and assume the

1 The non-renormalisation theorem states that any terms not present at leading order in the superpotential also do not appear through quantum corrections at any higher order.

2 Cf. $U(1)$ anomalies in the Standard Model: these perturbative terms would break gauge invariance in case they do not add up to zero. Similar but *non*-perturbative effects can arise through graviton interactions.

3 One could hence argue that the problem of electroweak symmetry breaking is merely shifted to a higher energy scale and that supersymmetry provides no additional understanding of the mechanism at all.

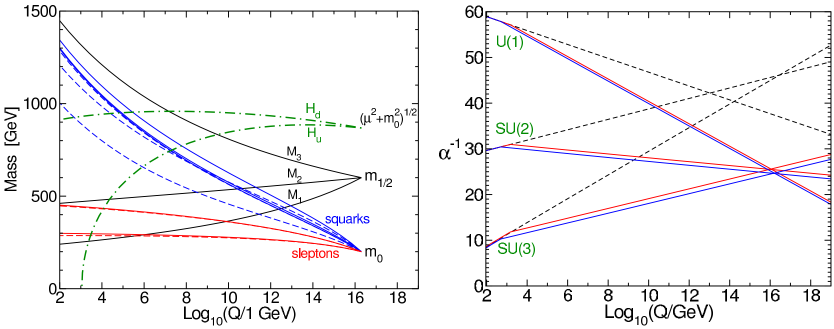

Fig. 2.2 · Evolution of scalar and gaugino mass parameters with boundary conditions imposed at $Q_0 = 2 \times 10^{16}$ GeV; the parameter $\mu^2 + m^2_{H_u}$ runs negative, provoking electroweak symmetry breaking (left). Two-loop renormalisation group evolution of the inverse gauge couplings $\alpha^{-1}(Q)$ in the Standard Model (dashed lines) and the MSSM (solid lines) (right). Taken from [37].

model to be an effective low-energy theory[1] with terms that break the symmetry added simply because they are needed. These terms should be soft (of positive mass scale) to maintain a hierarchy between the electroweak scale and higher mass scales. The possible soft terms in their most general form are

$$\mathcal{L}_{\text{soft}} = -m^2_{ij}\phi^*_i\phi_j - \left(\frac{1}{2}\sum_a M_a\lambda^a\lambda^a + \frac{1}{6}a^{ijk}\phi_i\phi_j\phi_k + \frac{1}{2}b^{ij}\phi_i\phi_j + c^i\phi_i + \text{h.c.}\right), \quad (2.36)$$

which consist of gauginos λ^a with masses M_a for each of the gauge groups, a scalar mass term m^2_{ij}, scalar tri- and bilinear couplings a^{ijk} and b^{ij}, and tadpole couplings c^i. Adding these explicit mass terms to the Lagrangian breaks the mass degeneracy between Standard Model particles and their superpartners.

Renormalisation group equations (RGEs) are used to run down the masses to the weak scale. The Higgs mass is now protected by additional loop corrections to the propagator that are equal but opposite in sign to the ones in the Standard Model. As a consequence the SUSY particles that correct the divergences in (2.22) cannot be too heavy, or fine-tuning would still be required. Generally, fine-tuning of the order of 1 % is deemed acceptable[2]; this leads to a mass scale of several TeV for SUSY particles. Moreover, the backward evolution of m^2_h to the weak scale is particularly useful: m^2_h may become negative. The consequence is not that the Higgs is a tachyon, but that the arbitrary sign $\mu^2 < 0$ can be explained in an elegant way: electroweak symmetry breaking occurs naturally. As an additional bonus the couplings of the three forces in the Standard Model appear to unify at a scale $\sim 10^{16}$ GeV. Both of these features are illustrated in fig. 2.2.

2.3.3 Phenomenology

The explicit breaking of the mass degeneracy in the MSSM has the consequence that 105 additional parameters are added to the theory. In addition to the parameters of the Standard Model, the

---

1 Clearly, the qualification 'low energy' is rather relative in this context.

2 The amount of fine-tuning using a set of MSSM parameters $\{a_i\}$ is quantified through the effect varying them has on the Z mass: $(\Delta m_Z/m_Z) < c_i\,\Delta a_i/a_i$. Typically, $c_i \sim 10 - 100$ is considered acceptable fine-tuning [see 36, p. 213; 83].

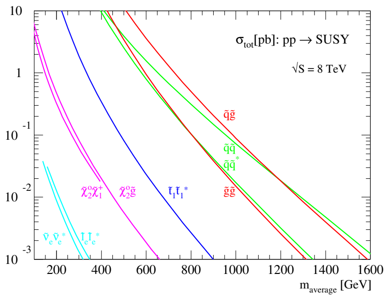

Fig. 2.3 · LHC SUSY production cross-sections at $\sqrt{s} = 8\,\text{TeV}$ for various processes as a function of sparticle mass. Squarks and gluinos are the most abundantly produced sparticles.

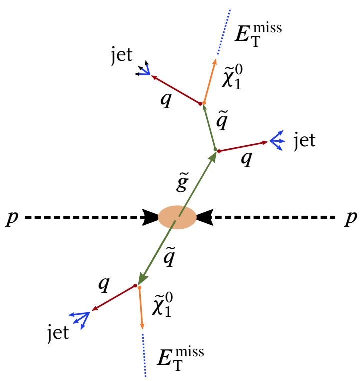

Fig. 2.4 · Schematic view of squark–gluino production at the LHC. A squark $\tilde{q}$ and gluino $\tilde{g}$ are produced that each decay directly to quarks and neutralinos. Supersymmetrical particles are indicated in green.

MSSM thus has 124 independent parameters. Searches for supersymmetry face an uphill battle in exploring this parameter space. If SUSY is indeed realised in nature, what can be produced at a collider experiment depends on the masses at the weak scale and the mixing matrices.

For any given mass, the most abundantly produced sparticles will be squarks and gluinos, whose coupling to the coloured particles in the proton is the strongest. The production cross-section of sparticles at a centre-of-mass energy $\sqrt{s} = 8\,\text{TeV}$ is shown in fig. 2.3. Depending on their masses, either production mechanism is dominant. For $m_{\tilde{q}} \ll m_{\tilde{g}}$ squark production will be the most abundant, and vice versa. In the case $m_{\tilde{q}} \sim m_{\tilde{g}}$, associated squark–gluino production may occur.

The dominant decay of these particles is $\tilde{q} \to q\tilde{\chi}_1^0$ and $\tilde{g} \to q\bar{q}\tilde{\chi}_1^0$, leading to an experimental signature of jets and missing energy. A graphical example is shown in fig. 2.4.

In order to guide the experimental searches, simplifying assumptions must be made. These are described in the next sections.

The constrained MSSM

The phenomenology of supersymmetric theories depends greatly on the exact SUSY breaking mechanism. Minimal supergravity (MSUGRA) [84] and the constrained MSSM (CMSSM) [85] are two popular theories. In these models, gravity is the mediating force between the hidden, unbroken sector at high energy and the MSSM. The soft breaking terms are generated naturally in such a way: the gauge group $SU(5)$ breaks into the Standard Model's gauge group using RGEs from the Planck to the GUT scale [36, p. 272].

In the minimal theory, several assumptions are made on the full supergravity Lagrangian. Next to coupling unification at the GUT scale, the masses in the model are unified as well. Gauginos have a common mass $M_1 = M_2 = M_3 = m_{1/2}$; all scalars have a common mass $m_{\tilde{q}}^2 = m_{\tilde{\ell}}^2 = m_{H_u}^2 = m_{H_d}^2 = m_0^2$. Moreover, all trilinear couplings are assumed to be equal to A_0 at the GUT scale. Using RGEs the full MSSM spectrum can be predicted and parametrised by five parameters: m_0 and $m_{1/2}$, the trilinear coupling A_0, $\tan\beta = v_u/v_d$ and $\text{sgn}(\mu)$. In MSUGRA models, the gaugino mass parameters are related; at the LHC one expects a mass ratio $m_{\tilde{g}} : m_{\tilde{W}} : m_{\tilde{B}}$ of approximately $6:2:1$ [37, p. 99].

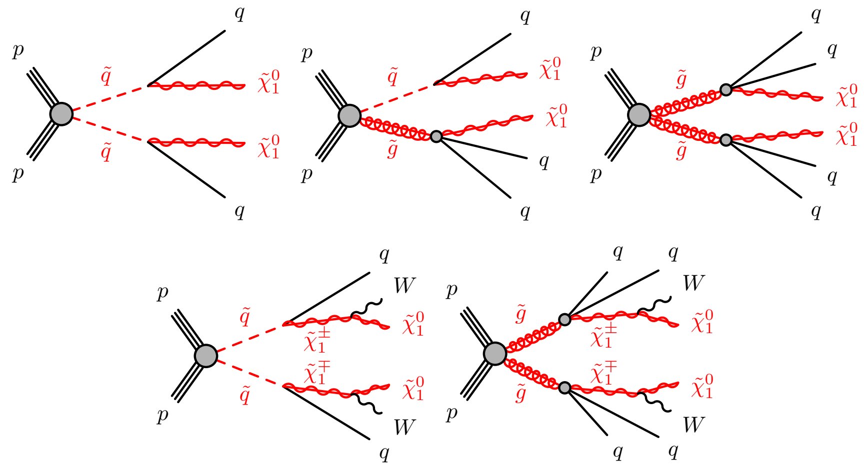

Fig. 2.5 · Feynman diagrams for the direct production of squarks and gluinos. In the bottom row, the produced sparticles decay through a $\tilde{\chi}^{\pm}$, leading to a W boson in the final state. No distinction between quark flavours and between particles and antiparticles is made.

Simplified models

The enormous parameter space of even a theory such as MSUGRA makes it difficult to define a search strategy. Limits on a particle mass obtained using one particular model with a set of parameters do not necessarily correspond with another model. To remedy this, ATLAS and CMS rely on so-called *simplified models* [86]. These models serve several purposes: to identify the reach of search strategies; to aid the characterisation of any signals of new physics [87]; and to use the results in the setting of limits on larger models. Simplified models in which only one type of sparticle is accessible are further motivated by scenarios of split supersymmetry [88–90].

Simplified models rely on an effective Lagrangian that describes a subset of particles and interactions while integrating out the rest. In other words, only a certain particle, e.g. a gluino, can be produced at the LHC. Such a process would be governed by the Lagrangian

$$\mathcal{L}_{\text{int}} = \frac{\lambda_i^2}{M_i^2} \tilde{g} q_i \overline{q}_i \tilde{\chi}^0 + \text{h.c.}, \tag{2.37}$$

where i runs over the quark flavours, λ_i is the Yukawa coupling for the quark–gluino–neutralino vertex and M_i is the effective scale of the interaction.

In case of a non-observation, limits on simplified models can be used to obtain limits in larger models [91]. For each of the possible decays in the larger model the expected number of events in the signal region of an analysis can be calculated:

$$N = \sigma_{\text{tot}} \times \mathcal{L}_{\text{int}} \times \sum_i \epsilon_i \times P_i \times \mathcal{B}_{1i} \times \mathcal{B}_{2i}, \tag{2.38}$$

where σ_{tot} is the total production cross-section for the model, $\mathcal{L}_{int}$ the integrated luminosity used and the sum runs over all simplified models considered. In the sum, ϵ_i is the acceptance times efficiency for a model, P_i the production fraction of the model and $\mathcal{B}_{1i}$ and $\mathcal{B}_{2i}$ the branching ratios for the observed decays, which are identical in the case of pair production.

Simplified models used later in this thesis include the pair production of gluinos and of squarks, and squark–gluino associated production, first proposed in [92]. In the pair-production models, the produced sparticle either decays directly ($\tilde{q} \to q\tilde{\chi}_1^0$ or $\tilde{g} \to q\bar{q}\tilde{\chi}_1^0$), or via an intermediate chargino $\tilde{\chi}^{\pm}$ ($\tilde{q} \to q\tilde{\chi}^{\pm} \to qW\tilde{\chi}_1^0$ or $\tilde{g} \to q\bar{q}\tilde{\chi}^{\pm} \to q\bar{q}W\tilde{\chi}_1^0$). An additional simplified model where all processes contribute (a phenomenological MSSM model) is also used for interpretations. Fig. 2.5 shows the decays in these simplified models.

Several drawbacks to the use of simplified models must be noted. First of all, they emphatically do not include any other parameters than the ones considered. Given the context of supersymmetry trying to elegantly solve the Standard Model's shortcomings, this lack of complexity is a gross oversimplification of the parameter space. Moreover, in the case of certain simplified models, e.g. squark-pair production, the cross-section can depend hugely on the parameters not considered (in this case, the gluino mass). Finally, the assumption of a branching ratio of 100 % is a further oversimplification.

2.3.4 Existing constraints

In order to discover sparticles, one needs to have an idea of where to start looking. In many previous experiments SUSY has already been sought, including at dark matter detection experiments (both direct and indirect) and at colliders (LEP, Tevatron). Many of these searches have concentrated on specific models, such as the CMSSM. Their limits are not easily translated to different scenarios. Limits set by ATLAS and CMS are not discussed here; they are included in the discussion on the results obtained in this thesis. R-parity violating models are outside the scope of this thesis and therefore ignored.

Limits on direct production of sparticles were set by both LEP and the Tevatron. The CDF and DØ experiments obtained limits near 400 GeV on the masses of squarks and gluinos in the CMSSM [93, 94]. These were obtained by searching for events without leptons, hard jets and a large amount of missing transverse energy. The electroweak SUSY sector is harder to constrain due to the mixing matrices. A combination of LEP searches set a limit of 47 GeV on the lightest neutralino and of 92 GeV on the lightest chargino in the CMSSM [95, 96]. Light sleptons were excluded up to masses of 80 GeV to 100 GeV by DELPHI [97] and ALEPH [98], again in the CMSSM. However, relaxing the model's assumptions, no masses are excluded at all [99].

Astrophysical constraints go beyond those obtained at colliders, and primarily set limits on the lightest supersymmetrical particle as a stable WIMP (weakly interacting massive particle). Several experiments have obtained results searching for WIMP annihilation. Non-null results include annual modulation in DAMA/LIBRA [100] and COGENT [101] light WIMP signals and an excess of positrons over electrons in cosmic rays observed by PAMELA [102] and AMS [103, 104]. However, constraints from XENON100 [105] and LUX [106] on the WIMP–nucleon cross-section would rule out all WIMP interpretations of these signals.

A more stringent limit comes from the observed dark matter relic density. Assuming dark matter is a (thermal) relic from the early universe, the current observations can be explained by a balance in the annihilation conditions caused by the universe's expansion. The current measurements are $\Omega_\chi h^2 = 0.1148 \pm 0.0019$ from WMAP [107] and $\Omega_\chi h^2 = 0.1199 \pm 0.0027$ by the Planck collaboration [74].[1] These results rule out large swaths of SUSY parameter space, but not all models [108].

Precision tests from flavour physics and electroweak observables complement these direct measurements. Restrictions come from the non-observation of flavour-changing neutral currents (FCNCs) [109], and from measurements of the branching fractions of $b \to s\gamma$, $B_s \to \mu^+\mu^-$ and other observables in the flavour sector [110]. In particular the measurement of $B_s \to \mu^+\mu^-$ [111, 112] caused a stir for being in agreement with the Standard Model, but most SUSY scenarios not ruled out by the observed Higgs mass are in fact compatible with the observation [113]. However, an observed excess in $\overline{B} \to D^{(*)}\tau^-\overline{\nu}_\tau$ bodes ill for supersymmetry: it purports to rule out Higgs doublet models at 99.8 % confidence level [114]. Finally, the latest measurement of $(g-2)_\mu$ is incompatible [115] with the Standard Model[2], and favours certain SUSY models [117].

The discovery of a Higgs boson with a mass around 125 GeV has additional consequences for supersymmetry. At tree level, the lightest Higgs boson mass in the MSSM is bounded from above by $m_h < m_Z|\cos(2\beta)|$, or roughly 90 GeV. Radiative corrections raise the mass at one-loop level to approximately

$$m_h^2 = m_Z^2 \cos^2(2\beta) + \frac{3m_t^4}{2\pi^2 v^2}\left[\log\left(\frac{M_S^2}{m_t^2}\right) + \frac{X_t^2}{M_S^2}\left(1 - \frac{X_t^2}{12M_S^2}\right)\right], \quad (2.39)$$

where m_t is the top mass and $M_S = \sqrt{m_{\tilde{t}_1} m_{\tilde{t}_2}}$. The stop mixing parameter X_t is given by $X_t = A_t - \mu\cot\beta$, where A_t is the stop trilinear coupling. For maximal stop mixing, this gives an upper bound $m_h \leq 135$ GeV [118]: the observation of the current Higgs boson is perfectly compatible with the MSSM. The more constrained GMSB and AMSB models can reach a lightest Higgs with $m_h \sim 121$ GeV and are ruled out in their current form. The CMSSM can produce a 125 GeV Higgs boson, but with high stop masses, high $\tan\beta$ and large fine-tuning [119].

In summary, most these constraints do not rule out much of supersymmetry, with the notable exception of the Higgs mass. Squarks and gluinos are allowed to be as light as several hundred GeV, depending on their decay while the LSP is barely constrained at all. Light sleptons are permitted, provided they are heavier than 92 GeV. Finally, the discovery of the Higgs boson with a mass of 125 GeV implies that either most sparticles are in the range of 1 TeV to 3 TeV or that near-maximal mixing of the top squarks occurs, in which case the lightest stop has $m_{\tilde{t}} > 200$ GeV.

---

[1] The universe's matter density is written as a fraction of the closure density ρ_c, the density required to stop the expansion: $\Omega = \rho/\rho_c$. In the expression for the dark matter relic density, h is a dimensionless constant; see e.g. [36, p. 223].

[2] It must be noted the excess of 3.6 σ decreases to 2.4 σ when using τ data rather than e^+e^- and strong theoretical uncertainties on the calculation remain [116].

CHAPTER THREE

The LHC and the ATLAS detector

IN ORDER TO study the properties of elementary particles and to discover new heavy particles, one needs a way of producing these particles in a controlled environment and be able to measure their decay products precisely. In order to do so, particle accelerators are used to boost two beams of particles to high energies, before these beams are made to collide with each other or with stationary targets. Purpose-built detectors observe and record the results of these collisions.

This chapter describes the Large Hadron Collider (LHC), a circular proton–proton collider located at the Franco-Swiss border, that is operated by the European Organisation for Nuclear Research, more commonly known by its acronym CERN, for the provisional *Conseil Européen pour la Recherche Nucléaire*. It also describes the ATLAS experiment, A Large LHC Apparatus, one of the purpose-built detectors used to identify particles produced in collisions at the LHC. The design, configuration and performance of both the accelerator and the detector are discussed.

3.1 The Large Hadron Collider

The Large Hadron Collider [120] is a circular proton–proton accelerator located at CERN, on the border between France and Switzerland close to Geneva. Housed in the 26.7 km-circumference tunnel originally built for its predecessor LEP, the Large Electron Position collider [121], which shut down in 2000, the machine is located 170 m below ground near the Jura mountains and 45 m below ground on the side of Lac Léman. Constructed between 1998 and 2008, the LHC is designed to collide beams of protons at a centre-of-mass energy of $\sqrt{s} = 14\,\text{TeV}$ at an instantaneous luminosity of $10^{34}\,\text{cm}^{-2}\,\text{s}^{-1}$.

Following an incident during commissioning in 2008, the collider has been operated during Run I at a lower centre-of-mass energy of $\sqrt{s} = 7\,\text{TeV}$ in 2010 and 2011, followed by a period of data taking at 8 TeV in 2012. Its design luminosity and energy will only be reached in Run II, from 2015 onwards. Nevertheless, the LHC is the world's most powerful particle accelerator, a title previously held by the Tevatron, formerly operated by Fermilab and located in Batavia, Ill., US, which collided protons and antiprotons at $\sqrt{s} = 1.96\,\text{TeV}$ until 2011.

Next to colliding protons, the LHC also has a programme to study the collisions of heavy ions, as well as protons with heavy ions. Such collisions are not studied in this thesis, however.

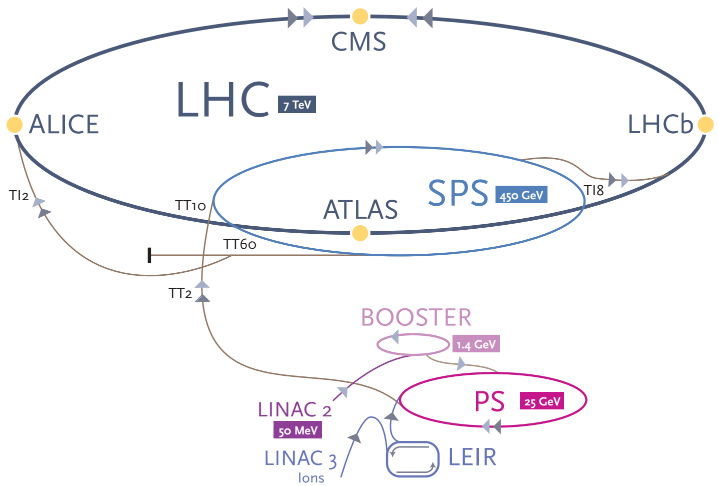

Fig. 3.1 · CERN's accelerator complex (not to size) with the accelerator chain used for this analysis. The four flagship experiments are located along the LHC ring. The energies indicate the design energy per beam. Adapted from [129].

3.1.1 Experiments at the LHC

At four *interaction points* along the ring, the beams inside the LHC collide. Around these points, detectors have been built to measure the decay products of the collision. ATLAS [122] and CMS (compact Muon solenoid) [123] are two *general-purpose* detectors located on opposite sides of the ring, while LHCb (LHC-beauty) [124] and ALICE (A Large Ion collider Experiment) [125] are two specialised experiments, respectively used for investigating the decay of B hadrons and studying the properties of high energy density nucleus–nucleus interactions.

Three smaller experiments are also located at the LHC: LHCf [126], two calorimeters located 140 m from ATLAS and for the study of very forward production of neutral particles; MOEDAL [127], an experiment in the LHCb cavern dedicated to searching for magnetic monopoles; and TOTEM [128], which is used to study elastic scattering and the total proton–proton cross-section, a measurement used by all other experiments.

3.1.2 Accelerator complex and design

The LHC relies on previous accelerators built at CERN for the production of its proton beams. Protons are pre-accelerated in several stages before being injected into the LHC. Fig. 3.1 shows this accelerator complex schematically.

Sample production and acceleration

All protons used in the experiments originate from a single bottle of hydrogen. Hydrogen atoms are stripped of their orbital electrons to obtain protons, which are then accelerated to approximately 50 MeV in the linear accelerator LINAC 2. These protons are injected into the proton booster to form the first bunches, squeeze these bunches and accelerate them to 1.1 GeV. Subsequently, the beam is transferred to the Proton Synchrotron (PS), accelerated to 25 GeV, and transferred to the Super Proton Synchrotron (SPS), before finally being injected into the LHC at 450 GeV. Once injected, the protons are ramped up to their operating energy: 3.5 TeV in 2010–2011 and 4 TeV in 2012.

Heavy ions are produced from ionised lead vapour, heated to approximately 550 °C. From the resulting sample, Pb^{29+} ions are selected and accelerated to an energy per nucleon of 4.2 MeV/u in LINAC 3. After being passed through a carbon foil to obtain Pb^{54+}, the ions are accelerated to 72 MeV/u in the Low Energy Ion Ring (LEIR) [130]. The procedure then proceeds similar to the one for protons: the PS prepares the first bunch structure and further accelerates the beam to 5.9 GeV/u. A next stripping foil selects the final sample of Pb^{82+}, and the SPS accelerates the beam to 177 GeV/u. Finally, the ions are injected into the LHC in both clockwise and anti-clockwise directions and accelerated to their final energy of 2.76 TeV/u.

The LHC design

The LHC collides bunches of protons grouped into small bunches, each of them containing approximately 10^{11} protons and separated in time by 25 ns.[1] In order to keep these bunches on their trajectories, 1232 superconducting 14.3 m-long dipoles are employed, providing a maximum magnetic field of 8.33 T. To achieve their high field strength, the magnets are cooled using liquid helium at a temperature of 1.9 K. Due to the diameter of the tunnel, which is only 3.7 m, the LHC employs a novel design where two separate vacuum beam pipes and separate dipole systems are both housed within the same iron yoke and both rely on the same cryostat.

Beams are accelerated using Radio Frequency (RF) cavities placed at a single point along the ring. These cavities accelerate the protons each revolution through an electric field of 2 MV oscillating at 400 MHz. In 2012, ramping up the beam energy from the injection energy of 450 GeV to the collision energy of 4 TeV took approximately 20 minutes.

Collisions take place at four points along the ring, with an incidence angle of 300 µrad. The produced number of events N for a process with a cross-section σ depends on the machine luminosity L:

$$N = L \times \sigma, \tag{3.1}$$

where, for a Gaussian beam distribution, L is given by

$$L = \frac{N_{b_1} N_{b_2} n_{b_1} n_{b_2} f \gamma}{4\pi \epsilon \beta^*} F, \tag{3.2}$$

with N_b the number of particles per bunch, n_b the number of bunches per beam, f the revolution frequency of the machine, γ the relativistic gamma factor, ϵ_n the normalised beam emittance, β^* the β-function at the point of interaction, and F the geometric reduction factor due to the crossing angle of the beams.

The beam emittance is determined during the preparation of bunches and defines the phase space volume the beam occupies. The amplitude function β is a parameter of the dipole config-

[1] The bunch spacing of 25 ns is the design value. In 2012, a spacing of 50 ns was used.

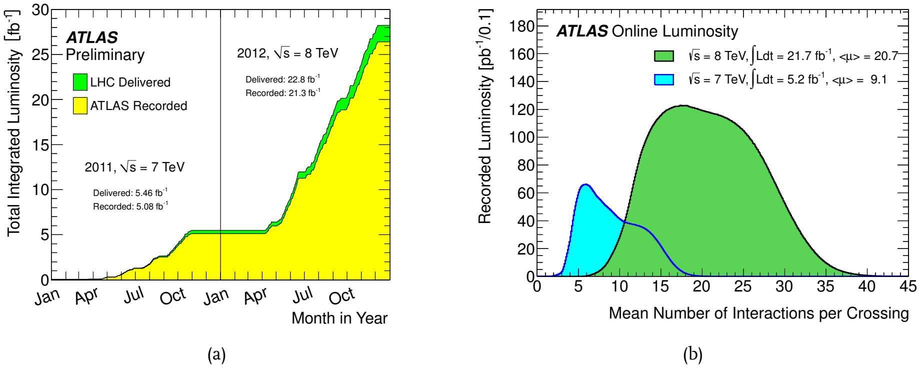

Fig. 3.2 · Total luminosity delivered to and recorded by ATLAS in 2011 and 2012 during p–p runs (left) and the mean number of interactions per crossing during those data-taking periods (right).

uration; it is given by $\beta = \pi\sigma^2/\epsilon$, where σ is the cross-sectional size of the beam. In 2012, the LHC operated using 1380 bunches and $\beta^* = 0.6\,\text{m}$.

At the LHC, the design instantaneous luminosity is $\sim 10^{34}\,\text{cm}^{-2}\,\text{s}^{-1}$, which is two orders of magnitude greater than the value achieved at the Tevatron.

The instantaneous luminosity (3.2) decreases with time, due to beam emittance growth and the decreasing number of protons per bunch. During typical operations, beams are *dumped* after the instantaneous luminosity becomes too low and the whole injection process starts anew. In practice, the beams get dumped also for other reasons and the time after a beam is dumped is used for short-term required maintenance, leading to an up-time of the accelerator of around 30 %. At the LHC, the instantaneous luminosity is determined once per second. Stored luminosity information is averaged over *luminosity blocks*, each approximately 2 min long.

The total number of events produced is proportional to the *integrated* luminosity

$$\mathcal{L} = \int L\,\mathrm{d}t, \tag{3.3}$$

which is typically quoted, together with the collision energy, as the size of an experiment's data-set. The adjective integrated is often dropped, in which case the term luminosity refers to the integrated luminosity. Fig. 3.2a shows the integrated luminosity for ATLAS during 2011 and 2012.

Closely related to the instantaneous luminosity is the mean number of collisions per bunch crossing, known as *pile-up*, and defined as

$$\mu = \frac{L\sigma_{\text{inel.}}}{n_b f}, \tag{3.4}$$

where $\sigma_{\text{inel.}}$ is the total inelastic proton–proton cross-section. Fig. 3.2b shows the luminosity-weighted mean number of interactions per crossing for 2011 and 2012. With the higher instantaneous luminosity in 2012, $\langle\mu\rangle$ increased from ~ 9 to ~ 21.

3.1.3 Proton–proton collisions at the LHC

In collisions at a centre-of-mass energy $\sqrt{s} = 14\,\text{TeV}$, the total proton–proton cross-section is expected to be approximately 80 mb, corresponding to 10^9 interactions per second at the LHC's design luminosity. The vast majority of these events will be uninteresting events with high longitudinal momentum and a transverse momentum of around 500 MeV. These events are called *minimum-bias events* and not particularly interesting to study at the LHC. Instead, one is interested in *hard scattering* events: inelastic collisions that lead to high transverse momentum in the decay products. The effective energy for such collisions is given not by the collision energy of the protons, but of the partons involved in the interaction:

$$\sqrt{\hat{s}} = \sqrt{x_1 x_2}\sqrt{s}, \tag{3.5}$$

where $x_{1,2}$ refers to the fraction of the incoming proton energy in the interacting partons.

For the production of heavy elementary particles, this has important consequences. Whereas for the production of a particle with a mass of around 100 GeV each parton needs to carry only $\sim 1\,\%$ of the proton's energy, this number increases fast for larger masses. Taking the proton's parton distribution function (PDF) into account, quark–anti-quark processes are rapidly suppressed w.r.t. quark–quark induced processes, which in turn are already small compared to gluon–gluon processes. These effects are important for the strong production of e.g. heavy supersymmetrical particles, as we shall also see in chapter 8.

3.2 The ATLAS experiment

The ATLAS detector [122] is a general-purpose detector, designed for detecting processes with a wide range of experimental signatures. Its physics programme covers the full range of the LHC programme and has multiple goals:

1. to perform precise measurements of Standard Model particles and processes, in particular the top quark;
2. to elucidate the origin and working of the electroweak symmetry breaking mechanism; in particular, discovering or excluding the Higgs boson;
3. to search for direct evidence of physics beyond the Standard Model, such as particles predicted by supersymmetry;
4. to study the properties of quark–gluon plasmas resulting from heavy-ion collisions;
5. to study flavour physics and CP-violation.

The scope of these signatures has led to a detector design that covers many possible decay scenarios. The LHC physics goals and environment translate to the following detector requirements:

- fast and high-granularity detectors, in order to cope with the large number of particles coming from the high-luminosity collisions and to reduce the effects of pile-up;
- a large acceptance: almost full angular coverage in order to detect leptons and jets, and in order to precisely reconstruct missing energy;

Table 3.1 · Summary of the performance requirements for the ATLAS detector, with units in GeV [122].

Detector component	Resolution	Coverage	
		Measurement	Trigger
Tracking	$\sigma(p_T)/p_T = 0.05 \times p_T \oplus 0.01$	$\|\eta\| < 2.5$	–
EM calorimetry	$\sigma(E)/E = 0.10/\sqrt{E} \oplus 0.007$	$\|\eta\| < 3.2$	$\|\eta\| < 2.5$
Hadronic calorimetry	$\sigma(E)/E = 0.50/\sqrt{E} \oplus 0.03$	$\|\eta\| < 3.2$	$\|\eta\| < 3.2$
	$\sigma(E)/E = 1.00/\sqrt{E} \oplus 0.10$	$3.1 < \|\eta\| < 4.9$	$3.1 < \|\eta\| < 4.9$
Muon spectrometer	$\sigma(p_T)/p_T = 0.10$ ($p_T = 1$ TeV)	$\|\eta\| < 2.7$	$\|\eta\| < 2.4$

- excellent charged-particle momentum resolution, and good efficiency in reconstruction of tracks coming from such particles;
- excellent calorimetry in order to detect electrons and photons, and a hadronic calorimeter with full coverage for accurate jet measurements and accurate reconstruction of missing energy;
- good identification and reconstruction of muons.

The requirements on the various subdetectors ATLAS consists of are listed in table 3.1. In addition, the design requirements include the error on the impact parameters and the resolution of reconstructed vertices.

For high-momentum particles in the detector's central region, the resolution on the transverse impact parameter d_0 is required to be 10 µm; that on the longitudinal impact parameter $z_0 \sin\theta$ to be 91 µm. The impact parameter d_0 is defined as the perpendicular distance between the point of closest approach of a track to the primary vertex; z_0 the distance between that point and the z-axis. The resolution on the azimuthal angle ϕ is 70 µrad; for the polar angle the resolution on $\cot\theta$ is required to be 0.7×10^{-3}.

The resolution requirement on the reconstructed primary vertex is less than 1 mm in the z direction, necessitated by the lifetimes and Lorentz boosts of τ leptons and B hadrons.

3.2.1 Detector layout

As illustrated in fig. 3.3, ATLAS is built out of several subdetectors. The *inner detector* (ID) sits closest to the interaction point (IP), and is composed of three tracking detectors: the pixel detector, the *semiconductor tracker* (SCT) and the *transition radiation tracker* (TRT). All tracking systems operate in the presence of a solenoidal magnetic field in order to enable the measurement of charged-particle momenta. Two calorimeters, a *liquid-argon* (LAr) *calorimeter* and the *tile calorimeter* surround the inner detector, and are used to measure the energies of electrons, photons and hadrons, and to reconstruct jets. Finally, the *muon spectrometer* (MS) is employed for momentum and position measurements of muons. The muon systems are housed inside a toroidal magnetic field.

All of the detector components are discussed in §3.2.2–3.2.5. The layered detector construction ensures all visible particles can be uniquely reconstructed, as illustrated in fig. 3.4. Very weakly

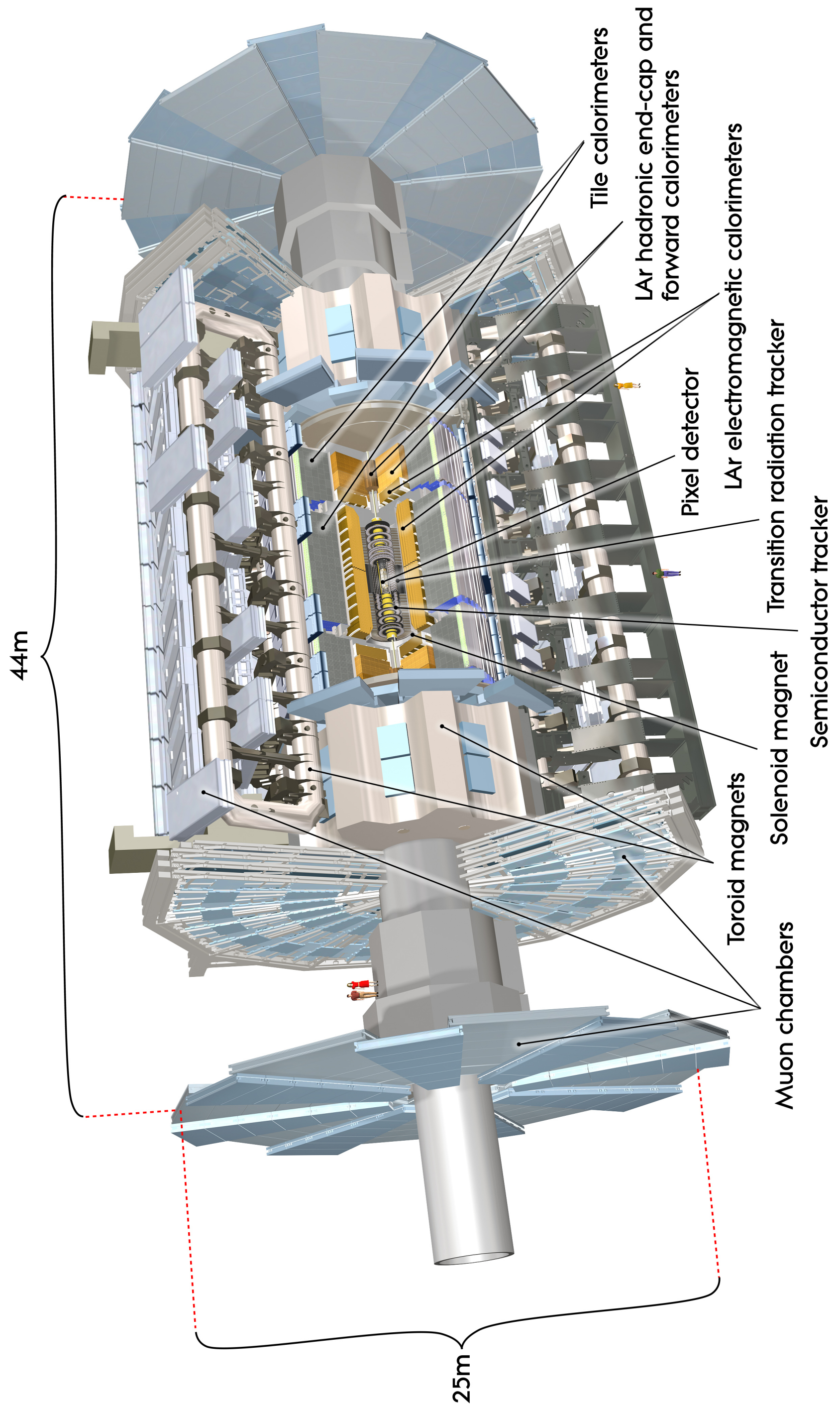

Fig. 3.3 · A schematic illustration of the ATLAS detector, with its size and various components indicated [131].

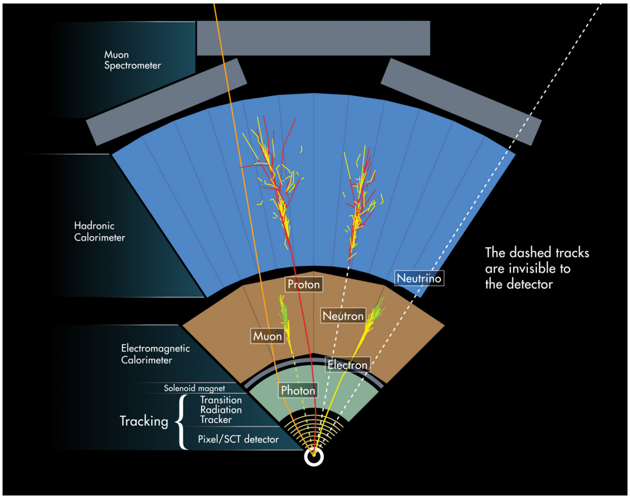

Fig. 3.4 · An illustration of the ways different particles are detected in ATLAS [132].

interacting particles such as neutrinos and stable non-interacting particles such as the lightest supersymmetrical particle escape ATLAS undetected; their presence must be inferred from a total momentum imbalance in the transverse plane.

Coordinate system

ATLAS uses a right-handed coordinate system, with the interaction point as the origin. The z-axis corresponds to the beam direction, with $z > 0$ in the anti-clockwise direction. The x-axis points to the centre of the LHC ring, and the y-axis points upwards. A cylindrical coordinate system is normally used, defined by

1. $R^2 = x^2 + y^2$, the distance from the interaction point;
2. $\phi \in [-\pi, \pi]$, the azimuthal angle measured around the beam axis;
3. $\theta \in [0, \pi]$, the angle with respect to the beam axis.

The polar angle θ is commonly re-expressed as the *pseudo-rapidity* $\eta = -\ln\tan(\theta/2)$, which has the benefit that differences are invariant under Lorentz boosts. Geometric distances in the (η,ϕ)-plane are defined as $\Delta R = \sqrt{(\Delta\eta)^2 + (\Delta\phi)^2}$. Transverse momenta are calculated with $p_T = p\sin\theta$. Since the total momentum in the z direction is zero prior to a collision, any momentum p_z along the beam axis after the interaction is commonly attributed to the underlying event, as it is due to any imbalance between the incoming momenta $x_1 p_1$ and $x_2 p_2$.

3.2.2 Magnet system

The magnet system [133] used in ATLAS consists of two parts: a solenoid to provide the magnetic field for the inner detector, and a toroid to provide the magnetic field for the muon spectrometer. Schematically, the magnet system is shown in fig. 3.5. All magnets in ATLAS are superconducting and cooled to a temperature of 4.5 K.

Solenoid magnet system

The solenoid magnet system of the inner detector is 5.8 m long, has a diameter of 2.5 m and is built inside the electromagnetic calorimeter. The homogeneous magnetic field of 2 T runs parallel to the beam axis and is generated by a nominal current of 8 kA running through the bore. It provides a bending power of $\langle BL \rangle \sim 2.3\,\mathrm{T\,m}$. To keep the amount of material before the calorimeters minimal, the solenoid has been designed to have only a thickness of two-thirds of the radiation length.

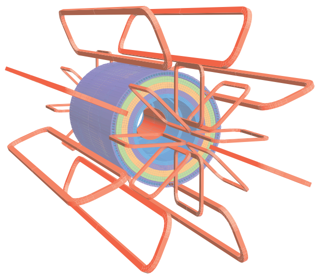

Fig. 3.5 · Geometry of the ATLAS magnet system and Tile Calorimeter steel. The solenoid lies inside the calorimeter volume [122].

Toroid magnet system

ATLAS' toroidal magnetic field is generated in three air-core superconducting toroids: a barrel toroid and two end-cap toroids at both sides of the detector. The barrel toroid consists of eight coils that give ATLAS its characteristic shape, and provides a bending power of $\langle BL \rangle \sim 3.2\,\mathrm{T\,m}$. Each of the two end-cap toroids, which provide the magnetic field between the first two layers of the muon spectrometer's end-caps, have a bending power of $\langle BL \rangle \sim 6.3\,\mathrm{T\,m}$. Both toroidal systems are powered by a 21 kA current.

3.2.3 Inner detector

The inner detector [134, 135] is used for tracking and vertexing. Contained inside the 2 T field generated by the solenoid, it identifies primary and secondary vertices, measures impact parameters at high resolution and provides a p_T measurement for charged particles with a resolution of 30 % at $p_\mathrm{T} = 500$ GeV. The pseudo-rapidity coverage is $|\eta| \geq 2.5$.

Two requirements drive the design of the tracking system: the need to properly reconstruct tracks and vertices in the high-density environment of the LHC, and the need to operate in high levels of radiation. Balancing these against the desire to keep the amount of material at a minimum, the inner detector has been built out of three subsystems:

pixel detectors closest to the interaction point [137]. The pixel detector is made of three concentric layers around the beam axis in the barrel region at a radial distance of 5–13 cm and two end-caps. Each end-cap consists of three discs perpendicular to the beam direction at 495 mm, 580 mm and 650 mm from the interaction point.

In total, 1744 modules with pixels of $50 \times 400\,\mu\mathrm{m}^2$ result in 80.4 million readout channels, with a resolution of $\sigma_{R-\phi} = 10\,\mu\mathrm{m}$ in the radial direction and $\sigma_z = 115\,\mu\mathrm{m}$ in the z direction. To suppress noise and protect the detector from radiation damage, the silicon modules are cooled between $-5\,^\circ\mathrm{C}$ to $10\,^\circ\mathrm{C}$.

silicon strips together form the semiconductor tracker (SCT) [138, 139], which adds four additional possible space-point measurements to a track. The barrel consists of four concentric layers

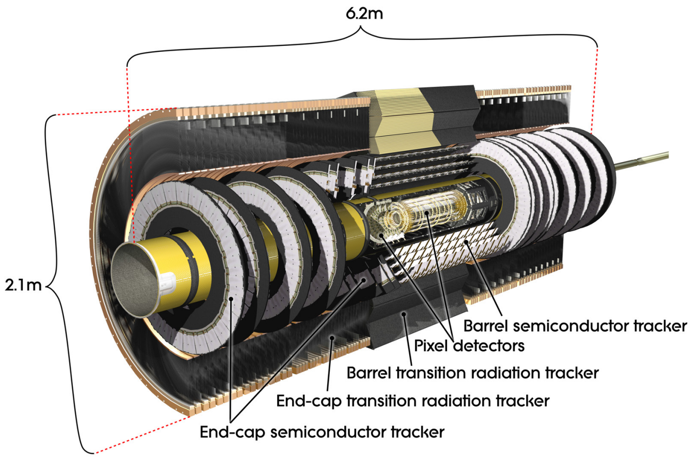

Fig. 3.6 · Layout of the ATLAS inner detector [136].

of strip detectors for $|\eta| < 1.4$ and has a radial distance of 24–55 cm to the interaction points. Each end-cap is constructed of 9 discs, in such a way that four space-points can be measured up to $|\eta| < 2.5$.

The SCT has 4088 modules of $6.36 \times 6.40\,\text{cm}^2$ with 768 strips each, giving an additional 6 million readout channels. Each strip is built of two layers with an angular offset of 40 mrad to provide a z-measurement. The strip pitch, the distance between the middle of two neighbouring strips, is 80 µm in the barrel. Ultimately, the resolution is $\sigma_{R-\phi} = 17\,\mu\text{m}$ and $\sigma_z = 580\,\mu\text{m}$. The SCT is cooled to the same temperature as the pixel detector.

gas-filled tubes form the final tracking system, the transition radiation tracker (TRT) [140, 141]. Its design provides many additional space-points, and also allows electron identification through transition radiation. In the barrel region, 73 layers are installed; in the end-cap region, 160 layers are installed. The end-caps cover the region 55–107 cm from the interaction point. The TRT is composed of 370,000 straws.

Each barrel tube is 144 cm long, 4 mm in diameter, contains a 31 µm tungsten wire plated with 0.5–0.7 µm of gold and is filled with a gas mixture of 70 % Xe, 27 % CO_2 and 3 % O_2. End-cap tubes are identical to barrel tubes, but 37 cm in length. The potential difference of −1530 V between the tube and wire causes free electrons created by charged particles to drift towards the wire, with a drift time proportional to the distance of the original particle to the wire.

By embedding the tubes in polypropylene fibres and foil with varying refractive indices, electrons and hadrons can be distinguished: the total energy loss caused by photon emission is directly proportional to a particle's Lorentz factor γ. By applying two thresholds, one optimised for direct ionisation detection and the other to detect transition radiation coming from electrons, the TRT can distinguish between pions and electrons.

The resolution of each tube is 170 μm; the combined resolution is approximately 50 μm. The TRT operates at ambient temperature.

3.2.4 Calorimetry

The calorimeter system is composed of two calorimeters: an electromagnetic calorimeter with a coverage of $|\eta| < 3.2$ to detect electrons and photons, and a hadronic calorimeter covering the region $|\eta| < 4.9$ to measure the energy of hadrons and hadronically decaying τ leptons.

Both calorimeters are sampling calorimeters: they consist of alternating layers of active medium and an absorber. Particles that interact with the medium lose their energy and will create showers of particles, allowing for an energy determination. Absorbing material is used to prevent the calorimeters from becoming prohibitively large and expensive.

Electromagnetic calorimeter

To detect electrons and photons with $|\eta| < 3.2$, a liquid-argon filled electromagnetic (EM) calorimeter (ECAL) is used [143]. It consists of a barrel ($|\eta| < 1.475$) and two end-caps (EMEC, $1.375 < |\eta| < 3.2$), with a transition region at $1.37 < |\eta| < 1.52$. Liquid argon is used for its linear response function and its radiation hardness. Lead is used as an absorbing material. The detector's geometry is accordion shaped to provide full azimuthal coverage.

To stop all electromagnetic showers, the ECAL has a size that corresponds to between 22 and 33 radiation lengths X_0 in the barrel and between 24 and 38 radiation lengths in the end-caps. However, the material corresponds to only ~ 1.5 nuclear interaction lengths λ, to provide maximum transparency to hadronic objects.

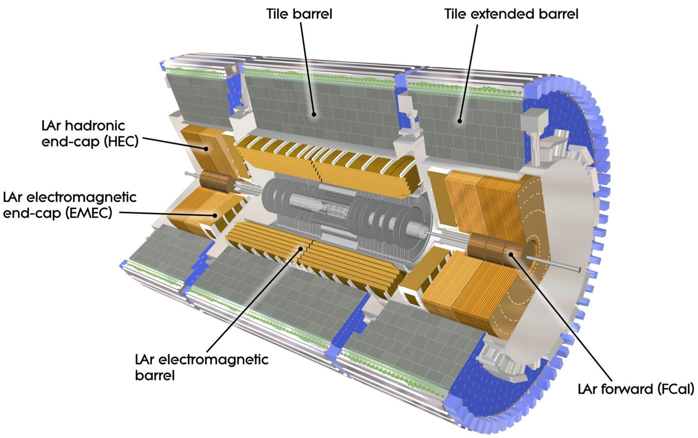

Fig. 3.7 · Layout of the ATLAS calorimeters [142].

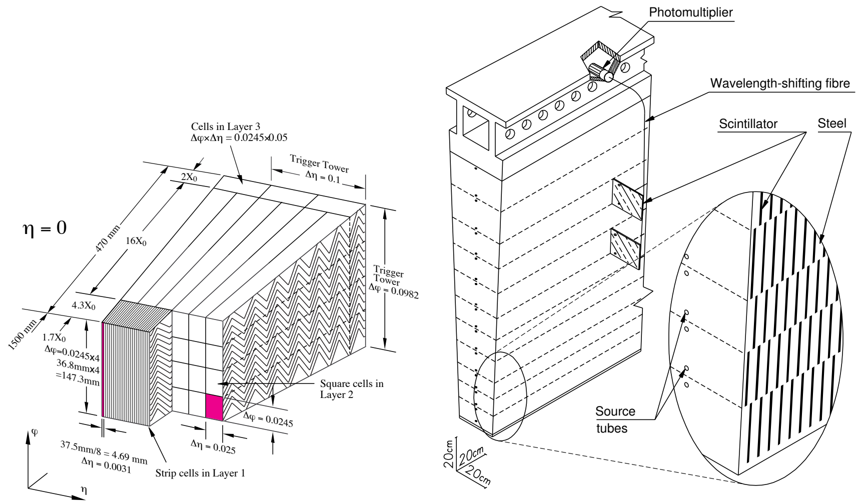

Fig. 3.8 · Schematic overview of an EM calorimeter module (left) and a hadronic calorimeter module (right). The three layers in the ECAL module are indicated; the accordion-shaped structure is clearly visible. Taken from [122].

In the barrel section $|\eta| < 2.5$, the calorimeter modules are divided into three layers. The inner layer has a depth of 4.3 X_0 and size of $\Delta\eta \times \Delta\phi = 0.003 \times 0.1$. Its fine granularity allows better separation of electrons from photons and pions. The middle layer, making up most of the calorimeter with a depth of 16 X_0, is $\Delta\eta \times \Delta\phi = 0.025^2$ and typically contains most of a shower's energy. Finally, the outermost layer is even coarser with a size of $\Delta\eta \times \Delta\phi = 0.05 \times 0.0245$ and serves to distinguish electromagnetic from hadronic showers, which deposit most of their energy at a greater distance.

Each end-cap consists of two co-axial wheels, each divided into eight wedge-shaped modules. As for the barrel, the end-cap calorimeters are divided into three layers. The inner layer is segmented in strips in the η direction and $\sim 4.4\, X_0$ thick. The middle layer consists of cells of $\Delta\eta \times \Delta\phi = 0.025^2$; the back layer is twice as coarse in η.

Any energy loss before the ECAL is estimated through the use of a presampler detector, an active LAr layer of 1.1 cm in the barrel and 0.5 cm in the end-cap, which is placed in front of the inner surface of the electromagnetic calorimeter.

Between the barrel and end-caps there is a *crack* region at $1.37 < |\eta| < 1.52$ that has a degraded energy resolution; in precision measurements, this region is never used.

Hadronic calorimeter

Surrounding the ECAL, the hadronic calorimeter (HCAL) [144] is designed to measure the energy of hadronic particles up to $|\eta| < 3.2$. It is constructed from a central barrel for $|\eta| < 1.0$, two

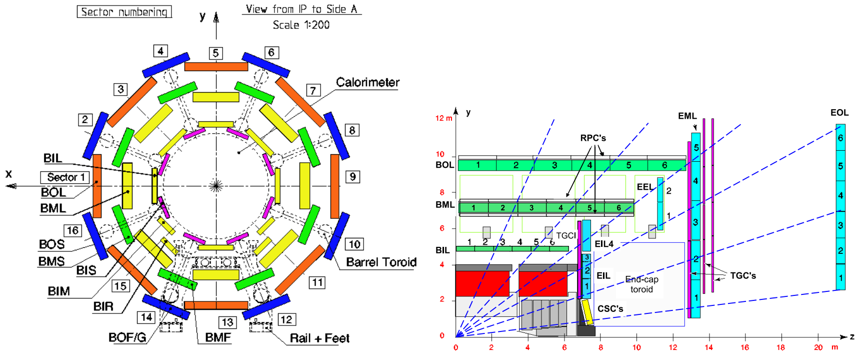

Fig. 3.9 · Transverse (left) and lateral (right) cross-sections of the muon systems [122].

barrel extensions at $0.8 < |\eta| < 1.7$ and two end-caps at $1.5 < |\eta| < 3.2$. Additional coverage is provided by the forward calorimeters described in the next section.

The barrel sections are called the Tile Calorimeter, and constructed from steel layers with a thickness of 14 mm for the absorber. Scintillator tiles with a thickness of 4 mm are employed as the active material. Both the central barrel and the two extensions consist of 64 separate azimuthal modules. Each of these modules is radially further separated in three layers, with a size of $\Delta\eta \times \Delta\phi = 0.1^2$ in the first two and 0.2×0.1 in the last. At $\eta = 0$, the total thickness of the calorimeter is 9.7 λ.

Each end-cap (HEC) is a liquid-argon calorimeter employing copper plates as absorbers and is located directly behind its electromagnetic counterpart. Built out of 32 wedge-shaped modules, the end-caps cover the region up to $|\eta| < 3.2$. For $|\eta| < 2.5$ the size of a module is $\Delta\eta \times \Delta\phi = 0.1^2$, for $|\eta| > 2.5$, modules are $\Delta\eta \times \Delta\phi = 0.2^2$ in size.

To minimise the probability of *punch-through*, where a shower is not fully stopped in the calorimeter but enters the muon spectrometer, the depth in the barrel is typically 7.5 λ. The end-cap has a thickness of 10 λ.

Forward calorimeter

A precise measurement of any missing transverse energy in an event requires hermetic coverage around the interaction point. To that end, a separate forward calorimeter (FCAL) is used. Designed to withstand high particle fluxes in the forward region, it is placed at $3.1 < |\eta| < 4.9$, which corresponds to an approximate radius of 8 cm around the z-axis.

In the same fashion as the other calorimeters, the FCAL uses a layered design. Three layers, all liquid-argon based, are used on either side of the detector. The innermost wheel is designed for electromagnetic showers and uses copper absorbers; the outer two determine the energy of hadronic showers and employ tungsten as the absorbing material.

To cope with the high particle flux in the forward direction, the wheels have a depth of 27.6, 91.3 and 89.2 electromagnetic radiation lengths.

3.2.5 Muon spectrometer

Muons traverse the inner detector and both the calorimeters due to their long lifetime and low energy emission, to finally be measured in the muon spectrometer. An illustration is shown in fig. 3.9. The muon spectrometer is used, together with the inner detector, to obtain both position and momentum measurements for muons. Momenta can be measured by the muon system alone between 3 GeV and 3 TeV, although for low-energy muons the resolution is worse than the inner detector's. For muons with a p_T of 1 TeV, the resolution is 10 %. Next to precise tracking, the spectrometer also provides a muon trigger for the experiment for muons with $|\eta| < 2.4$, using various p_T thresholds.

Tracking

Muon tracks are measured by two separate subdetectors. Monitored drift tubes (MDTs) are used in three barrel layers ($|\eta| < 2.0$) at 5 m, 7.5 m and 10 m from the interaction point. Each layer consists of 16 *chambers* with a slight overlap, with a small hole at $\eta = 0$ to provide services for other detectors and the solenoid magnet system. In the forward region ($2.0 < |\eta| < 2.7$), four muon wheels are used, placed at 7.4 m, 10.8 m, 14 m and 21.5 m from the interaction point. The innermost wheel is constructed of cathode-strip chambers (CSCs), to better deal with the high particle flux closer to the interaction point. An additional gap at high η is due to the support structure for the wheels.

MDT chambers contain three to eight layers of drift tubes. Each drift tube is made of a 30 mm-diameter aluminium tube containing a tungsten-rhenium (W-Re) wire 50 μm in diameter, and is filled with a gas mixture of 93 % Ar and 7 % CO_2 at 3 bar. The potential difference is maintained at 3080 V to ensure the MDTs operate in the avalanche regime, providing a maximum electron drift time of 700 ns. The average resolution is 80 μm per tube, depending on the drift time and distance, and 35 μm per chamber.

CSCs are multi-wire proportional chambers (MWPC) filled with a gas mixture of 80 % Ar and 20 % CO_2. Each chamber contains four of these MWPC's and has a resolution of 40 μm in the bending plane and 5 mm in the transverse plane. The operating voltage is 1900 V.

Trigger chambers

Triggering on muons is performed by two subsystems. Resistive plate chambers (RPCs) provide a trigger in the barrel region ($|\eta| < 1.05$) and consist of parallel resistive plates placed 2 mm apart that have a 9.8 kV electric field between them. Charged tracks traversing a chamber ionise the gas, leading to an avalanche and a signal on readout chips on the anode. The design resolution of the RPCs is 10 mm and ~ 1.5 ns. The gas mixture is 94.7 % $C_2H_2F_4$, 5 % Iso-C_4 and 0.3 % SF_6.

Thin-gap chambers (TGCs) allow for triggering on forward muons. The chambers are placed in two concentric rings in the end-cap regions, covering the range $1.05 < |\eta| < 2.4$. Similar to the CSCs, they are also MWPCs. However, the distance between the wires (1.4 mm) is shorter than between each wire and the anode (1.8 mm). Such a design ensures the drift time is shorter than 25 ns, the design bunch spacing of the LHC. The gas mixture used is 55 % CO_2 and 45 % n-C_5H_{12}.

3.2.6 Triggering and data acquisition

The LHC's 25 ns bunch spacing corresponds to an event rate of 40 MHz. Combined with the average ATLAS event size of 1.6 MB, i.e. the amount of data read from the detector for each event, the approximate bandwidth needed to store data from all collisions is $\sim$ 65 TB/s: reading all the data is unfeasible. Considering also the need to reconstruct, store and analyse all the obtained events, the need for rapid, on-the-fly filtering is apparent. ATLAS employs a system of *triggers* to decrease the amount of data to be read out, stored and reconstructed, in the process keeping the most interesting events. The process is illustrated in fig. 3.10.

Limited mostly by storage space, the trigger system used needs to decrease the event rate to approximately 400 Hz. ATLAS uses a customisable system of three trigger *levels*, each serving to reduce the amount of events. The three consecutive levels each select events based on certain criteria, which become more refined as the data rate gets reduced. Trigger level 1 (L1) is a hardware-based level, level 2 (L2) a simple software-based trigger, while the last level is an event filter (EF) running on a computing farm.

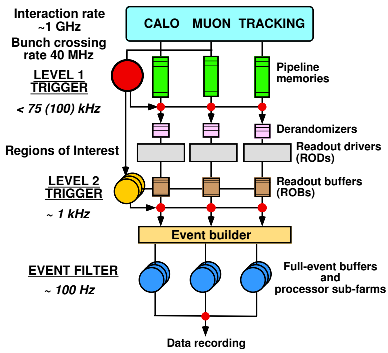

Fig. 3.10 · The trigger system [145, 146].

The L1 trigger

The Level 1 trigger performs an initial hardware-based selection on high-p_T electrons, photons, muons and jets, and missing transverse energy. It relies on reduced-granularity information from the calorimeter as well as the RPC and TGC and selects events at a data rate that cannot exceed 75 kHz (upgradable to 100 kHz), with a maximum latency of 2.5 µs.

The L1 calorimeter trigger L1CALO [147] identifies large energy deposits in the calorimeters in approximately 7000 *towers* of $\Delta\eta \times \Delta\phi = 0.1^2$. Thresholds can be placed on the required energy for each object type. The L1 muon trigger identifies high-p_T muons coming from the interaction point using the trigger chambers. The location of an object triggered on is used to define a *region of interest* (RoI), a cone in (η,ϕ)-space with its apex at the interaction point. All regions of interest are passed on to subsequent triggers.

Information from the calorimeter and muon triggers is combined and compared to 256 items in the trigger menu by the central trigger processor (CTP). The L1 trigger can identify electrons, photons, muons, jets and hadronic τ leptons. Events passing any of the triggers in the menu are passed on to the L2 trigger together with their regions of interest, their data held in read-out buffers (ROBs), integrated circuits close to the detector.

The L2 trigger

Events that passed the L1 trigger are passed on the the L2 trigger, a software-based trigger seeded by the regions of interest defined at L1. Within each of these regions, the event is reconstructed and compared to trigger requirements. Events passing the requirements are reconstructed fully in less than 40 ms and subsequently passed on to the last trigger level. At this stage, the event rate has been reduced by an additional factor 30.

The event filter

The final stage of the trigger chain, the event filter, reduces the data rate to around 400 Hz. Only events that passed any L2 criteria are processed, using the full information of the ATLAS detector. Detailed reconstruction algorithms from the offline analysis procedures can be used, leading to a per-event processing time of 4 s.

Not only does the event filter select events, it also separates them into three distinct *streams* according to their significant object: the `Muons`, `Egamma` and `JetTauEtmiss` streams. Events may be stored in multiple streams. A fourth stream, the minimum-bias stream `MinBias`, contains a random sample of minimum-bias events.

3.3 Monte Carlo simulation

In any experiment, the obtained result must be compared to an expectation in order to be able to obtain a conclusion. Research statistical in nature, such as the search for new elementary particles, requires a good understanding of the expected measurement as well as its error. In high energy physics, one relies on computer simulation of the interactions of elementary particles, of the decay of particles produced in a collision, and of the interaction of particles with matter.

Simulated datasets are obtained in ATLAS in four separate steps: event generation, detector simulation, digitisation, and finally event reconstruction. The first three steps simulate a collision in the detector; the last step reconstructs the simulated event in exactly the same fashion as measured ones.

Events are generated from the initial proton–proton collision: the hard scatter between the proton constituents, the showering of partons, hadronisation and the underlying event all need to be simulated. Event generator software programs rely on Monte Carlo (MC) methods to randomly generate the initial hard interactions, and are hence also known as Monte Carlo simulations. Processes are simulated depending on their differential cross-section.

Two ingredients are needed for such a calculation: the matrix element of the process being simulated, and the PDF of the proton. The uncertainty on the PDF is driven by the uncertainty on the distribution on the incoming gluons; typically, different sets of PDFs are considered to evaluate a theoretical uncertainty. Examples of such sets are CTEQ6L1 [59] and MSTW2008 [58].

Matrix elements are calculated perturbatively; most generators employed in the ATLAS collaboration work at leading order (LO). Next-to-leading order (NLO) corrections to the cross-section are accounted for by calculating a *k-factor*, the ratio between the leading and next-to-leading order processes, which can depend on the kinematics of the process. Next-to-leading log (NLL) resummation techniques are also employed in the calculation of the cross-sections. In the work described in this thesis, simulated datasets of supersymmetric processes have been generated with cross-sections calculated using NLO+NLL techniques.

The simulation of gluon radiation is performed after the initial hard scattering has been simulated: the incoming partons as well as produced particles can radiate gluons, which in turn can radiate more gluons or decay in quark–anti-quark pairs. This process is called *parton showering*. In turn, quarks and gluons group into tight cones of particles (jets) due to confinement, a process known as *hadronisation*. The final parton distribution of the jets reflects the uncertainty on the modelling of parton showers, and is typically tuned to the jet distribution in data.

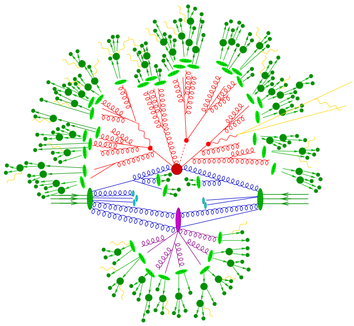

Fig. 3.11 · Pictorial representation of a simulated event [148], with the hard interaction (red, big blob) followed by decays of the produced particles (red blobs). Generated QCD radiation is shown in red, with a second interaction shown (purple) before hadronisation and decay (green). Radiated photons are shown in yellow.

Different simulations follow different approaches. SHERPA [148], Herwig [149] and PYTHIA [150, 151] calculate matrix elements and perform showering, but only take into account $2 \rightarrow 1$ and $2 \rightarrow 2$ processes. Other generators calculate $2 \rightarrow n$ processes, but must be interfaced to a leading-order calculation to perform showering; examples are MadGraph [152] and ALPGEN [153]. Finally, MC@NLO [154] and POWHEG [155] calculate matrix elements at next-to-leading order level with both real and virtual corrections. Also these must be interfaced to different generators to perform showering.

After simulating the hard interaction and the showering, the behaviour and interaction of the outgoing particles with the detector must be simulated. Particle propagation of particles in the ATLAS detector is modelled using a detector simulation implemented in GEANT4 [156]. The *digitisation*, i.e. the translation of these simulated interactions to detector responses, is the next step simulated. Finally, the simulated event is reconstructed from the obtained response by the same algorithms and applying the same calibrations as used for measured events.

The full simulation of the detector is precise, but often slow and unwieldy due to the long time spent simulating calorimeter processes. For that purpose, *fast simulation* software programs exist, trading accuracy for speed. An event with jets will take approximately 45 minutes to simulate fully on a benchmark machine[1], while using the fast simulation the computation time can be decreased to around 90 s [158]. The fast simulation of the ATLAS detector is implemented in `AtlFast-II` [159], and is used in the generation of SUSY events used in the work described in this thesis.

In the absence of an exact detector description or simulation, one may also rely on assumptions on the reconstruction resolution and efficiency. Reconstructed objects in *truth-level* events[2] can be convolved with a term modelling the resolution, for example a Gaussian distribution, to incorporate the uncertainty on e.g. a jet's p_{T}. Such a method is employed in chapter 8 in a study of the prospects for supersymmetry at the high-luminosity LHC.

[1] The time units here refer to times in the SPECINT2000 benchmark suite [157].

[2] A *truth-level* event is a Monte Carlo simulated event for which the detector response has not been simulated; instead, each object is reconstructed directly from the simulated process.

CHAPTER FOUR

Event reconstruction

THE NEXT STEP after obtaining a detector response, whether real or simulated, is attributing these responses to physical objects. First, detector responses have to be grouped to correspond to decay products: tracks originate from a vertex, which must be identified, and are the result of charged particles traversing the detector. Calorimeter responses must be matched to particles interacting electromagnetically or hadronically, and any jets in the detector have to be reconstructed. Tracks from signals in the muon spectrometer are likely to come from muons, and must be matched to ones found in the inner detector. Finally, care must be taken to identify any missing transverse energy in the event. Having algorithmically reconstructed each event, objects in the event must be identified. Electrons, photons, τ leptons, muons and jets have to be labelled for an event. Care must also be taken to identify jets coming from decays of b quarks.

This chapter describes the event and object reconstruction procedures used in ATLAS. All algorithms are implemented in the framework ATHENA [160], based on GAUDI [161].

4.1 Tracking and vertexing

Tracks are reconstructed using data from the inner detector using a sequence of algorithms [162, 163]. Two approaches can be used to reconstruct a track:

inside-out tracking starts with 3-point seeds from the silicon detectors and moves away from the interaction point, adding new track points using a Kalman filter [164]. Tracks are required to have a transverse momentum $p_{\mathrm{T}} > 400\,\mathrm{MeV}$. It is the default algorithm for reconstructing primary charged particles coming from the proton–proton interaction, and from the decay of particles with a lifetime shorter than 3×10^{-11} s;

outside-in tracking, also known as back-tracking, uses TRT segments and extends them towards the interaction point by adding silicon hits. Back-tracking is used to reconstruct secondary particles, i.e. particles coming from the decay of primary particles.

Track seeds for inside-out tracking are formed by a combination of three *space points*, three-dimensional representations of measurements, in the pixel detector and the first layer of the SCT. The track defined by these three points defines a *road* along which to extend it to the outer layers of the SCT.

To minimise the selection of fake tracks, a set of quality criteria is used based on the number of *hits*, *holes* and *outliers* found. A hit is a space point; an outlier is a space point that reduces the

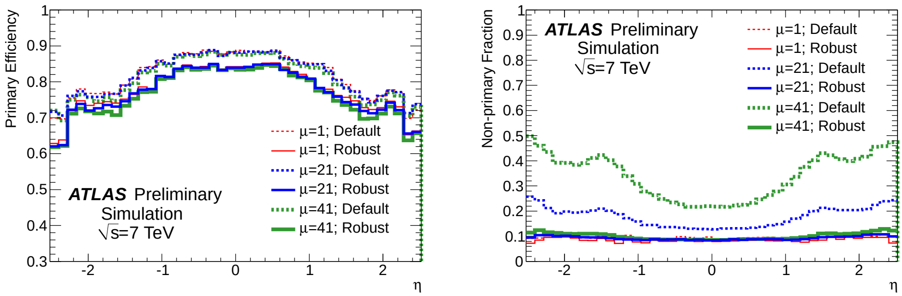

Fig. 4.1 · The primary reconstruction efficiency in minimum bias Monte Carlo samples containing exactly one and on average 21 or 41 interactions (left) and the non-primary fraction, the sum of the contributions from secondaries and from fake tracks (right) [163].

fit quality; a hole is a location where a hit was expected but not found. Once track candidates have been identified, any overlap between them has to be resolved. Tracks are scored based on the numbers of holes and hits; ambiguous hits are assigned to the highest-scoring track. The other track is fitted without the overlapping hit and scored again, continuing the procedure until no overlaps between tracks exist. Next, the tracks are extended into the TRT and fitted again.

For every reconstructed track its *impact parameters*, the distance d_0 between the point of closest approach and the z-axis in the (x, y)-plane and z_0, the z-coordinate at the point of closest approach to the z-axis, are determined from the fit to all assigned hits.

The track reconstruction efficiency is determined using Monte Carlo simulation. The fraction of truth particles with $p_T > 100$ MeV and $|\eta| < 2.5$ that can be matched to a reconstructed track gives the efficiency. How efficiently tracks can be reconstructed depends on the exact pile-up conditions: in a high pile-up environment, many space points are found in the initial stages of reconstruction, leading to a higher chance of fake tracks[1]. Two classes of tracks are used. *Default* tracks are optimised for high efficiency at low pile-up and are required to have at least 7 hits in the silicon detectors; two holes in the pixel detector are allowed. *Robust* tracks require at least 9 hits in the silicon detectors, and no holes in the pixel detector. Fig. 4.1 shows that selecting robust tracks decreases the efficiency by 5 %, irrespective of pile-up [163]. However, they decrease the amount of non-primary tracks by a factor 2–5.

4.1.1 Vertex reconstruction

After tracks are found, their origin has to be determined. Interaction points are called *primary* vertices; *secondary* vertices are due to particle decays. Primary vertices are identified by an iterative vertex finding algorithm [165]. The parameters of vertices are then found through a vertex fit. The vertex finding algorithm works as follows:

1. reconstructed tracks matching certain quality criteria compatible with the interaction region [166] are preselected;

[1] A fake track is a “track” that does not correspond to a real charged particle having traversed the detector.

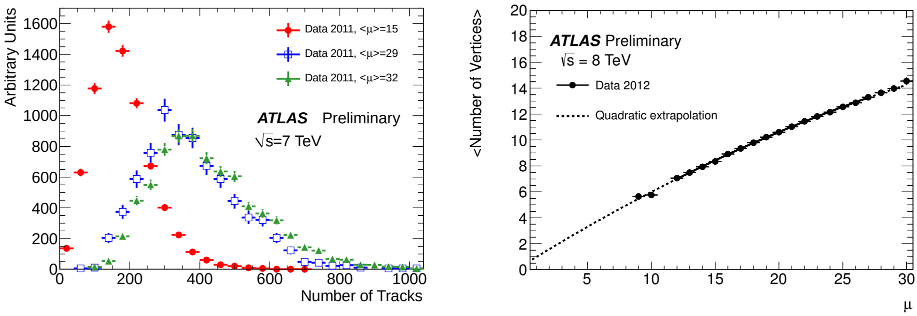

Fig. 4.2 · The number of primary tracks at different pile-up scenarios in simulation (left) [163] and the number of primary vertices as a function of the average number of interactions in 2012 data with a second-order polynomial fit performed at high values of μ (right) [168].

2. a seed is found by identifying the global maximum in the distribution of z coordinates;
3. the vertex position is determined using an adaptive vertex fitting algorithm [167];
4. tracks incompatible by more than $7\,\sigma$ are used to seed a new vertex.

This fitting procedure continues until no new vertices are identified. The primary vertex of the event is defined to be the primary vertex with the highest $\sum p_{\mathrm{T}}^2$.

The resolution on the vertex position has been obtained during a special fill of LHC in 2012 with a very low average number of interactions of about 0.01. It depends on the number of tracks associated to a vertex, and ranges from 0.65 mm (one track) to 0.030 mm (80 tracks) in the z-direction. In the x-direction, the resolution ranges from 0.35 mm (one track) to 0.015 mm (80 tracks) [168].

Moreover, the number of reconstructed vertices is strongly correlated with the average number of interactions in a collision. Fig. 4.2 shows the number of primary tracks at various pile-up scenarios as well as the performance of the primary number of vertices obtained in 2012.

4.2 Lepton identification

4.2.1 Electrons

Electrons are reconstructed in the central region ($|\eta| < 2.47$) of the detector starting from energy deposits (clusters) in the calorimeter, which are then associated to tracks in the inner detector [169, 170]. The ECAL is divided into a grid of *towers* of $\Delta\eta \times \Delta\phi = 0.025^2$ to construct these clusters. Inside each tower, the energy deposit in all calorimeter cells is summed together to obtain an energy measurement. Clusters are searched for using a sliding-window algorithm with windows of 3×5 towers and used as a seed if they have a transverse energy greater than 2.5 GeV [171]. Forward electrons can only be reconstructed using the calorimeter and are hence indistinguishable from photons; they are not used in this thesis.

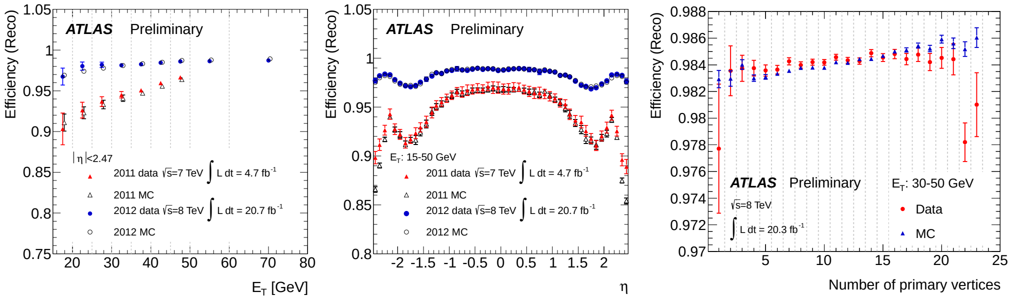

Fig. 4.3 · Measured electron reconstruction efficiencies as a function of E_{T} and η for the 2011 and 2012 datasets and the number of primary vertices for the 2012 dataset [173].

Next, clusters are matched to tracks in the inner detector. Bremsstrahlung effects on the $p_{\mathrm{true}}/p_{\mathrm{reco}}$ distribution of tracks are taken into account using a Gaussian Sum Filter [172], which models energy losses as a sum of weighted Gaussian components. Electron candidate tracks with $p_{\mathrm{T}} > 400$ MeV and $|\eta| < 2.5$ are refitted to incorporate these effects. The track with closest $\Delta R = \sqrt{(\Delta\eta)^2 + (\Delta\phi)^2}$ to a cluster is considered the best match. Tracks with silicon hits are preferred over tracks without them, which are considered more likely to originate from electrons from photon conversions.

Real electrons are identified from these electron candidates by requirements both on the tracks and on the calorimeter information. Three sets of requirements, optimised in bins of η and E_{T}, determine *loose, medium* and *tight* electrons. Loose electrons are selected using shower shape variables in the middle layer in the ECAL, and hadronic leakage variables. Medium electrons are selected using the first strip layer of the ECAL, the track quality, and the track–cluster match in addition. Tight electrons, finally, add requirements on E/p, where E is the energy measurement in the calorimeter and p the track momentum, on particle identification from the TRT, and on discrimination against converted photons.

In 2012, these requirements were further enhanced into loose++, medium++ and tight++ electrons to deal with the increased pile-up. Requirements on the most pile-up sensitive variables were loosened, while requirements on the other variables were tightened to keep the performance as a function of the number of reconstructed primary vertices constant [173].

The electron efficiency is estimated using a tag-and-probe method [173, 174]. It can be factorised in four terms:

$$\epsilon_e = \epsilon_{\mathrm{reco}} \times \epsilon_{\mathrm{ID}} \times \epsilon_{\mathrm{trigger}} \times \epsilon_{\mathrm{additional}}, \tag{4.1}$$

where the last term comes from any additional selection criteria applied in a specific analysis, for example on the isolation of electrons. The determination of the identification and reconstruction efficiencies relies on $Z \to ee$ and $J/\psi \to ee$ samples, respectively used for electrons with $E_{\mathrm{T}} > 10$ GeV and electrons with 7 GeV $< E_{\mathrm{T}} <$ 20 GeV. The efficiency is reconstructed in four bins of E_{T}, with results for bins between 10 GeV and 20 GeV combined to obtain a final efficiency.

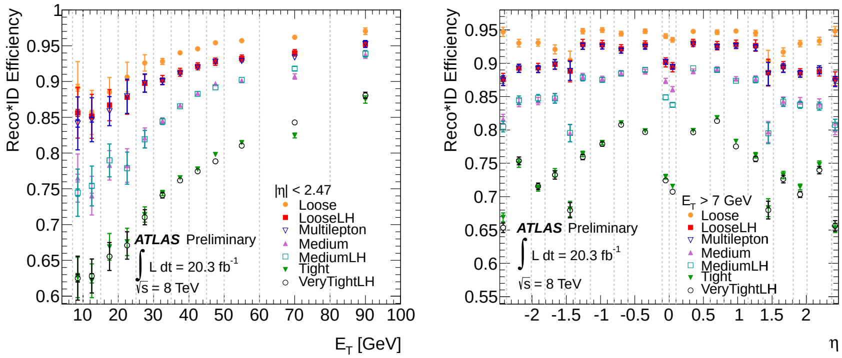

Fig. 4.4 · Measured combined electron reconstruction and identification efficiencies as a function of E_T and η for the 2012 dataset for loose, medium and tight electrons [173].

Efficiencies on data are obtained by applying data-to-MC efficiency ratios to simulated $Z \to ee$ events.

Fig. 4.3 shows the obtained electron reconstruction efficiency for 2011 and 2012 data as a function of E_T and η, and as a function of the number of primary vertices for 2012 data. With respect to the 2011 efficiency, the 2012 efficiencies have been increased by 2 % in the barrel and 8 % in the end-cap regions. Averaged over η, the efficiency as a function of E_T has increased by approximately 5 %, depending on the electron type. Fig. 4.4 shows the combined reconstruction and identification efficiencies for various types of electrons, both cut- and likelihood-based [173].

The electron trigger efficiency is evaluated in a similar fashion, using tag-and-probe methods on $Z \to ee$, $J/\psi \to ee$ and $W \to e\nu$ samples to determine it for several categories of E_T [175].

4.2.2 Muons

Muons can be identified by the muon spectrometer, the calorimeter, or both. In ATLAS, four muon types are distinguished, based on the way they are reconstructed: stand-alone, combined, segment tagged, and calorimeter tagged [176].

stand-alone muons are reconstructed only in the muon spectrometer. Their momentum is corrected for the parametrised loss in the calorimeter to obtain the muon momentum at the interaction point. Track parameters are obtained by extrapolating the track back to the beam line;

combined muons are reconstructed by combining information from both the muon spectrometer and the inner detector. Tracks are combined based on the χ^2 difference between the track parameters in both systems. Due to the inner detector's coverage, combined muons are limited to $|\eta| < 2.5$. Track momenta are calculated as a weighted combination of the two p_T values. Combined muons are the standard type of muon used in ATLAS;

segment tagged muons are trajectories in the inner detector that, when extrapolated to the muon spectrometer, can be associated to a straight track segment in the muon chambers. Primarily, they are used to identify low-p_T muons that do not traverse the entire muon spectrometer;

calorimeter tagged muons are trajectories in the inner detector that are identified as a muon if matching energy deposits in the calorimeters compatible with the hypothesis of a minimum ionising particle are found.

ATLAS has used two independent reconstruction algorithms for muons during Run I [177]. STACO [178], or Chain 1, combines track parameters from the inner detector and muon spectrometer in a statistical way: the two sets of parameters are treated as two independent measurements of a parameter vector. MUID [179], or Chain 2, globally refits entire tracks using hits from both the inner detector and the muon spectrometer.

Efficiencies and fake rates

The reconstruction efficiency of muons is given by the product of the reconstruction efficiencies in both detector and the matching efficiency:

$$\epsilon(\text{type}) = \epsilon(\text{type}|\text{ID}) \cdot \epsilon(\text{ID}), \tag{4.2}$$

where $\epsilon(\text{ID})$ is the efficiency in the inner detector, and $\epsilon(\text{type}|\text{ID})$ the matching efficiency. The efficiency is not uniform in $|\eta|$ and ϕ; in particular, it decreases around $|\eta| \sim 0$, where services for the inner detector and the calorimeter are provided and around $|\eta| \sim 1.2$, where there are regions in ϕ in which one layer of chambers is traversed.

Through a tag-and-probe method the reconstruction efficiency is studied on samples of $Z \to \mu\mu + X$ and $J/\psi \to \mu\mu$ events [180]. One muon, the *tag*, is selected as a muon. The probability of the other muon, the *probe*, being correctly reconstructed as a muon is studied for each type of muon as a function of η and ϕ.

For the $Z \to \mu\mu$ sample, events are required to have two opposite-charge isolated tracks, with an invariant mass corresponding to m_Z, and one combined muon as the tag. Isolated muons are defined as muons where the sum of momenta of tracks with $p_T > 1$ GeV in a cone of $\Delta R = 0.4$ around the muon is less than 15 % of the muon's p_T. For the $J/\psi \to \mu\mu$, tags are required to be combined muons with $p_T > 4$ GeV and $|\eta| < 2.5$.

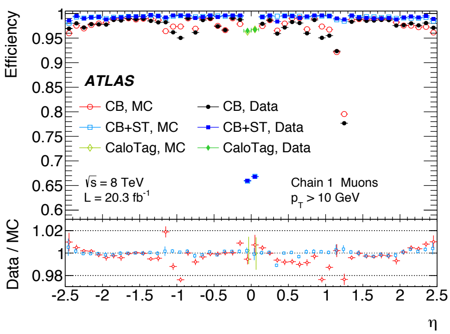

Fig. 4.5 · Muon reconstruction efficiency as a function of η measured in $Z \to \mu\mu$ events for muons with $p_T > 10$ GeV and different muon reconstruction types [180].

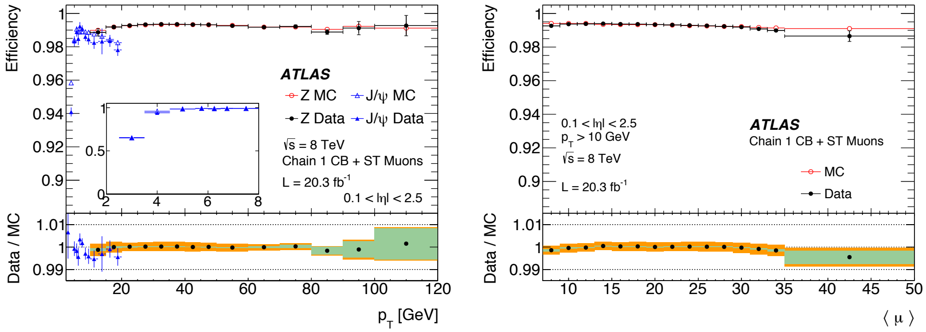

Fig. 4.6 · Reconstruction efficiency for combined+segment-tagged muons as a function of the p_T of the muon (left) and as a function of the average number of interactions for muons with $p_T > 10$ GeV (right); both for muons with $0.1 < |\eta| < 2.5$ in both data and samples of $Z \to \mu\mu$ and $J/\psi \to \mu\mu$ events [180].

To ensure efficiencies in simulation match the one in data, a scale factor

$$\mathrm{SF} = \frac{\epsilon^{\mathrm{data}}}{\epsilon^{\mathrm{MC}}} \tag{4.3}$$

is defined and applied to simulated muons. The obtained efficiency is shown in fig. 4.5 for various muon types as a function of η, and is approximately 99 % over all detector regions. The gap at $|\eta| \approx 0$ is recovered by the use of calorimeter-tagged muons. For combined+segment-tagged muons the efficiency dependence on the muon p_T and on the average number of interactions is shown in fig. 4.6. An efficiency of almost 99 % is obtained over a wide range of muon p_T, very slowly decreasing with increasing pile-up.

The main systematic uncertainties on the efficiency scale factors are the uncertainty on the data-driven background selection, the uncertainty of the cone size used to match reconstructed muons to probe objects, possible biases in the tag-and-probe method (such as differences between probes and truth muons and correlations between inner detector and muon spectrometer efficiencies) and the uncertainty on low-p_T muons.

The trigger efficiency for muons is also obtained with a tag-and-probe method on $Z \to \mu\mu$ events [181, 182].

4.2.3 Tau leptons

The τ lepton is similar to electrons and muons; however, due to its large mass of 1776.82 ± 0.16 MeV [109], it is the only lepton that decays into both hadrons and leptons. Their short lifetime ensures τ leptons decay inside the beam pipe; τ decay products are used for identification. Leptonic decays, which occur 35.2 % of the time, are indistinguishable from primary electrons and muons and treated as such. The remainder, hadronically decaying τ leptons, must be identified in the detector. Their signature is very similar to that of quark- and gluon-initiated jets (QCD jets). When referring to τ leptons in the following, τ leptons decaying into hadrons are meant. These decays are classified based on the number of tracks, or *prongs*, associated to a reconstructed τ lepton.

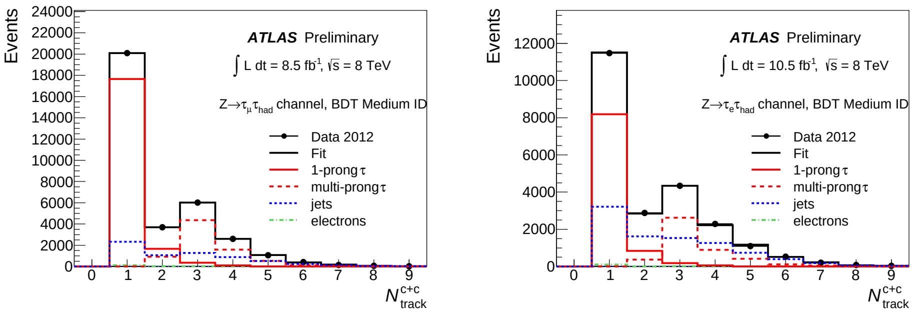

(a) $Z \to \tau_\mu \tau_{\text{had}}$ channel (b) $Z \to \tau_e \tau_{\text{had}}$ channel

Fig. 4.7 · Fit result after BDT medium τ identification for the measurement of the 1-prong and multi-prong identification efficiencies in the muon (left) and electron (right) channels [188]. Shown is the number of core and p_{T}-correlated tracks.

Reconstructing a τ lepton starts from either a calorimeter seed or a track seed [183]. In 2011 and 2012, ATLAS used calorimeter-seeded candidates consisting of calorimeter jets (see §4.4) reconstructed using the anti-k_t algorithm [184] with a radius $R = 0.4$. Topological clusters [171] of calorimeter cells calibrated with Local Hadronic Calibration [185] are used as inputs to reconstruct jets. All jets with $|\eta| < 2.5$ and $p_{\text{T}} > 10$ GeV seed the reconstruction algorithm.

The visible part of the decays, $\tau_{\text{had-vis}}$ is then reconstructed as follows [186]. Track candidates are associated to each τ candidate if they are within $\Delta R = \sqrt{(\Delta\eta)^2 + (\Delta\phi)^2} < 0.2$ from the candidate's axis and pass a set of quality requirements based on impact parameters and the number of hits in the silicon detectors. The number of tracks associated to the candidate classifies it as single- or multi-prong.

Two sets of requirements, one based on boosted decision trees (BDTs), the other on a log-likelihood ratio, separate τ candidates from QCD jets. Each has dedicated bins for 1-prong and 3-prong τ decays. A separate BDT is used to reject electrons misidentified as τ leptons. Variables used to separate the τ leptons from background include the invariant mass measured in the topological clusters, the invariant mass of the tracks, the leading track momentum, the fraction of energy inside the core ($\Delta R < 0.1$) of a candidate, the fraction of energy deposited in the ECAL, the number of tracks in the annulus $0.2 < \Delta R < 0.4$ around the candidate, and the distance of the track furthest to the axis [186–188]. Both the BDT and the likelihood-ratio method provide loose, medium and tight τ candidates.

Scale factors for simulated τ leptons are derived from the efficiency ratio between data and simulation:

$$\text{SF} = \frac{\epsilon_{\text{data}}}{\epsilon_{\text{MC}}}, \tag{4.4}$$

where this correction is obtained for different combinations of working points for the electron and muon vetoes. Three processes are employed: $Z \to \tau_{\text{lep}}\tau_{\text{had}}$ as the main measurement, $W \to$

$\tau_{\text{had}}\nu_\tau$ events as a cross check, and $t\bar{t} \to \tau_{\text{had}} +$ jets as an alternative for the region $40\,\text{GeV} < p_{\text{T}} < 100\,\text{GeV}$.

In these estimations, p_{T}-correlated track counting [187, 188] is used to improve the discrimination power between real $\tau_{\text{had-vis}}$ and QCD jets. Since QCD events are unlikely to have many jets in the narrow core $\Delta R < 0.2$ cone, tracks with $0.2 < \Delta R < 0.6$ are also used. These tracks are selected if they are p_{T}-correlated to the ones in the core cone. For any given outer track with $p_{\text{T}} > 500\,\text{MeV}$, the distance to the inner track is calculated as

$$D^{\text{outer}} = \frac{p_{\text{T}}^{\text{inner}}}{p_{\text{T}}^{\text{outer}}} \times \Delta R(\text{inner}, \text{outer}), \tag{4.5}$$

and tracks that have $D^{\text{outer}} < 4.0$ are selected. The final track multiplicity is then defined as the sum of selected tracks and the number of tracks in the core cone. For real events, this distribution still peaks at 1 and 3. The fit result for the main measurement of the efficiency is shown in fig. 4.7. From the results, scale factors are obtained for all types of selected τ leptons.

4.3 Photon identification

Photons are identified in the same fashion as electrons, with a distinction between *converted* and *unconverted* photons [189]. Converted photons, photons that decayed into an e^+e^- pair, are characterised by the presence of tracks originating inside the calorimeter volume. Unconverted photons do not have such a track. Any cluster without tracks matched to it is considered to be an unconverted photon candidate.

Similar to leptons, two sets of requirements for photon identification exist: *loose* and *tight* photons. Loose photons are selected based on hadronic leakage and on shower shape requirements in the middle layer of the EM calorimeter. Tight photons are optimised to reject $\pi^0 \to \gamma\gamma$ decays. Tighter requirements on the loose variables are used, as well as additional requirements that include the energy deposit in the strip layer. With its fine granularity it provides good π^0–γ separation. As a consequence, tight photons are only defined for $|\eta| < 2.37$, excluding the transition region $1.37 < |\eta| < 1.52$ between the barrel and end-cap.

Photon candidates are required to be isolated: in a cone of $\Delta R = 0.4$ around the photon, the additional energy is required to be $E_{\text{T}}^{\text{iso}} < 4\,\text{GeV}$.

The photon identification efficiency is obtained by using three data-driven methods [190]: one using a pure photon sample of radiative $Z \to \ell^+\ell^-\gamma$ decays, with ℓ an electron or muon; another using electrons from Z decays and remapping their discriminating variables to photons; and finally through the use of a *matrix method* making use of the track isolation. In this way, an efficiency for the range $10\,\text{GeV} < E_{\text{T}}^{\gamma} < 500\,\text{GeV}$ is obtained.

$Z \to \ell^+\ell^-\gamma$ events are selected by requiring two leptons with $p_{\text{T}} > 15\,\text{GeV}$ with the three-body mass near the Z pole ($80\,\text{GeV} < m_{\ell\ell\gamma} < 96\,\text{GeV}$), and $40\,\text{GeV} < m_{\ell\ell} < 80\,\text{GeV}$ to minimise the contribution of Z+jets events. $Z \to ee$ events require two isolated electrons with $80\,\text{GeV} < m_{ee} < 100\,\text{GeV}$, both electrons having $E_{\text{T}} > 25\,\text{GeV}$ and $|\eta| < 2.37$, excluding the region $1.37 < |\eta| < 1.52$. The matrix method relies on a sample of events passing single-photon triggers, with

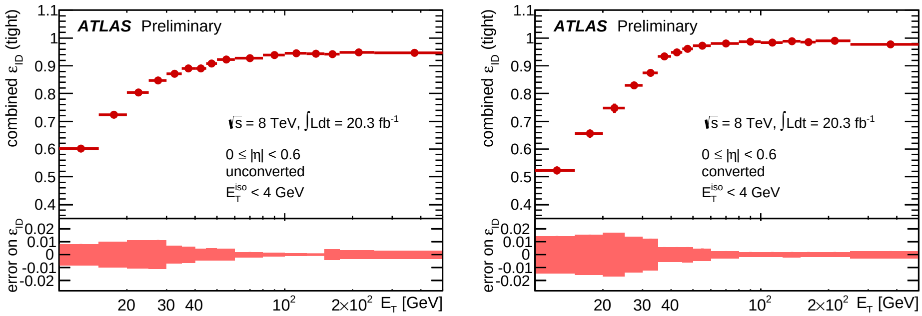

Fig. 4.8 · Combination of the data-driven measurements of ϵ_{ID} for unconverted photons (left) and converted photons (right) in the transverse energy range 10 GeV $< E_{\text{T}} <$ 500 GeV for $|\eta| < 0.6$ [191].

at least one photon with $E_{\text{T}} > 20$ GeV. A system of two equations for the number of loose and tight photons is then solved for ϵ_{ID}. Each of these methods leads to a separate photon efficiency that can be combined with the others. The resulting combined photon efficiency is shown in fig. 4.8.

The dominant systematic uncertainty on the photon efficiency is statistical. In addition, the $Z \to \ell\ell\gamma$ method has a small systematic contribution from the presence of background in the selected sample, mostly from Z+jets events. The extrapolation method from $Z \to ee$ events has systematic errors due to differences for the discriminating variables between electrons and photons. These errors amount to at most 2 % for unconverted photons and 1 % for converted photons. In addition, the transformation mapping electrons to photons leads to an additional uncertainty of at most 5 % for converted and at most 15 % for unconverted photons, due to the sensitivity of the transformation to the amount of material in front of the ECAL end-cap. Finally, the uncertainty on the matrix method is driven by the uncertainty on track isolation criteria.

4.4 Jet reconstruction

Due to confinement, quarks and gluons hadronise in the detector and are not directly detected. Instead, a collimated bundle of particles will be measured. From such collimated sets of particles, one can reconstruct *jets*: composite objects contained in cones in (η, ϕ)-space.

In ATLAS, jets are reconstructed using solely calorimeter information. Calorimeter energy deposits are combined into clusters using a *topological cluster algorithm* [171]. Clustering starts at seed cells that have a signal-to-noise ratio above a predefined threshold t_{seed}. Clusters are then created by adding neighbouring cells with a signal-to-noise ratio above a low threshold t_{cell}. Neighbours with a signal-to-noise ratio above a third ratio $t_{\text{neighbour}}$ can serve as an additional seed to further expand the cluster. Only clusters with positive energy are considered. EM clusters are "633" clusters; hadronic clusters are "420" clusters. The numbers refer to, in order, t_{seed}, $t_{\text{neighbour}}$ and t_{cell}.

From these clusters, jets can be identified using a jet finding algorithm. Such algorithms should be both infrared and collinear safe: the emission of soft or collinear gluons should not affect the definition of the reconstructed jets. The algorithm of choice in ATLAS is the anti-k_t algorithm [184, 192], an extension to the earlier k_t [193] and Cambridge/Aachen [194] algorithms, which is both infrared and collinear safe. The FASTJET package is utilised to perform the jet reconstruction [195].

As in other jet algorithms, the distance between two objects i and j and the distance between an object and the beam have to be defined. In the anti-k_t case, these are given by

$$d_{ij} = \min\left(p_{\mathrm{T}_i}^{-2}, p_{\mathrm{T}_j}^{-2}\right)\frac{\Delta R_{ij}^2}{R}, \tag{4.6a}$$

$$d_{iB} = \frac{1}{p_{\mathrm{T}_i}^2}, \tag{4.6b}$$

where p_{T_i} is the transverse momentum of object i. The parameter R defines the size of the jet: typically, it is chosen to be $R = 0.4$ or $R = 0.6$.

Starting from the object i with the smallest distance to the beam, which has the highest p_{T}, objects are recombined into jets. Given a pair of objects i and j, the two are combined into a new object k if $d_{ij} < d_{iB}$. The procedure is repeated for all other objects $j \neq k$, until no more pairs of objects are combined into one. The object k is then called a jet, and the procedure starts again from the object with the next highest p_{T}. Once no more combinations occur, all jets in the event have been identified. The jet definition ensures the centres of jets are at least $2R$ apart.

4.4.1 Jet energy calibration

Before jets are formed by a jet algorithm, their energy needs to be calibrated. ATLAS employs a *local cluster weighting* (LCW) method to do so. Topologically connected calorimeter clusters are classified as either electromagnetic or hadronic. Based on this classification, energy corrections derived from single-pion Monte Carlo simulations are applied. Energy lost due to the non-compensation and non-instrumented regions of the calorimeters, as well as noise suppression is taken into account, without reference to a jet definition [196].

To relate the measured energy of a jet to its true energy of its constituents, it must be calibrated by the use of *jet energy scale* (JES) corrections. These corrections are derived by evaluating the transfer function between the energy of measured jets and of their particle-level constituents and exploit a momentum balance between a jet and a reference object:

$$\mathcal{R}(p_{\mathrm{T}}^{\mathrm{jet}}, \eta) = \frac{\langle p_{\mathrm{T}}^{\mathrm{jet}} / p_{\mathrm{T}}^{\mathrm{ref}} \rangle_{\mathrm{data}}}{\langle p_{\mathrm{T}}^{\mathrm{jet}} / p_{\mathrm{T}}^{\mathrm{ref}} \rangle_{\mathrm{MC}}}. \tag{4.7}$$

The inverse of this quantity is the JES correction factor applied to data. The full calibration scheme used to calibrate jets goes under the name LCW+JES.

Jets are further calibrated in four subsequent steps: by applying pile-up corrections, correcting the jet direction so that it points to the primary vertex, applying corrections to the energy and

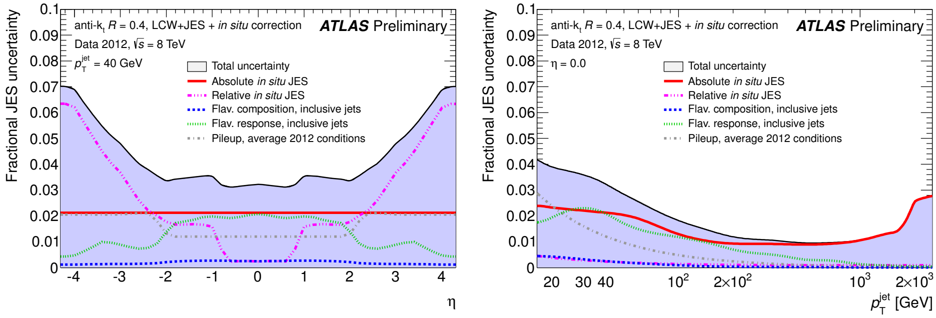

Fig. 4.9 · The fractional JES uncertainty at average pile-up conditions as a function of η and p_T [197].

pseudorapidity distributions from data/MC ratios, and by applying residual in-situ corrections based on momentum balances in various well-modelled processes [198].

The systematic uncertainty on the jet energy scale is derived by estimating the uncertainties on the various in situ techniques used to derive the jet energy scale. By varying the selection criteria on the processes used, an uncertainty on the result can be obtained [198]. The resulting JES uncertainty is shown in fig. 4.9. For central jets with $p_T < 2$ TeV, the maximum uncertainty is 4 %. For very forward jets with $p_T = 40$ GeV, the maximum uncertainty is 7 %.

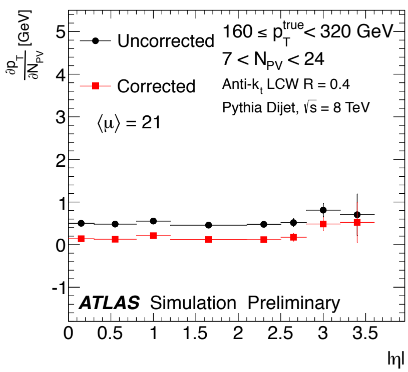

Fig. 4.10 · Jet p_T dependence on the number of primary vertices as a function of η [199].

Pile-up affects jet reconstruction: by virtue of their size in the calorimeters, the chance of particles originating from pile-up to end up in a jet increases with both $\langle\mu\rangle$ and the jet size R. The dependence is mitigated through the application of a correction to each jet's p_T using the median p_T density ρ in events and the jet's size A [199]:

$$p_T^{\text{jet,corr}} = p_T^{\text{jet}} - \rho \cdot A, \tag{4.8}$$

with further residual corrections to describe the pile-up sensitivity of high-occupancy regions in the calorimeter applied afterwards. Fig. 4.10 illustrates the dependence of the average jet p_T on the number of primary vertices before and after the application of the $\rho \cdot A$ correction.

4.4.2 Identifying b quark decays

Jets originating from the decay of b quarks can be distinguished from other light-flavour jets through the use of vertex information. Due to the relatively long lifetime of ~ 1.5 ps, B hadrons will typically travel a few millimetres in the detector before decaying. Many algorithms exist to

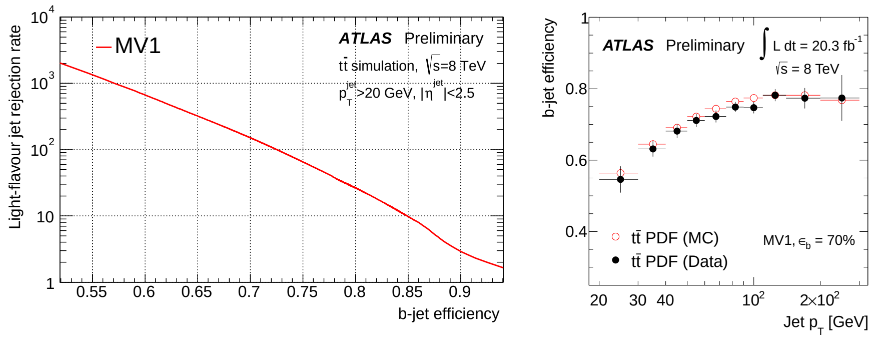

Fig. 4.11 · The light-flavour rejection rate as a function of the b-tagging efficiency for the MV1 algorithm [204] (left) and the measured b-tagging efficiency for MV1 at the 70 % working point [203] (right).

tag these b jets [200, 201]. In the work described in this thesis, the MV1 algorithm has been used, a neural network-based algorithm that uses the output weights of the IP3D, SV1 and JetFitter-CombNN algorithms as inputs [202].

For a b-tagging algorithm, operating points (working points) are defined based on the inclusive b-tag efficiency in a simulated sample of $t\bar{t}$ events. The MV1 tagger has operating points for ϵ_b at 60 %, 70 %, 75 % and 85 %. The choice of an operating point is a trade-off between the tagging efficiency and the light-flavour rejection ratio, which decreases with increasing efficiency.

These operating points are derived using a combinatorial likelihood fit on a data sample of dileptonic $t\bar{t}$ events with two oppositely charged leptons in the final state. Backgrounds to this process containing real isolated leptons include Wt production, Z+jets events with $Z \to \tau\tau$ decays and subsequent leptonic τ decays, and diboson production with leptonic boson decays. Events with fake leptons are estimated from data by requiring same-sign leptons after such simulated events are substracted from the Monte Carlo samples. A combinatorial likelihood built from per-event unbinnned likelihoods in the $e\mu$, e^+e^- and $\mu^+\mu^-$ channels for both two- and three-jet events is used to extract the b-tag efficiency and scale factors as a function of jet p_{T} [203].

Fig. 4.11 shows the rejection rate for light-flavour jets for MV1 as a function of the b-tag efficiency. At the 70 % operating point, the ratio at which light-flavour jets are rejected is approximately 150-to-1. It also shows the b-tagging efficiency for MV1 as a function of the jet p_{T} with its statistical and systematic uncertainty. The systematic uncertainty is mostly driven by uncertainties on the $t\bar{t}$modelling and the modelling of hadronisation in the $t\bar{t}$ events, an uncertainty due to the top p_{T} reweighting used, experimental uncertainties related to jets, and the mis-tag rate.

4.5 Missing transverse energy

Having identified all measurable objects in the detector, particles that escape the detector undetected have to be taken into account. Examples are the neutrino, as well as the hypothetical lightest supersymmetrical particle. A *missing momentum* of $\vec{p}_{\mathrm{T}}^{\,\mathrm{miss}} = \sum_i \vec{p}_{\mathrm{T}}^{\,\mathrm{i}}$ is left, where the sum runs over all invisible particles. Using the momentum imbalance in an event, the term is in practice calculated as $\vec{p}_{\mathrm{T}}^{\mathrm{miss}} = -\sum_j \vec{p}_{\mathrm{T}}^{\,\mathrm{j}}$, where the sum now runs over all *visible* particles. Assuming all invisible particles are massless, the magnitude can be expressed as $p_{\mathrm{T}}^{\mathrm{miss}} = E_{\mathrm{T}}^{\mathrm{miss}} = \left|\vec{E}_{\mathrm{T}}^{\mathrm{miss}}\right|$.

Invisible particles are a source of real $E_{\mathrm{T}}^{\mathrm{miss}}$, while many other effects, such as misreconstructed objects, imperfect resolutions, or detector efficiencies, can lead to fake $E_{\mathrm{T}}^{\mathrm{miss}}$. Energy deposits in the calorimeters and muons reconstructed in the muon spectrometer are used to calculate the missing transverse energy. Segment-tagged muons are also included, as are further low-p_{T} tracks of particles that are missed in the calorimeters. $E_{\mathrm{T}}^{\mathrm{miss}}$ is calculated using reconstructed and calibrated objects as follows [205]:

$$E_{\mathrm{x,y}}^{\mathrm{miss}} = E_{\mathrm{x,y}}^{\mathrm{miss,e}} + E_{\mathrm{x,y}}^{\mathrm{miss,}\gamma} + E_{\mathrm{x,y}}^{\mathrm{miss,}\tau} + E_{\mathrm{x,y}}^{\mathrm{miss,jets}} + E_{\mathrm{x,y}}^{\mathrm{miss,SoftTerm}} + E_{\mathrm{x,y}}^{\mathrm{miss,}\mu}, \tag{4.9}$$

where each term is the negative sum of transverse energy of the objects used to calculate it.[1]

In the calculation of $E_{\mathrm{T}}^{\mathrm{miss}}$ defined in (4.9), electrons are calibrated using the standard ATLAS calibration (medium++ electrons with a $p_{\mathrm{T}} > 10\,\mathrm{GeV}$), photons are calibrated at the EM scale, τ jets are calibrated using local cluster weighting (LCW) with an offset to suppress pile-up effects (τ energy scale, [206]). Jets with $p_{\mathrm{T}} > 20\,\mathrm{GeV}$ are calibrated using the LCW+JES scheme. The soft term contains jets with $p_{\mathrm{T}} < 20\,\mathrm{GeV}$, as well as topological clusters and tracks not associated to high-p_{T} objects, which are calibrated using the LCW scheme with any overlap between the clusters and tracks removed. To prevent ambiguities in the definition of $E_{\mathrm{T}}^{\mathrm{miss}}$, objects are added in the order specified in (4.9), with overlapping clusters removed from components added later.

Pile-up can not only distort the energy reconstructed in jets, but also create additional jets. To suppress jets coming from pile-up, a requirement is applied on the jet vertex fraction [183], the fraction of tracks of a jet coming from a primary vertex:

$$\mathrm{JVF} = \sum_{\mathrm{tracks_{jet}},\mathrm{PV}} p_{\mathrm{T}} \Big/ \sum_{\mathrm{tracks_{jet}}} p_{\mathrm{T}}. \tag{4.10}$$

Jets with $p_{\mathrm{T}} < 50\,\mathrm{GeV}$ and $|\eta| < 2.4$ that do not satisfy $|\mathrm{JVF}| > 0$ are discarded, as these have no associated tracks. Further care must especially be taken to model pile-up effects on the soft term. These effects are reduced by applying tracking-based pile-up corrections and jet-area-based pile-up suppression [207].

The performance of $E_{\mathrm{T}}^{\mathrm{miss}}$ reconstruction can be evaluated on samples of $Z \rightarrow \mu\mu$ and $W \rightarrow e\nu$ events, to validate the modelling of both fake and real missing transverse energy [205]. Fig. 4.12 shows the $E_{\mathrm{T}}^{\mathrm{miss}}$ distribution for both samples after pile-up suppression using a soft-term vertex fraction requirement[2]. Good agreement between data and simulation is observed for the $Z \rightarrow \mu\mu$ sample, while for the $W \rightarrow e\nu$ sample a larger discrepancy is seen. This may in part be due to the fact that the QCD background, which should dominate at low $E_{\mathrm{T}}^{\mathrm{miss}}$, is not included in the expectations shown. The resolution of $E_{\mathrm{T}}^{\mathrm{miss}}$ for various Monte Carlo samples is shown in fig. 4.13. The degradation in the resolution for $t\bar{t}$ and SUSY events is probably due to the large number of jets: removing one and/or reducing the soft term can create an imbalance.

[1] The missing transverse energy can also be calculated without a specific term for τ leptons. In that case, these are either counted in the jet or soft term, depending on the p_{T} of the associated jet(s).

[2] The soft term vertex fraction (STVF) is defined similar to the JVF, but using jets in the soft term of $E_{\mathrm{T}}^{\mathrm{miss}}$.

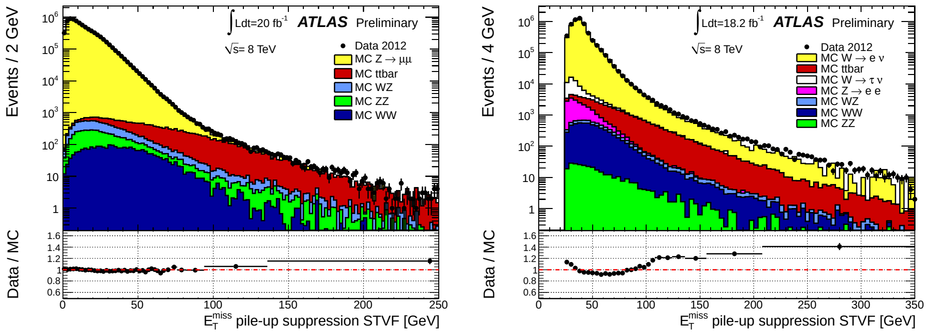

Fig. 4.12 · Distribution of $E_{\mathrm{T}}^{\mathrm{miss}}$ as measured in a data sample of $Z \to \mu\mu$ events (left) and $W \to e\nu$ events (right) after pile-up suppression using STVF requirements [205].

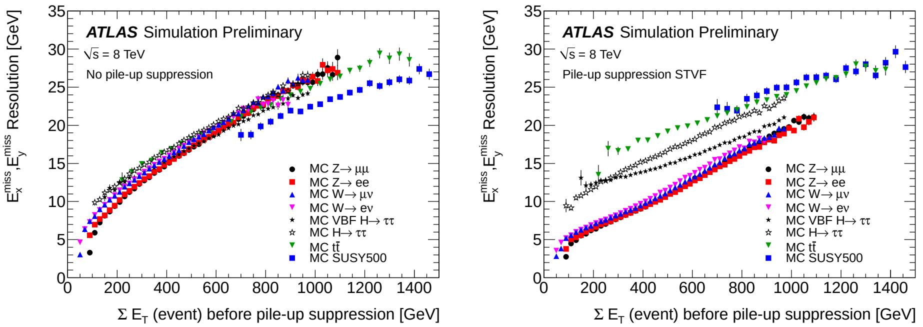

Fig. 4.13 · $E_{\mathrm{T}}^{\mathrm{miss}}$ resolution for various Monte Carlo samples before (left) and after (right) STVF pile-up suppression [205].

Uncertainties on the missing transverse energy can come from any of its ingredients. The overall systematic uncertainty on $E_{\mathrm{T}}^{\mathrm{miss}}$ is evaluated by combining the uncertainty on all individual terms. Lepton energy and resolution uncertainties, and jet energy scale and resolution uncertainties are the largest ones. Finally, a smaller uncertainty comes from the soft term, arising from Monte Carlo modelling and effects of pile-up and can be evaluated in situ on $Z \to \mu\mu$ events; it ranges from 2 % to 7.9 % [205].

CHAPTER FIVE

SUSY without leptons

Particles predicted by supersymmetry can decay in many different ways, depending on the mass spectrum and the mixing matrices. In this thesis, we focus on strongly produced squarks and gluinos that decay into final states without electrons or muons. These final states are motivated by the large number of R-parity-conserving [208–212] models in which squarks (including anti-squarks) and gluinos can be produced in pairs ($\tilde{g}\tilde{g}$, $\tilde{q}\tilde{q}$, $\tilde{q}\tilde{g}$) and decay through $\tilde{q} \to q\tilde{\chi}_1^0$ and $\tilde{g} \to q\bar{q}\tilde{\chi}_1^0$ to weakly interacting lightest neutralinos, $\tilde{\chi}_1^0$. The $\tilde{\chi}_1^0$ is the lightest SUSY particle (LSP) in these models and escapes the detector unseen. Additional decay modes can include the production of charginos via $\tilde{q} \to q\tilde{\chi}^{\pm}$ (where $\tilde{q}$ and q are of different flavour) and $\tilde{g} \to q\bar{q}\tilde{\chi}^{\pm}$. Subsequent decay of these charginos to $W^{\pm}\tilde{\chi}_1^0$ can lead to final states with still larger multiplicities of jets. This inspires our choice of searching for supersymmetry in final states with 2 to 6 jets, no leptons, and a large amount of missing energy.

As many analyses within ATLAS, the one presented here has been performed in a team of approximately 10–15 people. My contribution to the analysis lies in the determination of the final signal and control regions and the setting of exclusion limits on the most important simplified models: those with squark-pair, gluino-pair and associated squark–gluino production. Further limits on natural gauge mediation models, bilinear R-parity violating MSUGRA/CMSSM models, and gluino-mediated $\tilde{t}$ decays, have also been set by me. I further contributed a new interpretation of gluino-mediated $\tilde{t}$ production, where the $\tilde{t}$ decays via c quarks $\tilde{g} \to \tilde{t}\bar{t} \to c\bar{t}\tilde{\chi}_1^0$ with $\Delta m(\tilde{t}, \tilde{\chi}_1^0) = 20\,\text{GeV}$.

The final choice of baseline Monte Carlo samples was determined using results from validation fits for various combinations of generators that I studied. Moreover, I studied the possible benefit of using binned fits in several variables in the analysis. Finally, I was responsible for setting the model-independent upper limits shown. Further contributions lay in the development of the fitting framework used in this analysis and the maintenance thereof.

The analysis described here presents the final results in the 0-lepton channel using the $\sqrt{s} = 8\,\text{TeV}$ dataset and has been published in [213]. It updates previous ATLAS results [214–218].

5.1 Analysis strategy

If supersymmetric particles exist and are not too heavy, they can be produced at the LHC. Squarks and gluinos will then be the most abundantly produced, due to their coupling to the strong force. As most Standard Model particles, the produced SUSY particles are unstable and decay into lighter particles. Squarks and gluinos can decay either directly into quarks that will form jets, or go through a longer cascade of decays, resulting in (multiple) jets, plus possibly photons or leptons. Assuming R-parity is conserved, the lightest supersymmetrical particle is stable and cannot be detected, leading to a large amount of missing transverse energy ($E_{\mathrm{T}}^{\mathrm{miss}}$).

Overview

The analysis presented here searches for heavy resonances. The analysis has been designed by using the MSUGRA/CMSSM and three simplified models: direct $\tilde{q}\tilde{q}$, $\tilde{g}\tilde{g}$ and $\tilde{q}\tilde{g}$ production. In the simplified models, supersymmetrical particles decay immediately into quarks and $\tilde{\chi}_1^0$, the LSP. Typical events are hence characterised by missing energy, and 2 jets ($\tilde{q}\tilde{q}$), 3 jets ($\tilde{q}\tilde{g}$) or 4 jets ($\tilde{g}\tilde{g}$). Cascade decays through a $\tilde{\chi}^{\pm}$ will lead to at least one additional jet, as will any initial-state or final-state radiation (ISR, FSR). Events are therefore required to have a minimum number high-p_{T} jets that ranges from two to six. Rejecting events with leptons suppresses several background processes. Notwithstanding the motivation of finding supersymmetry, the analysis is hence sensitive to the existence of *any* strongly interacting heavy particle that decays into at least two jets.

Backgrounds

Searches in high energy physics are statistical in nature. We must thus first determine what our expected observation is, caused by *background events* from known processes. Any Standard Model process that leads to high-p_{T} jets and $E_{\mathrm{T}}^{\mathrm{miss}}$ without a lepton is a background to the signal searched for. These are QCD multijet events, events with top quarks (both $t\bar{t}$ and single-top), W+jets and Z+jets events, and, finally, diboson processes. All of these backgrounds are described in more detail in §5.2.

Processes such as $W \to \ell\nu$ are suppressed in the signal region by requiring selected events to have no electrons or muons present. Since hadronically decaying τ leptons are hard to identify, their presence is not used to reject events. An adverse effect of requiring no leptons is that the QCD background is higher than when selecting events with at least one lepton; as will become clear later, this is mitigated by different selections.

All datasets and Monte Carlo samples used in this analysis are listed in §5.3. The object definitions used are shown in §5.4; the trigger and event selection are discussed in §5.5.

Obtaining predictions

The analysis described here is a *cut-and-count* analysis: after a set of selections ("cuts") on the dataset is applied, the total amount of events N is counted and compared to an expected number $N_{\mathrm{exp}} \pm \sigma_{\mathrm{exp}}$ in *signal regions*, regions in phase space where one expects to see events in which SUSY particles are produced. The final variable used to discriminate between signal and background events, the effective mass, is described in §5.5.3. All signal regions used are described in §5.5.4. These signal regions were defined through an optimisation procedure discussed at the end of the chapter in §5.A and §5.B.

The expected number of events in the signal regions is obtained using a semi-data-driven method. The method relies on *control regions*, regions in phase space enhanced in a particular background, to constrain the normalisation of all background processes simultaneously using a likelihood fit. The background normalisations obtained are then used in the signal region, as described in §5.6.

To validate the procedure, a further set of regions where no signal is expected, called *validation regions*, is used to compare the background predictions determined with the fit to data. This procedure also allows us to test whether the total background prediction takes decays such as $W \to \tau\nu$ into account correctly, e.g. by using special τ lepton validation regions. Graphically, the concept of signal, control and validation regions is illustrated in fig. 5.1. All control and validation regions are presented in §5.6.1.

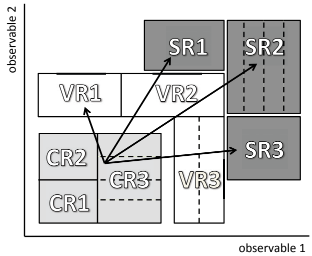

Fig. 5.1 · Illustration of signal, control and validation regions.

Interpretation

After having obtained the number of expected events in the signal region, it can be compared to a measurement to test the validity of the Standard Model hypothesis as well as alternative hypotheses, e.g. from a simplified model. The interpretation of results is performed using a log-likelihood ratio described in §5.9. An overview of the entire procedure used to obtain and interpret results is shown in fig. 5.2.

The results of the simultaneous fit are shown in §5.10 for the control and validation regions, and in §5.10.2 for the signal regions. The interpretation of these results in various models is presented in §5.11 and discussed in §5.12.

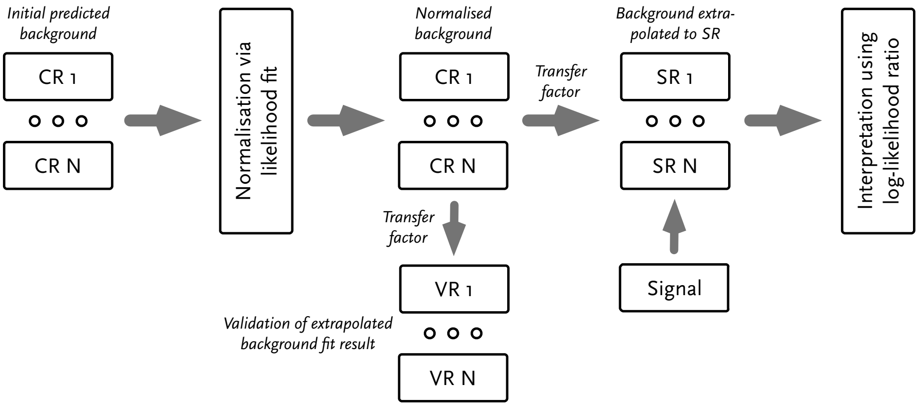

Fig. 5.2 · Overview of the procedure used to obtain and interpret results in this analysis. The control regions (CR) are used to constrain the background in the signal regions (SR); the extrapolation is validated using validation regions (VR).

5.2 Standard Model backgrounds

QCD multijet production is the most abundant process occurring in proton–proton collisions at the LHC. Multijet events are the result of parton scattering: two-parton interactions can result in high-p_T dijet events, in which the emission of hard gluons can lead to additional jets. The misreconstruction of produced jets can lead to fake E_T^{miss}, usually aligned with one of the jets. Additionally, multijet events may come from heavy-flavour interactions. In semileptonic decays of the quarks, the lepton can be misreconstructed, again resulting in high-p_T jets and E_T^{miss}.

W bosons decay either hadronically (67.6 %) or leptonically (10.8 % per flavour). The production of a W boson can occur with associated jets, the cross-section decreasing by approximately $1/\alpha_s$ with each additional jet. In the case of $W \to \tau\nu$ or misidentified electrons or muons, the process is a background to supersymmetrical events without leptons.

Unlike W bosons, Z bosons can also decay invisibly. The decay into hadrons occurs 70 % of the time; the decay into two leptons 10 %, summed over all flavours.[1] The remaining 20 % of Z bosons decay invisibly into neutrinos via $Z \to \nu\nu$. Z+jets events where the Z decays into neutrinos form an irreducible background: their signature cannot be discerned from a supersymmetrical event.

The production of two vector bosons leads to kinematics similar to W+jets and Z+jets events, albeit with a much lower cross-section.

Top quark decays form the final background in this analysis. Pair-production occurs via $q\bar{q} \to t\bar{t}$ or gluon fusion ($gg \to t\bar{t}$), with the latter the dominant mechanism at the LHC: antiquarks are only available as sea quarks. Their short lifetime ensures top quarks decay before they hadronise, predominantly into a W boson and a b quark due to the CKM-matrix element $|V_{tb}| > 0.999$ [109]. A produced $t\bar{t}$ pair hence decays fully hadronically, semileptonically or dileptonically. Semi- and dileptonic decays lead to real E_T^{miss}, and form a background to the study in case the lepton is a τ, or misidentified. Events with fake E_T^{miss} can come from hadronic decays or dileptonic decays, in case both leptons are τ leptons and/or misidentified.

Single-top production occurs together with a W boson, or with another quark in s- and t-channel diagrams. The top quark decays into Wb and forms a background for the same reasons as decaying $t\bar{t}$ pairs.

All other backgrounds are negligible due to either their very small cross-section or the event selection.

5.3 Datasets and Monte Carlo samples

The dataset used in this analysis was recorded by the ATLAS detector from April to December 2012 and corresponds to a raw recorded luminosity of 21.7 fb^{-1}. Applying data quality requirements the dataset is reduced in size to 20.3 fb^{-1}, the loss a consequence of requiring that all sub-detector systems record data of good quality. The preliminary uncertainty on the luminosity is 2.8 %, obtained using dedicated beam-separation scans performed in 2012, known as Van der Meer scans, following the same procedure as in [219]. The main analysis uses data from the `JetTauEtmiss` stream; control region measurements also rely on the `Egamma` and `Muon` streams.

[1] Decays of Z bosons into τ leptons that in turn decay hadronically are treated as Z+jets events.

5.3.1 Monte Carlo samples

Monte Carlo samples are used to obtain background predictions via the use of transfer factors and to assess the sensitivity to various SUSY models. Samples for Standard Model processes are produced using the full simulation of the detector; all SUSY signal models were generated with AtlFast-II, except MSUGRA/CMSSM, for which the full detector simulation was used.[1]

Pile-up simulation

In order to correctly model pile-up effects, every sample is overlaid with minimum-bias events during digitisation. These events are generated using PYTHIA 8.160 [151] with the AM2 tune [220] and the leading-order PDF set MSTW2008LO [58]. To ensure the same performance is used as for data samples, Monte Carlo events are weighted as a function of the average number of interactions per crossing $\langle\mu\rangle$.

Additional uncertainties coming from the unknown total inelastic cross-section and possible biases in the Monte Carlo sample are addressed by scaling the simulated $\langle\mu\rangle$ distribution by the factors 0.9 and 1.1. Any difference in the number of simulated events after this rescaling is taken as an uncertainty included in the final fit.

Background samples

Vector boson samples

Samples of W+jets, Z/γ^*+jets and γ+jets are generated using SHERPA 1.4.X [148] and ALPGEN 2.14 [153]. To improve the description of events with hard jets, up to 4 or 5 extra partons are generated at matrix-element level. Subsequent merging of matrix-element level events to the parton shower algorithm is based on the CKKW scheme [221–223] for SHERPA and on the MLM scheme [224] for ALPGEN. Events generated using SHERPA use the CT10 next-to-leading order PDF set [225]. Parton shower and fragmentation processes for the ALPGEN samples are simulated using Herwig 6.520 [226], with JIMMY [227] using the AUET2 tune [220] for the underlying event, and with CTEQ6L1 for the PDF set [59]. $W \to \ell\nu$ samples are normalised to a reference cross-section of 12.19 nb, based on NNLO predictions given by DYNNLO [228]. Z samples are also normalised to NNLO, whereas γ+jets samples are normalised to the cross-section given by the generator. Z and γ samples are generated using a setup as close as possible, to minimise any potential impact on the ratio Z/γ. The importance of that ratio becomes clear during the discussion on background estimation in §5.6.1.

Events generated using SHERPA serve as a baseline for the prediction of the number of events, whereas ALPGEN serves as a comparison and is used to obtain theoretical uncertainties. SHERPA samples are generated with massive b and c quarks, which improves the description of flavour-tagging variables. For ALPGEN, datasets are generated with light quarks and with massive b quarks. The overlap[2] between baseline samples and those with massive quarks is removed using a dedicated tool. Several W+jets samples are generated with a generator-level filter of

[1] For several signal model points, the use of fast simulation was validated against the full simulation.

[2] ALPGEN makes no attempt to match b and c quarks explicitly when generating extra partons. As a consequence, the same event may be used twice when generating samples with extra partons in e.g. W+N2p and Wc+N1p.

Table 5.1 · The Standard Model background Monte Carlo generators used.

Sample	Generator	Alt. generator
W+jets	SHERPA	ALPGEN + Herwig
Z/γ^*+jets	SHERPA	ALPGEN + Herwig
γ+jets	SHERPA	ALPGEN + Herwig
$t\bar{t}$	POWHEG + PYTHIA 6	MC@NLO + Herwig
single-top t-channel	AcerMC + PYTHIA 6	–
single-top s-channel, Wt	MC@NLO + Herwig	–
$t\bar{t}$ + EW boson	MadGraph 5 + PYTHIA 6	–
Diboson	SHERPA	–
QCD	PYTHIA 8	–

$E_{\mathrm{T}}^{\mathrm{miss}} > 100$ GeV and $p_{\mathrm{T}} > 80$ GeV for the leading parton to improve the number of events in the phase space region relevant for the analysis.[1] $Z \rightarrow \ell\ell$ events are generated using an invariant mass $m_{\ell\ell} > 40$ GeV. To obtain enough events in the tails of the momentum distributions, all samples are sliced as a function of the vector boson transverse momentum.

Top quark samples

Samples with pair-produced top quarks are generated using POWHEG-BOX 1.0 [229, 230, 155] interfaced to PYTHIA 6.426 [150] for the fragmentation and hadronisation processes. The mass of the top quark is fixed to $m_t = 172.5$ GeV, the CT10 PDF set is used, and the PERUGIA2011C tune [231, 232] is used to set PYTHIA 6 parameters. To cope with differences between the $t\bar{t}$ p_{T} spectrum in data and POWHEG events, weights are derived in four bins of p_{T} [233] and applied to simulation. Alternative samples are generated with MC@NLO 4.03 using the CT10 PDF set, using Herwig 6.520 with JIMMY for the underlying event, and with SHERPA and POWHEG interfaced to PYTHIA 6.426, using a different tune (AUET2). No $p_{\mathrm{T}}(t\bar{t})$ correction is applied to MC@NLO events: it correctly reproduces the $p_{\mathrm{T}}(t\bar{t})$ distribution.

The $t\bar{t}$ cross-section is obtained from NNLO QCD calculations including next-to-next-to-leading logarithmic resummation of soft gluon terms and predicted to be $\sigma_{t\bar{t}} = 253^{+13.3}_{-14.5}$ pb [234–239].

Single-top production is simulated using MC@NLO 4.03 with Herwig 6.520 and JIMMY for the s-channel and Wt processes. The t-channel is simulated using AcerMC 38 [240] and PYTHIA 6.426 with the CTEQ6L1 PDF set, due to the mismodelling of initial states with b quarks in MC@NLO. The cross-sections used for these processes are (5.61 ± 0.22) pb for the s-channel [241], $87.76^{+3.44}_{-1.91}$ pb for the t-channel [242] and (22.37 ± 1.52) pb for the Wt channel [243].

Production of $t\bar{t}$ in association with a W or Z is simulated using MadGraph 5.0 [152] interfaced to PYTHIA 6.426. $t\bar{t}$+γ is not simulated, although partly accounted for via QED FSR from the baseline $t\bar{t}$ sample. The ttH process is neglected in this analysis.

[1] The transverse mass m_{T} is defined as $m_{\mathrm{T}}^2 = m_1^2 + m_2^2 + 2[E_{\mathrm{T},1}E_{\mathrm{T},2} - \vec{p}_{\mathrm{T},1} \cdot \vec{p}_{\mathrm{T},2}]$ and is used to constrain the mass of a particle decaying into two particles of which one is invisible.

Diboson samples

The processes WW, WZ, ZZ, $W\gamma$ and $Z\gamma$ are simulated using SHERPA 1.40. Up to 3 extra partons are considered at matrix-element level; b and c quarks are treated as massive except for the processes $W\gamma$ and $Z\gamma$ (no MC samples with heavy quarks were available at the time of the analysis). The WW, WZ and ZZ cross-sections are calculated at NLO using MCFM [244, 245]. A flat uncertainty of 50 % on the diboson contribution to the signal regions is used, after the impact of varying the factorisation, renormalisation and matching scales was studied. Triboson processes (WWW, WWZ, ZZZ) were generated using MadGraph 5.0 with PYTHIA 6.426 and found to contribute negligibly; they are not used in this analysis.

QCD multijet samples

QCD jet events are simulated using PYTHIA 8.160 using the CT10 PDF set and the ATLAS tune AU2 [246]. They are only used for data–MC comparisons, since the background is estimated using a data-driven method; no theoretical uncertainty is evaluated.

Summary of generators used

A summary of the choices for the Monte Carlo generators is shown in table 5.1. These choices have been determined with the aid of blinded validation fits, and to be in line as much as possible with commonly used baseline samples in the ATLAS SUSY working group. The alternative samples are used to derive a theoretical uncertainty on a particular background prediction.

Signal samples

For every model studied, a set of simulated SUSY models need to be generated. Each model investigated relies on a grid of points defined in its two- or three-dimensional parameter space. In MSUGRA/CMSSM, the parameters are m_0 and $m_{1/2}$, with $\tan\beta$, A_0 and $\text{sgn}\,\mu$ fixed (see §5.11). For simplified models the masses of the relevant particles in the model are used. Models with generic squarks assume that 4 flavours ($\tilde{u}$, $\tilde{d}$, $\tilde{s}$ and $\tilde{c}$) are degenerate and have the same mass; $\tilde{t}$ and $\tilde{b}$ quarks are decoupled. Both chirality states are also assumed to be degenerate.

For MSUGRA/CMSSM, SUSY-HIT [247] interfaced to SOFTSUSY 3.1.6 [248] is used to generate a mass spectrum for each point, to calculate the decay tables and to guarantee consistent electroweak symmetry breaking. The top mass is set to 173.2 GeV when calculating these spectra. Samples are generated using Herwig++ 2.5.2 with the underlying event tune UE-EE-3 [249] and the CTEQ6L1 PDF set, and use the full detector simulation.

Samples for the simplified models are generated using MadGraph 5.0 interfaced to PYTHIA 6.426 and PDFs from CTEQ6L1, with one extra parton in the matrix element.[1] The merging of matrix elements and parton shower is performed using the MLM scheme, with the matching scale set to $\min(500\,\text{GeV}, m_{\text{SUSY}}/4)$. Simplified model samples use AtlFast-II for the detector simulation. All samples used are listed in table 5.2.

[1] Modelling ISR and FSR correctly is important in scenarios with small $\Delta m(\tilde{q}, \tilde{\chi}_1^0)$, as these lead to soft jets.

Table 5.2 · Parameters for the different SUSY signal grids used in this analysis.

Grid name	Parameters	Generator
mSUGRA/CMSSM	$\tan\beta = 30$, $A_0 = -2 \times m_0$, $\mu > 0$, $m_0 \in [400, 6000]$ GeV with 200 GeV step, $m_{1/2} \in [400, 1000]$ GeV with 50 GeV step	Herwig++
Squark–gluino–neutralino (pheno. MSSM)	$m_{\tilde{q},\tilde{g}} \in [400, 4000]$ GeV with 200 GeV step, $m_{\tilde{\chi}_1^0} = 0$ GeV, 395 GeV, 695 GeV	MadGraph 5 + PYTHIA 6
Squark pair, direct decay	$m_{\tilde{q}} \in [87, 1575]$ GeV, $m_{\tilde{\chi}_1^0} \in [0, 1200]$ GeV	idem
Gluino pair, direct decay	$m_{\tilde{g}} \in [87, 1800]$ GeV, $m_{\tilde{\chi}_1^0} \in [0, 1200]$ GeV	idem
Squark–gluino production direct decays	$m_{\tilde{q}} = 0.96 \times m_{\tilde{g}}$, $m_{\tilde{g}} \in [87, 1987]$ GeV, $m_{\tilde{\chi}_1^0} \in [0, 1200]$ GeV	idem
Squark pair, decay via an intermediate $\tilde{\chi}^\pm$	$m_{\tilde{q}} \in [200, 1500]$ GeV, fixed $m_{\tilde{\chi}_1^0} = 60$ GeV or $x = (m_{\tilde{\chi}^\pm} - m_{\tilde{\chi}^0})/(m_{\tilde{q}} - m_{\tilde{\chi}^0}) = 0.5$	idem
Gluino pair, decay via an intermediate $\tilde{\chi}^\pm$	$m_{\tilde{g}} \in [200, 1500]$ GeV, fixed $m_{\tilde{\chi}_1^0} = 60$ GeV or $x = (m_{\tilde{\chi}^\pm} - m_{\tilde{\chi}^0})/(m_{\tilde{g}} - m_{\tilde{\chi}^0}) = 0.5$	idem
Gluino-pair production, $\tilde{g} \to \bar{t}\tilde{t}, \tilde{t} \to c\tilde{\chi}^0$	$m_{\tilde{g}} \in [400, 1400]$ GeV with 100 GeV step, $m_{\tilde{t}} \in [200, 1100]$ GeV with 100, 200 GeV step, $m_{\tilde{\chi}_1^0} = m_{\tilde{t}} - 20$ GeV	Herwig++

Signal cross-sections are calculated using next-to-leading order calculations and next-to-leading log resummation of soft gluon emission (NLO+NLL) [250–254]. The nominal cross-section and its uncertainty are calculated using a procedure that averages calculations using various PDF sets, values of α_s, and factorisation and renormalisation scales [63].

5.4 Object definition

The objects used in this analysis are defined in chapter 4. However, additional offline criteria are used, e.g. on the isolation of objects. Furthermore, we must take care to remove overlapping objects.

Jets are reconstructed using the anti-k_t algorithm with $R = 0.4$ and are calibrated using the LCW+JES scheme. The η- and p_T-dependent jet energy scale uncertainty is correctly described by a single constraining parameter in the likelihood; the full parametrisation in several terms is not used. All jets are required to have $p_T > 20$ GeV and $|\eta| < 2.8$, except during the calculation of E_T^{miss}. Further jet quality requirements are applied after the overlap removal described in §5.4.1; events containing jets failing these criteria are not selected.

***b*-jets** are identified using the MV1 tagger at the 70 % efficiency working point. Only candidates with $p_{\mathrm{T}} > 40\,\mathrm{GeV}$ and $|\eta| < 2.5$ will be identified as b-jets. Uncertainties on the b-tag weights are taken into account in the fit procedure.

Electrons are required to pass medium++ identification criteria. In addition, the transverse momentum $p_{\mathrm{T}} = E^{\mathrm{clust}} / \cosh\eta$ should exceed 10 GeV, where η is taken to be η^{track} if the track has at least 4 silicon hits, and η^{clust} otherwise. Its quality flag must also indicate the electron is good. Finally, we require $\eta^{\mathrm{clust}} < 2.47$.

Candidates to be used in control regions selecting leptons must pass the tight++ criteria, have $p_{\mathrm{T}} > 25\,\mathrm{GeV}$, pass the isolation selection $p_{\mathrm{T}}^{\mathrm{cone20}} / p_{\mathrm{T}} < 0.10$, where cone20 refers to a cone of $R = 0.2$ around the electron, and satisfy the primary-vertex constraints $\left|d_0^{\mathrm{PV}}\right| < 1\,\mathrm{mm}$ and $\left|z_0^{\mathrm{PV}}\right| < 2\,\mathrm{mm}$.

Photons are required to pass the loose identification criteria and in addition have $E_{\mathrm{T}} > 130\,\mathrm{GeV}$ to pass the lowest unprescaled single-photon trigger. As for electrons, the quality flag must also indicate the photon is good. Candidates for use in the Z control region must pass the tight photon criteria and be isolated in the calorimeter: $E_{\mathrm{T}}^{\mathrm{topo40}} < 4\,\mathrm{GeV}$, where topo40 refers to a cone of size $R = 0.4$ around the photon.

Muons are combined or segment-tagged STACO [178] muons that are isolated: $p_{\mathrm{T}}^{\mathrm{cone20}} < 1.8\,\mathrm{GeV}$. Acceptance selections of $p_{\mathrm{T}} > 10\,\mathrm{GeV}$ and $|\eta| < 2.4$ are applied. Muons must pass the loose identification criteria and selections on the track quality in the inner detector. Muons for use in a control region selecting leptons must further have $p_{\mathrm{T}} > 25\,\mathrm{GeV}$ and satisfy the primary-vertex constraints $\left|d_0^{\mathrm{PV}}\right| < 0.2\,\mathrm{mm}$ and $\left|z_\mu - z_0^{\mathrm{PV}}\right| < 1\,\mathrm{mm}$.

Missing transverse energy is calculated using (4.9) as described in §4.5 and reconstructed using an algorithm that does not specifically take hadronic τ leptons into account. These instead are counted in the soft term or as jets.

τ leptons are selected if they pass the standard identification criteria. Candidates that overlap with medium electrons or b-tagged jets within $\Delta R < 0.2$ are rejected. In order to use jets with a small chance of misidentification, candidates are required to have $p_{\mathrm{T}} > 20\,\mathrm{GeV}$. In case of overlapping candidates, the one with the highest p_{T} is selected.

5.4.1 Overlap removal

Candidates that overlap with one another must be classified as a single object: all but one candidate must be removed from the event. The overlap criteria used are based on the simple distance $\Delta R = \sqrt{(\Delta\eta)^2 + (\Delta\phi)^2}$, and are applied in the following order:

1. a jet found within $\Delta R < 0.2$ of an electron is ignored;
2. a muon found within $\Delta R < 0.4$ of a jet is ignored;
3. an electron found within $0.2 < \Delta R < 0.4$ of a jet is ignored.

In the control region using photons (see §5.6.1), jets within $\Delta R < 0.2$ of a photon are ignored.

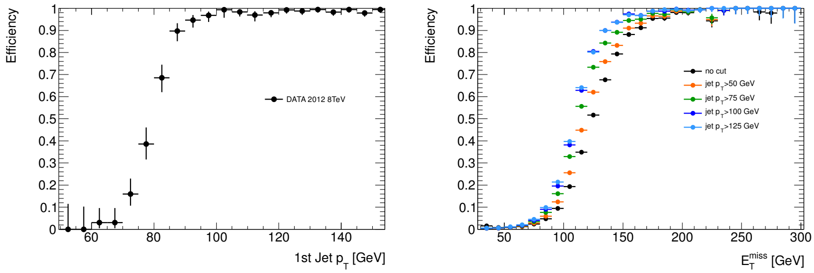

Fig. 5.3 · Efficiency of the used jets+$E_{\mathrm{T}}^{\mathrm{miss}}$ trigger as a function of leading jet p_{T} (left) and $E_{\mathrm{T}}^{\mathrm{miss}}$(right).

5.5 Event selection

After having obtained both datasets of simulated and measured events, we can proceed to select events from these datasets. Selections are placed on the datasets to classify events as background-like, for a control region, or signal-like, for the signal region.

5.5.1 Trigger

The baseline trigger in the event selection for the signal regions is a combined jet+$E_{\mathrm{T}}^{\mathrm{miss}}$ trigger called `EF_j80_a4tchad_xe100_tclcw_veryloose`, which is seeded by the L1 trigger `L1_j50_xe40` and the L2 trigger `L2_j75_c4cchad_xe55`. It requires at least one anti-k_t $R = 0.4$ jet with $p_{\mathrm{T}} > 80$ GeV and $E_{\mathrm{T}}^{\mathrm{miss}} > 100$ GeV. Fig. 5.3 illustrates that in the region selected after the offline selection $E_{\mathrm{T}}^{\mathrm{miss}} > 160$ GeV and $p_{\mathrm{T}}(j_1) > 130$ GeV, the trigger is 100 % efficient.

In the control regions using photons, `EF_g120_loose` is used to select photons with $E_{\mathrm{T}} > 120$ GeV. The control regions requiring leptons rely on the lowest available single-lepton triggers: `EF_mu24i_tight` (tight muons with $p_{\mathrm{T}} > 24$ GeV), `EF_e24vhi_medium1` (isolated medium electrons with $p_{\mathrm{T}} > 24$ GeV) and `EF_e60_medium1` (medium electrons with $p_{\mathrm{T}} > 60$ GeV).

QCD seed events used to estimate the multijets background (see §5.6.3) are selected using 9 prescaled single-jet triggers. The prescale decreases with increasing E_{T} threshold, which ranges from 55 GeV to 460 GeV. Seed events used are weighted with the average prescale for their respective data-taking period.

5.5.2 Event cleaning

Non-collision backgrounds, bad calorimeter regions and fake muons can lead to fake $E_{\mathrm{T}}^{\mathrm{miss}}$. By applying *cleaning selections* to reduce these effects and estimating the residual non-collision background, the amount of fake missing transverse energy can be reduced. Non-collision background events come from other sources than the proton–proton collision, such as beam-gas events or cosmic ray events.

Events in a time window around a noise burst in the liquid-argon calorimeter are vetoed by rejecting error and warning states. Corrupted readouts in the tile calorimeter are also vetoed.

Finally, after a restart of the timing, trigger and control systems (TTC restart), some events can have incomplete information. These are rejected as well.[1]

Jet cleaning

Jets are cleaned using the procedure described in [255]. For each jet, the measured pulse in the calorimeter cells is compared to simulation of the electronics response. The quadratic difference $Q_{\text{cell}}^{\text{LAr}}$ between the expected and measured pulse shape is used to discriminate between noise and real energy deposits. Selections on the average jet quality $\langle Q \rangle$, the normalised energy-squared weighted average of the pulse quality in the calorimeter cells in the jet; on f_Q^{LAr}, the fraction of cells in the liquid-argon calorimeter with poor shape quality; and on f_Q^{HEC}, the fraction of cells in the hadronic end-caps with poor shape quality, are used to reject bad jets.

Four sets of cleaning selections for jets are defined. In this analysis, the 'looser' set of cleaning selections is used. Spikes in the hadronic end-cap (HEC) are identified using $|E_{\text{neg}}| > 60\,\text{GeV}$, or $f_{\text{HEC}} > 0.5$ and $\left|f_Q^{\text{HEC}}\right| > 0.5$ and $\langle Q \rangle > 0.8$. Coherent EM noise is identified with $f_{\text{EM}} > 0.95$ and $f_Q^{\text{LAr}} > 0.8$ and $\langle Q \rangle > 0.8$. Any event containing such jets with $p_{\text{T}} > 20\,\text{GeV}$ is rejected.

Additional cleaning

Data corruption in the tile calorimeter can lead to cells and topological clusters with a large negative energy, which leads in turn to a large fake $E_{\text{T}}^{\text{miss}}$. Since jets are reconstructed from cells with positive energy, the jet cleaning procedure does not suffice to reject such events. Events are rejected if the $E_{\text{T}}^{\text{miss}}$ term for unassociated clusters contributes significantly:

$$\frac{E_{\text{T}}^{\text{miss,CellOut}}}{E_{\text{T}}^{\text{miss}}} \cos\left(\phi\left(E_{\text{T}}^{\text{miss,CellOut}}\right) - \phi\left(E_{\text{T}}^{\text{miss}}\right)\right) > 0.5. \tag{5.1}$$

The inefficiency of this requirement has been found to be negligible.

Next to the standard jet cleaning requirements, an additional selection is placed on the charged fraction of a leading jet. The charged fraction is defined as $f_{\text{ch}} = \sum |p_{\text{T}}^{\text{track}}|/p_{\text{T}}^{\text{jet}}$. Events are rejected in case either $f_{\text{ch}} < 0.02$ and $|\eta| < 2.0$, or $f_{\text{ch}} < 0.05$ and $f_{\text{EM}} > 0.9$ and $|\eta| < 2.0$, where f_{EM} is the fractional electromagnetic contribution to the jet. These selections are efficient at rejecting cosmic-ray events, beam background and events where no track is expected. Its efficiency has been studied on back-to-back dijet events using the QCD samples used in this analysis and found to be approximately 99.5 %.

Several hot regions in the tile calorimeter were accidentally not masked in the reconstruction in multiple data-taking periods. Events are vetoed if a jet points in the direction of these modules and has most of its energy deposited in the second layer: $E_{\text{layer}}/E_{\text{jet}} > 0.6$. Moreover, events with any of the leading jets pointing in the direction of the hot cells are vetoed if $f_{\text{ch}} < 0.3$ and $f_{\text{EM}} < 0.25$.

Dead calorimeter cells can cause fake missing energy if a jet falls inside them. The energy in a dead cell is estimated through the use of information on the jet shape from simulation, giving an estimate $B_{\text{corr}}^{\text{jet}}$ for the fraction of the lost energy in measurements. Events with jets

[1] Selected events have `larError == 0`, `tileError == 2` and `coreFlags&0x40000 == 0`.

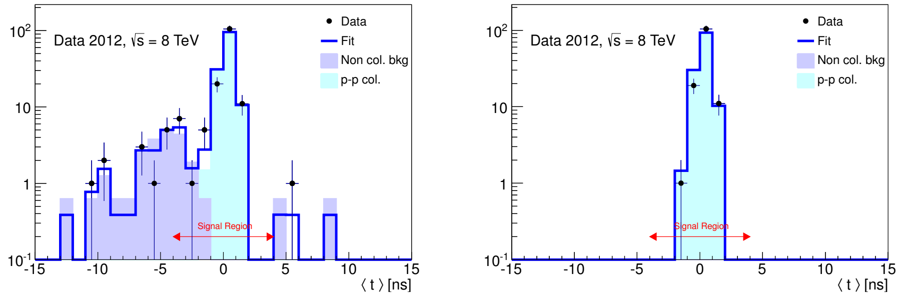

Fig. 5.4 · Distribution of the mean jet time before (left) and after (right) the jet cleaning for SR2jm.

with $p_T > 40$ GeV pointing in the direction of dead modules ($\Delta\phi(j, E_T^{miss}) < 0.2$) are vetoed if $B_{corr}^{jet} > 0.05$. The loss of efficiency for SUSY events has been estimated using simulated samples and found to be less than 1 %.

Finally, fake muons can lead to a large fake missing energy. Fake muons are reconstructed muons that do not correspond with real muons coming from the proton–proton interaction. Instead, they are created when very energetic jets end up in the muon system, or when bad tracks in jets are wrongly matched to segments in the muon spectrometer. In order to reject these fake muons, two criteria are applied:

- any event with a muon with $\frac{\sigma(q/p)}{q/p} > 0.2$ before the overlap removal is vetoed;
- veto events with $\frac{E_T^{miss,muon}}{E_T^{miss}} \cos\left(\phi(E_T^{miss,muon}) - \phi(E_T^{miss})\right) > 0.5$.

The first of these rejects muons where the error on charge-over-momentum ratio q/p is large. The other rejects events with large E_T^{miss} due to badly reconstructed muons that are not rejected by a lepton veto because these muons are non-isolated.

Residual non-collision background

The residual non-collision background is estimated using jet timing information. For each signal region, the energy-weighted mean jet time of the selected amount of jets is calculated as

$$t_{N_j} = \frac{\sum_i^{N_j} t_i E_i}{\sum_i^{N_j} E_i}, \tag{5.2}$$

where N_j ranges from 2 to 6 depending on the signal region. It is used to reject additional events with $|t_{N_j}| < 4$ ns to reject events with out-of-time jets not produced in the initial collision, where jets have $t = 0$.

To estimate the residual background, the rejected events serve as a control region for the non-collision background. The timing distribution for the 2-jet signal region SR2jm, defined later, is shown in fig. 5.4.

An upper limit on the amount of residual background events is obtained using the dijet signal regions, with several criteria changed to obtain a sample dominated by non-collision background and orthogonal to the signal region. Using the efficiency of the selection on the leading jet and a tightened window in m_{eff} (see §5.5.3), an upper limit is derived on the remaining non-collision background in the signal region.[1] For the loose dijet region, an estimated 0.39 events remain; for the tight dijet region 0.07. For higher jet multiplicities, no events with $|t_{N_j}| < 4\,\mathrm{ns}$ are present. Beam background can be safely neglected in these channels.

5.5.3 The effective mass

In order to discriminate between events likely to come from supersymmetry processes and events from Standard Model processes, we need quantities that separate the two. Next to selections to reject QCD multijet events and to suppress other Standard Model backgrounds, the final discriminating variable used to separate the remaining background from any signal is the effective mass m_{eff} [256, 257].

Consider an event in which a heavy SUSY particle with mass m_1 is produced. Assuming it undergoes a cascade decay to a lighter SUSY particle with mass m_2, and a Standard Model particle, the latter's transverse momentum in the lab frame is related to the masses of the two SUSY particles[2]:

$$p_{\mathrm{T}} \propto \frac{1}{2}\left(m_1 - \frac{m_2^2}{m_1}\right). \tag{5.3}$$

Variables using the p_{T} of particles are thus sensitive to the masses of SUSY particles. Analogously we can for a supersymmetrical model define an *effective mass scale* as

$$M_{\mathrm{SUSY}}^{\mathrm{eff}} = \left(M_{\mathrm{SUSY}} - \frac{M_\chi^2}{M_{\mathrm{SUSY}}}\right), \tag{5.4}$$

where M_χ is the mass of the LSP and M_{SUSY} the cross-section-weighted mean of the masses of the initial particles (two in R-parity conserving models).

The effective mass scale $M_{\mathrm{SUSY}}^{\mathrm{eff}}$ corresponds to the mass of the particle initially produced. Since the initial particles contribute the most to the p_{T} of the decay products and the invisible LSP leads to missing energy, we define the *effective mass* m_{eff} of an event, an observable given by

$$m_{\mathrm{eff}} = E_{\mathrm{T}}^{\mathrm{miss}} + \sum_i |p_{\mathrm{T}}^i|, \tag{5.5}$$

where the sum runs over all jets and leptons in an event. In scenarios with a large mass difference, m_{eff} is strongly correlated with the masses of pair-produced SUSY particles in an event, as well as with the typical mass of SUSY particles in models such as MSUGRA/CMSSM [257]. Due to the high

[1] The requirement on the jet charge fraction rejects all events in the control region, leading to the conclusion that no non-collision background remains. It is therefore estimated using looser selections. Since the rejection power increases with jet p_{T}, an upper limit on the number of remaining events can be derived through the use of this looser sample.

[2] Two assumptions are made here: that the initial SUSY particle is produced at threshold, and that its decay products are primarily produced in the central region; hence $p_{\mathrm{T}} = p\sin\theta \approx p$ and $p_z \sim 0$ for the Standard Model particle. The calculation is not meant to be exact, only to show a better estimate for m_1 can be found by using not only the p_{T} of jets but also any missing energy. This estimation is the most accurate in case of heavy squarks or gluinos produced at threshold and a light LSP.

mass of supersymmetrical particles, m_{eff} serves as a good discriminant between Standard Model events and SUSY events.

5.5.4 Signal regions

Following the trigger and event cleaning selections, the main signal selection criteria are applied. To reject leptonic W+jets and $t\bar{t}$ events in which the neutrino is the source of $E_{\text{T}}^{\text{miss}}$, a lepton veto is applied in the signal region. Leptons used in this veto have $p_{\text{T}} > 10\,\text{GeV}$ to ensure a good identification efficiency. To ensure the trigger is operating efficiently, selections on the missing energy and leading jet p_{T} are applied. We require $E_{\text{T}}^{\text{miss}} > 160\,\text{GeV}$ and $p_{\text{T}}(j_1) > 130\,\text{GeV}$.

Five jet multiplicities are used in this analysis in order to be sensitive to a range of models. For each sub-leading jet, we require $p_{\text{T}} > 60\,\text{GeV}$. The signal regions are named after the jet multiplicity: for example, SR3j is a 3-jet signal region. The procedure used to optimise the final definitions of the signal regions described below is presented in §5.A.

To suppress QCD events with fake $E_{\text{T}}^{\text{miss}}$, the angle between the jets and the direction of the missing energy is used. In events with fake $E_{\text{T}}^{\text{miss}}$, it will often have the same direction as a mis-measured jet. In contrast, in events with real missing energy, such as the supersymmetrical interactions searched for, $E_{\text{T}}^{\text{miss}}$ has recoiled against an object. To select such events, the angular separation between the jets and missing energy is used. For the two- and three-jet regions, jets with $p_{\text{T}} > 40\,\text{GeV}$ are required to have $\Delta\phi(j_{2,3}, E_{\text{T}}^{\text{miss}})_{\text{min}} > 0.4$. For higher jet multiplicities, $\Delta\phi(j_{i>3}, E_{\text{T}}^{\text{miss}})_{\text{min}} > 0.2$ is imposed on the remaining jets.

Two signal regions specifically target the decay of gluinos and squarks via an intermediate chargino in which a W boson is produced. Depending on the W boson's boost, which is proportional to the mass difference between the $\tilde{\chi}^{\pm}$ and the $\tilde{\chi}_1^0$, we can reconstruct the W candidate from either a single high-mass jet, or two separate jets with an invariant mass around m_W. This further rejects background events. Two signal regions using W bosons are used. Signal region SR2jW requires two $W \to j$ candidates with $60\,\text{GeV} < m_W < 100\,\text{GeV}$; signal region SR4jW requires one $W \to j$ and one $W \to jj$ candidate with the same mass requirement.[1] In order to ensure enough events pass the selection for SR4jW, the jet p_{T} requirements are relaxed to $p_{\text{T}}(j_{3,4}) > 40\,\text{GeV}$. The addition of these two signal regions improves the exclusion limits at high $x = (m_{\tilde{\chi}^{\pm}} - m_{\tilde{\chi}_1^0})/(m_{\tilde{q},\tilde{g}} - m_{\tilde{\chi}_1^0})$.

The final signal region is defined using two selections. One is placed on the effective mass, calculated as (5.5), where the sum runs over all jets with $p_{\text{T}} > 40\,\text{GeV}$ in the event. The effective mass including all jets is referred to as $m_{\text{eff}}(\text{incl.})$; in contrast, $m_{\text{eff}}(N_j)$ includes the first N jets.

The other selection is made on either $E_{\text{T}}^{\text{miss}}/m_{\text{eff}}(N_j)$ or $E_{\text{T}}^{\text{miss}}/\sqrt{H_{\text{T}}}$ (called the $E_{\text{T}}^{\text{miss}}$ significance), where $H_{\text{T}} = m_{\text{eff}}(N_j) - E_{\text{T}}^{\text{miss}}$. The use of $m_{\text{eff}}(N_j)$ in the calculation of H_{T} has been found to better reject QCD events.

The combination of these selections amounts to a strict selection based on $E_{\text{T}}^{\text{miss}}$, in that way further suppressing the QCD background. Since additional jets in a SUSY event decrease the

[1] The reader might notice that only 3 jets are used to reconstruct W bosons, and indeed the name of this signal region was originally intended to be SR3jW. However, a bug was found in the implementation of the function that finds W candidates. Rather than 3 jets, 4 jets with $p_{\text{T}} > 40\,\text{GeV}$ were required. The region was hence renamed.

probability of an LSP with a high momentum, the selection on $E_{\mathrm{T}}^{\mathrm{miss}}/m_{\mathrm{eff}}(N_j)$ decreases with increasing jet multiplicity. The requirement on $E_{\mathrm{T}}^{\mathrm{miss}}/\sqrt{H_{\mathrm{T}}}$ is used in several two- and four-jet regions: studies showed that it leads to enhanced sensitivity to models with $\tilde{q}\tilde{q}$ production.

For each jet multiplicity, several signal regions are defined using various requirements on $m_{\mathrm{eff}}(\mathrm{incl.})$ and $E_{\mathrm{T}}^{\mathrm{miss}}/m_{\mathrm{eff}}(N_j)$ or $E_{\mathrm{T}}^{\mathrm{miss}}/\sqrt{H_{\mathrm{T}}}$. These define *very loose*, *loose*, *medium*, *tight* and *very tight* cut-and-count regions. Not every jet multiplicity uses the same amount of regions. All signal regions are shown in table 5.3. It is important to note that the inclusive selections on the jet multiplicities and on $m_{\mathrm{eff}}(\mathrm{incl.})$ lead to non-orthogonal signal regions.

The signal acceptances times reconstruction efficiencies for squark- and gluino-pair production models are shown in fig. 5.5 and 5.6. The remaining Standard Model background in the signal regions is determined using a semi-data-driven method described in the next section.

5.6 Background estimation

The estimation of the number of background events in each signal region is performed using a semi-data-driven procedure. For each major background, a dedicated control region (CR) is defined, with selections chosen such that the region is enriched in one particular background. The selections used to determine control regions are defined as close in phase space to the signal region as possible, while adding requirements for the background to be estimated. The choice is a trade-off: the further away from the signal region a control region is defined, the larger the systematic error on the extrapolation will be. However, the statistical error will decrease by virtue of the increased number of background events. Additionally, the closer to the signal region, the higher the risk of signal contamination in the control region becomes. In practice, one or two requirements used for the signal region are often inverted or dropped, and one or two additional criteria are imposed for each background, as we shall also see in §5.6.1.

Having defined control regions for all backgrounds, their contribution to the signal region can be estimated by a simultaneous background fit in all control regions using a likelihood function given in §5.9. The result of that fit is extrapolated to the signal region. For each background, it is assumed that

$$\frac{N_{\mathrm{SR}}^{\mathrm{data}}}{N_{\mathrm{SR}}^{\mathrm{MC}}} = \frac{N_{\mathrm{CR}}^{\mathrm{data}}}{N_{\mathrm{CR}}^{\mathrm{MC}}}, \tag{5.6}$$

allowing us to define *transfer factors* from the control region to the signal region and obtain the prediction for each background i as

$$N_{\mathrm{SR}}^{\mathrm{data},i} = N_{\mathrm{SR}}^{\mathrm{MC},i} \times \frac{N_{\mathrm{CR}}^{\mathrm{data},i}}{N_{\mathrm{CR}}^{\mathrm{MC},i}} = N_{\mathrm{SR}}^{\mathrm{MC},i} \times \mu_i\,. \tag{5.7}$$

This choice is particularly useful due to fact that many systematic uncertainties cancel out in the ratio $N_{\mathrm{SR}}^{\mathrm{MC},i}/N_{\mathrm{CR}}^{\mathrm{MC},i}$. The assumption that (5.6) holds needs to be validated and leads to systematic errors on the background prediction.

Table 5.3 · Selection criteria used to define each of the signal regions in the analysis. Each region is labelled with the inclusive jet-multiplicity considered ('2j', '3j' etc.) together with an indication for the requirement on the effective mass, which is (very) *loose*, *medium* or (very) *tight*.

Selection	**Signal region**					
	2jl	**2jm**	**2jt**	**2jW**	**3j**	**4jW**
$E_{\mathrm{T}}^{\mathrm{miss}}$[GeV] >	160					
$p_{\mathrm{T}}(j_1)$ [GeV] >	130					
$p_{\mathrm{T}}(j_2)$ [GeV] >	60					
$p_{\mathrm{T}}(j_3)$ [GeV] >	–				60	40
$p_{\mathrm{T}}(j_4)$ [GeV] >	–					40
$\Delta\phi(j_{1,2,(3)}, E_{\mathrm{T}}^{\mathrm{miss}})_{\mathrm{min}} >$	0.4					
$\Delta\phi(j_{i>3}, E_{\mathrm{T}}^{\mathrm{miss}})_{\mathrm{min}} >$	–					0.2
W candidates	–			$2(W \to j)$	–	$(W \to j) + (W \to jj)$
$E_{\mathrm{T}}^{\mathrm{miss}}/\sqrt{H_{\mathrm{T}}}$ [GeV$^{1/2}$] >	8	15		–		
$E_{\mathrm{T}}^{\mathrm{miss}}/m_{\mathrm{eff}}(N_j)$ >	–			0.25	0.3	0.35
m_{eff}(incl.) [GeV] >	800	1200	1600	1800	2200	1100

Selection	**Signal region**								
	4jl-	**4jl**	**4jm**	**4jt**	**5j**	**6jl**	**6jm**	**6jt**	**6jt+**
$E_{\mathrm{T}}^{\mathrm{miss}}$[GeV] >	160								
$p_{\mathrm{T}}(j_1)$ [GeV] >	130								
$p_{\mathrm{T}}(j_2)$ [GeV] >	60								
$p_{\mathrm{T}}(j_3)$ [GeV] >	60								
$p_{\mathrm{T}}(j_4)$ [GeV] >	60								
$p_{\mathrm{T}}(j_5)$ [GeV] >	–				60				
$p_{\mathrm{T}}(j_6)$ [GeV] >	–					60			
$\Delta\phi(j_{1,2,(3)}, E_{\mathrm{T}}^{\mathrm{miss}})_{\mathrm{min}} >$	0.4								
$\Delta\phi(j_{i>3}, E_{\mathrm{T}}^{\mathrm{miss}})_{\mathrm{min}} >$	0.2								
$E_{\mathrm{T}}^{\mathrm{miss}}/\sqrt{H_{\mathrm{T}}}$ [GeV$^{1/2}$] >	10		–						
$E_{\mathrm{T}}^{\mathrm{miss}}/m_{\mathrm{eff}}(N_j)$ >	–		0.4	0.25	0.2			0.25	0.15
m_{eff}(incl.) [GeV] >	700	1000	1300	2200	1200	900	1200	1500	1700

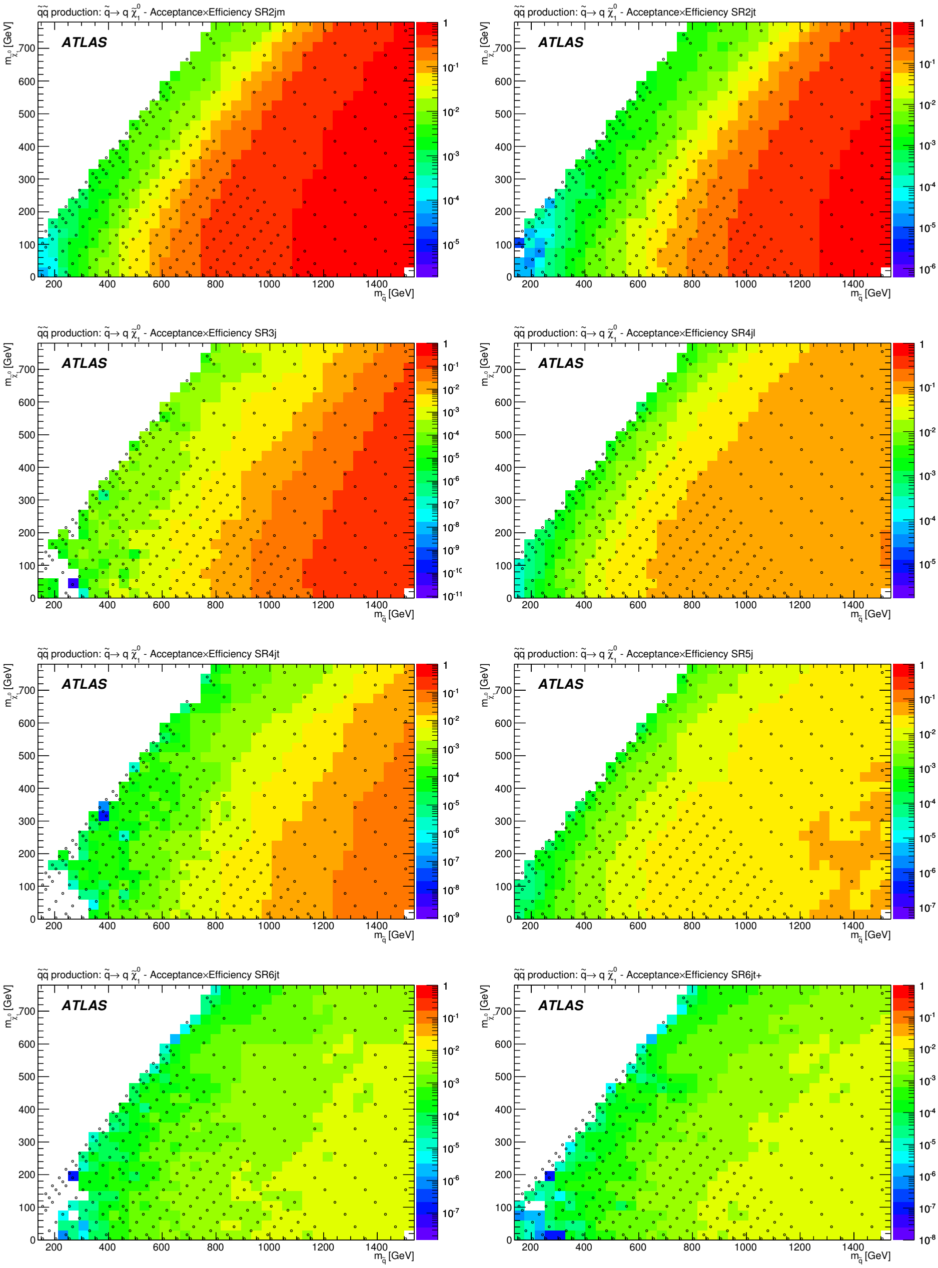

Fig. 5.5 · Distribution of the signal acceptance times reconstruction efficiency for signal regions 2jm, 2jt, 3j, 4jl, 4jt, 5j, 6j and 6j+ for squark-pair production models with direct decays. The markers indicate the locations of the grid points used in the interpolation. The signal regions are representative for the best signal regions for the squark- and gluino-pair production models, as shown in §5.11.

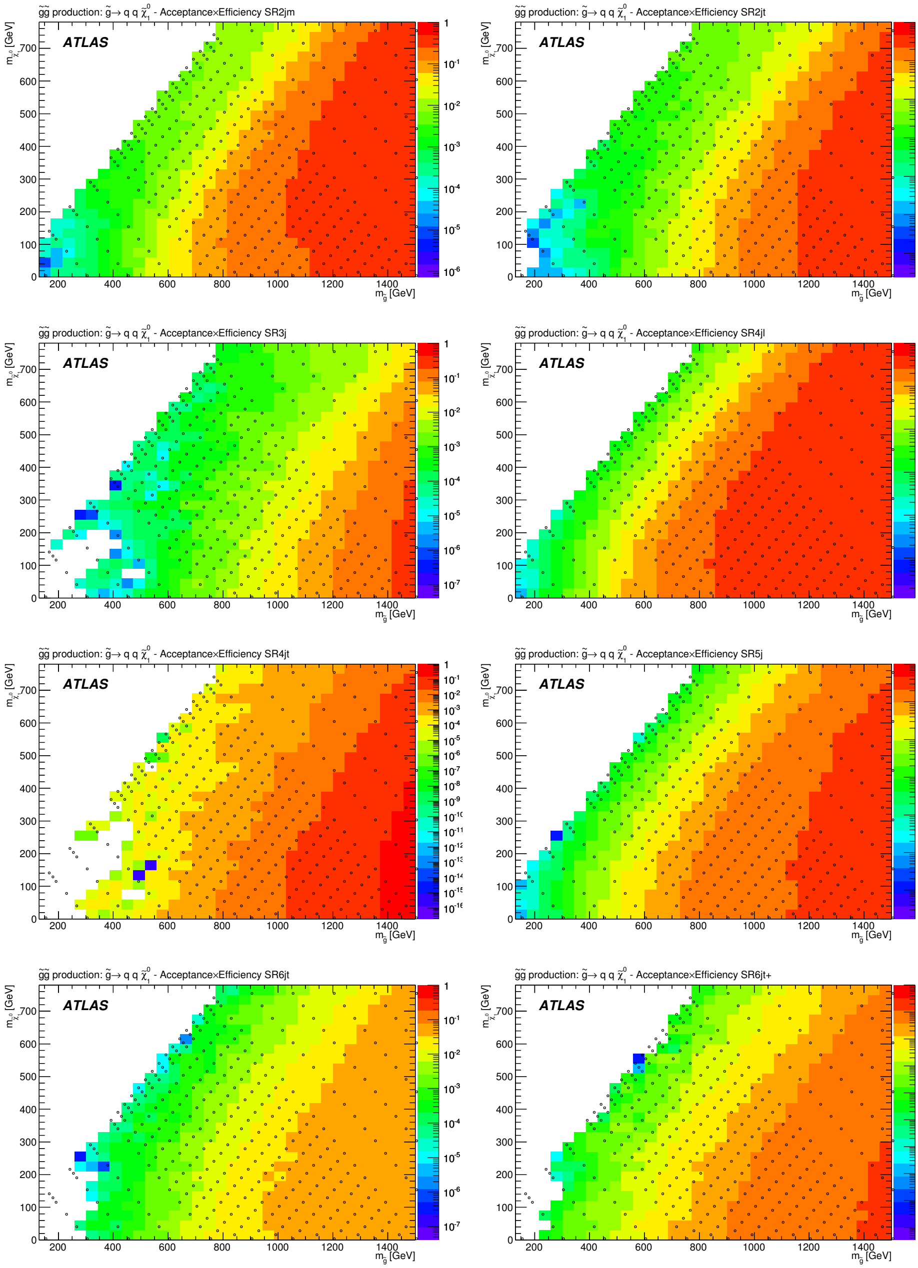

Fig. 5.6 · Distribution of the signal acceptance times reconstruction efficiency for signal regions 2jm, 2jt, 3j, 4jl, 4jt, 5j, 6j and 6j+ for gluino-pair production models with direct decays. The markers indicate the locations of the grid points used in the interpolation. The signal regions are representative for the best signal regions for the squark- and gluino-pair production models, as shown in §5.11.

Table 5.4 · Control regions used in the analysis. Also listed are the main targeted background in the signal region in each case, the process used to model the background, and the main control region requirement(s) used to select this process.

Control region	Background	Estimated with	Control region selection
CRY	$Z(\to \nu\nu)$+jets	γ+jets	Isolated photon
CRQ	Multijets	Multijets	Reversed criteria on (i) $\Delta\phi(j, E_{\mathrm{T}}^{\mathrm{miss}})_{\mathrm{min}}$ and (ii) $E_{\mathrm{T}}^{\mathrm{miss}}/m_{\mathrm{eff}}(N_j)$ or $E_{\mathrm{T}}^{\mathrm{miss}}/\sqrt{H_{\mathrm{T}}}$
CRW	$W(\to \ell\nu)$+jets	$W(\to \ell\nu)$+jets	30 GeV $< m_{\mathrm{T}}(\ell, E_{\mathrm{T}}^{\mathrm{miss}}) <$ 100 GeV, b veto
CRT	$t\bar{t}$ and single-t	$t\bar{t} \to b\bar{b}qq'\ell\nu$	30 GeV $< m_{\mathrm{T}}(\ell, E_{\mathrm{T}}^{\mathrm{miss}}) <$ 100 GeV, b tag

It is important to note that this method relies solely on the *normalisation* of the backgrounds. Any discrepancies in the *shape* of a distribution between a control and a signal region will not be taken into account by the procedure described, as will differences between data and simulation in any correlations between variables of interest.

5.6.1 Control regions

For every signal region, four control regions are defined to constrain the major background processes. The diboson background is relatively small and estimated using simulation only. All control regions are listed in table 5.4 and are further motivated below.

W+jets and $t\bar{t}$

The control regions CRW and CRT are used to select events with $W(\to \ell\nu)$+jets and semileptonic $t\bar{t}$ decays ($t\bar{t} \to b\bar{b}qq'\ell\nu$) by requiring a lepton and by requiring that the transverse mass of the lepton–$E_{\mathrm{T}}^{\mathrm{miss}}$ system is consistent with a leptonic W decay: 30 GeV $< m_{\mathrm{T}}(\ell, E_{\mathrm{T}}^{\mathrm{miss}}) <$ 100 GeV. To distinguish between W+jets and $t\bar{t}$ events, b-tagging information is used: CRT selects events with at least one b-tagged jet, while CRW selects only events with zero b-tagged jets. Requirements on the angular separation $\Delta\phi(j_i, E_{\mathrm{T}}^{\mathrm{miss}})_{\mathrm{min}}$ and $E_{\mathrm{T}}^{\mathrm{miss}}/m_{\mathrm{eff}}(N_j)$, or $E_{\mathrm{T}}^{\mathrm{miss}}/\sqrt{H_{\mathrm{T}}}$, are not applied, except for the control regions for SR2jl; the same selection on m_{eff}(incl.) as in the signal region is used. In the control regions for SR2jW, the requirement on the number of W candidates is relaxed from two to one $W \to j$ candidate to obtain enough events. For the same reason, the control regions for SR6jt use m_{eff}(incl.) $>$ 1300 GeV.

Motivated by the fact that for both backgrounds 75 % of the events in the signal region contain leptons that have faked jets (through misidentification or the lepton being a τ), the selected lepton must satisfy the same angular and p_{T} criteria as a jet. Although a simple assumption (no attempt is made to determine the mechanism by which the lepton is lost), it can be used to normalise the background in the signal regions, provided the treatment is also used in the control regions.

Other minor backgrounds with top quarks (fully leptonic $t\bar{t}$, single-top and $t\bar{t}$+V events) in the signal region are estimated using the normalisation for the semileptonic component. The small $Wb\bar{b}$ background is scaled using the normalisation obtained for $W(\to \ell\nu)$+jets events.

Z+jets

The selection in the signal regions cannot distinguish $Z(\to \nu\nu)$+jets events from supersymmetrical ones; the background is irreducible. A different, but kinematically similar, process needs to be used to determine its contribution. The main control region, CRY, uses γ+jets events, the kinematics of which have been found to very closely resemble $Z(\to \nu\nu)$+jets events, provided $p_{\mathrm{T}}(Z) \gg m_Z$. To estimate the p_{T} of the Z boson, $E_{\mathrm{T}}^{\mathrm{miss}\prime} = E_{\mathrm{T}}^{\mathrm{miss}} + p_{\mathrm{T}}(\gamma)$ is used in the event.

An alternative method is the use of $Z(\to \ell\ell)$+jets events, with ℓ an electron or muon. A same-flavour opposite-sign pair e^+e^- or $\mu^+\mu^-$ is selected with $66\,\mathrm{GeV} < m_{\ell\ell} < 116\,\mathrm{GeV}$ to define the region VRZ. As for CRY, $E_{\mathrm{T}}^{\mathrm{miss}\prime} = E_{\mathrm{T}}^{\mathrm{miss}} + p_{\mathrm{T}}(Z)$ is used in the event. No angular selection $\Delta\phi(j_i, E_{\mathrm{T}}^{\mathrm{miss}})_{\mathrm{min}}$ and requirement on $E_{\mathrm{T}}^{\mathrm{miss}}/m_{\mathrm{eff}}(N_j)$, or $E_{\mathrm{T}}^{\mathrm{miss}}/\sqrt{H_{\mathrm{T}}}$, is applied. Since the combined branching ratios are a factor 3 lower than $Z \to \nu\nu$, VRZ selects too few events for use as a control region. Instead, it is used as a validation region for the Z background.

Cross-section scaling

When using CRY to constrain the Z+jets background, the cross-section ratio between γ+jets and Z+jets must be taken into account. Depending on the generator, this ratio varies as a function of p_{T}. The difference between SHERPA and ALPGEN for the transfer factor $\mathrm{TF}\big(\gamma \to Z(\to \nu\nu)\big)$, shown in fig. 5.7a, can be as large as 30 %. As a consequence, the theoretical uncertainty on the Z+jets background becomes one of the dominant uncertainties on the total background prediction. This uncertainty was one of the primary components in the uncertainty on the squark-pair production limit in more compressed scenarios in the previous version of this analysis [214].

We can reduce this discrepancy between the two generators by using the $Z \to \ell\ell$ background at low p_{T}, in a looser control region where enough events are available. The amount of $Z \to \nu\nu$ events can then be obtained from a *scaled* amount of γ+jets events:

$$N_{\mathrm{SR}}^{Z\to\nu\nu,\mathrm{pred}} = N_{\mathrm{SR}}^{Z\to\nu\nu,\mathrm{MC}} \frac{N_{\mathrm{SR}}^{\gamma+\mathrm{jets},\mathrm{data}}}{\kappa \cdot N_{\mathrm{SR}}^{\gamma+\mathrm{jets},\mathrm{MC}}}, \tag{5.8}$$

where κ is a correction factor derived using $Z \to \ell\ell$ events at low p_{T}. To determine κ, two very loose control regions called CRZVL and CRYVL are defined analogous to VRZ and CRY, except that the selections on $m_{\mathrm{eff}}(\mathrm{incl.})$ and $E_{\mathrm{T}}^{\mathrm{miss}}/m_{\mathrm{eff}}(N_j)$ are replaced by $160\,\mathrm{GeV} < E_{\mathrm{T}}^{\mathrm{miss}\prime} < 300\,\mathrm{GeV}$. The ratio of data/MC can then be used to obtain κ, provided other backgrounds in CRZVL and CRYVL are substracted from the measurement:

$$\begin{aligned}\kappa &= \frac{N_{\mathrm{CRYVL}}^{\gamma+\mathrm{jets},\mathrm{data}}}{N_{\mathrm{CRYVL}}^{\gamma+\mathrm{jets},\mathrm{MC}}} \Bigg/ \frac{N_{\mathrm{CRZVL}}^{Z\to\ell\ell,\mathrm{data}}}{N_{\mathrm{CRZVL}}^{Z\to\ell\ell,\mathrm{MC}}} \\ &= \frac{N_{\mathrm{CRYVL}}^{\mathrm{data}} - N_{\mathrm{CRYVL}}^{\mathrm{bkg}}}{N_{\mathrm{CRYVL}}^{\gamma+\mathrm{jets},\mathrm{MC}}} \Bigg/ \frac{N_{\mathrm{CRZVL}}^{\mathrm{data}} - N_{\mathrm{CRZVL}}^{\mathrm{bkg}}}{N_{\mathrm{CRZVL}}^{Z\to\ell\ell,\mathrm{MC}}},\end{aligned} \tag{5.9}$$

where 'data' refers to a measured number of events, 'MC' to a simulated number of events, and 'bkg' to the amount of background events to the process of interest in a region.

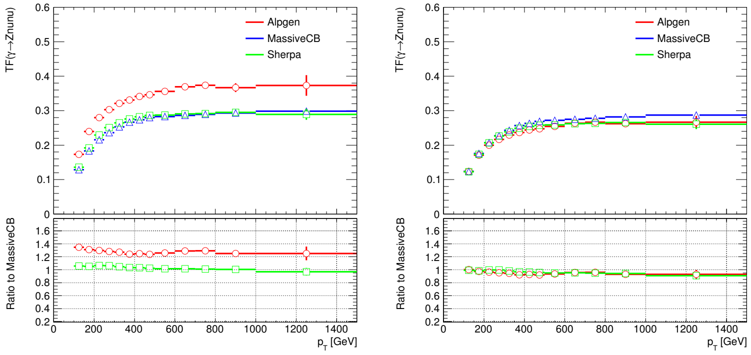

(a) (b)

Fig. 5.7 · Distribution of the transfer factor $\mathrm{TF}(\gamma \to (Z \to \nu\nu))$ before (left) and after (right) correction. The lower panel shows the ratio to the sample with massive b and c quarks.

The correction is derived on a dataset of dijet events with $p_\mathrm{T}(j_1) > 130\,\mathrm{GeV}$, $p_\mathrm{T}(j_2) > 60\,\mathrm{GeV}$, where enough $Z(\to \ell\ell)$+jets events are available. The QCD background used for subtraction has been obtained using the ABCD method discussed in §5.6.3. On this dataset, the ALPGEN prediction for $Z \to \ell\ell$ is off by approximately 40 % when obtained from γ+jets, leading to the large uncertainty on the Z+jets background. The derived correction factors are $\kappa_\mathrm{SHERPA} = 1.04 \pm 0.01\,(\mathrm{stat.}) \pm 0.06\,(\mathrm{syst.})$ and $\kappa_\mathrm{ALPGEN} = 1.40 \pm 0.03\,(\mathrm{stat.}) \pm 0.08\,(\mathrm{syst.})$. Due to κ being a ratio, many systematic uncertainties drop out in its calculation. The remaining uncertainties are the photon selection (6 % for SHERPA, 8 % for ALPGEN), the lepton selection (both 2 %), and on the background in the regions. For the QCD background a variation of 50 % was used, leading to a 2 % error. The other backgrounds were varied 25 %, leading to a 1 % error.

The resulting $\mathrm{TF}(\gamma \to (Z \to \nu\nu))$ is shown in fig. 5.7b. It can be seen that the difference between SHERPA and ALPGEN is now small, although a slight p_T-dependence persists.

QCD multijets

To normalise the QCD background (see §5.6.3), a sample of events CRQ with similar kinematics as in the signal regions is selected, but enriched in QCD events. The angular selection $\Delta\phi(j_i, E_\mathrm{T}^\mathrm{miss})_\mathrm{min}$ is reversed to ensure the $E_\mathrm{T}^\mathrm{miss}$ has the same direction as one of the jets: a topology characteristic of events in which one of the jets has been mis-measured or has generated neutrinos through heavy-flavour decay. To improve the purity of the sample, the selection on $E_\mathrm{T}^\mathrm{miss}/m_\mathrm{eff}(N_j)$ or $E_\mathrm{T}^\mathrm{miss}/\sqrt{H_\mathrm{T}}$ is reversed. Events coming from W or $t\bar{t}$ decays involving a τ lepton with low $\Delta\phi(j, E_\mathrm{T}^\mathrm{miss})_\mathrm{min}$ are rejected in this way.

To minimise errors due to the extrapolation to the signal region, a lower selection on either $E_\mathrm{T}^\mathrm{miss}/m_\mathrm{eff}(N_j)$ or $E_\mathrm{T}^\mathrm{miss}/\sqrt{H_\mathrm{T}}$ is added: windows in these variables are used for the selection. Events are selected using $X - \Delta < E_\mathrm{T}^\mathrm{miss}/m_\mathrm{eff}(N_j) < X$ or $Y - \Delta < E_\mathrm{T}^\mathrm{miss}/\sqrt{H_\mathrm{T}} < Y$, where X

and Y are the values used in the signal region. The value of Δ depends on the signal region used. Those with selections on $E_{\mathrm{T}}^{\mathrm{miss}}/m_{\mathrm{eff}}(N_j)$ use

- $\Delta = 0.05$ for $X \leq 0.2$;
- $\Delta = 0.15$ for $0.2 < X < 0.4$;
- $\Delta = 0.25$ for $X \geq 0.4$.

Regions selecting on $E_{\mathrm{T}}^{\mathrm{miss}}/\sqrt{H_{\mathrm{T}}}$ use

- $\Delta = 2\,\mathrm{GeV}^{1/2}$ for $Y \leq 8\,\mathrm{GeV}^{1/2}$;
- $\Delta = 4\,\mathrm{GeV}^{1/2}$ for $8\,\mathrm{GeV}^{1/2} < Y \leq 10\,\mathrm{GeV}^{1/2}$;
- $\Delta = 6\,\mathrm{GeV}^{1/2}$ for $Y > 10\,\mathrm{GeV}^{1/2}$.

5.6.2 Validation regions

A further set of event selections is used to validate the background estimations obtained through the use of the control regions. For each of the background processes, a set of validation regions is defined for each signal region. The fit result in the control regions is extrapolated to these regions in the same way as to the signal region, allowing us to test our background predictions in regions where no SUSY events are expected. Note that not all validation regions are exclusive and uncertainties can be correlated between them.

VRZ has been described in §5.6.1 and uses $Z(\rightarrow \ell\ell)$+jets events;

VRZf uses the same selections as VRZ and adds the signal region selections on $\Delta\phi(j_i, E_{\mathrm{T}}^{\mathrm{miss}})_{\mathrm{min}}$ and $E_{\mathrm{T}}^{\mathrm{miss}}/m_{\mathrm{eff}}(N_j)$, or $E_{\mathrm{T}}^{\mathrm{miss}}/\sqrt{H_{\mathrm{T}}}$;

VRWf and **VRTf** use the same selections as CRW or CRT, and add the signal region selections on $\Delta\phi(j_i, E_{\mathrm{T}}^{\mathrm{miss}})_{\mathrm{min}}$ and $E_{\mathrm{T}}^{\mathrm{miss}}/m_{\mathrm{eff}}(N_j)$, or $E_{\mathrm{T}}^{\mathrm{miss}}/\sqrt{H_{\mathrm{T}}}$;

VRWM and **VRTM** are identical to CRW or CRT, but treat the lepton as a missing particle rather than as a jet;

VRWMf and **VRTMf** are the same as VRWf or VRTf, with the lepton as a missing particle;

VRT2L is the same as VRZ, instead selecting events with with $m_{\ell\ell} > 116\,\mathrm{GeV}$ and extra requirements $p_{\mathrm{T}}(\ell_1) < 200\,\mathrm{GeV}$ and $p_{\mathrm{T}}(\ell_2) < 100\,\mathrm{GeV}$, in order to be sensitive to fully leptonic $t\bar{t}$ production.

VRWT+ is a combination of CRW+CRT, but keeps only events with a positively charged lepton;

VRWT- is identical, but with a negatively charged lepton;

VRWTf+ is the same as VRWT+, adding the signal region requirements on $\Delta\phi(j_i, E_{\mathrm{T}}^{\mathrm{miss}})_{\mathrm{min}}$ and $E_{\mathrm{T}}^{\mathrm{miss}}/m_{\mathrm{eff}}(N_j)$, or $E_{\mathrm{T}}^{\mathrm{miss}}/\sqrt{H_{\mathrm{T}}}$;

VRTWf- is identical, but with a negatively charged lepton;

VRQ1 is CRQ with the $E_{\mathrm{T}}^{\mathrm{miss}}/m_{\mathrm{eff}}(N_j)$ or $E_{\mathrm{T}}^{\mathrm{miss}}/\sqrt{H_{\mathrm{T}}}$ requirement of the signal region, to test extrapolation along these variables;

VRQ2 is CRQ with the $\Delta\phi(j_i, E_{\mathrm{T}}^{\mathrm{miss}})_{\mathrm{min}}$ selection of the signal region added, to test extrapolation along this variable;

VRQ3 is VRQ1, but at intermediate $\Delta\phi(j_i, E_{\mathrm{T}}^{\mathrm{miss}})_{\mathrm{min}}$ values;

VRQ4 is VRQ2, but at intermediate $\Delta\phi(j_i, E_{\mathrm{T}}^{\mathrm{miss}})_{\mathrm{min}}$ values;

VRWTau uses the same selections as the signal region, but at intermediate $\Delta\phi(j_i, E_{\mathrm{T}}^{\mathrm{miss}})_{\mathrm{min}}$, and with at least one τ lepton and no b jet.

VRttbarTau is the same as VRWTau, with at least one b jet.

All regions lie in between the signal region and the used control regions in the phase space of one or more variables. They are used to test the extrapolation from the control region to the signal region, and to determine the baseline Monte Carlo generators used in the analysis. The four regions VRTW(f)$\pm$ are used to test for lepton charge asymmetry. The τ validation regions test whether the contributions of the $W(\rightarrow \tau\nu)$+jets and $t\bar{t}(\rightarrow \tau\nu)$+jets backgrounds are correctly estimated.

5.6.3 QCD estimation

The multijets background is estimated using a fully data-driven method [258]. A *jet response function* $R = p_{\mathrm{T}}^{\mathrm{reco}}/p_{\mathrm{T}}^{\mathrm{true}}$ that quantifies the fluctuation in jet p_{T} is measured and applied to simulated data. Jet four-vectors with low $E_{\mathrm{T}}^{\mathrm{miss}}$ are convolved with the function to obtain an estimate of the QCD multijet distribution in CRQ that minimally depends on Monte Carlo. The smearing method works in four steps:

1. a set of low-$E_{\mathrm{T}}^{\mathrm{miss}}$ *seed* events is selected in data;
2. initially, the jet response function is measured in simulation by comparing truth-level p_{T} to reconstructed jet p_{T};
3. the response function is modified by smearing the seed events. Its width is parametrised and the tail modified, until agreement between the obtained pseudo-data and data in a control region sensitive to the jet response is obtained;
4. the selected seed events using the data-constrained smearing function are used to obtain estimated distributions in the control and signal regions.

Jet smearing assumes that all sources of jet fluctuation (both true and fake) can be included in one response function. It further assumes that $E_{\mathrm{T}}^{\mathrm{miss}}$ in a multijet event is dominated by jet fluctuation, and that the jet response does not depend on event-wide properties. These assumptions have been justified by the obtained result in the QCD validation regions. The largest uncertainty on the method comes from the modified tails of the response function. Fig. 5.8 shows the result for the 2-jet and 4-jet control regions before the final selections that define a signal region ($E_{\mathrm{T}}^{\mathrm{miss}}/m_{\mathrm{eff}}(N_j)$ and m_{eff}) are applied.

To check whether the number of events obtained with the smearing method is correct, the QCD background has also been estimated using an ABCD-method using the variables $\Delta\phi(j, E_{\mathrm{T}}^{\mathrm{miss}})$

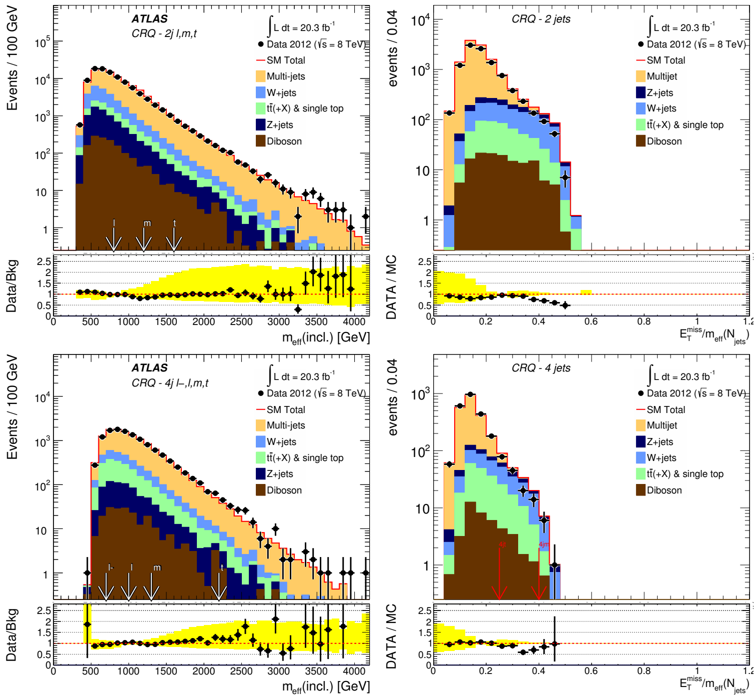

Fig. 5.8 · Distribution of m_{eff} and $E_{\text{T}}^{\text{miss}}/m_{\text{eff}}(N_j)$ for the QCD control region CRQ for 2 jets (top) and 4 jets (bottom). The arrows indicate the selections used in the signal region.

and $\Delta\phi(E_{\text{T}}^{\text{miss}}, E_{\text{T,track}}^{\text{miss}})$. $E_{\text{T,track}}^{\text{miss}}$ is defined as $E_{\text{T,track}}^{\text{miss}} = \left| -\sum_i p_{\text{T}}^i \right|$, where the sum runs over all tracks associated to the primary vertex. The two methods are in agreement within their errors.

5.7 Systematic uncertainties

Systematic uncertainties impact both the background prediction and the prediction for SUSY models. An uncertainty can be either fully correlated across the different regions and the different physics processes; fully correlated across the different regions but independent per process; or fully uncorrelated (e.g. Monte Carlo statistical errors), with one parameter per bin. Systematic uncertainties with limited impact, for example much smaller than the luminosity uncertainty, are neglected. The full list of parameters implemented in the likelihood fit is shown in table 5.5. The major uncertainties are discussed in turn below.

Background uncertainties

Three distinct types of systematic uncertainties on the Standard Model background prediction can be distinguished:

- experimental uncertainties related to detector performance: first, the jet energy scale and the jet energy resolution affect the p_{T} distribution of jets and the $E_{\text{T}}^{\text{miss}}$ calculation; second,

Table 5.5 · Summary of systematic uncertainties included in the likelihood fit.

Name	**Characteristic scale**	**Treatment**	**Comment**
Luminosity	2.8 %	Fully correlated	Pure MC estimates
Statistical uncertainty	–	Uncorrelated	All MC samples
	Physics process modelling		
Pile-up	$\langle\mu\rangle \times [0.9, 1.1]$	Fully correlated	All MC samples
Total cross-section	Diboson	Partially correlated	Pure MC estimates
μ_R/μ_F scale variation	$\mu \times [0.5, 2.0]$	Per process	W+jets/Z+jets/γ+jets
Matching scale variation	$p_T(j)_{min} = [15, 25]$ GeV	Per process	W+jets/Z+jets/γ+jets
Number of extra partons	Decreased by 1	Per process	W+jets/Z+jets/γ+jets
Generator comparison	ALPGEN VS SHERPA	Per process	W+jets/Z+jets/γ+jets
W + heavy-flavour	$\simeq 25 - 50$ %	Per process	W+jets
γ+jets κ correction	$\simeq 6$ %	Per process	γ+jets
Generator comparison	MC@NLO VS POWHEG	Per process	$t\bar{t}$
$t\bar{t}$ diff. cross-section	Vary weights	Per process	$t\bar{t}$
Multijets method (Gauss)	$\sigma_{corr} \pm 0.05$	Per process	QCD
Multijets method (Tails)	p_T dependent	Per process	QCD
	Object modelling		
Jet energy scale	Jet dependent	Fully correlated	
Jet energy resolution	Jet dependent	Fully correlated	
Soft E_T^{miss} scale	5 %	Fully correlated	
Soft E_T^{miss} resolution	2 %	Fully correlated	
Lepton/photon efficiency	$5 - 7$ % for γ	Fully correlated	Only in CRY
b-tagging	Jet dependent	Fully correlated	Only in CRW and CRT

the soft term in E_T^{miss}; third, the b-tagging efficiency in CRT and CRW; and finally the pile-up, which affects the jet multiplicity and E_T^{miss};

- uncertainties in the control region that are extrapolated to the signal region:
  - theoretical uncertainties on the simulation: the choice of generator, PDF, factorisation scale and renormalisation scale all influence the simulated events;
  - the statistical uncertainty in the control region.

Theoretical uncertainties that affect the normalisation of a distribution are irrelevant due to use of transfer factors between the control and signal regions (see §5.6). However, uncertainties that affect the shape of distributions need to be taken into account. For each of the backgrounds, the uncertainties are discussed below.

For vector-boson processes, theoretical uncertainties are obtained by varying parameters of the generators:

- the renormalisation and factorisation scale parameters are multiplied by ½ and 2;

- the matrix-element–parton-shower matching scale is increased by 10 GeV;
- the number of partons at matrix-element level is reduced by 1;
- different members of a given PDF set are used.

The difference between SHERPA and ALPGEN is considered an additional theoretical uncertainty on the background prediction.

For W+jets events a further uncertainty is applied to the production of W bosons in association with heavy-flavour quarks, which are important in regions using b-tagged jets. Wbb and Wcc events are reweighted by 26 % to 51 % depending on the number of partons in the event, based on the measured fiducial W+b cross-section in 2-jet events and its extrapolation to higher jet multiplicities [259].

The uncertainty on the $p_{\mathrm{T}}(t\bar{t})$ reweighting of POWHEG events is evaluated by varying the weights with their uncertainties. Uncertainties on ISR for top-quark processes are evaluated using specific samples generated with different parton shower setups. The difference between MC@NLO and POWHEG is considered an additional theoretical uncertainty. For the production of $t\bar{t}$ in association with a W or Z a flat uncertainty of 50 % is applied to the predicted background due to its relatively small contribution: $\sim$ 4 % of the top background in the tightest 6-jet region.

For the QCD background, the uncertainty on the width of the response function and on the modelling of its tails are taken into account.

Although acceptance differences between the control and signal regions are automatically taken into account in the fit, we must take care not to include fake events in the control regions. The fake-lepton background in CRW and CRT was obtained using a matrix method and found to be less than 4 % in CRW in the 7 TeV analysis and even smaller in CRT. In VRZ, the requirement of two tight leptons reduces this even further. The fake-photon background was estimated using the same matrix method as in the inclusive isolated prompt photon cross-section measurement [260]. Its contribution is less than 2 % in CRY for all signal regions. These backgrounds are therefore ignored.

Uncertainties on the signal

Systematic uncertainties on the theoretical prediction of the number of SUSY events related to ISR and FSR are evaluated by:

- varying the factorisation and renormalisation scale parameters by a factor ½ and 2;
- taking the 68 % uncertainty band from MSTW2008LO as the uncertainty on the PDF;
- varying the parameters for QCD radiation in MadGraph and PYTHIA simultaneously by a factor ½ and 2;
- varying the matching scale parameter by a factor ½ and 2.

The resulting effect on the signal efficiency and acceptance can be described as an exponential function of the mass splitting $\Delta m(\tilde{q}, \tilde{\chi}_1^0)$ or $\Delta m(\tilde{g}, \tilde{\chi}_1^0)$ and can be parametrised for each signal region. Separate parametrisations for both direct decays of gluinos and squarks and for their decays through a chargino are obtained. Models of squark–gluino production use the same parametrisation as the direct decay of gluino pairs. For mass splittings $\Delta m < 100$ GeV, the uncertainty ranges from 10 % to 40 %. With increasing Δm, it falls off exponentially; the decay constant ranges between 200 GeV and 300 GeV, depending on the SUSY model and the signal region. This uncertainty is taken into account in every fit performed that includes a signal hypothesis.

5.8 Pre-fit background agreement

Several effects are observed when comparing data in the control regions to the various Monte Carlo simulated samples *before* the simultaneous fit:

- in CRW, both SHERPA and ALPGEN overestimate the amount of events with large p_T^W. The selection on m_{eff} ensures the used data is in the tails: this effect only leads to a normalisation offset;
- in CRT, both MC@NLO and POWHEG overestimate the data, although the latter has been corrected with data-driven weights. The excess comes from W+jets and could be corrected with p_T-dependent reweighting, but its impact is marginal. In contrast to the used $t\bar{t}$ reweighting, this method has not been applied: the method was developed for the ATLAS SUSY mono-jet analysis [261, 262] and is not an official measurement nor a method that has been validated outside the scope of that analysis yet. Moreover, the likelihood fit will take care of most of the discrepancy. As the impact on the final result is therefore very limited, no reweighting has been used. Fig. 5.11 shows the final distributions;
- in CRY at high jet multiplicities ($N_j > 5$), a tendency to simulate too many jets is observed in the case of SHERPA. ALPGEN describes the data better. SHERPA was still used as the default generator: the number of events generated with ALPGEN is relatively small. Moreover, for lower jet multiplicities, the SHERPA result agrees with ALPGEN or describes the data better. The application of the difference as an uncertainty is a conservative solution. Finally, the use of SHERPA is consistent with other analyses in ATLAS;
- the same effect is seen in CRW for high jet multiplicities, although much smaller.

The discrepancies between the generators reinforce the choice of using two generators for each background, and considering the difference as an additional theoretical uncertainty. Fig. 5.9, 5.10 and 5.11 show the final pre-fit m_{eff}(incl.) and $E_T^{\text{miss}}/m_{\text{eff}}(N_j)$ distributions in CRY, CRW and CRT.

5.9 Statistical procedure

Using the predictions from Monte Carlo simulation for all backgrounds in the control regions and the signal regions, we can start comparing the number of events in the signal region to the prediction. First, the prediction in the signal region is constrained using data in the control regions using transfer factors. Any excess over the expected background can be a sign of signal events in the signal region. If there is no excess, we can exclude specific hypotheses.

To obtain the expected number of background events, a fit based on the likelihood function described in §5.9.1 is used. The use of a likelihood function ensures cross-contamination between

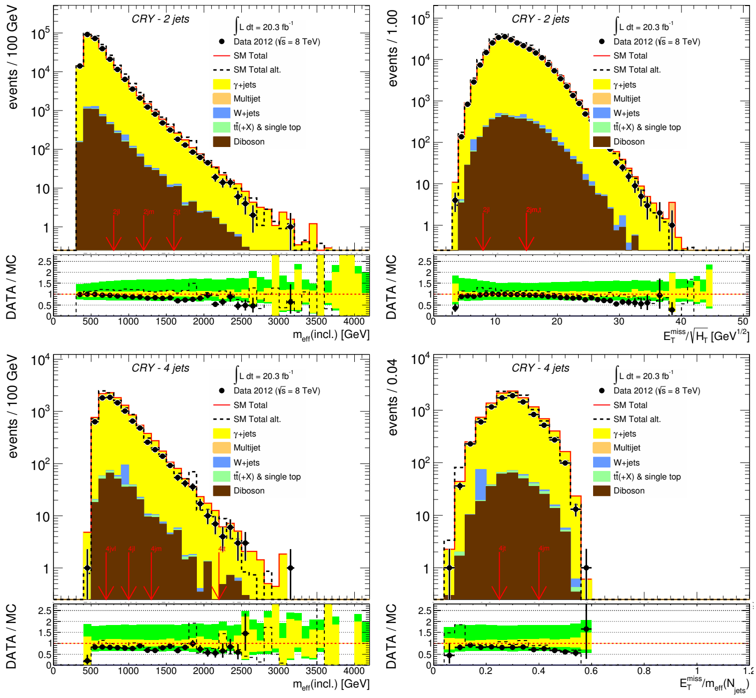

Fig. 5.9 · Distribution of m_{eff} and $E_{\text{T}}^{\text{miss}}/\sqrt{H_{\text{T}}}$ or $E_{\text{T}}^{\text{miss}}/m_{\text{eff}}(N_j)$ for the Z+jets control region CRY for 2 and 4 jets. The arrows indicate the selections used in the signal region.

regions is automatically taken into account, an important property given the control regions' purity is not 100 %: it ranges from 48 % to 97 %.[1]

Given an estimation of the number of events in a signal region, we can then test two hypotheses: the background-only hypothesis (null hypothesis) or the signal-plus-background hypothesis of a specific model (alternative hypothesis). To quantify the compatibility of the observation with either hypothesis, a profile log-likelihood ratio [263] is used as the test statistic, as described in §5.9.2.

5.9.1 Likelihood function

A likelihood function is used to determine how well an observation fits a prediction. The likelihood function L is defined for every signal region separately, and is given by

$$L(\mathbf{n}|\boldsymbol{\mu}, s, \mathbf{b}, \boldsymbol{\theta}) = \prod_i P_i\left(n_i \middle| \lambda_i(\boldsymbol{\mu}, s_i, \mathbf{b}, \boldsymbol{\theta})\right) \prod_j G\left(\theta_j - \theta_j^0\right), \tag{5.10}$$

where $\mathbf{n}$ is a set of measurements in all regions, P_i the Poisson probability to observe n_i events in region i given λ_i expected events (further described below), and $G\left(\theta_j - \theta_j^0\right)$ a Gaussian distri-

[1] The purity of the control regions is 76 % (65–86 %) for CRW, 71 % (48 − 89 %) for CRT, 95 % (89 − 97 %) for CRY and 72 % (48 − 90 %) for CRQ. The first number is the average; the other two the minimum and maximum across the set of control regions defined.

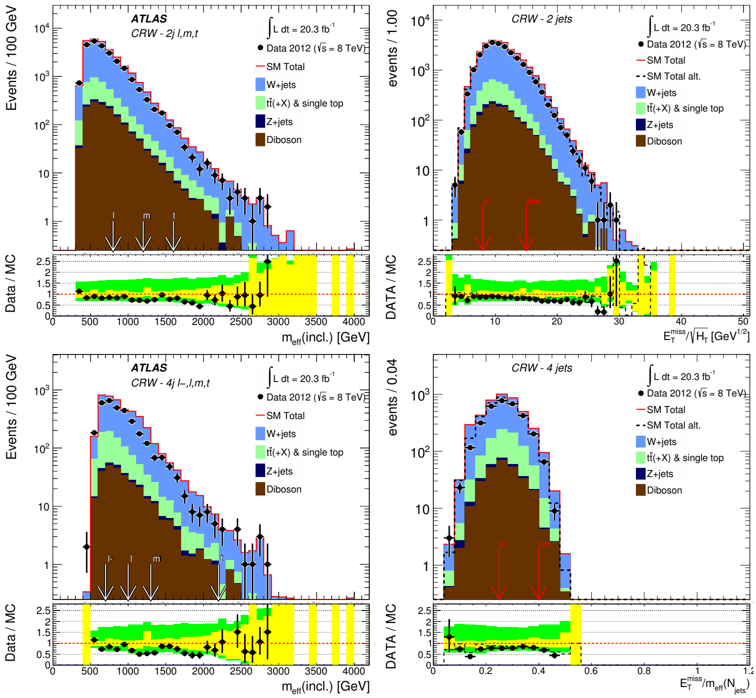

Fig. 5.10 · Distribution of m_{eff} and $E_{\mathrm{T}}^{\mathrm{miss}}/\sqrt{H_{\mathrm{T}}}$ or $E_{\mathrm{T}}^{\mathrm{miss}}/m_{\mathrm{eff}}(N_j)$ for the W+jets control region CRW for 2 and 4 jets. The arrows indicate the selections used in the signal region.

bution to constrain the nuisance parameter θ_j around its nominal prediction θ_j^0. The maximum likelihood corresponds with the best measurement of the signal strengths and nuisance parameters. In practice, a negative log likelihood definition is used to avoid the numerical evaluation of a function with multiplication terms.

Since all background processes are taken into account in all control regions, the estimated number of events in a region i can be written as

$$\lambda_i(\boldsymbol{\mu}, s_i, \mathbf{b}, \boldsymbol{\theta}) = \mu_s s_i(\boldsymbol{\theta}) + \sum_j \mu_j b_{ij}(\boldsymbol{\theta}) + b_i^{\mathrm{VV}}(\boldsymbol{\theta}), \tag{5.11}$$

where the sum runs over all background processes b. The last term describes the diboson background, which is taken from simulation. All backgrounds and the signal s can be multiplied with a normalisation factor μ, also called a signal strength. Uncertainties are described as a set of nuisance parameters $\boldsymbol{\theta}$. Depending on the type of region and fit, the signal normalisation is fixed to $\mu_s = 0$, to $\mu_s = 1$, or left free.

The nuisance parameters are typically re-parametrised to a normal distribution with mean 0 and width 1, where the mean corresponds to the nominal prediction and the $\pm 1\,\sigma$ variations to the number observed with the nuisance parameter one standard deviation away from its nominal prediction. Such a treatment prevents loosely constrained nuisance parameters with a large ex-

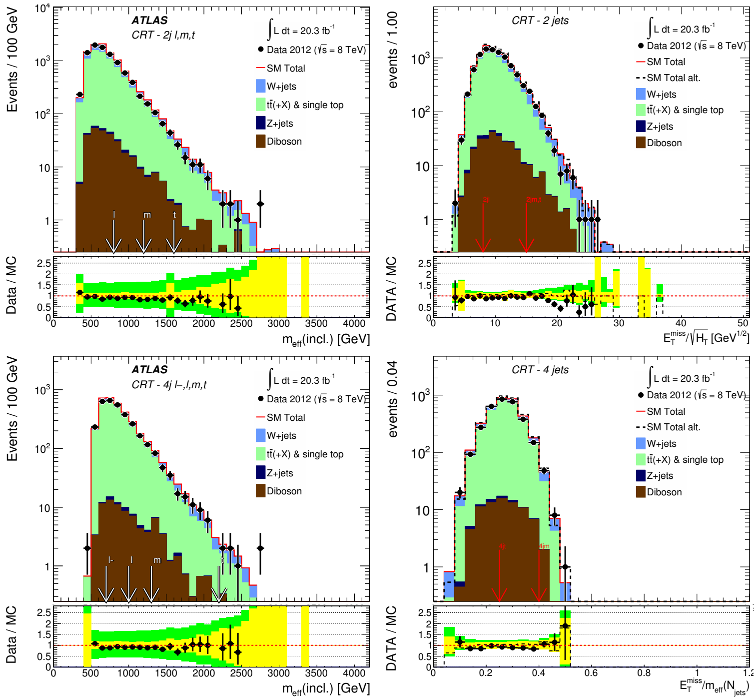

Fig. 5.11 · Distribution of m_{eff} and $E_{\mathrm{T}}^{\mathrm{miss}}/\sqrt{H_{\mathrm{T}}}$ or $E_{\mathrm{T}}^{\mathrm{miss}}/m_{\mathrm{eff}}(N_j)$ for the top control region CRT for 2 and 4 jets. The arrows indicate the selections used in the signal region.

pected impact on the total prediction (e.g. theory errors) from competing with μ to normalise a background.

Three different likelihood fits are used in this analysis: the background-only fit, the model-independent fit and the model-dependent exclusion fit.

The first is used to determine the compatibility of the observation in each signal region with the corresponding background expectation. The fit is performed using only measurements in the control regions associated with the signal region, but not the signal region itself, as constraints. No events from physics beyond the Standard Model are assumed to contribute to the expectation. The significance of an excess of events observed above the resulting expectation is quantified by the probability that the yield obtained in a single hypothetical background-only experiment is greater than that observed in this dataset. The fit is also used to estimate the backgrounds in the validation regions.

If no excess is observed, the model-independent fit is used to set upper limits on the number of BSM signal events in each signal region. These limits may be interpreted as upper limits on the visible cross-section of BSM physics $\langle\epsilon\sigma\rangle$. The model-independent fit proceeds in the same way as the background-only fit, except that the number of events observed in the signal region is added as an input to the fit and the BSM signal strength, constrained to be non-negative, is added as a free parameter. By construction, this fit can only be performed in regions with a single bin, in order to avoid assumptions on the shape of a signal. Possible contamination in the control regions of the signal is non-existent by design.

A third class of likelihood fit (the 'model-dependent exclusion fit') is used to set limits on the signal cross-sections for specific models. The exclusion fit proceeds in the same way as the model-independent fit, except that signal contamination in the control regions is taken into account. Theoretical and experimental uncertainties on the production cross-section and kinematic distributions are also considered. Correlations between signal and background systematic uncertainties are also taken into account where appropriate.

All fitting is performed using the HistFitter package [264] (see chapter 9), which relies on HistFactory [265], a tool in the RooStats/RooFit framework [266, 267] based on ROOT [268, 269].

5.9.2 Profile log-likelihood ratio

Using the likelihood function described in the previous section, a test statistic $\tilde{q}_\mu$ is constructed based on the $\tilde{\lambda}(\mu)$ likelihood ratio

$$\tilde{\lambda}(\mu) = \begin{cases} \frac{L\left(\mu,\hat{\hat{\boldsymbol{\theta}}}(\mu)\right)}{L\left(\hat{\mu},\hat{\boldsymbol{\theta}}(\mu)\right)} & \text{if } \hat{\mu} \geq 0, \\ \frac{L\left(\mu,\hat{\hat{\boldsymbol{\theta}}}(\mu)\right)}{L\left(0,\hat{\boldsymbol{\theta}}(0)\right)} & \text{if } \hat{\mu} < 0, \end{cases} \tag{5.12}$$

where single-hatted quantities are the best values under the observation and doubled-hatted quantities maximise the likelihood given μ.

For discovery of a positive signal, the test statistic used is

$$q_0 = \begin{cases} -2\ln\lambda(\mu) & \text{if } \hat{\mu} \geq 0, \\ 0 & \text{if } \hat{\mu} < 0, \end{cases} \tag{5.13}$$

where

$$\lambda(\mu) = \frac{L\left(\mu, \hat{\hat{\boldsymbol{\theta}}}\right)}{L\left(\hat{\mu}, \hat{\boldsymbol{\theta}}\right)}. \tag{5.14}$$

When testing specific models, the test statistic is given by

$$\tilde{q}_\mu = \begin{cases} -2\ln\tilde{\lambda}(\mu) & \text{if } \hat{\mu} \leq \mu, \\ 0 & \text{if } \hat{\mu} > \mu. \end{cases} \tag{5.15}$$

This choice of test statistics ensures that q_0 is zero when the best-fitted value is smaller than zero, i.e. the number of events is below the expectation. It further ensures that in exclusion fits, q_1 is zero when the best-fitted value on μ is greater than one, meaning that no models with such values of $\hat{\mu}$ are excluded. The level of (dis)agreement between data and the null hypothesis is quantified by the p-value

$$p_0 = \int_{q_{\text{obs}}}^{\infty} f(q_0|0)\,\mathrm{d}q_0, \tag{5.16}$$

where q_{obs} is the value of the test statistic observed in data. For testing alternative hypotheses, the following p-value is used:

$$p_\mu = \int_{q_{\text{obs}}}^{\infty} f(\tilde{q}_\mu|\mu)\,\mathrm{d}\tilde{q}_\mu. \tag{5.17}$$

The distribution f for the test statistic can be either obtained using approximate formulae [270] or sampled using the generation of toy datasets.

Instead of using the p-value for a result, it is often more convenient to use the significance Z, given by

$$Z = \Phi^{-1}(1 - p_0), \tag{5.18}$$

where Φ^{-1} is the quantile function of the normal distribution. By convention in high-energy physics, $Z \geq 3$ constitutes *evidence* for a new signal, while $Z \geq 5$, or $p_0 \leq 2.87 \cdot 10^{-7}$ for a one-sided test, constitutes a *discovery*.

For exclusion tests one must be careful not to exclude models a test is not sensitive to. A trivial example is the case where less background events were observed than expected, and p_0 is (much) smaller than 0.5: we could reject both the null and alternative hypotheses at the same time. Hence, instead of quoting p_1 directly, we define a variable CL_s [271] as

$$\text{CL}_\text{s} = \frac{p_1}{1 - p_0}, \tag{5.19}$$

and use $\text{CL}_\text{s} < 0.05$ to exclude models at 95 % confidence level. By construction, CL_s overcovers and is conservative. However, using CL_s is inappropriate for measurements or discovery tests as it is not a true probability.

Upper limits are determined by varying the signal strength used in a hypothesis test. Through interpolation the signal strength that is excluded at 95 % CL_s is found. Exclusion limits in a phase space, such as that of the CMSSM or of a simplified model, are set by calculating the confidence level for a set of points in the plane. Limits for the entire plane are then obtained through triangulation.

The fit results obtained through the background fit are presented in the next section.

5.10 Fit results

The fitted normalisation per process as a function of the signal region is shown in fig. 5.12. From the results, the following observations can be made:

- the scale factor for Z+jets events decreases with N_j and m_{eff}(incl.), reflecting the fact that SHERPA produces a harder jet spectrum for γ+jets than measured;
- the W+jets scale factor is on average lower than 1 and slightly decreases with N_j;
- the scale factor associated to top quark processes is close to 1 in all regions, except SR2jW. The obtained value is 3.07 ± 3.04, which, taking into account the statistical uncertainty, is compatible with 1;

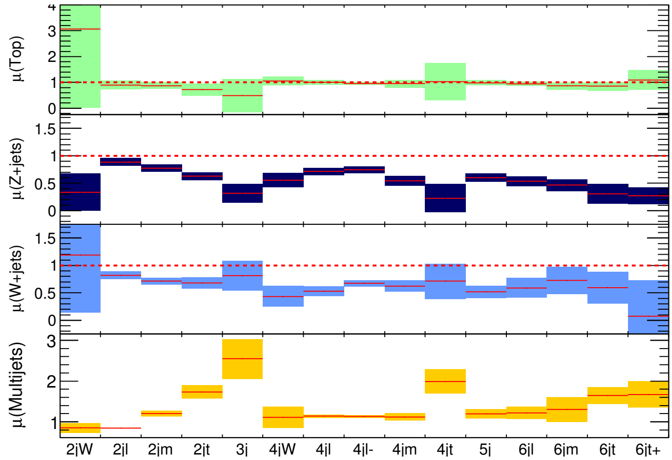

Fig. 5.12 · Fitted μ parameters per process as a function of the channel considered. The dashed horizontal line at 1 would correspond to pure Monte Carlo estimates when relevant. For the multijets background, the fitted μ is relative to the pre-normalisation.

- the scale factor associated to multijets is obtained using a pre-normalisation. Since the smeared data sample does not have a corresponding luminosity, pre-normalisation factors are calculated, for every region separately, by normalising pseudo-data to data in CRQ before the final m_{eff}(incl.) cut. The fitted normalisation factors correct this prediction.

5.10.1 Validation results

To test the robustness of the background fit, the background fit results have been extrapolated to the validation regions described earlier. Fig. 5.13 shows a summary of the obtained pull distributions. The pull is defined as $(n_{\text{obs}} - n_{\text{pred}})/\sigma_{\text{tot}}$, where n_{obs} is the observed number of events, n_{pred} the predicted number of events and $\sigma_{\text{tot}} = \sigma_{\text{stat}} \oplus \sigma_{\text{pred}}$, with σ_{pred} the background uncertainty obtained in the fit and σ_{stat} the 68 % confidence interval of the Poisson distribution with mean σ_{pred}. Recall that not all validation regions are exclusive and uncertainties can be correlated between them: the numbers should not be used with a χ^2-test directly.

All validation regions show reasonable agreement between data and expectation, with three notable exceptions. First, VRZf for SR5j shows an excess above $2\,\sigma$. The number of observed events is 13, while the expectation is 6.1 ± 1.3. Prior to the fit, the expectation is 8.8. We conclude the excess is a consequence of an excess of data over Monte Carlo and the rescaling of the Z+jets background by ~ 0.59 using measurements in CRY. Second, a similar effect is seen for SR4jW. Finally, the excess of $3.2\,\sigma$ seen in VRQ3 for SR3j is a statistical fluctuation, given the small number of data and MC events in the region. The $E_{\text{T}}^{\text{miss}}/m_{\text{eff}}(N_j)$, $\Delta\phi(j_i, E_{\text{T}}^{\text{miss}})$ and $N_{b\text{-jet}}$ distributions have been checked; the excess is not due to either the $t\bar{t}$ or multijets background. We now proceed to extrapolate the fit results to the signal regions.

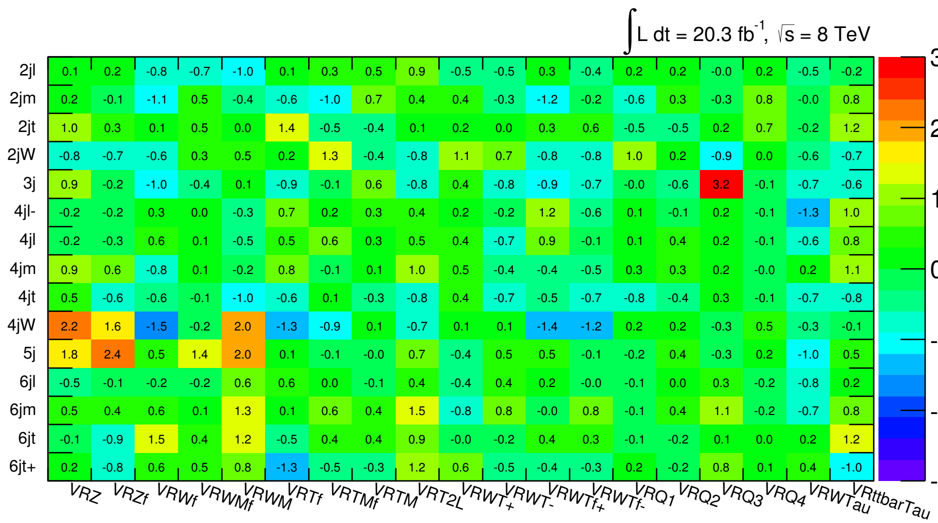

Fig. 5.13 · Differences between the numbers of observed events in data and Standard Model background expectations for each validation region, expressed as fractions of the uncertainties on the latter.

5.10.2 Results in the signal regions

Distributions of m_{eff}(incl.) and, for SR2jW and SR4jW, the jet and dijet masses before the final selections on these variables are shown for data and the background in fig. 5.14, 5.15 and 5.16. Included in the figures are several benchmark points to illustrate typical expected SUSY signals. The models chosen correspond to processes to which each region is sensitive.

Note that the histograms indicate the background *before* the simultaneous likelihood fit in the control regions: the increasing difference between data and simulation at higher values of the kinematic variables does not affect the signal region, due to the use of the fit.

The number of events observed and the number of Standard Model events expected in each of the signal regions is shown in table 5.6. The fit to the control regions compensates for the disagreement between data and pre-fit background expectations seen in the figures; the most significant excess across all signal regions is $p_0 = 0.24$ for SR3j. The results in all signal regions are shown in fig. 5.17. The Standard Model can hence not be excluded.

5.10.3 Impact of systematic uncertainties

Systematic uncertainties in background estimates arise through the use of the transfer factors relating observations in the control regions to background expectations in the signal regions, and from the Monte Carlo modelling of minor backgrounds. The total background uncertainties for all signal regions, broken down into the main contributing sources, are presented in table 5.7. The overall background uncertainties range from 5 % in SR4jl-, where the loose selection minimises theoretical uncertainties and the impact of statistical fluctuations in the control regions, to 40 % in SR4jt, where the opposite is true.

Table 5.6 · Numbers of events observed in the signal regions used in the analysis compared with background expectations obtained from the fits described in the text. No signal contribution is considered in the control regions for the fit. Empty cells correspond to estimates lower than 0.01. The p-values give the probabilities of the observations being consistent with the estimated backgrounds and are bounded to 0.5. Between parentheses, p-values are also given in number of equivalent Gaussian sigma (Z). Also shown are 95 % CL upper limits on the visible cross-section ($\langle\epsilon\sigma\rangle^{95}_{\text{obs}}$), the observed number of BSM events (S^{95}_{obs}) and the expected number of BSM events (S^{95}_{exp}) given the expected number (and $\pm 1\,\sigma$ uncertainty) of background events.

Signal Region	**SR2jl**	**SR2jm**	**SR2jt**	**SR2jW**	**SR3j**	**SR4jl-**	**SR4jl**
				MC expected events			
Diboson	879	72	13	0.41	0.36	175	70
Z/γ^*+jets	6709	552	103	1.2	5.5	885	333
W+jets	5472	303	59	0.82	3.1	832	284
$t\bar{t}$(+EW) + single top	1807	54	9	0.14	0.85	764	167
				Fitted background events			
Diboson	900 ± 400	70 ± 40	13 ± 6	0.41 ± 0.21	0.36 ± 0.18	180 ± 90	70 ± 34
Z/γ^*+jets	5900 ± 900	430 ± 40	65 ± 8	0.4 ± 0.4	1.7 ± 1.0	660 ± 60	238 ± 28
W+jets	4500 ± 600	216 ± 26	40 ± 6	1.0 ± 1.0	2.5 ± 0.9	560 ± 80	151 ± 28
$t\bar{t}$(+EW) + single top	1620 ± 320	47 ± 8	6.5 ± 2.2	$0.4^{+0.8}_{-0.4}$	$0.4^{+0.5}_{-0.4}$	730 ± 50	167 ± 18
Multi-jets	115^{+140}_{-120}	$0.4^{+1.4}_{-0.4}$	$0.1^{+0.4}_{-0.1}$	0.03 ± 0.03	$0.03^{+0.06}_{-0.03}$	$1.7^{+4.0}_{-1.7}$	$0.7^{+1.6}_{-0.7}$
Total bkg	13000 ± 1000	760 ± 50	125 ± 10	2.3 ± 1.4	5.0 ± 1.2	2120 ± 110	630 ± 50
Observed	12315	715	133	0	7	2169	608
$\langle\epsilon\sigma\rangle^{95}_{\text{obs}}$ [fb]	60	4.3	1.9	0.09	0.40	13	4.5
$\langle\epsilon\sigma\rangle^{95}_{\text{obs}}$ [fb] (asymp.)	62	3.98	1.8	0.12	0.40	13	4.3
S^{95}_{obs}	1223	86	38	3.2	8.2	273	91
S^{95}_{obs} (asymp.)	1259	81	37	2.5	8.1	268	87
S^{95}_{exp}	1680^{+580}_{-500}	108^{+43}_{-27}	32^{+11}_{-10}	$4.2^{+1.8}_{-1.1}$	$6.4^{+2.9}_{-1.3}$	244^{+91}_{-66}	103^{+34}_{-29}
S^{95}_{exp} (asymp.)	1590^{+560}_{-420}	105^{+39}_{-29}	31^{+12}_{-8}	$4.1^{+2.4}_{-1.4}$	$6.3^{+3.2}_{-2.0}$	242^{+87}_{-65}	97^{+35}_{-25}
p_0 (Z)	0.50 (0.0)	0.49 (0.0)	0.29 (0.5)	0.50 (0.0)	0.24 (0.7)	0.35 (0.4)	0.50 (0.0)

Signal Region	**SR4jm**	**SR4jt**	**SR4jW**	**SR5j**	**SR6jl**	**SR6jm**	**SR6jt**	**SR6jt+**
				MC expected events				
Diboson	7.2	0.34	2.1	16	9	4	1.6	0.21
Z/γ^*+jets	30	2.9	11	51	18	7	1.8	2.1
W+jets	16	1.2	6.1	54	26	12	2.1	3.4
$t\bar{t}$(+EW) + single top	4.0	0.6	3.1	52	80	19	2.2	3.4
				Fitted background events				
Diboson	7 ± 4	0.34 ± 0.17	2.1 ± 1.0	16 ± 8	9 ± 4	4 ± 2	1.6 ± 0.8	0.2 ± 0.1
Z/γ^*+jets	16 ± 4	$0.7^{+0.8}_{-0.7}$	5.9 ± 2.1	31 ± 8	9 ± 4	3 ± 2	0.6 ± 0.6	$0.6^{+0.8}_{-0.6}$
W+jets	10 ± 4	0.9 ± 0.4	2.7 ± 1.6	28 ± 8	15 ± 7	9 ± 5	1.2 ± 0.9	$0.3^{+1.2}_{-0.3}$
$t\bar{t}$(+EW) + single top	4 ± 2	0.6 ± 0.6	3.2 ± 3.1	51 ± 9	76 ± 7	16 ± 4	1.8 ± 0.6	3.7 ± 1.7
Multi-jets	–	–	–	$1.0^{+2.6}_{-1.0}$	$1.7^{+3.0}_{-1.7}$	$0.4^{+0.8}_{-0.4}$	$0.01^{+0.03}_{-0.01}$	$0.3^{+0.4}_{-0.3}$
Total bkg	37 ± 6	2.5 ± 1.0	14 ± 4	126 ± 13	111 ± 11	33 ± 6	5.2 ± 1.4	4.9 ± 1.6
Observed	24	0	16	121	121	39	5	6
$\langle\epsilon\sigma\rangle^{95}_{\text{obs}}$ [fb]	0.52	0.15	0.68	1.7	1.9	1.2	0.32	0.39
$\langle\epsilon\sigma\rangle^{95}_{\text{obs}}$ [fb] (asymp.)	0.45	0.12	0.63	1.6	1.8	1.1	0.30	0.36
S^{95}_{obs}	10	3.1	14	35	39	25	6.6	7.9
S^{95}_{obs} (asymp.)	9.2	2.5	13	32	37	22	6.1	7.3
S^{95}_{exp}	16^{+6}_{-4}	$4.0^{+1.8}_{-0.9}$	11^{+5}_{-3}	37^{+13}_{-10}	31^{+12}_{-6}	20^{+6}_{-4}	$6.2^{+2.6}_{-1.3}$	$6.6^{+2.6}_{-1.6}$
S^{95}_{exp} (asymp.)	15^{+6}_{-4}	$4.0^{+2.4}_{-1.4}$	11^{+5}_{-3}	35^{+13}_{-10}	30^{+12}_{-8}	18^{+7}_{-5}	$6.3^{+3.1}_{-2.0}$	$6.4^{+3.2}_{-2.0}$
p_0 (Z)	0.50 (0.0)	0.50 (0.0)	0.34 (0.4)	0.50 (0.0)	0.27 (0.6)	0.25 (0.7)	0.50 (0.0)	0.36 (0.4)

Table 5.7 · Breakdown of the systematic uncertainties on background estimates. Note that the individual uncertainties can be correlated, and do not necessarily sum quadratically to the total background uncertainty. Uncertainties relative to the total expected background yield are shown as bars. When a dash is shown, the resulting relative uncertainty is lower than 1 per mil. The red bars indicate the fractional total uncertainty with the thin lines corresponding to 100 %. The blue bars indicate the fractional contribution of each uncertainty, normalised to 100 %.

Channel	2jl	2jm	2jt	2jW	3j	4jl-	4jl
Total bkg	13000	760	125	2.3	5.0	2120	630
Total bkg unc.	1000	50	10	1.4	1.2	110	50
CR stats: Z/γ^* + jets	100	15	5	0.4	0.7	22	12
CR stats: W + jets	300	21	5	0.7	0.8	60	25
CR stats: top quark	200	5	1.6	0.35	0.5	40	16
CR stats: multijets	–	–	0.1	–	0.1	–	–
MC statistics	130	6	2.1	0.34	0.35	18	6
Jets/$E_{\mathrm{T}}^{\mathrm{miss}}$	140	8	0.7	0.27	0.23	40	7
Leptons	80	2.5	0.6	0.04	0.06	20	5
Z/γ TF	500	35	5	0.028	0.14	50	19
Theory: Z/γ^* + jets	900	6	5	0.17	0.32	–	20
Theory: W + jets	400	16	0.8	0.28	0.3	50	7
Theory: top quark	13	1.7	–	0.8	0.2	30	13
Theory: diboson	400	40	6	0.2	0.18	90	34
Theory: scale unc.	90	4	0.7	0.11	0.12	23	7
Multijets method	140	1.4	0.4	0.04	0.06	4	1.6
Other	32	0.6	0.4	0.24	0.02	5	5

Channel	4jm	4jt	4jW	5j	6jl	6jm	6jt	6jt+
Total bkg	37	2.5	14	126	111	33	5.2	4.9
Total bkg unc.	6	1.0	4	13	11	6	1.4	1.6
CR stats: Z/γ^* + jets	2.3	0.5	1.3	3.0	1.4	0.7	0.33	0.31
CR stats: W + jets	1.3	0.4	1.0	6	4	2.4	0.5	0.7
CR stats: top quark	0.5	0.4	0.5	7	7	2.3	0.31	1.1
CR stats: multijets	–	–	–	0.08	0.19	0.08	–	0.04
MC statistics	1.3	0.26	0.7	2.8	2.8	1.5	0.7	0.4
Jets/$E_{\mathrm{T}}^{\mathrm{miss}}$	0.15	0.06	0.6	4	6	1.2	0.5	0.29
Leptons	0.27	0.08	0.06	1.8	1.8	0.7	0.05	0.32
Z/γ TF	1.3	0.06	0.5	2.5	0.8	0.27	0.04	0.04
Theory: Z/γ^* + jets	2.9	0.5	2.6	10	5	3.0	0.6	0.9
Theory: W + jets	3.0	0.08	1.1	3.3	2.1	4	0.7	0.11
Theory: top quark	1.8	0.4	1.8	7	2.8	3.5	0.07	1.1
Theory: diboson	4	0.17	1.0	8	4	1.9	0.8	0.1
Theory: scale unc.	0.4	0.13	0.12	2.5	1.1	0.8	0.11	0.6
Multijets method	–	–	–	2.6	2.9	0.8	0.032	0.4
Other	0.23	0.06	0.12	0.9	2.5	0.9	0.14	0.03

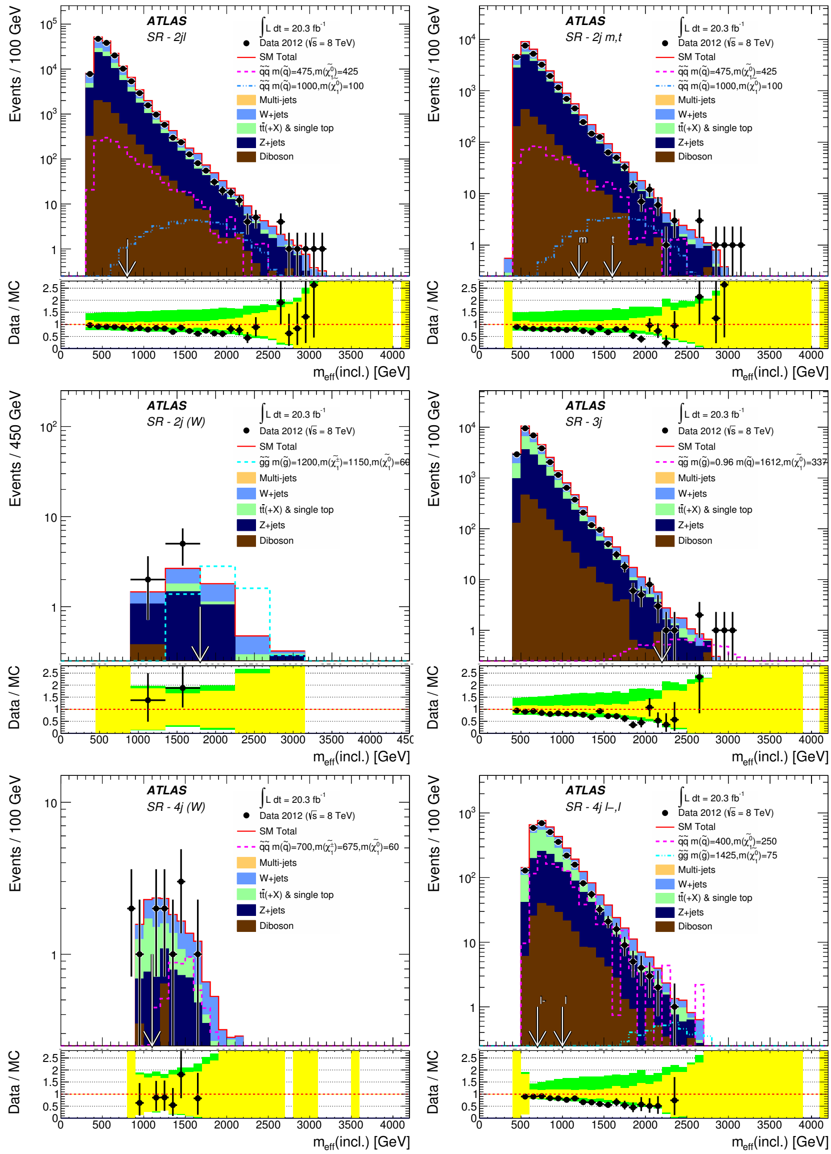

Fig. 5.14 · Observed m_{eff}(incl.) distributions for the 2-jet (top and middle-left), 3-jet (middle-right) and 4-jet (4jW, 4jl- and 4jl) signal regions (bottom) before the likelihood fit. In the lower panels the light (yellow) error bands denote the experimental and MC statistical uncertainties, while the medium dark (green) bands include also the theoretical modelling uncertainty. The arrows indicate the values at which the requirements on m_{eff}(incl.) are applied. Expected distributions for benchmark model points are also shown for comparison (masses in GeV).

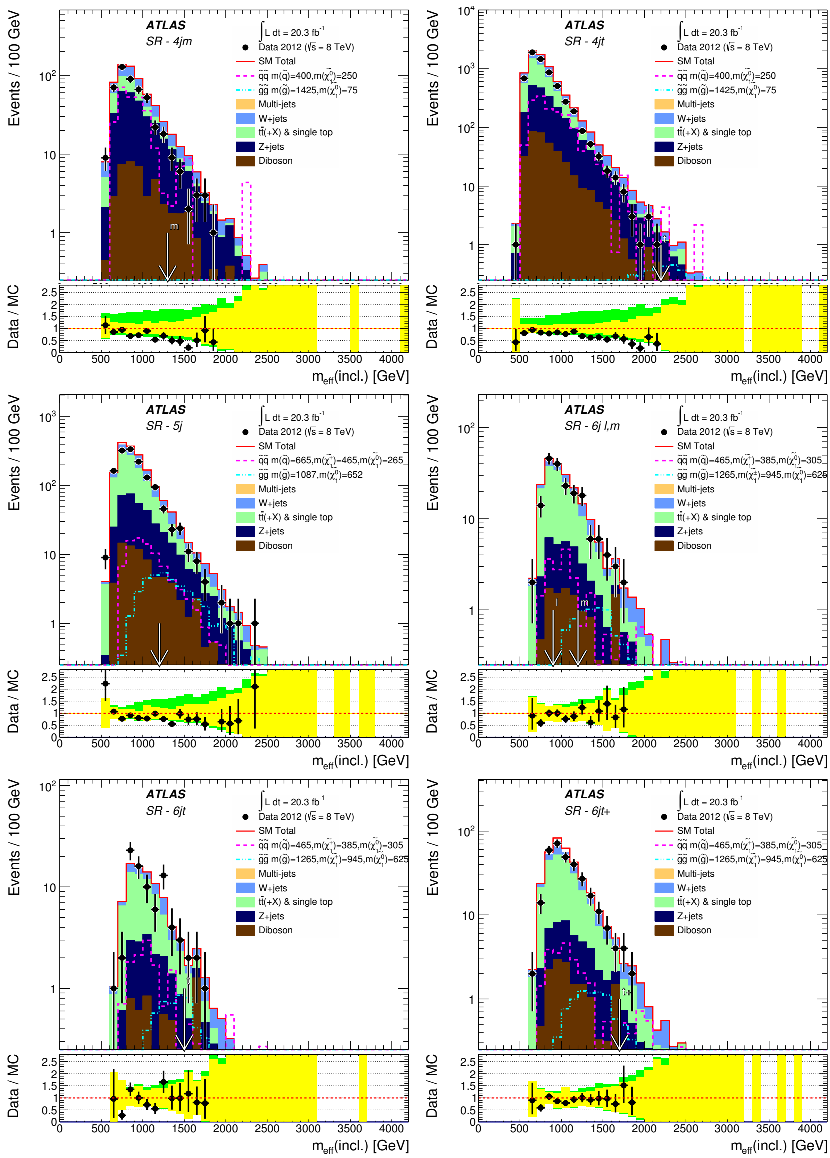

Fig. 5.15 · Observed m_{eff}(incl.) distributions for the medium and tight 4-jet (top), 5-jet (middle-left) and 6-jet (middle-right and bottom) signal regions before the likelihood fit. In the lower panels the light (yellow) error bands denote the experimental and MC statistical uncertainties, while the medium dark (green) bands include also the theoretical modelling uncertainty. The arrows indicate the values at which the requirements on m_{eff}(incl.) are applied. Expected distributions for benchmark model points are also shown for comparison (masses in GeV).

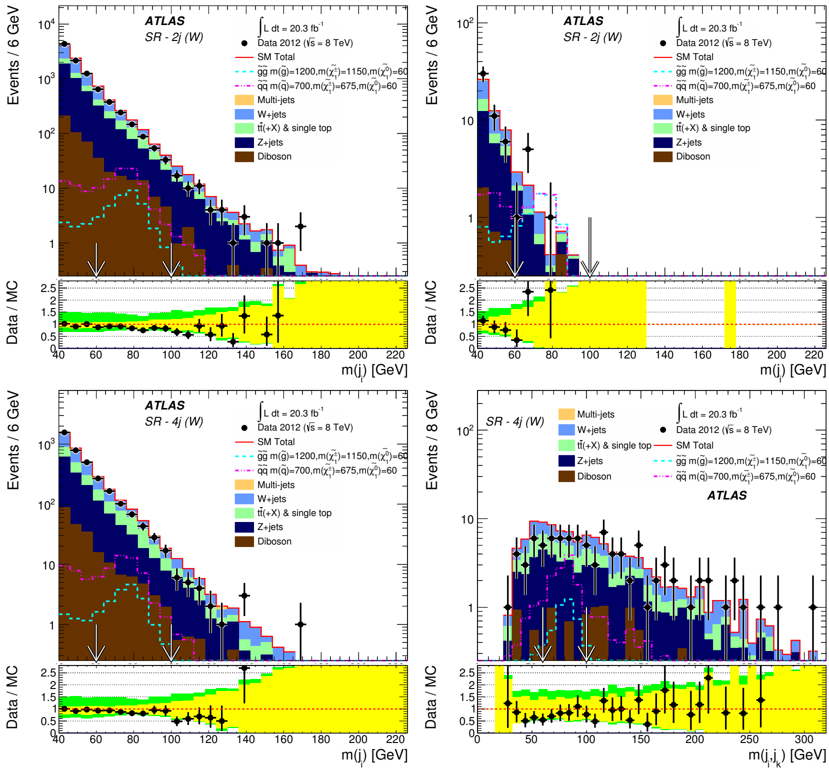

Fig. 5.16 · Observed jet and dijet mass distributions for the 2jW (top) and 4jW (bottom) signal regions for all unresolved W candidates (left) and for an additional W candidate after requiring at least one unresolved W candidate (right), before the likelihood fit. The additional W candidate is unresolved (SR2jW, top-right) or resolved (SR4jW, bottom-right). In the lower panels the light (yellow) error bands denote the experimental and MC statistical uncertainties, while the medium dark (green) bands include also the theoretical modelling uncertainty. The arrows indicate the values at which the requirements on m_{eff}(incl.) are applied. Expected distributions for benchmark model points are also shown for comparison (masses in GeV).

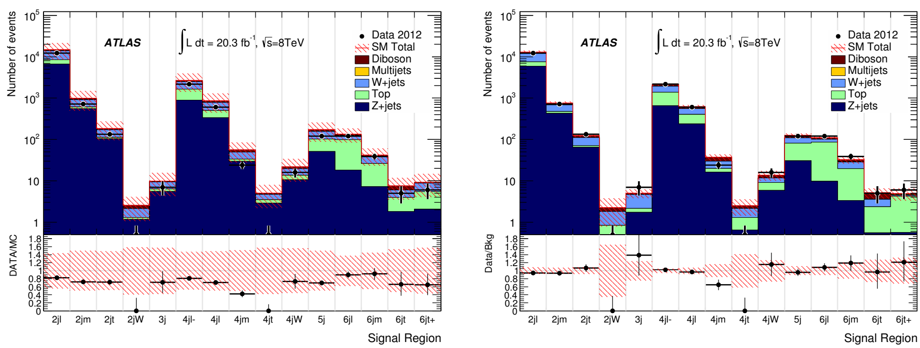

Fig. 5.17 · Comparison of the observed and expected event yields per signal region before (left) and after (right) the simultaneous fit in the control regions. In signal regions 2jW and 4jt no events are observed.

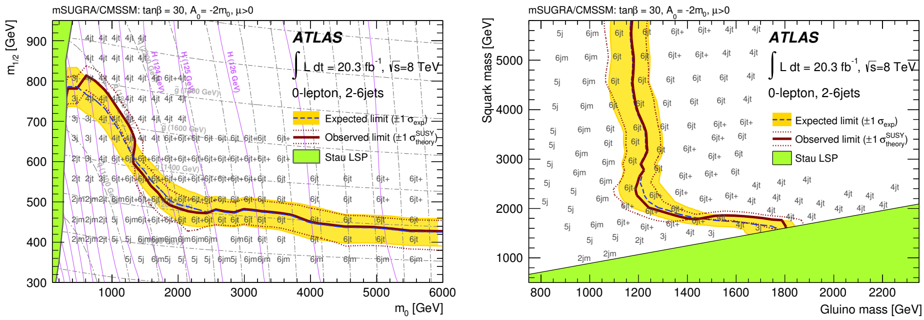

Fig. 5.18 · Exclusion limits for MSUGRA/CMSSM models with $\tan\beta = 30$, $A_0 = -2m_0$ and $\mu > 0$ presented (left) in the $(m_0, m_{1/2})$-plane and (right) in the $(m_{\tilde{g}}, m_{\tilde{q}})$-plane. The blue dashed lines show the expected limits at 95 % CL, with the light (yellow) bands indicating the 1σ uncertainty due to experimental and background-only theoretical uncertainties.

5.11 Interpretation

Without a statistically significant excess of events, limits are set on the number of events from BSM physics in each of the signal regions. 95 % CL upper limits on N_{BSM} and the corresponding visible cross-section are derived using model-independent fits. These limits are evaluated using both asymptotic formulae and Monte Carlo pseudo-experiments and shown in table 5.6.

Limits on SUSY models are set using the signal region with the best expected sensitivity for each point in each model's parameter space. These limits are calculated using asymptotic formulae only, and take any signal contamination in the control regions into account. The observed 95 % CL exclusion limits are calculated from the number of observed events in the signal regions, and shown for both the nominal SUSY cross-section and its $\pm 1\,\sigma$ uncertainties. In addition, an uncertainty related to ISR is also applied, as discussed in §5.3, and included in the uncertainty on the expected limits. The expected limits are derived using the number of expected events in the signal region. Upper limits on the visible cross-section in each model's parameter space are also set. The grey labels in the limit plots indicate the best expected signal region for each point.

5.11.1 Constrained MSSM

Fig. 5.18 shows the results interpreted in a slice of MSUGRA/CMSSM. These models are parametrised by the ratio between the vacuum expectation values of the two Higgs fields, $\tan\beta$; the universal trilinear coupling A_0; the universal scalar mass m_0; the universal gaugino mass $m_{1/2}$ and the sign of the Higgsino mass parameter, μ. The model used has $\tan\beta = 30$, $A_0 = -2m_0$ and $\mu > 0$; all parameters are defined at the GUT scale. The mass of the lightest neutral Higgs boson in this model can be compatible with the mass of the particle discovered in 2012. The best signal regions are 6jt for $m_0 \gtrsim 1300$ GeV and 4jt for $m_0 \lesssim 1300$ GeV. For $m_0 \lesssim 400$ GeV, the 3-jet region provides additional sensitivity.

The lower limit on $m_{1/2}$ is greater than 380 GeV for $m_0 < 6$ TeV and is 770 GeV for low values of m_0. Light-flavour squarks and gluinos of equal mass are excluded below 1700 GeV.

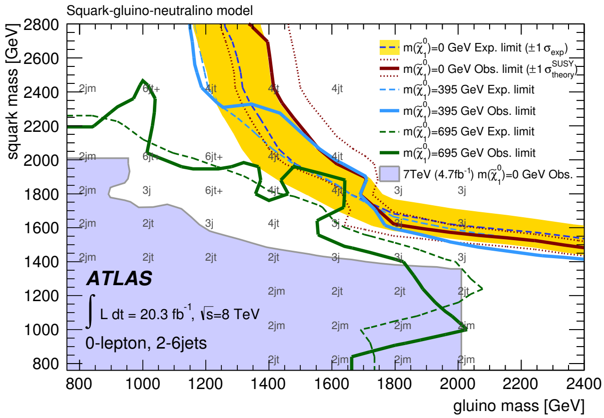

Fig. 5.19 · Exclusion limit for a simplified phenomenological MSSM scenario with only strong production of gluinos and first- and second-generation squarks (of common mass), with direct decays to quarks and lightest neutralinos. The mass of the lightest neutralino is set to zero, 395 GeV or 695 GeV.

An additional interpretation in the $(m_{\tilde{q}}, m_{\tilde{g}})$-plane for a simplified set of phenomenological MSSM points is shown in fig. 5.19. These models use a universal squark mass for the first two generations and have $m_{\tilde{\chi}_1^0}$ equal to 0 GeV, 395 GeV or 695 GeV. The gluino and light-flavour squark masses are set to the values shown on the axes. All other particles are treated as decoupled. In this scenario, a lower limit for light-flavour squarks and gluinos of equal mass of 1650 GeV is found for massless $\tilde{\chi}_1^0$.

5.11.2 Direct decays

Limits for the three classes of simplified models in which only direct production of gluino pairs, light-flavour squarks and gluinos, or light-flavour squark pairs is considered are shown in fig. 5.20. All other particles except the LSP $\tilde{\chi}_1^0$ are decoupled by assuming these are heavy. For squark–gluino production, the mass of squarks is related to the gluino mass through $m_{\tilde{q}} = 0.96 \times m_{\tilde{g}}$ [272, 273]. Squark-pair production is considered for all light-flavour squarks ($\tilde{q}_L$ and $\tilde{q}_R$) and for one non-degenerate light-flavour squark produced [274]. Upper limits on the cross-section times branching ratio are also calculated.

In the case of massless $\tilde{\chi}_1^0$, the lower limit on the gluino mass is 1330 GeV for gluinos that decay directly. Degenerate light-flavour squarks are excluded up to 850 GeV; the lower limit on the mass of non-degenerate single light-flavour squarks is 440 GeV.

Fig. 5.21 presents upper limits on the squark-pair production cross-section times branching ratio for a subset of points shown in fig. 5.20. These are presented both as a function of $m_{\tilde{q}}$ for a massless $\tilde{\chi}_1^0$ and as a function of $m_{\tilde{\chi}_1^0}$ for $m_{\tilde{q}} = 450$ GeV.

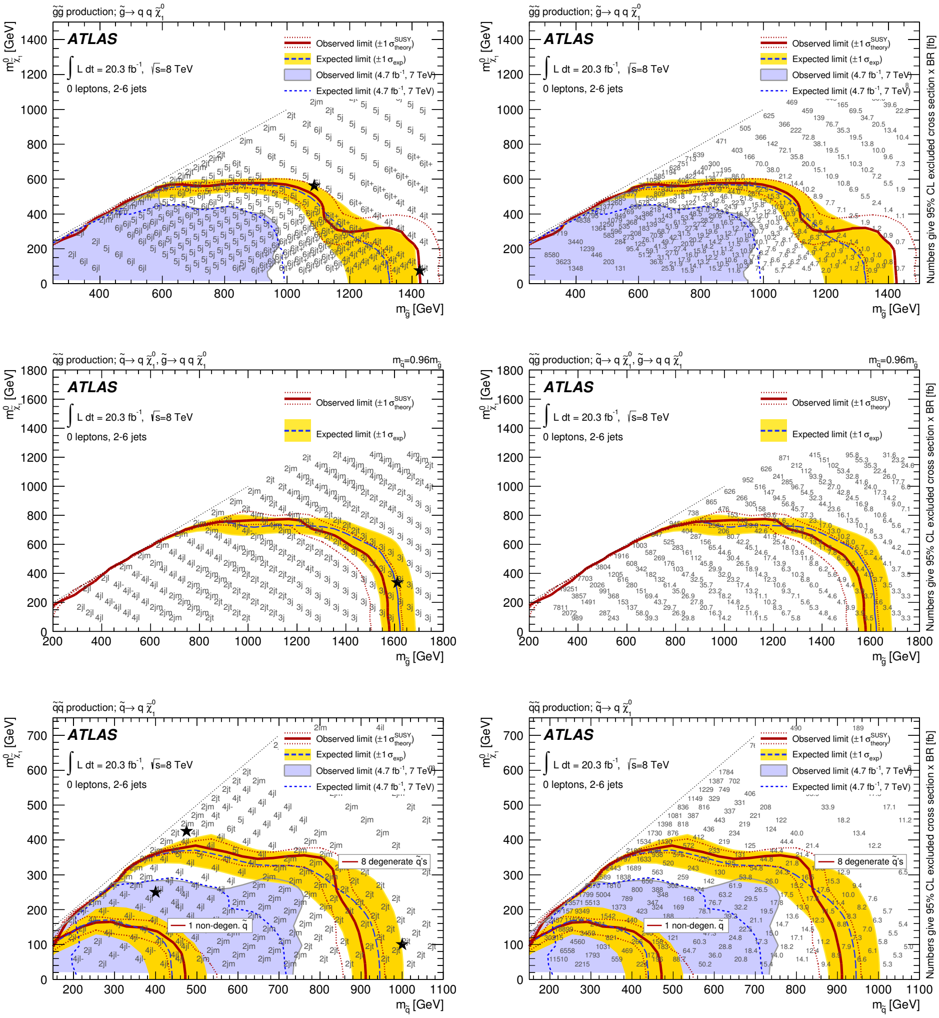

Fig. 5.20 · Exclusion limits for direct production of gluino pairs with decoupled squarks (top), of light-flavour squarks and gluinos (middle) and of light-flavour squark pairs with decoupled gluinos (bottom). In the bottom figures, limits are shown for scenarios with eight degenerate light-flavour squarks ($\tilde{q}_L + \tilde{q}_R$), or with only one non-degenerate light-flavour squark produced. The left-hand figures show the best signal region for each point; the right-hand figures show the obtained upper limits.

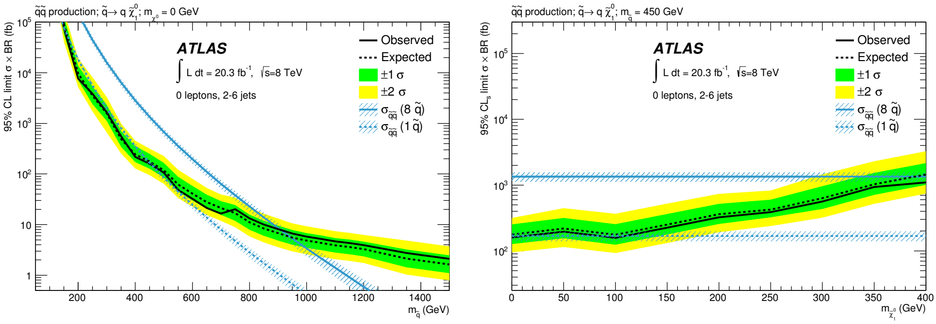

Fig. 5.21 · Limits on the light-flavour squark-pair production cross-section times branching ratio for models with squark pairs decaying directly into quarks and $\tilde{\chi}_1^0$ as a function of $m_{\tilde{q}}$ for a massless $\tilde{\chi}_1^0$ (left) and as a function of $m_{\tilde{\chi}_1^0}$ for $m_{\tilde{q}} = 450$ GeV (right). Exclusion limits are obtained by using the signal region with the best expected sensitivity at each point. The hatched bands around the theoretical curves denote the scale and PDF uncertainties.

5.11.3 Decays via charginos

Fig. 5.22 shows the result on pair-produced squarks and gluinos decaying via an intermediate $\tilde{\chi}^{\pm}$. In the cascade, an additional W boson is produced. Results are presented for both a fixed $\tilde{\chi}_1^0$ mass of 60 GeV, and for a fixed relative mass splitting x between the $\tilde{\chi}^{\pm}$ and $\tilde{\chi}_1^0$ of $x = (m_{\tilde{\chi}^{\pm}} - m_{\tilde{\chi}_1^0})/(m_{\tilde{q},\tilde{g}} - m_{\tilde{\chi}_1^0}) = 0.5$.

The lower limit on the gluino mass extends to 1100 GeV for massless $\tilde{\chi}_1^0$; for squarks this limit is 700 GeV. The introduction of SR2jW and SR4jW improves the sensitivity to models with large x: these signal regions improve the expected limit around $x \sim 1$ for gluinos by approximately 100 GeV and for squarks by 40 GeV.

5.11.4 Gluino-mediated stop production

In fig. 5.23 limits are presented for a simplified model of gluino-pair production. Each of these gluinos decays to a stop quark and a top quark, with the $\tilde{t}$ decaying to a charm quark and $\tilde{\chi}_1^0$. The model is motivated by 'natural' supersymmetry scenarios with a light $\tilde{t}$ and a small mass difference between the $\tilde{t}$ and $\tilde{\chi}_1^0$, leading to co-annihilation between stop quarks and $\tilde{\chi}_1^0$ dark matter particles in the early universe.

The lower limit on the gluino mass is 1100 GeV for a stop quark mass of 400 GeV. In studies on Monte Carlo truth samples this limit has been shown to be robust as a function of the mass difference $\Delta m(\tilde{t}, \tilde{\chi}_1^0)$, which was taken to be 10 GeV, 20 GeV and 50 GeV.

5.12 Conclusion and discussion

In this chapter, a search for supersymmetry in events with jets, no lepton and a large amount of $E_{\mathrm{T}}^{\mathrm{miss}}$ was presented. No excess over the Standard Model expectation has been observed and lower

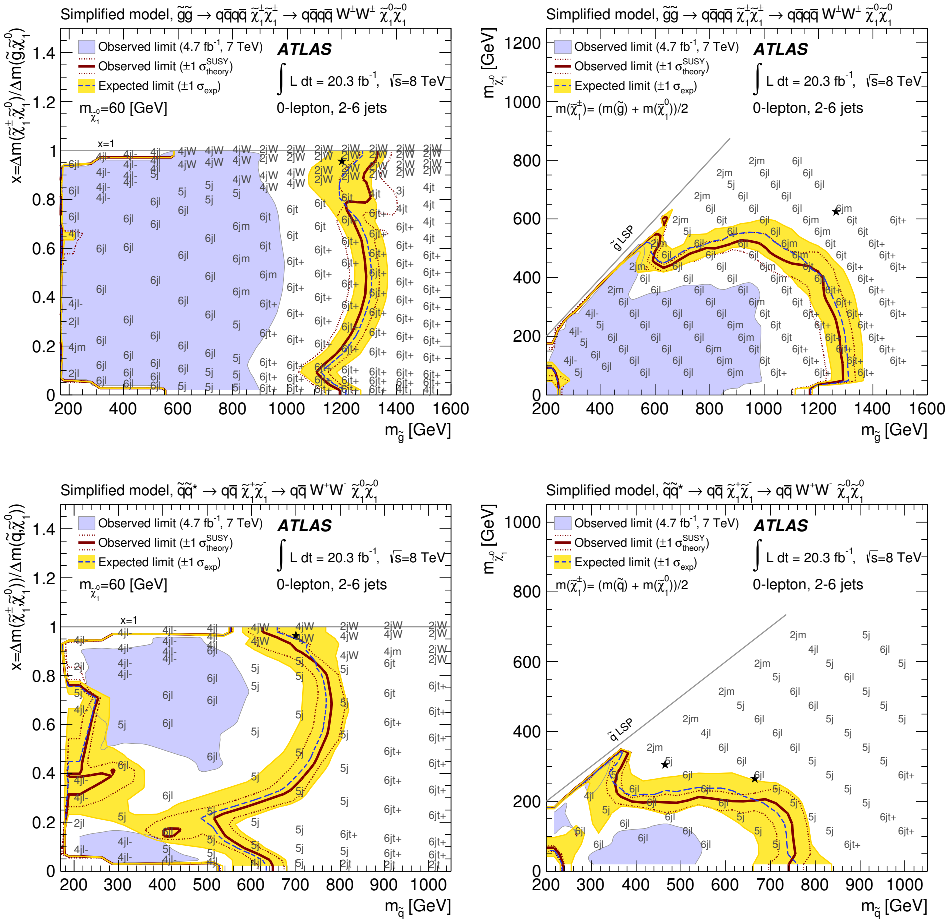

Fig. 5.22 · Exclusion limits for pair-produced gluinos each decaying via an intermediate $\tilde{\chi}_1^{\pm}$ to two quarks (see fig. 2.5), a W boson and a $\tilde{\chi}_1^0$ (top) or pair-produced light squarks each decaying via an intermediate $\tilde{\chi}_1^{\pm}$ to a quark, a W boson and a $\tilde{\chi}_1^0$ (bottom). The left-hand figures show results for models with fixed $m_{\tilde{\chi}_1^0} = 60$ GeV and varying values of $x = (m_{\tilde{\chi}_1^{\pm}} - m_{\tilde{\chi}_1^0})/(m_{\tilde{q},\tilde{g}} - m_{\tilde{\chi}_1^0})$ for the top (bottom) figure. The right-hand plots show results for models with a fixed value of $x = ½$ and varying values of $m_{\tilde{\chi}_1^0}$.

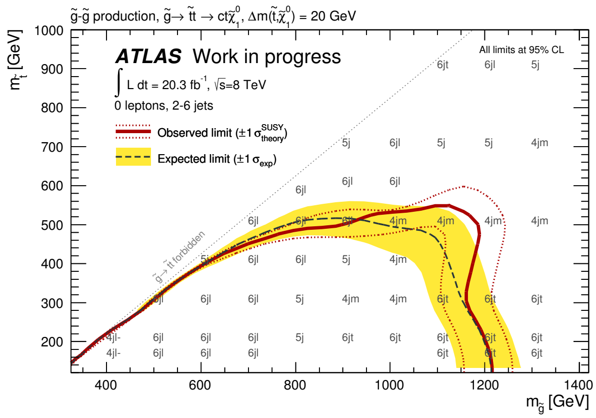

Fig. 5.23 · Exclusion limits in a gluino-mediated stop-pair production model, with $\tilde{t} \to c\ \tilde{\chi}^0$ decay and $\Delta m(\tilde{t}, \tilde{\chi}_1^0) = 20\,\text{GeV}$.

limits on allowed sparticle masses in MSUGRA/CMSSM have been set. The observations have also been interpreted in various simplified models.

Theoretical errors on the Standard Model background and the number of events in the control regions form the largest errors to the background prediction. In particular the error on the diboson background is large for the low jet multiplicity channels. For searches to be performed at $\sqrt{s} = 14\,\text{TeV}$, a control region for this background will be needed. The statistical errors for the control regions for high jet multiplicity channels, in particular those with somewhat looser selections on m_{eff}, should decrease as more data becomes available.[1] Chapter 8 further discusses the prospects of a search for supersymmetry in this channel at higher energy.

Binned fits, possibly in multiple dimensions, offer a method of setting even stronger limits. However, they do not offer a straightforward way of performing a discovery test: assumptions on the shape of the signal would have to be made. Unlike the search for the Standard Model Higgs boson, the number of free parameters for supersymmetry is too large. In future searches, a dual strategy could be followed using a set of cut-and-count regions optimised for the discovery of SUSY and a set of of binned regions optimised for exclusion.

New discriminating variables may also be investigated. However, these do not easily offer better results than $E_{\text{T}}^{\text{miss}}/m_{\text{eff}}(N_j)$ and $m_{\text{eff}}(\text{incl.})$. In particular for compressed scenarios dedicated studies will be required, including the possible addition of a monojet region.

The limits presented in this chapter do not rule out supersymmetry: assumptions on the simplified models are very strong. Moreover, models such as MSUGRA/CMSSM are a very particular slice of supersymmetrical phase space. In chapter 6 the limits will be used to perform a global fit to the MSSM using also other experimental results. Chapter 7 presents a combination of the results presented in this chapter with those from other channels in ATLAS, leading to stronger limits.

[1] This argument does not hold for the tight regions, which are designed to maximise the reach in squark or gluino mass: for these regions the selection on m_{eff} will simply become tighter, as also seen in chapter 8.

5.A Signal region optimisation

The signal regions described earlier in this chapter were determined through an optimisation of the sensitivity to the exclusion of several supersymmetry models, assuming a luminosity of $21\,\text{fb}^{-1}$. For these models, the excluded cross-section's dependence on several variables was studied. Rather than using a simple significance-based calculation relying on Monte Carlo predictions, the full likelihood, including normalisation in the control regions, was used.[1]

At the time of the optimisation, $14.1\,\text{fb}^{-1}$ of data were available. Data in the control regions were scaled to a luminosity of $21\,\text{fb}^{-1}$ to obtain the results presented below. Data in the signal regions were *not* used: the optimisation was performed blind, using Monte Carlo expectations in these regions.

Overview

To determine the optimal selections on the most suitable variable for the 2–5 jet signal regions, the three simplified models of direct production were used. In all cases, the supersymmetric particles are expected to decay directly into quarks and $\tilde{\chi}_1^0$. The 6-jet signal regions were optimised for decays through a $\tilde{\chi}^{\pm}$ using a similar method as described in this section.

Vetoes on b jets and τ leptons in the signal regions were also studied, but found to yield no improvement. A combined veto on both objects performs similar to the kinematic selection on a W boson, as eventually used in the analysis.

Optimisation in the full two-dimensional phase space of each model is prohibitive from a computational perspective. Instead, for each model three slices of its two-dimensional phase space have been selected, two corresponding either to a constant squark or gluino mass and one to a massless $\tilde{\chi}_1^0$. Models with constant squark or gluino mass are useful to test the sensitivity to compressed scenarios, by increasing the $\tilde{\chi}_1^0$ mass. Models with massless neutralinos are used to maximise the reach in terms of squark or gluino mass.

Choice of discriminating variables

In the previous version of this analysis [214], signal regions were defined by different selections on $m_{\text{eff}}(\text{incl.})$ and $E_{\text{T}}^{\text{miss}}/m_{\text{eff}}(N_j)$. These variables were once again considered in the optimisation procedure. In addition, several new variables were used: m_{CT} [275], m_{T2} [276], α_{T} [277, 278] and $E_{\text{T}}^{\text{miss}}/\sqrt{H_{\text{T}}}$.

Early in the optimisation process, the variables m_{CT}, m_{T2} and α_{T} were shown not to bring any improved performance compared with respect to existing variables, and were not further studied. Only $E_{\text{T}}^{\text{miss}}/\sqrt{H_{\text{T}}}$ was considered in the final optimisation as an alternative to $E_{\text{T}}^{\text{miss}}/m_{\text{eff}}(N_j)$: both variables are expected to be efficient at rejecting the multijets background. The jet multiplicity was also varied in the optimisation procedure. Requirements used in the optimisation procedure are shown in table 5.8. The definitions of the control regions were modified accordingly.

[1] Optimisation based purely on simulation was tested, but led to different results than the ones presented. Also, since the full likelihood is a more accurate description than a simple formula, this approach was followed.

Table 5.8 · Selections tested for simplified models.

Squark-pair production	
N_j	$\geq 2, \geq 3, \geq 4$
$m_{\text{eff}}(\text{incl.})$ [GeV]	$> 700, > 800, > 1000, > 1200, > 1400, > 1600, > 1800$
$E_{\text{T}}^{\text{miss}}/m_{\text{eff}}(N_j)$	$> 0.15, > 0.2, > 0.25, > 0.3, > 0.35, > 0.4$
$E_{\text{T}}^{\text{miss}}/\sqrt{H_{\text{T}}}$ [GeV$^{1/2}$]	$> 8, > 10, > 15, > 20, > 25$
Squark–gluino production	
N_j	$\geq 2, \geq 3, \geq 4, \geq 5$
$m_{\text{eff}}(\text{incl.})$ [GeV]	$> 800, > 1000, > 1200, > 1400, > 1600, > 1800, > 2000, > 2200, > 2400$
$E_{\text{T}}^{\text{miss}}/m_{\text{eff}}(N_j)$	$> 0.15, > 0.2, > 0.25, > 0.3, > 0.4$
$E_{\text{T}}^{\text{miss}}/\sqrt{H_{\text{T}}}$ [GeV$^{1/2}$]	$> 5, > 8, > 10, > 15, > 20, > 25$
Gluino-pair production	
N_j	$\geq 2, \geq 3, \geq 4, \geq 5$
$m_{\text{eff}}(\text{incl.})$ [GeV]	$> 800, > 1000, > 1200, > 1400, > 1600, > 1800, > 2000, > 2200$
$E_{\text{T}}^{\text{miss}}/m_{\text{eff}}(N_j)$	$> 0.15, > 0.2, > 0.25, > 0.3, > 0.4$
$E_{\text{T}}^{\text{miss}}/\sqrt{H_{\text{T}}}$ [GeV$^{1/2}$]	$> 10, > 15, > 20, > 25$

Optimisation procedure

The optimisation was performed by minimising the ratio $\lambda^{\text{exp}} = \sigma_{\text{excluded}}^{\text{expected}}/\sigma_{\text{nominal}}$. All combinations of selections were tested; those with the smallest cross-section for at least one model point were used. The minimum set of selections covering the excluded region was then selected.

Fig. 5.24 shows the distributions of λ^{exp} for the three selected lines in the planes $(m_{\tilde{q}}, m_{\tilde{\chi}_1^0})$ and $(m_{\tilde{g}}, m_{\tilde{\chi}_1^0})$. In all figures, the naming SRA–SRE refers to 2-jet to 6-jet signal regions. The squares show the lowest λ^{exp} obtained for each point in the optimisation procedure, taking into account all signal regions used. The red lines show the lowest λ^{exp} obtained with regions used in [279]. The blue lines show the lowest λ^{exp} obtained using regions with selections on $m_{\text{eff}}(\text{incl.})$ and $E_{\text{T}}^{\text{miss}}/meff(N_j)$; the green ones use $m_{\text{eff}}(\text{incl.})$ and $E_{\text{T}}^{\text{miss}}/\sqrt{H_{\text{T}}}$ instead. From these distributions, we conclude that $E_{\text{T}}^{\text{miss}}/\sqrt{H_{\text{T}}}$ performs slightly better than $E_{\text{T}}^{\text{miss}}/m_{\text{eff}}(N_j)$ for squark-pair production.

Fig. 5.25 and 5.26 show the distributions of λ^{exp} for the analyses that have the lowest λ^{exp} for at least one point, shown separately for regions using $E_{\text{T}}^{\text{miss}}/\sqrt{H_{\text{T}}}$ and regions using $E_{\text{T}}^{\text{miss}}/m_{\text{eff}}(N_j)$. Regions performing suboptimal for all models are not shown.

Based on these results, the signal regions shown in table 5.3 were selected. These regions maximally cover the various grids, including also the scenario with non-degenerate squarks for which the squark production cross-section is divided by 8.

5.B Cut-and-count versus binned fits

For the analysis published in [214], the use of multiple bins in m_{eff} was studied using a procedure similar to the cut-and-count analysis optimisation. The cut-and-count regions were used as a

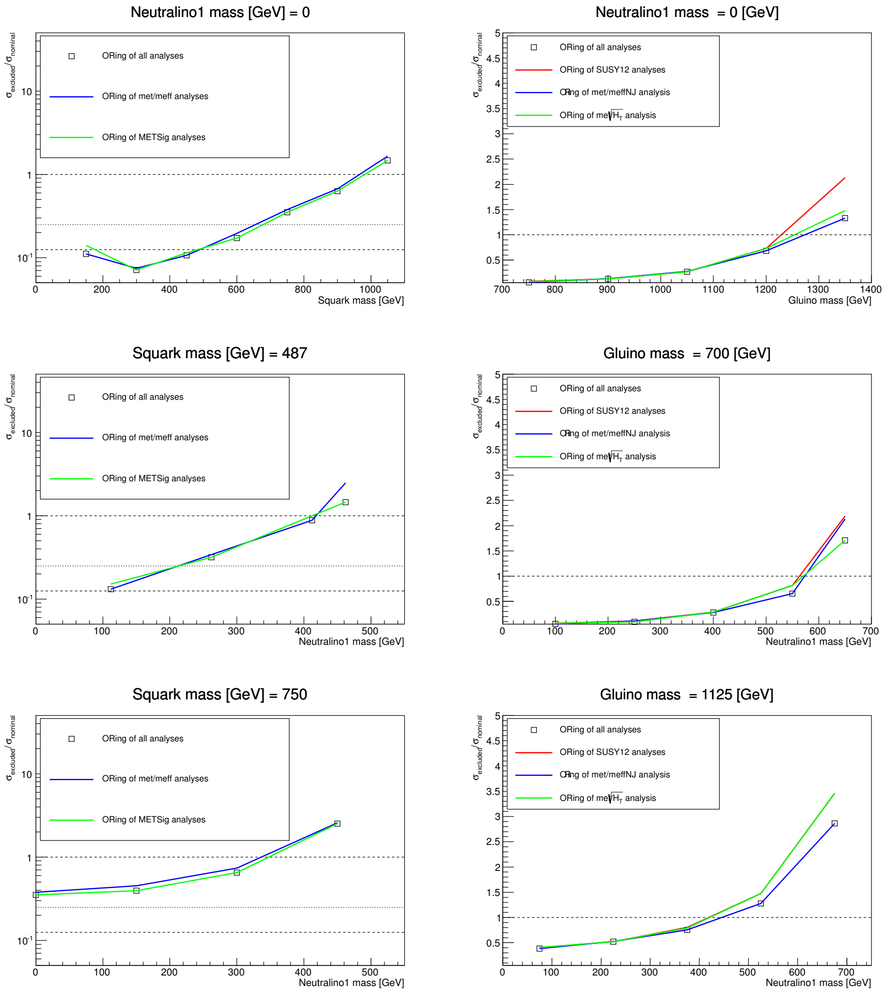

Fig. 5.24 · $\sigma_{\text{excluded}}^{\text{expected}}/\sigma_{\text{nominal}}$ as a function of the squark mass (left) and gluino mass (right), for three cases: massless $\tilde{\chi}_1^0$ (top); as a function of the $\tilde{\chi}_1^0$ mass for $m_{\tilde{q}} = 487$ GeV and $m_{\tilde{g}} = 700$ GeV (middle); and for $m_{\tilde{q}} = 750$ GeV and $m_{\tilde{g}} = 1125$ GeV (bottom), for simplified models of squark-pair and gluino-pair production with direct decays to quarks and $\tilde{\chi}_1^0$.

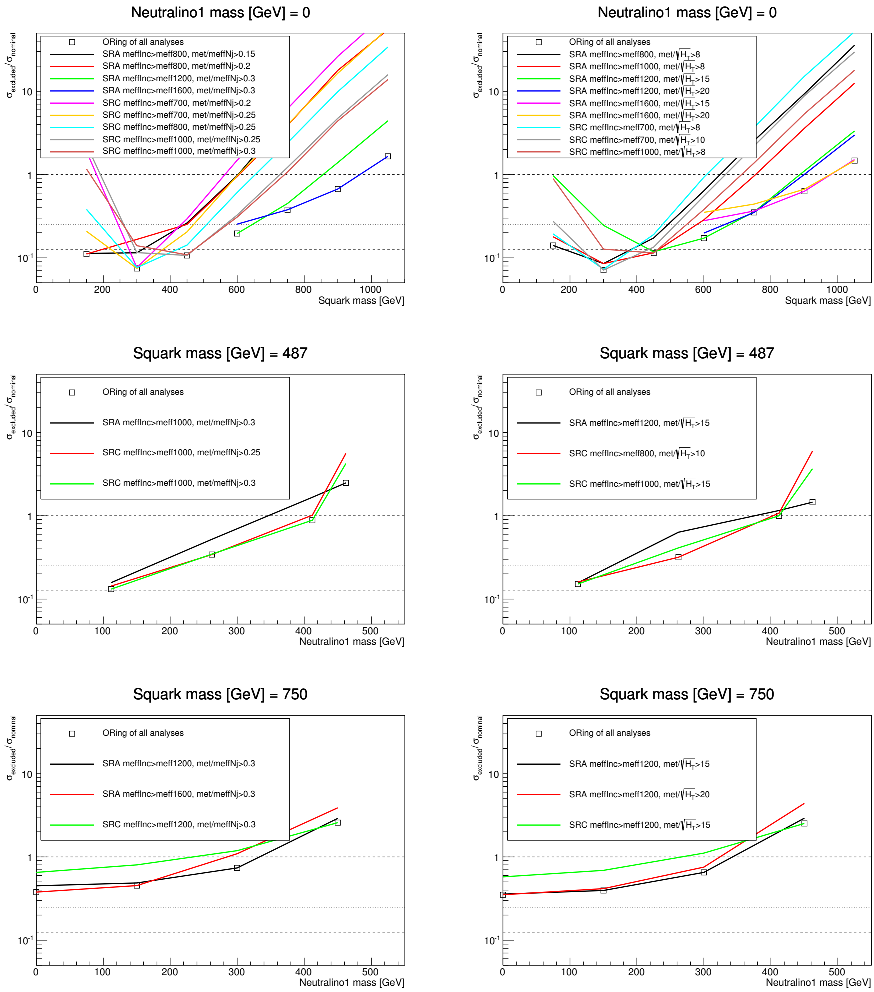

Fig. 5.25 · $\sigma^{\text{expected}}_{\text{excluded}}/\sigma_{\text{nominal}}$ as a function of the squark mass for massless $\tilde{\chi}^0_1$ (top), as a function of the $\tilde{\chi}^0_1$ mass for $m_{\tilde{q}} = 487\,\text{GeV}$ (middle) and for $m_{\tilde{q}} = 750\,\text{GeV}$ (bottom) for simplified models of squark-pair production and direct decays to quarks and $\tilde{\chi}^0_1$. On the left (right), only analyses with $E_{\text{T}}^{\text{miss}}/m_{\text{eff}}(N_j)$ ($E_{\text{T}}^{\text{miss}}/\sqrt{H_{\text{T}}}$) are considered.

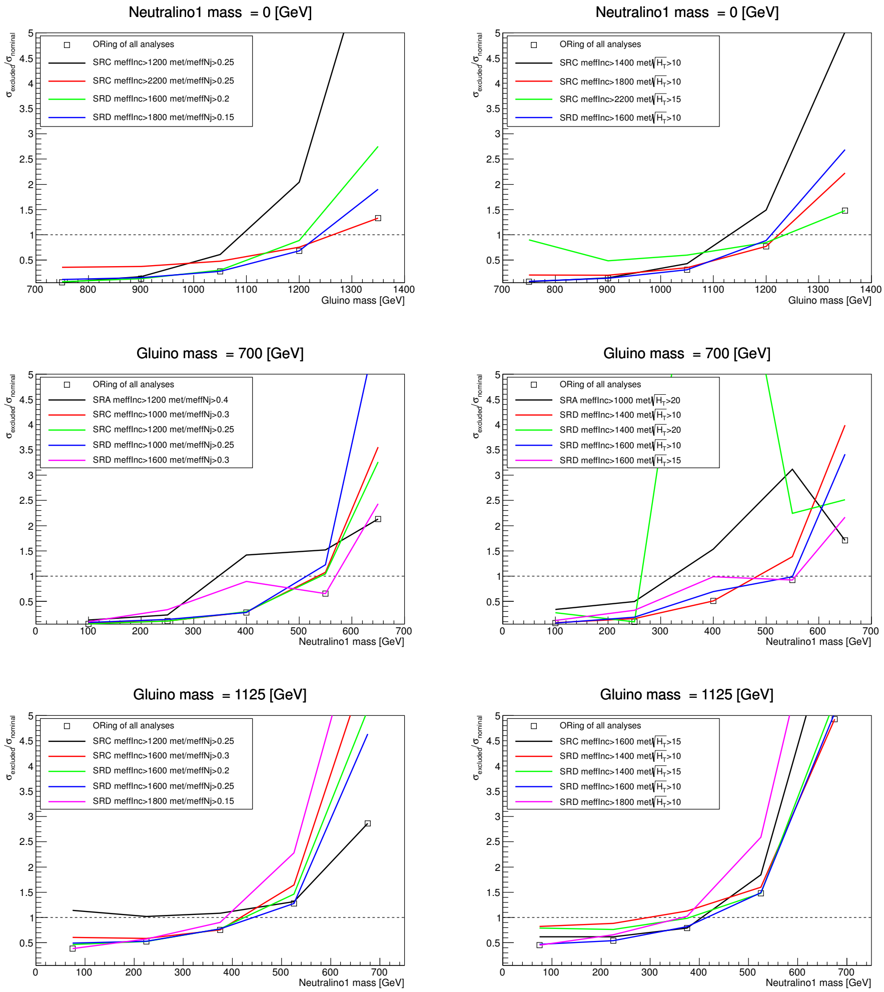

Fig. 5.26 · $\sigma^{\text{expected}}_{\text{excluded}}/\sigma_{\text{nominal}}$ as a function of the gluino mass for massless $\tilde{\chi}^0_1$ (top), as a function of the $\tilde{\chi}^0_1$ mass for $m_{\tilde{g}} = 700\,\text{GeV}$ (middle) and for $m_{\tilde{g}} = 125\,\text{GeV}$ (bottom) for simplified models of gluino-pair production and direct decays to quarks and $\tilde{\chi}^0_1$. On the left (right), only analyses with $E_{\text{T}}^{\text{miss}}/m_{\text{eff}}(N_j)$ ($E_{\text{T}}^{\text{miss}}/\sqrt{H_{\text{T}}}$) are considered.

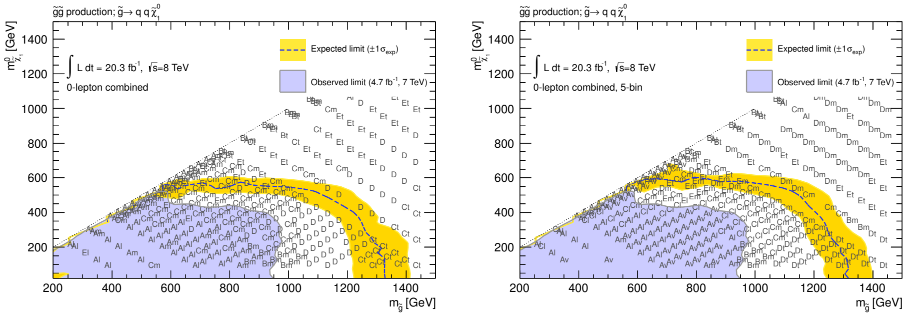

Fig. 5.27 · Comparison of the gluino-pair production limit of [214] prior to unblinding using a cut-and-count fit (left) and a 5-bin fit in m_{eff} (right). No improvement in terms of gluino mass is seen; a slight increase of approximately 25 GeV along the diagonal can be observed. The letters A–E refer to 2-jet to 6-jet signal regions.

starting point to determine the optional binned regions, by varying the requirement on m_{eff} by -300, -200, -100, 0, 100 or 200 GeV to determine the lower bin. The number of bins and the width of the bins were also varied: a range of 1000 GeV with 5 bins was found to be the optimal choice.

Fig. 5.27 shows the result for the optimised cut-and-count fit and the optimised 5-bin fit in m_{eff} for gluino-pair production. As expected, no increase in the gluino mass reach is found: such signals are easy to discriminate from background with a cut-and-count fit. For more compressed spectra, the increase in $\tilde{\chi}_1^0$ mass is approximately 25 GeV. The increase for such scenarios is also understood: the shape of the m_{eff} distribution for the signal is much more comparable to the background distribution. Similar results were obtained for the squark-pair production and squark–gluino production models. With the increase in reach being relatively small and the added complexity of a binned fit, binned fits were not used in that stage of the analysis. Moreover, a single-bin fit is advantageous for reinterpretation.

In addition, a study into the use of a binned fit with a generic exponential background and a normally distributed signal was performed. It concluded that for a typical SUSY signal, the maximum improvement for the significance was 8 %. For narrower signals or steeper background distributions, improvements of up to 30 % can be reached. However, the actual backgrounds and signals used do not have these general, optimal, properties. Higher-dimensional shape fits are a possible solution to separate signal and background better. A preliminary investigation using the 2011 $\sqrt{s} = 7$ TeV dataset was performed in 2012, but found these to be problematic due to low numbers of events in several bins and the large statistical errors associated to them.

Considering all the above, shape fits have not been used to obtain the limits presented earlier in this chapter.

CHAPTER SIX

Interpretation in the MSSM-15

EXPERIMENTAL DATA CAN be used to analyse the phase space of supersymmetrical models and provide best-fit values for a model's parameters. In this chapter, an interpretation using profile likelihood maps obtained via global fits of a phenomenological Minimal Supersymmetric Standard Model with 15 free parameters (the MSSM-15) is presented. The SUSY mass spectrum and dark matter properties that are preferred by current experimental constraints are derived.

ATLAS SUSY searches strongly impact the mass range preferred for light SUSY particles, and thus rule out a region of parameter space that is outside the reach of any current or future dark matter direct detection experiment. The best-fit point obtained after inclusion of all data corresponds to a squark mass of 2.3 TeV, a gluino mass of 2.1 TeV and a 130 GeV neutralino with a spin-independent cross-section of 2.4×10^{-10} pb, which is within the reach of future multi-ton scale dark matter direct detection experiments and of the upcoming LHC run at increased centre-of-mass energy.

This chapter focuses primarily on the implementation and impact of ATLAS searches in [280], a paper jointly written with C. Strege, G. Bertone, S. Caron, R. Ruiz de Austri, A. Strübig and R. Trotta. The ATLAS results used are the $\sqrt{s} = 7$ TeV 0-lepton analysis [216] and the 3-lepton analysis at the same centre-of-mass energy [281]. No published results at 8 TeV were available at the time of the work presented here.

6.1 Theoretical motivation

The simplest SUSY realisation, the Minimal Supersymmetric Standard Model (MSSM), has 124 free parameters, including complex phases, which makes its phenomenological study impractical. If a concrete mechanism that mediates SUSY breaking to the observable sector is applied, the number of parameters can be reduced significantly. For instance for models such as the constrained MSSM (CMSSM), in which universal scalar masses and gaugino masses are used and the trilinear couplings unify at a high energy scale, this is the case.

LHC results have severely constrained this model, so much that it is in tension with the naturalness of the electroweak breaking at the correct scale: the SUSY-breaking parameters are pushed to large values. One exception is the focus point region, where focus points in renormalisation group equation trajectories lead to the weak scale becoming independent of variations in the SUSY parameters. However, this region is becoming increasingly constrained by direct dark matter searches, such as the XENON100 [105] and LUX [106] experiments.

One approach to address this issue is to avoid explicitly assuming a SUSY breaking mechanism. Instead, the number of MSSM parameters can be reduced to 19 by using phenomenological constraints, that define the so-called phenomenological MSSM (pMSSM) [282]. The pMSSM has been studied in the past using random scans [283–285], as well as Bayesian methods [286–289]. Both approaches have limitations. While appearing uniformly distributed in one- and two-dimensional projections, random scans in large-dimensional parameter spaces are actually highly concentrated in a thin shell of the hypersphere in the scan box: only a negligible fraction of the pMSSM parameter space is explored by random scans. The Bayesian approach is much more efficient, but the prior dependence of the posterior distribution can be very strong, especially for high-dimensional models with a large number of effectively unconstrained parameters, such as the pMSSM.

A Bayesian approach to scanning with a full likelihood function and an algorithm that generates samples from the posterior distribution is used, after which profile likelihood maps are derived for a more robust statistical interpretation. These maps are in principle prior-independent. A profile likelihood analysis of a simplified version of the pMSSM with 15 parameter (called the MSSM-15) is performed. The number of model parameters is reduced by assumptions that retain the most relevant phenomenological aspects of the pMSSM in terms of collider and dark matter searches: the first- and second-generation up- and down-type sfermion masses are taken to be equal, left- and right-handed squarks are assumed to be degenerate, and unification of the bottom and tau trilinear parameters is assumed at the GUT scale so that $A_0 \equiv A_b = A_\tau$. This is motivated by the present lack of experimental evidence for SUSY.

This 15-dimensional realisation of the pMSSM encapsulates the phenomenologically relevant features of the full model that are of interest for dark matter and collider experiments. All of the input parameters are defined at the SUSY scale $\sqrt{m_{\tilde{t}_1} m_{\tilde{t}_2}}$, with the exception of A_0, which is defined at 10^{16} GeV and run to the SUSY scale using renormalisation group equations. All parameters and their priors are shown in table 6.1.

6.2 Scanning algorithm

A Bayesian approach to sample the MSSM-15 parameter space is used; the resulting posterior samples are used to produce profile likelihood maps. The large dimensionality of the pMSSM and the relatively weak constraints imposed by experimental data would otherwise result in a (Bayesian) posterior distribution suffering from severe prior-dependent volume effects. These would make the interpretation of the Bayesian posterior problematic.

Instead, the profile likelihood for one or two parameters at a time is used. The profile likelihood is obtained by maximising the likelihood function over the remaining parameters. For example, for a single parameter of interest θ_i the other parameters $\Psi = \{\theta_1, \ldots, \theta_n\} \backslash \{\theta_i\}$ are eliminated from the one-dimensional profile likelihood by maximising over them:

$$L(\theta_i) = \max_{\Psi} L(\theta_i, \Psi) = L(\theta_i, \hat{\hat{\Psi}}), \tag{6.1}$$

where $L(\theta_i, \Psi)$ is the full likelihood function. Samples of the pMSSM parameter space are distributed according to the posterior PDF, but their density in producing profile likelihood maps is

Table 6.1 · pMSSM parameters and top mass value used, and prior ranges for the two prior choices adopted in the scans. "Flat priors" are uniform on the parameter itself (within the ranges indicated), while "Log priors" are uniform in the log of the parameter (within the ranges indicated).

pMSSM parameters and priors			
Flat priors		**Log priors**	
M_1 [TeV]	$(-5, 5)$	$\text{sgn}\, M_1 \log \lvert M_1 \rvert/\text{GeV}$	$(-3.7, 3.7)$
M_2 [TeV]	$(0.1, 5)$	$\log M_2/\text{GeV}$	$(2, 3.7)$
M_3 [TeV]	$(-5, 5)$	$\text{sgn}\, M_3 \log \lvert M_3 \rvert/\text{GeV}$	$(-3.7, 3.7)$
m_L [TeV]	$(0.1, 10)$	$\log m_L/\text{GeV}$	$(2, 4)$
m_{L_3} [TeV]	$(0.1, 10)$	$\log m_{L_3}/\text{GeV}$	$(2, 4)$
m_{E_3} [TeV]	$(0.1, 10)$	$\log m_{E_3}/\text{GeV}$	$(2, 4)$
m_Q [TeV]	$(0.1, 10)$	$\log m_Q/\text{GeV}$	$(2, 4)$
m_{Q_3} [TeV]	$(0.1, 10)$	$\log m_{Q_3}/\text{GeV}$	$(2, 4)$
m_{U_3} [TeV]	$(0.1, 10)$	$\log m_{U_3}/\text{GeV}$	$(2, 4)$
m_{D_3} [TeV]	$(0.1, 10)$	$\log m_{D_3}/\text{GeV}$	$(2, 4)$
A_t [TeV]	$(-10, 10)$	$\text{sgn}\, A_t \log \lvert A_t \rvert/\text{GeV}$	$(-4, 4)$
A_0 [TeV]	$(-10, 10)$	$\text{sgn}\, A_0 \log \lvert A_0 \rvert/\text{GeV}$	$(-4, 4)$
μ [TeV]	$(-5, 5)$	$\text{sgn}\, \mu \log \lvert \mu \rvert/\text{GeV}$	$(-3.7, 3.7)$
m_A [TeV]	$(0.01, 5)$	$\log m_A/\text{GeV}$	$(1, 3.7)$
$\tan\beta$	$(2, 62)$	$\tan\beta$	$(2, 62)$
M_t [GeV]	$(170.6, 175.8)$	M_t [GeV]	$(170.6, 175.8)$

ignored by maximising over the hidden variables. Confidence intervals/regions from the resulting profile likelihood maps are determined using a profile likelihood ratio as test statistic. Values of $\Delta\chi^2 = -2\ln\lambda(\theta_i)$ corresponding to 68 %, 95 % and 99 % confidence intervals are obtained from Wilks' theorem [290].

In this Bayesian approach, the prior becomes a method to concentrate the scan in certain regions of parameter space. Two different sets of priors (flat priors and log priors) are used to sample as much of the parameter space as possible.[1] The results are then merged to obtain a prior-independent limit, as advocated in [291].

A likelihood of zero is assigned to unphysical points in parameter space, i.e. those that do not fulfil the conditions of radiative electroweak symmetry breaking or lead to tachyonic states. Additionally, all points for which the lightest neutralino is not the LSP are discarded.

`MultiNest` v2.18 [292, 293] is used to obtain samples from the posterior distributions. Multiple scans are run to compare the resulting best-fit points and profile likelihoods, in order to verify that a reliable exploration of the pMSSM parameter space is achieved and to confirm the results are robust.

[1] Flat priors tend to concentrate sampling towards large values of the parameters, as most of the prior volume lies there. Log priors concentrate the scan in the low-mass region, as every decade in the parameter values is given the same a priori probability under this metric.

6.3 Experimental constraints

Experimental constraints are implemented through a joint likelihood function, whose logarithm takes the following form:

$$\ln L_J = \ln L_{\mathrm{EW}} + \ln L_{B(D)} + \ln L_{g-2} + \ln L_{\Omega_\chi h^2} + \ln L_{\mathrm{DD}} + \ln L_{\mathrm{Higgs}} + \ln L_{\mathrm{SUSY}}, \quad (6.2)$$

where L_{EW} represents electroweak precision observables, $L_{B(D)}$ B- and D-physics constraints, L_{g-2} measurements of the anomalous magnetic moment of the muon, $L_{\Omega_\chi h^2}$ measurements of the cosmological dark matter relic density, L_{DD} direct dark matter detection constraints, L_{Higgs} LHC measurements of the properties of the Higgs boson and L_{SUSY} ATLAS SUSY searches.

Electroweak constraints come from measurements at LEP at the Z pole, and include the hadronic pole cross-section and the Z width. Constraints on asymmetry parameters are not used; they have been found to negligibly impact the result. Constraints from B and D physics are provided by the Heavy Flavour Averaging Group; recent precision measurements are also included. The Planck result on the dark matter relic abundance is used to further constrain the parameter space, under the assumption that the neutralino makes up all dark matter. Direct dark matter detection constraints are provided by the XENON100 2012 result. The measurement of the anomalous magnetic moment of the muon has a strong impact on the allowed models. Hence, results are presented both with and without this constraint included. Finally, the Higgs boson provides a strong constraint on allowed models. A weighted average of the ATLAS and CMS results on the Higgs mass m_h is used. The signal strengths in the various decay channels (WW, ZZ, $\gamma\gamma$, $\tau\tau$ and $b\bar{b}$) as obtained by CMS are also included.

The SUSY searches constraints applied come from bounds on sparticle masses from LEP and Tevatron for which the likelihood is applied as outlined in [294] and from LHC searches using final states with jets, missing transverse energy and no leptons, and final states with 3 leptons and missing transverse energy in the ATLAS experiment, both with data recorded at $\sqrt{s} = 7\,\mathrm{TeV}$ and a total integrated luminosity of $4.7\,\mathrm{fb}^{-1}$ [216, 281]. Details about the construction and validation of the LHC likelihood function associated with these two channels are given in the next section.

All constraints used are summarised in table 6.2.

6.4 Likelihood for ATLAS searches

An approximate construction is used to exploit 0-lepton and 3-lepton inclusive searches from ATLAS data. The ATLAS 0-lepton analysis [216] has 6 channels which are used to construct between one and three signal regions with *loose*, *medium* and/or *tight* m_{eff}(incl.) selections, giving in total 11 signal regions. The different channels have been constructed for different sparticle production mechanisms. Signal region A is designed for squark-pair production; signal region A' especially for those models with low mass splittings. Signal region B is designed for squark–gluino production, whereas signal regions C–E are constructed for gluino-pair production.

The selection criteria for each signal region are shown in table 6.3. As the analysis' name implies, a general veto on events containing leptons is used. The selection variables used are the minimum required number of jets and their respective transverse momentum, the missing

Table 6.2 · Summary of experimental constraints used in the likelihood. Measured observables are modelled with a Gaussian likelihood of mean μ, and standard deviation $(\sigma^2 + \tau^2)^{1/2}$, where σ is the experimental and τ the theoretical uncertainty. Observables for which only limits currently exist further constrain the scan. Experimental constraints tagged with # have been found to contribute an approximately constant value to the log-likelihood and hence have been omitted. Observables tagged with † are applied via post-processing of the samples.

Observable	Value	Exp. unc.	Theo. unc.	Ref.
m_t [GeV]	173.2	0.87	–	[295]
m_W [GeV]	80.385	0.015	0.01	[297]
$\sin^2\theta_{\text{eff}}$	0.23153	0.00016	0.00010	[297]
Γ_Z [GeV]	2.4952	0.0023	0.001	[297]
σ^0_{had} [nb]	41.540	0.037	–	[297]
R^0_l	20.767	0.025	–	[297]
R^0_b	0.21629	0.00066	–	[297]
R^0_c	0.1721	0.003	–	[297]
$^{\#}A^{0,l}_{\text{FB}}$	0.0171	0.001	–	[297]
$^{\#}A^{0,b}_{\text{FB}}$	0.0992	0.0016	–	[297]
$^{\#}A^{0,c}_{\text{FB}}$	0.0707	0.0035	–	[297]
$^{\#}A_l$ (SLD)	0.1513	0.0021	–	[297]
$^{\#}A_b$	0.923	0.02	–	[297]
$^{\#}A_c$	0.670	0.027	–	[297]
$\delta a^{\text{SUSY}}_\mu \times 10^{10}$	28.7	8.0	2.0	[116]
$\text{BR}(\bar{B} \to X_s\gamma) \times 10^4$	3.55	0.26	0.30	[110]
$R_{\Delta M_{B_s}}$	1.04	0.11	–	[308, 309]
$\frac{\text{BR}(B_u\to\tau\nu)}{\text{BR}(B_u\to\tau\nu)_{SM}}$	1.63	0.54	–	[110]
$\Delta_{0-} \times 10^2$	3.1	2.3	1.75	[310, 311, 109]

Observable	Value	Exp. unc.	Theo. unc.	Ref.
$^{\#}\frac{\text{BR}(B\to D\tau\nu)}{\text{BR}(B\to De\nu)} \times 10^2$	41.6	12.8	3.5	[296]
$^{\#}R_{l23}$	0.999	0.007	–	[298]
$A_{\text{FB}}(B \to K^*\mu^+\mu^-)$	-0.18	0.063	0.05	[299]
$\text{BR}(D_s \to \tau\nu) \times 10^2$	5.44	0.22	0.1	[110]
$^{\#}\text{BR}(D_s \to \mu\nu) \times 10^3$	5.54	0.24	0.2	[110]
$^{\#}\text{BR}(D \to \mu\nu) \times 10^4$	3.82	0.33	0.2	[110]
$\text{BR}(\bar{B}_s \to \mu^+\mu^-) \times 10^9$	3.2	1.5	0.38	[300]
$\Omega_{\tilde{\chi}^0_1} h^2$	0.1186	0.0031	0.012	[74]
m_h [GeV]	125.66	0.41	2.0	[301, 302]
$^{\dagger}\mu_{\gamma\gamma}$	0.78	0.27	15 %	[303]
$^{\dagger}\mu_{W^+W^-}$	0.76	0.21	15 %	[304]
$^{\dagger}\mu_{ZZ}$	0.91	0.27	15 %	[305]
$^{\dagger}\mu_{b\bar{b}}$	1.3	0.65	15 %	[306]
$^{\dagger}\mu_{\tau^+\tau^-}$	1.1	0.4	15 %	[307]

Observable	Limit (95 % CL)	Ref.
Sparticle masses	LEP, Tevatron; as in table 4 of [294]	[294]
†0-lepton SUSY search	ATLAS, $\sqrt{s} = 7\,\text{TeV}$, $4.7\,\text{fb}^{-1}$	[216]
†3-lepton SUSY search	ATLAS, $\sqrt{s} = 7\,\text{TeV}$, $4.7\,\text{fb}^{-1}$	[281]
$m_\chi - \sigma^{\text{SD}}_{\tilde{\chi}^0_1 - p}$	XENON100 2012 limits	[105]

Table 6.3 · Requirements for the inclusive channels A–E for the ATLAS 0-lepton analysis with an integrated luminosity of 4.7 fb^{-1}. For m_{eff}(incl.) the limits are given in the order *tight/medium/loose* (from [216]).

Signal region	A	A'	B	C	D	E
E_T^{miss} [GeV] >	160					
$p_T(j_1)$ [GeV] >	130					
$p_T(j_2)$ [GeV] >	60					
$p_T(j_3)$ [GeV] >	–	–	60	60	60	60
$p_T(j_4)$ [GeV] >	–	–	–	60	60	60
$p_T(j_5)$ [GeV] >	–	–	–	–	40	40
$p_T(j_6)$ [GeV] >	–	–	–	–	–	40
$\Delta\phi(j_i, E_T^{\text{miss}})_{\text{min}}$ >	0.4 (i=1,2,(3))			0.4 (i=1,2,3)		
	–	–	–	0.2 (for all jets p_T> 40 GeV)		
$E_T^{\text{miss}}/m_{\text{eff}}(N_j)$ >	0.3 (2j)	0.4 (2j)	0.25 (3j)	0.25 (4j)	0.2 (5j)	0.15 (6j)
m_{eff}(incl.) [TeV] >	1.9/1.4/–	–/1.2/–	1.9/–/–	1.5/1.2/0.9	1.5/–/–	1.4/1.2/0.9

Table 6.4 · Requirements for the signal regions 1a, 1b and 2 for the 3-lepton ATLAS analysis with an integrated luminosity of 4.7 fb^{-1}. In addition, the number of reconstructed leptons has to be three (from [281]).

Signal region	1a	1b	2
Lepton charge, flavour	at least one SFOS pair with $m_{\ell\ell}$ > 20 GeV		
E_T^{miss}[GeV] >	75	75	75
m_{SFOS} [GeV]	< 81.2 or > 101.2	< 81.2 or > 101.2	81.2–101.2
No. of b-jets	0	0	–
m_T [GeV] >	–	90	90
p_T of all leptons [GeV] >	10	30	10

transverse energy E_T^{miss}, the effective mass m_{eff} calculated as the scalar sum of all transverse jet momenta larger than 40 GeV and the missing transverse energy, the ratio of E_T^{miss} to m_{eff} (where m_{eff} only includes the required number of jets), the minimum angle between the required jets and the missing energy vector $\Delta\phi(j_i, E_T^{\text{miss}})_{\text{min}}$. For the signal regions C–E an additional criterion is applied, a cut on $\Delta\phi(j_i, E_T^{\text{miss}})_{\text{min}}$ for all jets with transverse momenta larger than 40 GeV.

The ATLAS 3-lepton analysis [281] consists of 3 signal regions. Signal regions 1a and 1b include a Z veto; signal region 2 is designed for an on-shell Z boson. All signal regions require exactly three leptons, of which two form a same-flavour opposite-sign (SFOS) lepton pair. The selection criteria are shown in table 6.4. The transverse mass m_T is calculated using the missing transverse energy and the third lepton.

6.4.1 The likelihood function

The likelihood for each bin in a signal region i ($i = 1, \ldots, 14$) is given by

$$L_i(n_i|s, b, \boldsymbol{\theta}) = P\big(n_i|\lambda_s(s, b, \boldsymbol{\theta})\big) \times L_C(\boldsymbol{\theta}), \tag{6.3}$$

where the first factor reflects the Poisson probability of observing a number of events n in the signal region given the signal (background) expected value s (b). The Poisson expectation value λ_s also depends on the nuisance parameters $\boldsymbol{\theta}$ that parametrise systematic uncertainties, such as luminosity or jet energy scale. Those uncertainties are constrained via the likelihood term $L_C(\boldsymbol{\theta})$, which is taken to be a multivariate Gaussian distribution around the nominal value $\boldsymbol{\theta} = 0$, with diagonal covariance matrix entries given by the quoted nominal uncertainties in each of the systematic factors. The Poisson expectation value may then be written as

$$\lambda_s = s\big(1 + \Delta_s \theta_s\big) + b\big(1 + \Delta_b \theta_b\big), \tag{6.4}$$

where s and b are the nominal values of the signal and background, Δ_s and Δ_b are their relative uncertainties and θ_s and θ_b are nuisance parameters, so that $\boldsymbol{\theta} = \{\theta_s, \theta_b\}$.

The uncertainties on the background estimate are provided by the official ATLAS result; the analysis is considered a single-bin counting experiment. For the signal, the uncertainty is decomposed into a cross-section uncertainty, a luminosity uncertainty and uncertainty on the acceptance and efficiency. The cross-section uncertainty is evaluated using NLL-fast [250–254] and Prospino [250, 312]; the luminosity uncertainty is small and neglected; and the uncertainty on the acceptance and efficiency is studied using PYTHIA 6.4 [150] with the ATLAS MC09 tune [313] and DELPHES3 [314] to simulate the detector response. The obtained efficiencies are validated in Appendix C of [280].

6.4.2 Approximate joint likelihood for inclusive searches

The method for combining different SUSY analyses depends on whether the analyses are exclusive (i.e., without overlapping data samples) or inclusive (i.e., with overlapping data samples).

For exclusive analyses, the corresponding data samples are statistically independent, whether they are signal regions or control samples used to constrain the background prediction. However, the combined likelihood of two exclusive analyses cannot be constructed as the simple product of the two individual likelihoods, as the systematics term L_C is in general correlated between the two searches. Every (fully) correlated systematic uncertainty must use the same nuisance parameter in both analyses, and only one constraint on this single parameter should be used in L_C.

For analyses with statistically overlapping data samples or signal regions that are not exclusive, the likelihoods for different signal regions are not statistically independent: a joint likelihood is difficult to construct. In this case, for each value of s tested, the best signal region based on the expected value of the likelihood $P(q_s|s+b)$ is selected, where q_s denotes the test statistic

$$q_s = \begin{cases} -2\ln\lambda(s) & \text{if } \hat{s} < s, \\ 0 & \text{if } \hat{s} > s, \end{cases} \tag{6.5}$$

with $\lambda(s)$ is the profile likelihood ratio

$$\lambda(s) \equiv \frac{L\big(s, \hat{\hat{\boldsymbol{\theta}}}\big)}{L\big(\hat{s}, \hat{\boldsymbol{\theta}}\big)}, \tag{6.6}$$

in which $\hat{\hat{\boldsymbol{\theta}}}$ denotes the conditional minimum likelihood estimator for the nuisance parameters $\boldsymbol{\theta}$; $\hat{s}$ is the unconditional minimum likelihood estimator for s; and $\hat{\boldsymbol{\theta}}$ the unconditional minimum likelihood estimator for $\boldsymbol{\theta}$. The distribution of the likelihood is obtained from Monte Carlo simulations (assuming the alternative $s + b$). The best signal region is the one leading to an expected likelihood with the smallest p-value. This procedure thus selects the signal region that is expected to give the strongest limits for each value of s.

The likelihood using the observed number of events $P(n_{\rm obs}|s + b_{\rm fit})$ in that optimal signal region is then evaluated, where $n_{\rm obs}$ is the observed number of events and 'fit' refers to the data-constrained background value.

However, in general this approach would lead to a discontinuity in the value of the likelihood whenever moving in parameter space across a boundary where the best signal region changes. A priori, there is no reason why absolute values of the likelihood function for different signal regions should be continuous across such boundaries. By defining the full likelihood as

$$L = L_i^{\rm obs} \prod_{j \neq i} E[L_j] \tag{6.7}$$

this potential issue can be circumvented. $L_i^{\rm obs}$ is the observed likelihood for the signal region selected by the above procedure, while $E[L_j]$ is the expected likelihood in signal region $j \neq i$, i.e., in all the other signal regions that are less optimal for the given s being tested, including overlapping regions. This ensures a continuous likelihood function across signal regions.

6.4.3 Validation

The likelihood (6.3) and the approach (6.7) in the case of non-overlapping signal regions is evaluated as follows. For every signal region i ($i = 1, \ldots, 14$) in the analyses used, the number of expected events in the signal region under the null hypothesis ($s = 0$) is given by the number of expected background events $b_i \pm \sigma_{b_i}$. In order to remain unbiased towards any particular SUSY model or particular number of expected signal events s_i in general, 10,000 toy events are generated around the background expectation only.

To take into account systematic and statistical fluctuations, the number of toy observed events is generated according to

$$n_{\rm toy_i} = \text{Poisson}(\text{Normal}(b_i, \sigma_{b_i})), \tag{6.8}$$

where the extra Gaussian smearing approximately accounts for systematic effects. For σ_{b_i} the uncertainty on the background prediction as given by ATLAS is used. The joint likelihood (6.7) for the simulated events for each non-exclusive signal region i is then computed.

The results of the validation studies are shown in fig. 6.1, for several of the signal regions of the 0-lepton analysis (the case of the 3-lepton analysis is similar). The distributions' shapes are identical, up to an irrelevant normalisation factor. The spikes are a normalisation issue, due to the fact that for regions with a small number of events the number of possible values for $L_{\rm obs_i}(n = n_{\rm toy_i})$ is smaller than it is for regions with high n_{b_j}.

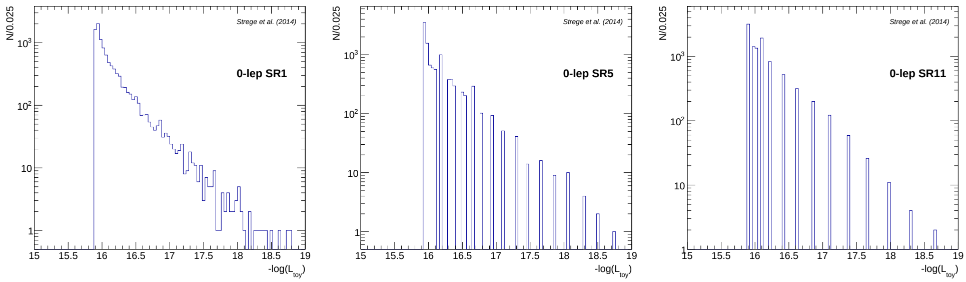

Fig. 6.1 · Distributions of $-\log(L_{\mathrm{toy}})$ using toy data generated in the respective signal region from the ATLAS 0-lepton inclusive analysis. All curves can be seen to follow the same distribution, which validates the approach used. Further figures are available in [280].

From this validation study it is clear that the procedure to use the most powerful signal region for each sampled value of the MSSM-15 parameter space, while normalising the likelihood via the expected value of the other signal regions, leads to no large bias.

6.5 Results

The best-fit values are obtained in two steps. First, a result without any LHC constraints is obtained. These results are presented first. Constraints on the Higgs couplings and results from SUSY searches are applied in a post-processing step. The best-fit value is re-derived with these additional constraints applied.

6.5.1 Best fits excluding LHC data

The profile likelihoods for several SUSY masses are displayed in fig. 6.2. The mass of the lightest Higgs boson measured by the LHC can easily be satisfied in the pMSSM. This is a reflection of the large number of degrees of freedom of the model, which allow to maximise the tree-level contribution to the Higgs mass by pushing A_0 and/or $\tan\beta$ to large values, while at the same time maximising the leading 1-loop corrections either via heavy stops or maximal stop mixing.

The mass of the neutralino LSP is shown in the top-central panel. For the analysis including all data, the neutralino mass is constrained to $m_{\tilde{\chi}_1^0} < 1.5\,\mathrm{TeV}$ at 99 % confidence level. In contrast, the one-dimensional profile likelihood for the analysis excluding the $g-2$ constraint reaches significantly larger masses $m_{\tilde{\chi}_1^0} \leq 3.0\,\mathrm{TeV}$. In both cases, the likelihood peaks at low values, with an almost identical best fit at $m_{\tilde{\chi}_1^0} \approx 60\,\mathrm{GeV}$.

The bump in the neutralino likelihood around $\sim 1\,\mathrm{TeV}$ corresponds to a higgsino-like neutralino (see §3.5 of [280] for details), and it is more pronounced for the case without $g-2$. In the latter case, the small bump at $m_{\tilde{\chi}_1^0} \sim 2\,\mathrm{TeV}$ in the likelihood corresponds to a wino-like neutralino.

The likelihood for the mass of the lightest chargino stretches to large values, close to the prior boundary around $\sim 5\,\mathrm{TeV}$ imposed by the prior on the input parameters. Nevertheless, similarly to what was observed for the neutralino mass, small chargino masses are favoured. In contrast, the likelihoods for the average squark mass, the lightest stop mass and the gluino mass remain

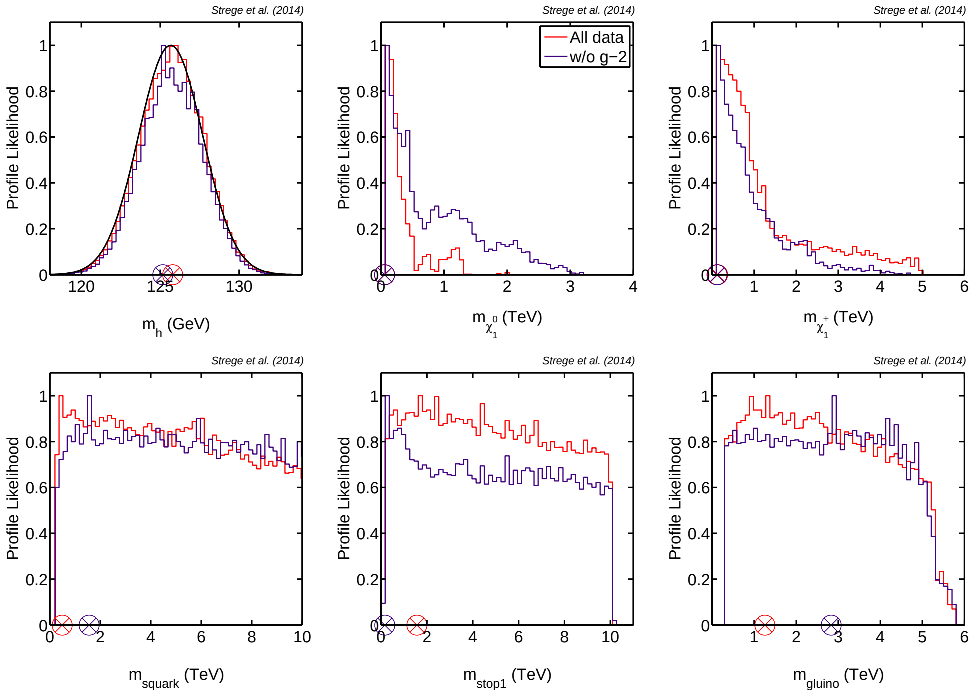

Fig. 6.2 · Results including all data except LHC SUSY searches and Higgs couplings (red) and further excluding the $g-2$ constraint (purple) for some relevant SUSY quantities. Encircled crosses represent the best-fit points. For quantities constrained in the scan, the likelihood function applied is shown in black. Recall that these results do not include null SUSY searches at the LHC (see §6.5.2).

almost unconstrained. The shape of the likelihood for these quantities is a direct consequence of the likelihood for the corresponding soft masses and M_3, respectively (see §3.1.1 of [280]).

6.5.2 Best fits including LHC data

The evaluation of the full LHC likelihood is numerically very demanding; post-processing all samples would be prohibitive. Instead, an intermediate approach that gives an indication of the extra constraining power from LHC SUSY searches and Higgs signal strengths measurements is used. In this "mini-chains" approach, profile likelihood maps from the full chains for several planes of interest, e.g. $(m_{\tilde{g}}, m_{\tilde{q}})$, are produced first. This leads to approximately 10^4 profile likelihood values for each two-dimensional plane. For each of those values, the combined χ^2 contribution from LHC constraints on the Higgs production cross-sections and LHC SUSY searches (0-lepton and 3-lepton) is computed, according to the procedure of §6.4.2. The extra χ^2 value is added to the pre-LHC χ^2 obtained using all other experimental constraints.

It must be stressed that this is not a fully consistent statistical approach, and that the ensuing maps cannot be interpreted probabilistically as likelihood maps (as the full likelihood has not been maximised in the parameters not shown; a figure similar to fig. 6.2 is thus impossible to

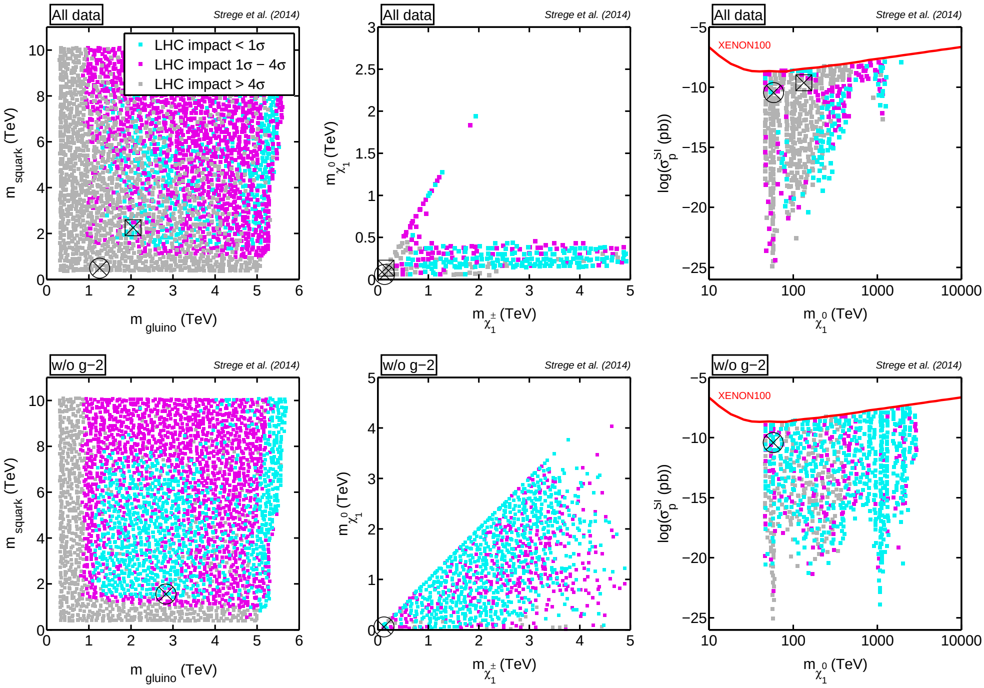

Fig. 6.3 · Scatter plots from the two-dimensional mini-chains, showing the impact of the LHC results on the chi-square of the best-fit point in each bin. The top (bottom) row shows results for the scans including all data (except the $g-2$ constraint). The encircled black cross indicates the best-fit point prior to inclusion of the LHC constraints; for the scans including all data, this point is ruled out by the LHC results, hence the next best-fit point that survives the LHC constraints is also shown (cross inscribed in the square). The best-fit point for the analysis excluding $g-2$ (bottom panels) remains viable after LHC data are included.

provide). However, it does allow us to draw some useful conclusions regarding the impact of LHC SUSY searches and measurements of the Higgs properties: mini-chain points that remain viable after inclusion of the LHC constraints would not be ruled out even under a full profile-likelihood approach. In this sense, the used approach gives an indication of the *maximal possible* constraints in each plane resulting from the included LHC limits. Moreover, the procedure shows whether best-fit points in the global fits remain viable in the light of the LHC constraints.

Fig. 6.3 shows the impact of the ATLAS null searches for SUSY in the 0-lepton and 3-lepton channels, and of the CMS measurements of the Higgs boson properties. Bins that are almost unaffected by the LHC constraints (impact $< 1\sigma$) are shown in cyan, bins that are disfavoured with a significance $> 1\sigma$ and $< 4\sigma$ level are shown in pink, and bins that are ruled out by the LHC (impact $> 4\sigma$) are displayed in grey. Note that only bins are shown that were included in the 99 % CL region before post-processing the mini-chains with the LHC constraints.

The impact of the LHC SUSY and Higgs searches in the plane of neutralino mass vs. spin-independent scattering cross-section is shown in the right-hand panels of fig. 6.3. The main impact of the LHC in this plane is to rule out points at low/intermediate neutralino masses that were previously strongly favoured, mainly as a consequence of the 0-lepton analysis. Therefore, for small $m_{\tilde{\chi}_1^0} \lesssim 300\,\mathrm{GeV}$ the LHC is extremely powerful, ruling out cross-sections orders of magnitudes below the reach of present and future direct detection experiments. For the analysis excluding the $g-2$ constraint, a much smaller fraction of points is affected by the LHC, and several points at small $m_{\tilde{\chi}_1^0}$ are still allowed. This is largely a result of the 0-lepton search having less of an impact on the analysis excluding $g-2$ (as very small squark masses are disfavoured for this analysis). Note that for $m_{\tilde{\chi}_1^0} \gtrsim 500\,\mathrm{GeV}$ the pMSSM parameter space is largely unaffected by constraints from LHC SUSY searches, but can be constrained by precise measurements of the Higgs production cross-sections.

6.6 Conclusions

This chapter presents results of global fits of a phenomenological Minimal Supersymmetric Standard Model with 15 free parameters, including all available accelerator constraints, as well as constraints from cosmology and direct detection experiments. In particular, the impact of the LHC results on the MSSM-15 is highlighted.

Most of the input parameters remain almost unconstrained by current experimental results. However, relatively stringent constraints are placed on the parameters related to the dark matter phenomenology, M_1, M_2 and μ, which are significantly affected by the relic density constraint, direct detection data, and several of the flavour observables, leading to a preference for small values of these quantities.

In all considered cases, the profile likelihood function for the mass of the neutralino LSP peaks at very small values $m_{\tilde{\chi}_1^0} \lesssim 100\,\mathrm{GeV}$. For the case excluding the $g-2$ constraint, the profile likelihood for the neutralino mass extends to significantly larger values, pushing the maximum value from 1.5 TeV to about 3 TeV. The profile likelihood functions for the squark and gluino masses are almost flat within the investigated parameter ranges.

Direct detection constraints are found to be complementary to accelerator searches. Whereas upcoming experiments will allow to probe high neutralino scattering cross-sections, the very long tails in the parameter space extending to extraordinarily small cross-section values further strengthen the case for a combined analysis of astro-particle and accelerator data. The current best-fit point, however, is within reach of the next generation of multi-ton scale direct detection experiments, exhibiting a spin-independent cross-section of 2.3×10^{-10} pb.

LHC SUSY searches, which provide stringent constraints in regions of the parameter space corresponding to very low values of $\sigma^{\mathrm{SI}}_{\tilde{\chi}_1^0-p}$ that are not accessible with astro-particle physics experiments in the foreseeable future, have a strong impact on the result. Constraints on the Higgs signal strengths in the various decay channels significantly impact the MSSM-15.

CHAPTER SEVEN

Combining analyses

STRONGLY PRODUCED SUPERSYMMETRY is not only searched for in channels without leptons. Analyses can rely on b jets or τ leptons, use different discriminating variables, or require a different number of electrons and muons. In the case where these analyses use non-overlapping datasets, they can be combined. The aim then is to achieve a better discovery or exclusion sensitivity: in this case, stronger limits on the masses of sparticles in MSUGRA/CMSSM and in simplified models.

This chapter presents a combination of searches for squarks and gluinos in final states containing jets; missing transverse energy; and no isolated electrons and muons, or at least one isolated electron or muon using 20 fb^{-1} of proton–proton collision data at $\sqrt{s} = 8$ TeV recorded by ATLAS in 2012. The work has been performed together with J. Lorenz and will be part of the official ATLAS LHC Run I summary paper [315].

7.1 Overview

The analyses combined in this chapter all select events with jets and missing transverse energy. In total, three analyses are used. The 0-lepton analysis, described in chapter 5, selects events without electrons or muons. Two 1-lepton analyses are also used: one selecting one *soft* lepton ($p_{\mathrm{T}} < 25$ GeV), the other one *hard* lepton ($p_{\mathrm{T}} > 25$ GeV).

The combination of these analyses consists, on a conceptual level, of creating a combined likelihood as the product of the individual likelihoods. Common nuisance parameters between the analyses must be identified and care must be taken that only one term constraining them is present.

Combining the analyses proceeds in two steps: first the analyses requiring at least one lepton are combined. In a subsequent step, the 0-lepton analysis is added. The motivation for following that procedure is a practical one: the channels selecting leptons are already combined and published in a dedicated paper [316]. Their combination has been performed using a similar method as described here.

The combined result is interpreted in MSUGRA/CMSSM and in several simplified models.

Table 7.1 · Simplified models used in the analyses. The parameter x is given by $x = \frac{m_{\tilde{\chi}_1^\pm} - m_{\tilde{\chi}_1^0}}{m_{\tilde{q},\tilde{g}} - m_{\tilde{\chi}_1^0}}$.

Grid	Main parameters	Main process	Final state
Squark pair decay via $\tilde{\chi}_1^\pm$	$m_{\tilde{q}}, m_{\tilde{\chi}_1^0}, m_{\tilde{\chi}_1^\pm}$ ($m_{\tilde{\chi}_1^0} = 60$ GeV or $x = 1/2$)	$\tilde{q} \to q\tilde{\chi}_1^\pm$, $\tilde{\chi}_1^\pm \to W\tilde{\chi}_1^0$	$qqWW\tilde{\chi}_1^0\tilde{\chi}_1^0$
Gluino pair decay via $\tilde{\chi}_1^\pm$	$m_{\tilde{g}}, m_{\tilde{\chi}_1^0}, m_{\tilde{\chi}_1^\pm}$ ($m_{\tilde{\chi}_1^0} = 60$ GeV or $x = 1/2$)	$\tilde{g} \to qq\tilde{\chi}_1^\pm$, $\tilde{\chi}_1^\pm \to W\tilde{\chi}_1^0$	$qqqqWW\tilde{\chi}_1^0\tilde{\chi}_1^0$
Squark pair decay via $\tilde{\chi}_1^\pm\tilde{\chi}_2^0$	$m_{\tilde{q}}, m_{\tilde{\chi}_1^0}$; $m_{\tilde{\chi}_1^\pm} = (m_{\tilde{q}} + m_{\tilde{\chi}_1^0})/2$; $m_{\tilde{\chi}_2^0} = (m_{\tilde{\chi}_1^\pm} + m_{\tilde{\chi}_1^0})/2$	$\tilde{q} \to q\tilde{\chi}_1^\pm$, $\tilde{\chi}_1^\pm \to W\tilde{\chi}_2^0$, $\tilde{\chi}_2^0 \to Z\tilde{\chi}_1^0$	$qqWWZZ\tilde{\chi}_1^0\tilde{\chi}_1^0$
Gluino pair decay via $\tilde{\chi}_1^\pm\tilde{\chi}_2^0$	$m_{\tilde{g}}, m_{\tilde{\chi}_1^0}$; $m_{\tilde{\chi}_1^\pm} = (m_{\tilde{g}} + m_{\tilde{\chi}_1^0})/2$; $m_{\tilde{\chi}_2^0} = (m_{\tilde{\chi}_1^\pm} + m_{\tilde{\chi}_1^0})/2$	$\tilde{g} \to qq\tilde{\chi}_1^\pm$, $\tilde{\chi}_1^\pm \to W\tilde{\chi}_2^0$, $\tilde{\chi}_2^0 \to Z\tilde{\chi}_1^0$	$qqqqWWZZ\tilde{\chi}_1^0\tilde{\chi}_1^0$

7.2 Signal models

The simplified models considered in these analyses are summarised in table 7.1. The result of the analysis is also interpreted in the MSUGRA/CMSSM grid of chapter 5. In all simplified models, the lightest SUSY particle is assumed to be the lightest neutralino $\tilde{\chi}_1^0$. It is stable, resulting in large $E_{\mathrm{T}}^{\mathrm{miss}}$ in the final state. These signal events are generated with up to one additional parton in the matrix element, using MadGraph 5 interfaced to PYTHIA 6.426, in order to ensure an accurate treatment of initial-state radiation (ISR).

7.2.1 Sparticle-pair production with one-step decay

This one-step intermediate decay simplified scenario assumes that a pair produced gluino (squark) decays exclusively via a $\tilde{\chi}_1^\pm$ and two (one) quarks, where the chargino decays exclusively to the LSP and a W boson. The final state contains four (two) light quarks, two W bosons and two neutralinos in the case of $\tilde{g}\tilde{g}$ ($\tilde{q}\tilde{q}$) production.

Two types of mass spectra have been considered. In the first, the intermediate chargino mass is exactly between the gluino (squark) mass and the LSP mass. The relative mass splitting $x = (m_{\tilde{\chi}_1^\pm} - m_{\tilde{\chi}_1^0})/(m_{\tilde{g}/\tilde{q}} - m_{\tilde{\chi}_1^0})$ is $x = 1/2$ for this spectrum.

The second scenario sets the $\tilde{\chi}_1^0$ mass constant at 60 GeV, but varies the gluino mass and the relative mass splitting x. A branching ratio of 100 % is assumed for $\tilde{q} \to q\tilde{\chi}_1^\pm \to qW\tilde{\chi}_1^0$ and $\tilde{g} \to q\bar{q}\tilde{\chi}_1^\pm \to q\bar{q}W\tilde{\chi}_1^0$ decays and all other sparticles are decoupled.

Table 7.2 · Signal region definitions for the analyses with leptons. Kinematic variables ($p_{\mathrm{T}}(j_i)$, $E_{\mathrm{T}}^{\mathrm{miss}}$, m_{T}, m_{eff}) are given in GeV. A dash indicates no selection is made.

Hard 1-lepton	N_ℓ	N_{jets}	$p_{\mathrm{T}}(j_i)$	$N_{b\text{-jets}}$	$E_{\mathrm{T}}^{\mathrm{miss}}$	m_{T}	m_{eff}
SR1L3JH	1	≥ 3	$> 80, 80, 30$, $p_{\mathrm{T}}(j_5) < 40$	–	> 300	> 150	> 800
SR1L5JH	1	≥ 5	$> 80, 50, 40, 40, 40$, $p_{\mathrm{T}}(j_6) < 40$	–	> 300	> 150	> 800
SR1L6JH	1	≥ 6	$> 80, 50, 40, 40, 40, 40$	–	> 250	> 150	> 600
Soft 1-lepton	N_ℓ	N_{jets}	$p_{\mathrm{T}}(j_i)$	$N_{b\text{-jets}}$	$E_{\mathrm{T}}^{\mathrm{miss}}$	m_{T}	m_{eff}
SR1L3JS	1	3, 4	$> 180, 25, 25(, 25)$	–	> 400	> 100	–
SR1L5JS	1	≥ 5	$> 180, 25, 25, 25, 25$	–	> 300	> 100	–
SR1L3JinclS	1	≥ 3	$> 130, 100, 25$	0	> 180	> 120	–

7.2.2 Sparticle-pair production with two-step decay

These simplified models consist of gluino (squark) decaying though two intermediate states to the LSP. The two-step decay chain considered is $\tilde{g} \to q\bar{q}\tilde{\chi}_1^\pm$ (or $\tilde{q} \to q\tilde{\chi}_1^\pm$) with $\tilde{\chi}_1^\pm \to W\tilde{\chi}_2^0$ and $\tilde{\chi}_2^0 \to Z\tilde{\chi}_1^0$.

The final state contains two or four light jets, two W bosons and two Z bosons. The masses of the intermediate sparticles are set such that the $\tilde{\chi}_1^\pm$ mass is exactly between the gluino (or squark) and the LSP masses and that the $\tilde{\chi}_2^0$ mass is exactly between the $\tilde{\chi}_1^\pm$ and the LSP masses.

The mass hierarchy presented in these simplified models, $m(\tilde{\chi}_1^\pm) > m(\tilde{\chi}_2^0) > m(\tilde{\chi}_1^0)$, is not normally realised in the MSSM. There, the second lightest neutralino is nearly degenerate with the lightest chargino (bino or higgsino LSP case) or has larger mass (wino LSP case). However, the cascade $\tilde{g} \to \tilde{W} \to \tilde{B} \to \tilde{S}$ (a superpartner of the NMSSM singlet) is common in next-to-MSSM (NMSSM) models [92], which is one of the solutions to alleviate the fine-tuning of a 125 GeV Higgs mass. Moreover, replacing the $\tilde{\chi}_1^\pm$ by a $\tilde{\chi}_2^\pm$ also makes these decays possible in the MSSM while the final state is kept unchanged.

The following mass hierarchy is used:

$$\begin{aligned} m_{\tilde{\chi}_1^\pm} &= m_{\tilde{\chi}_1^0} + 1/2\big(m_{\tilde{g},\tilde{q}} - m_{\tilde{\chi}_1^0}\big), \\ m_{\tilde{\chi}_2^0} &= m_{\tilde{\chi}_1^0} + 1/2\big(m_{\tilde{\chi}_1^\pm} - m_{\tilde{\chi}_1^0}\big) \end{aligned} \tag{7.1}$$

as this parametrisation maximises the difference from the other simplified models considered.[1]

7.3 Event selection

Events are selected using a combined jet+$E_{\mathrm{T}}^{\mathrm{miss}}$ trigger for the 0-lepton analysis, e+$E_{\mathrm{T}}^{\mathrm{miss}}$ and μ+$E_{\mathrm{T}}^{\mathrm{miss}}$ triggers for the hard 1-lepton analysis and an $E_{\mathrm{T}}^{\mathrm{miss}}$ trigger for the soft 1-lepton analysis. All signal regions used are listed in tables 5.3 and 7.2.

[1] Inverting the $\tilde{\chi}_1^\pm$ and $\tilde{\chi}_2^0$ masses in the spectrum would lead to a different final state ($WWWW$) that is not considered.

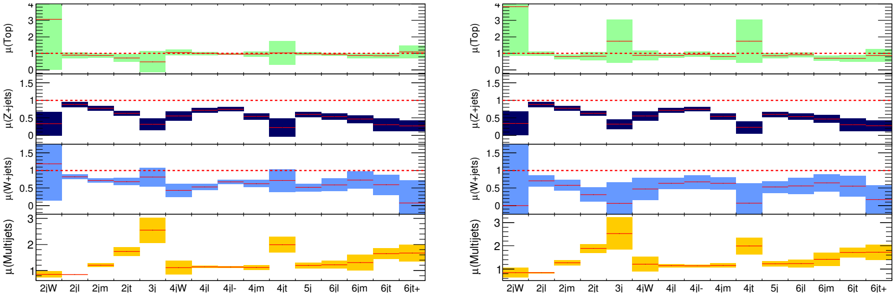

Fig. 7.1 · Summary of the background normalisation parameters in the 0-lepton analysis before (left) and after (right) events overlapping with the 1-lepton analysis were removed from the W and top control regions.

7.3.1 Overlap removal

An overlap exists between the W and top control regions of the hard 1-lepton and the 0-lepton analysis. For every region, the fraction of events in each of the other analysis' regions was estimated. The largest overlap between a pair of regions contributing to the results is approximately 30 %. As the 1-lepton jet definition contains a cut on the jet vertex fraction (4.10), it was decided to conservatively remove any of these overlapping events from the 0-lepton control regions.

Fig. 7.1 shows the background normalisation parameters in the 0-lepton analysis before and after the overlapping events were removed. Fig. 7.2 shows the effect on the exclusion limits for the one-step decay models for the 0-lepton analysis. Removing the overlapping events has a large impact on the statistical error for the W background in certain regions, but the limits are largely unaffected. The combined limits are thus produced with overlapping events removed.

The signal region for the soft 1-lepton analysis selects electrons and muons with $p_{\mathrm{T}} < 10\,\mathrm{GeV}$ that are not identified as leptons in the 0-lepton analysis. This overlap has been investigated: none of the events with such soft leptons would pass the 0-lepton signal region requirements.

7.4 Technical setup

For the various analyses used in this combination hypothesis tests are performed and limits are calculated using HistFitter [264], as discussed for the 0-lepton analysis in chapter 5. The combination of analyses is made by combining their RooFit workspaces[1] and correlating shared parameters in the likelihoods, through the `CombinationTool` ATLAS software package.

For the 0-lepton analysis the signal regions overlap. In the combination the best expected signal region (based on $\mathrm{CL_S}$) is used.

7.4.1 Systematic uncertainties

The correlated parameters in the fit are the following:

[1] For the purpose of this chapter, it suffices to know a workspace is a fully self-contained, persistable RooFit container that entirely describes, among others, the likelihood function used in the analysis.

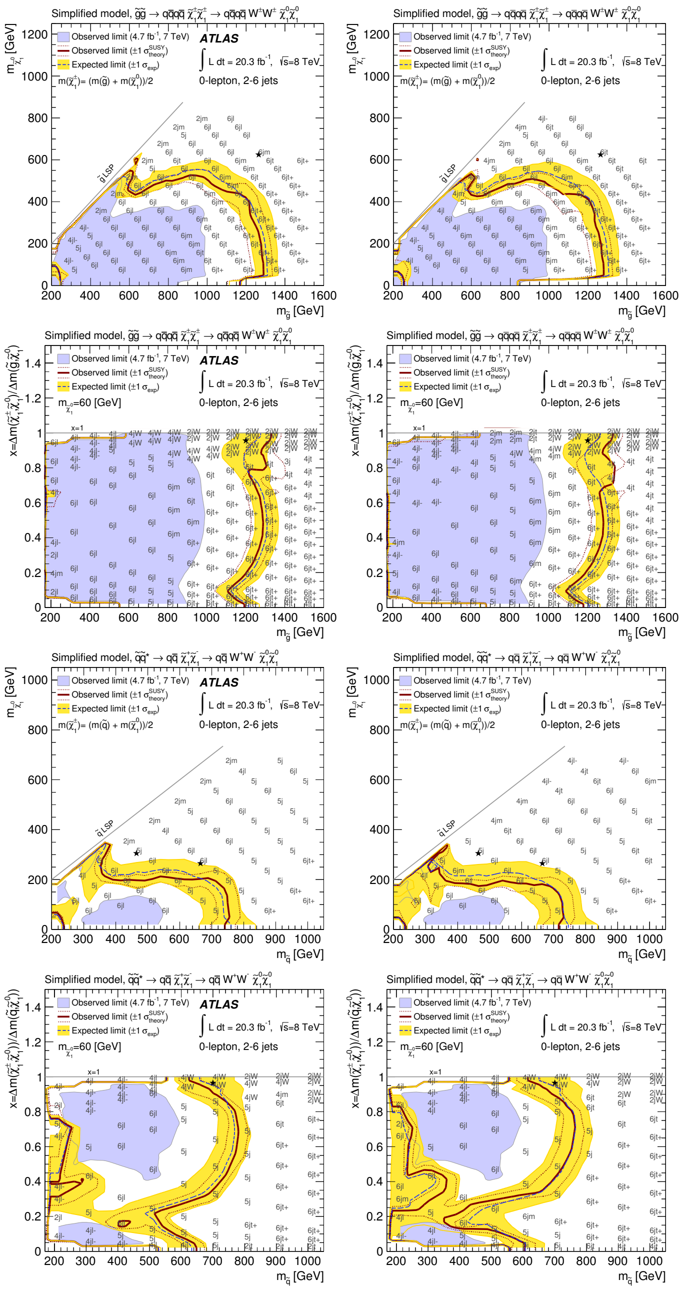

Fig. 7.2 · Exclusion curves for the 0-lepton analysis for the one-step models before (left) and after (right) overlapping events in the W and top control regions were removed.

- signal strength;
- uncertainty on signal cross-section;
- luminosity;
- jet energy resolution;
- b tagging (all 3 parameters);
- $E_{\mathrm{T}}^{\mathrm{miss}}$ and pile-up uncertainties (all 3 parameters).

The following parameters could not be correlated for various reasons:

- normalisations for backgrounds;
- cross-section uncertainties for backgrounds;
- jet energy scale uncertainties,

due to the fact that different Monte Carlo generators have been used in generating the background samples for the individual analyses. In addition, the 0-lepton analysis uses a simple one-parameter jet energy scale uncertainty, which cannot be correlated with the individual uncertainties used in the other analyses.

The validation of the correlation is discussed in the next section.

7.5 Results

The result of the combination is interpreted in MSUGRA/CMSSM and in four simplified models.

7.5.1 Combination in MSUGRA/CMSSM

The limit obtained from a combination of the 0-lepton and the 1-lepton analyses for MSUGRA/CMSSM is shown in fig. 7.3. For $m_0 \lesssim 1400$ GeV, the 0-lepton analysis perfoms close to optimal, as expected from the predominant decay mechanism in this region of phase space. For high m_0, the 1-lepton channel performs better. A further improvement could be gained if an analysis requiring exactly one b jet existed. Notably, the combination improves the limits around the region where the two individual limits cross.

7.5.2 Combination in one-step simplified models

The limits obtained from a combination of the 0-lepton and 1-lepton analyses are shown for the one-step simplified models in fig. 7.4. The obtained limits improve both the limits of the 0-lepton and of the soft/hard 1-lepton analyses significantly, reaching to higher LSP and higher squark/gluino masses. The combined analysis is also more sensitive to points closer to the LSP-gluino/squark mass diagonal in comparison to the individual analyses.

7.5.3 Combination in two-step simplified models

The limits obtained from a combination of the 0-lepton and 1-lepton analyses are shown for the two-step simplified models in fig. 7.5. The obtained limit for gluinos is slightly better than the indiviual results at intermediate gluino masses. In the squark-production scenario, the gap between

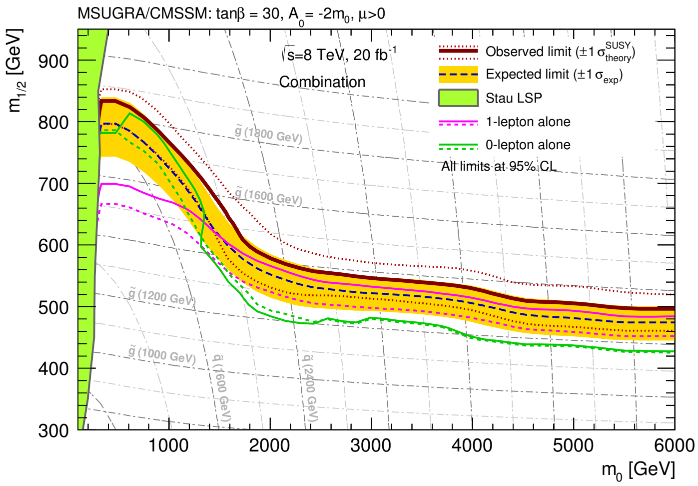

Fig. 7.3 · Observed and expected exclusion limits at 95 % CL for 8 TeV analysis in the $(m_0, m_{1/2})$ plane for the MSUGRA/CMSSM model with the remaining parameters set to $\tan(\beta) = 30$, $A_0 = -2 \times m_0$ and $\mu > 0$. The individual limits by the 0-lepton analysis and the soft/hard 1-lepton analysis are overlaid in green and magenta, respectively.

the two analyses is recovered by the combination. However, the overlap removal procedure diminishes the power of signal region SR4jl-, leading to degraded performance of the 0-lepton analysis along the diagonal. As a result, the combination does slightly worse in this region. The limit can be recovered by performing a combination of the 0-lepton and 3-lepton analyses and a combination of the 1-lepton and the 3-lepton analyses, and then using the best expected limit for each model point considered.

7.6 Validation

The result of the combination is validated by checking that:

1. the combination does not add additional profiling or shifts to any of the nuisance parameters, which could result in an artificial increase in the sensitivity w.r.t. the separate analyses due to reduced uncertainties;
2. in the event an increase in the sensitivity is observed, a *minimal combination* is performed, where only the signal strength and cross-section uncertainty are correlated, in order to ensure the increase is not primarily due to reduced uncertainties;
3. no large correlations between uncertainties are observed: the correlation matrices should be similar to those of the individual analyses.

No additional correlations between parameters with respect to the analyses have been observed. Studies of the fit parameters showed that only the jet energy resolution parameter changes between the individual analyses and the combination. In order to check the shift does not lead to an artificial increase in the expected sensitivity, a combination without it was made.

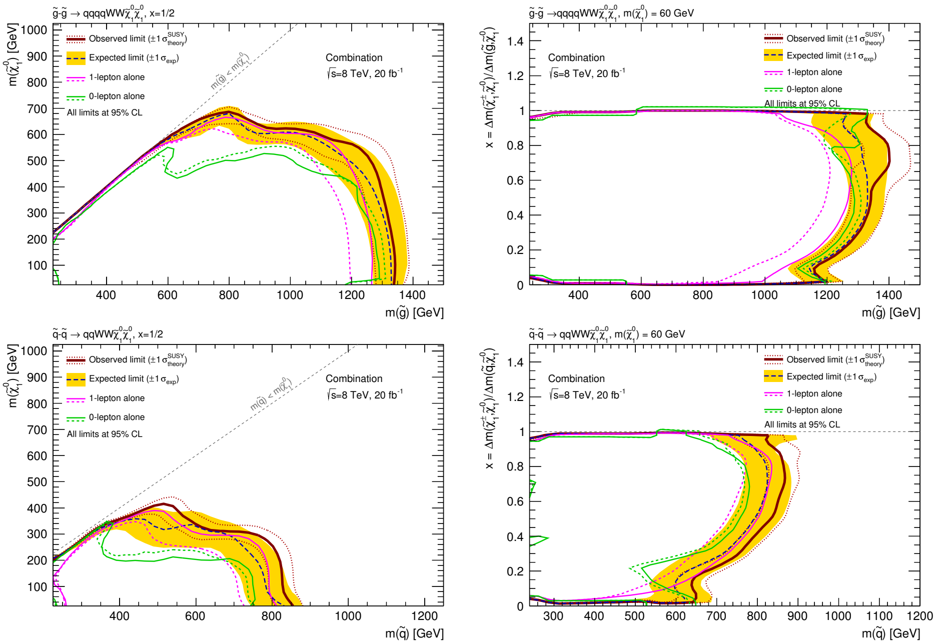

Fig. 7.4 · Observed and expected limits in the gluino (top) and squark (bottom) one-step simplified model for $x = 1/2$ (left) and $m_{\tilde{\chi}_1^0} = 60\,\text{GeV}$ (right) as obtained from the full statistical combination of the soft/hard 1-lepton and 0-lepton analyses. The individual limits by the 0-lepton analysis and the soft/hard 1-lepton analysis are overlaid in green and magenta, respectively.

Fig. 7.6 shows the combined exclusion contour in the one-step interpretation with a minimal set of correlated parameters (only signal strength, luminosity and cross-section uncertainty). Fig. 7.7 shows the combination without the jet energy resolution parameter correlated between the analyses. All results are similar to the full combination presented above. No excessive profiling of nuisance parameters in the combination occurs.

7.7 Conclusion

This chapter presented a combination of several analyses. The results of this combination have been interpreted in several models, all of which show improvement due to the combination. Future combinations could be made even more sensitive to these models by coordinating the choice of Monte Carlo generators and the implementation of nuisance parameters in the individual likelihoods better.

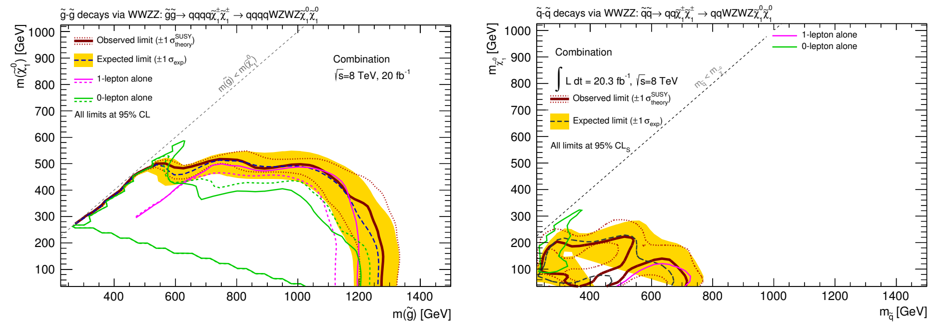

Fig. 7.5 · Observed and expected limits in the gluino (left) and squark (right) two-step simplified model as obtained from the full statistical combination of the soft/hard 1-lepton and 0-lepton analyses. The individual limits by the 0-lepton analysis and the soft/hard 1-lepton analysis are overlaid in green and magenta, respectively.

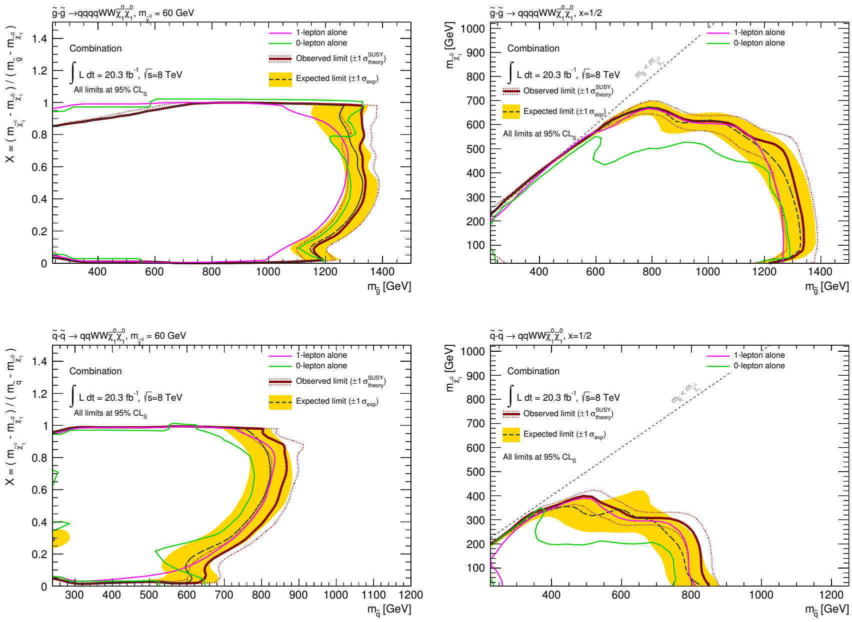

Fig. 7.6 · Combined exclusion limits in a minimal setup for the one-step decay models.

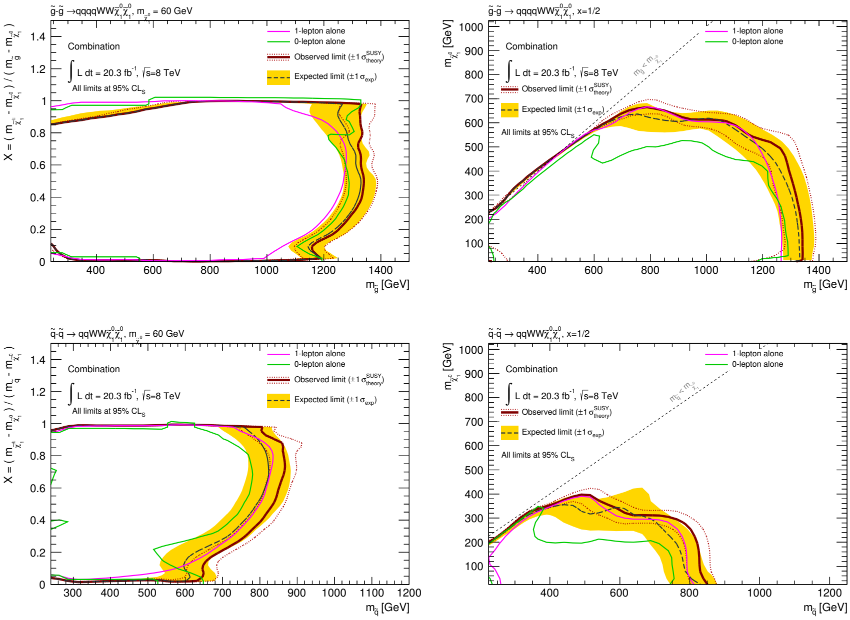

Fig. 7.7 · Combined exclusion limits in a setup without a correlated jet energy resolution parameter for the one-step decay models.

CHAPTER EIGHT

Prospects for SUSY at 14 TeV

THE DISCOVERY, OR exclusion, of weak-scale supersymmetry is one of the highest priorities in the LHC physics programme. Strongly produced SUSY particles are expected to have the highest production cross-section of all SUSY processes, provided they are light enough to be produced. The energy range accessible at the LHC and the future high-luminosity LHC (HL-LHC) can not be probed at any other existing facility.

In this chapter, the discovery and exclusion mass ranges for simplified models of gluino- and squark-pair production are investigated. In these models, gluinos are assumed to always decay directly into two quarks and the lightest supersymmetrical particle (LSP), which is the neutralino $\tilde{\chi}_1^0$. Squarks are also assumed to always decay directly; in this case, into a quark and the LSP. In both scenarios, signal events are characterised by many jets, large $E_{\mathrm{T}}^{\mathrm{miss}}$ and no leptons. An analysis building on the search described in chapter 5 is presented, which has been optimised for a maximum discovery potential.

The results presented in this chapter have been published in [317]. The analysis has been performed together with I. Deigaard.

8.1 LHC upgrades and the high-luminosity LHC

In 2012, the LHC delivered 22.8 fb^{-1} of proton–proton collisions at a centre-of-mass-energy of 8 TeV. During the shutdown following the end of data-taking (LS1), the machine will be consolidated to be able to operate at a centre-of-mass-energy of 13 TeV, with the possibility of future 14 TeV collisions.

8.1.1 Motivation

The planned large luminosity at the HL-LHC greatly increases the energy range at which various processes can be investigated. The mechanism of electroweak symmetry breaking can be studied in high energy boson–boson scattering, and signatures for physics beyond the Standard Model such as supersymmetry or extra dimensions can be searched for in the multi-TeV region. Such signatures would include, among others, high mass gauge bosons, more complex SUSY cascade decays and resonances in $t\bar{t}$-pairs.

Significant improvements in measurements involving the Higgs boson can also be made. Rare channels such as $H \to \mu\mu$ and $H \to Z\gamma$ can be studied in detail, and greater precision in $H \to \gamma\gamma$ in both the direct production and associated production with a top-quark pair ($t\bar{t}H$)

can be achieved. Finally, the Higgs self-coupling can be measured, in new channels such as $HH \rightarrow \tau\tau bb$ and $HH \rightarrow \gamma\gamma bb$.

8.1.2 Upgrades

During Run II, planned to last until the end of 2017, ATLAS is expected to record $\sim 100\,\text{fb}^{-1}$ of data. Following that data-taking period, the LHC facility will shut down (LS2) and the injection chain will be modified to allow for an increase of the instantaneous luminosities up to $2 \times 10^{34}\,\text{cm}^{-2}\,\text{s}^{-1}$, twice the design value. After the planned upgrades, the average number of pile-up events per bunch crossing is expected to be $\langle\mu\rangle \sim 60$. The total amount of data expected to be collected up to 2022 is approximately $300\,\text{fb}^{-1}$ [318].

Around 2022, the LHC itself is foreseen to be modified during another long shutdown (LS3) in order to achieve instantaneous luminosities of $5 \times 10^{34}\,\text{cm}^{-2}\,\text{s}^{-1}$. This *high-luminosity LHC* (HL-LHC) is expected to deliver an average number of pile-up events per bunch crossing of $\langle\mu\rangle \sim 140$. The size of the dataset collected from 2025 until 2032 is expected to be approximately $3000\,\text{fb}^{-1}$ [319, 320].

The pile-up values used have been obtained using the total inelastic proton–proton cross section [321]. With 2808 bunches, a cross-section of $81 \pm 3\,\text{mb}$, extrapolated from results at $\sqrt{s} = 7\,\text{TeV}$ [322], and the HL-LHC's design luminosity of $5 \times 10^{34}\,\text{cm}^{-2}\,\text{s}^{-1}$, the resulting pile-up is calculated using (3.4) to be 128 ± 5. Assuming the relative spread in the luminosity is similar as in 2012, where it was 8 %, this implies that 12 % of the bunch crossings have $\mu > 140$. ATLAS and CMS agreed to use $\langle\mu\rangle = 140$ in studies for the HL-LHC.

Due to the increased pile-up, the ability to measure and reconstruct quantities such as missing transverse momentum will be adversely affected. Expected event numbers in this study will not simply scale with the integrated luminosity; instead, they are recalculated for both pile-up conditions.

8.2 Backgrounds

The backgrounds taken into account in this study are W+jets, Z+jets, $t\bar{t}$, and diboson. The W+jets, Z+jets, and $t\bar{t}$ processes are estimated from Monte Carlo simulations. The diboson background is assumed to be 10 % of the total background and the QCD background is assumed to be negligible; both were the case in the 0-lepton analysis [213] described in chapter 5.

SHERPA 1.4.1 [148] is used to simulate the top pair, $W^{(*)}$+jets, and $Z^{(*)}$+jets processes. The SHERPA $W^{(*)}$+jets and $Z^{(*)}$+jets processes were generated with massive b and c quarks. The generator MadGraph-5.0 [323] is used for the production of $t\bar{t}V$ ($V = W, Z$) events. The top-quark pair-production contribution is normalised to approximate next-to-next-to-leading-order calculations (NNLO) [324]. The NNLO FEWZ [325, 326] cross-sections are used for normalisation of the inclusive W+light-flavour jets and Z+light-flavour jets. The CTEQ6L1 [59] parton distribution functions (PDFS) are used with MadGraph. With SHERPA and MC@NLO, the CT10 [225] PDFS are used. The signal MC samples are produced with Herwig++ 2.5.2 [149] for squark-pair production and MadGraph 5.0 for gluino-pair production.

Table 8.1 · Monte Carlo samples used to estimate the Standard Model background.

DSID	Dataset Name	σ [pb]	ϵ	N_{gen}	$\mathcal{L}_{int}$ [fb^{-1}]
117801	Sherpa_CT10_TtbarLeptTaulept	517.8	0.03058	12530000	791.32
117802	Sherpa_CT10_TtbarTauleptTaulept	517.8	0.00271	1320000	940.68
157534	Sherpa_CT10_WenuPt200	27.742	1.0	30780000	1109.51
157535	Sherpa_CT10_WmunuPt200	27.742	1.0	30800000	1110.23
157536	Sherpa_CT10_WtaunuPt200	27.771	1.0	30300000	1091.07
157539	Sherpa_CT10_ZnunuPt280	5.6657	1.0	18692000	3299.15
157728	Sherpa_CT10_TtbarLeptLept_MET120	517.8	0.0116	13189400	2195.86
157729	Sherpa_CT10_TtbarLeptHad_MET160	517.8	0.0179	9582000	1033.81
157730	Sherpa_CT10_TtbarLeptTauhad_MET120	517.8	0.00815	5720000	1355.43
157731	Sherpa_CT10_TtbarTauleptHad_MET120	517.8	0.0155	10226000	1274.13
157732	Sherpa_CT10_TtbarTauleptTauhadUpTo3Jets	517.8	0.0099	10450000	2038.54
157733	Sherpa_CT10_TtbarHadTauhad_MET160	517.8	0.00936	5010000	1033.71
157734	Sherpa_CT10_TtbarTauhadTauhadUpTo3Jets	517.8	0.00885	10320000	2252.03
119353	MadGraphPythia_AUET2BCTEQ6L1_ttbarW	0.315	1.0	3500000	11100
119354	MadGraphPythia_AUET2BCTEQ6L1_ttbarWj	0.456	1.0	3480000	7674
119355	MadGraphPythia_AUET2BCTEQ6L1_ttbarZ	0.358	1.0	3500000	9773
119356	MadGraphPythia_AUET2BCTEQ6L1_ttbarZj	0.763	1.0	3500000	4586

All used background samples are listed in table 8.1 together with their cross-section, number of generated events and the corresponding integrated luminosity. As a cross check on the simulation at 14 TeV, the obtained background distributions have been compared to the ones measured at Run I. Using the 8 TeV cross-sections and $\mathcal{L} = 20.3\,\text{fb}^{-1}$, the resulting distributions agreed well with data.

8.3 Cross-sections

With higher collision energy, the cross-section for strong production of sparticles increases faster than the cross-section for the background processes. In fig. 8.1, the 8 TeV and the 14 TeV production cross-sections as a function of the relevant mass are shown. The cross-section increases 30 to 100 times over the range between 1 TeV and 3 TeV with the increase in collision energy from 8 TeV to 14 TeV.

In the case of gluino-pair production, the production cross-section is calculated in the decoupling limit. The cross-section is not altered much if squarks are as light as a few TeV; t-channel processes barely contribute to the total cross-section.

For squark-pair production two scenarios are studied. In the first scenario, the squarks are completely decoupled from the gluino. In the second scenario, the gluino mass is set to $m_{\tilde{g}} = 4.5\,\text{TeV}$, which is above the expected HL-LHC exclusion reach. Here, t-channel gluino exchange processes, which are otherwise largely suppressed, do contribute to the total cross-section: the production cross-section for heavy squarks is largely enhanced. From fig. 8.1, it is clear that the production of squark pairs, rather than squark–anti-squark production, is the dominant mechanism at 14 TeV. The difference in selection efficiencies for these scenarios is found to be less than 30 % for the relevant signal regions.

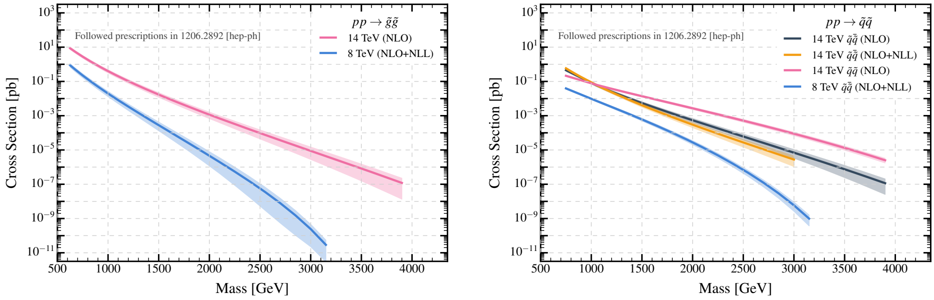

Fig. 8.1 · Cross-sections for gluino-pair production (left) at $\sqrt{s} = 8$ TeV (blue) and $\sqrt{s} = 14$ TeV (pink) and cross-sections for squark-pair production (right) at $\sqrt{s} = 8$ TeV with decoupled gluinos (blue) and $\sqrt{s} = 14$ TeV, for both decoupled gluinos (orange) and for $m_{\tilde{g}} = 4.5$ TeV (grey, pink).

The cross-section calculations at 14 TeV for non-decoupled gluinos are NLO calculations rather than NLO+NLL calculations: no NLL corrections for this case were available at the time of the analysis. The results for the case of decoupled gluinos are obtained using NLO+NLL cross-sections.

8.4 Estimated detector performance

Lacking a simulation of the ATLAS detector after LS2 and LS3, events are reconstructed directly from truth-level simulated events. Monte Carlo truth events are smeared according to (presumed) detector parameters [327, 328].

8.4.1 Jets

Additional interactions in each event at 14 TeV make the jet performance dependent on the average number of interactions $\langle\mu\rangle$. The jet performance has been estimated from Pythia dijet Monte Carlo samples at varying pile-up settings. The resolution is described by three parameters – noise (N), stochastic (S) and constant (C) terms – and is given by

$$\sigma_{p_\mathrm{T}}/p_\mathrm{T} = \sqrt{\frac{N^2}{p_\mathrm{T}^2} + \frac{S^2}{p_\mathrm{T}} + C^2}, \tag{8.1}$$

with the noise term given by the η-dependent linear function

$$N = a(\eta) + b(\eta) \cdot \mu. \tag{8.2}$$

The full parametrisation for $a(\eta)$ and $b(\eta)$ in the various bins can be found in [328].

8.4.2 Electrons

Current electron resolution functions are not expected to be affected significantly by large-pile-up conditions. The energy resolution is given in two bins in $|\eta|$ for E in GeV [327]:

$$\sigma/E = 0.3 \oplus 0.10 \times \sqrt{E} \oplus 0.1E \qquad \text{for } |\eta| < 1.4, \tag{8.3a}$$

$$\sigma/E = 0.3 \oplus 0.15 \times \sqrt{E} \oplus 0.15E \qquad \text{for } 1.4 < |\eta| < 2.47. \tag{8.3b}$$

8.4.3 Muons

The muon trigger efficiency is expected to be close to or above the single-muon efficiency measured in 2012. The momentum resolution has been derived separately for the Inner Detector and the Muon Spectrometer:

$$\begin{aligned} \sigma_{\mathrm{ID}}/p_{\mathrm{T}} &= \sqrt{a_1^2 + (a_2 \times p_{\mathrm{T}})^2}, \\ \sigma_{\mathrm{MS}}/p_{\mathrm{T}} &= \sqrt{\left(\frac{b_0}{p_{\mathrm{T}}}\right)^2 + b_1^2 + (b_2 \times p_{\mathrm{T}})^2}, \end{aligned} \tag{8.4}$$

where the parameters a_1, a_2, b_0, b_1 and b_2 have been derived from a parametrisation of results published in the ATLAS Phase-II Letter of Intent [320]; they depend on $|\eta|$ and are given in [328].

These resolution functions are subsequently combined into one resolution as follows:

$$\sigma_{\mathrm{CB}} = \frac{\sigma_{\mathrm{ID}} \times \sigma_{\mathrm{MS}}}{\sqrt{\sigma_{\mathrm{ID}}^2 + \sigma_{\mathrm{MS}}^2}}. \tag{8.5}$$

8.4.4 Missing transverse energy

Missing transverse energy in the event is smeared using the *total* missing transverse energy in the event; i.e. including interacting particles. Each smeared component is then given by

$$E_{\mathrm{T}}^{\mathrm{miss}\prime}{}_{x,y} = E_{\mathrm{T}}^{\mathrm{miss}}{}_{x,y} + \mathrm{Normal}\big(0, \sigma(\mu)\big), \tag{8.6}$$

where $\sigma(\mu)$ is the resolution, which depends on the average number of pile-up events. The parametrisation of $\sigma(\mu)$ has been derived from $Z' \to t\bar{t}$ samples, minimum bias samples and dijet samples, all simulated at $\sqrt{s} = 14\,\mathrm{TeV}$ using 25 ns bunch spacing and three different conditions for pile-up: $\langle\mu\rangle = 60,\ 80,\ 140$.

The resolution depends on the total $\sum E_{\mathrm{T}}$, which is given by the real transverse energy from the event, plus additional effects from pile-up. We can thus estimate the pile-up effects as

$$\sum E_{\mathrm{T}}^{\mathrm{PU}} = \sum E_{\mathrm{T}} - \sum E_{\mathrm{T}}^{\mathrm{True}}, \tag{8.7}$$

and estimate the total transverse energy by modelling this term by drawing random numbers from its distribution [328]. The default parametrisation relies on $Z' \to t\bar{t}$ samples. Dedicated variations for each of the three pile-up settings used are available.

Two types of systematic variations have been considered: the uncertainty due to differences in the nature of physics processes, and the uncertainty due to pile-up noise thresholds. The former is estimated by varying the distribution used, the latter by varying the cell noise thresholds in the calorimeter w.r.t. the expected optimum.

The resulting $E_{\mathrm{T}}^{\mathrm{miss}}$ resolution is shown in fig. 8.2.

8.5 Preselection and object selection

Before any smearing is performed at truth level to mimic the detector effects of the upgrade of the ATLAS detector, a preselection is made to save computing time. This preselection consists of

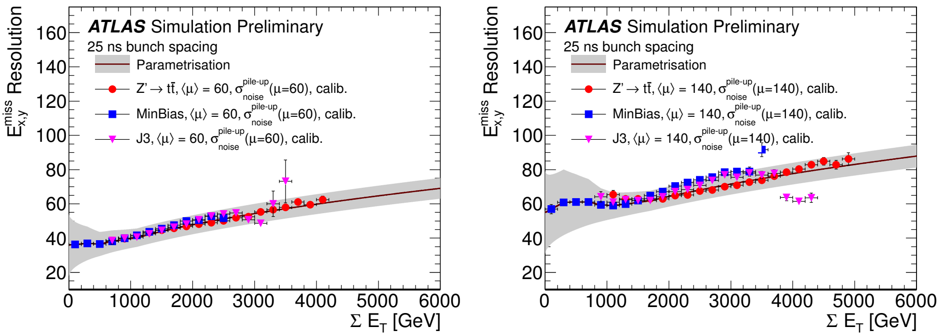

Fig. 8.2 · The $E_{\mathrm{T}}^{\mathrm{miss}}$ resolution as a function of the true transverse energy $\sum E_{\mathrm{T}}$ obtained from different samples for $\langle\mu\rangle = 60$ (left) and $\langle\mu\rangle = 140$ (right), compared with the obtained parametrisation [328]. J3 refers to the dijet sample with a jet p_{T} range of 200–500 GeV.

the following cuts: $E_{\mathrm{T}}^{\mathrm{miss}} > 110$ GeV, for the leading jet $p_{\mathrm{T}} > 90$ GeV and for the sub-leading jet $p_{\mathrm{T}} > 40$ GeV. Also, both jets are required to have $|\eta| < 3.6$.

Truth events not passing these preselection cuts may still pass the final cuts after smearing, especially due to the smearing of $E_{\mathrm{T}}^{\mathrm{miss}}$. The amount of events smeared to high enough $E_{\mathrm{T}}^{\mathrm{miss}}$ and jet p_{T} to pass these cuts has been estimated to be appoximately 1 %.

Jet candidates are reconstructed from objects in truth-level simulated events using an anti-k_t algorithm with a radius parameter of 0.4. These jets are then smeared following the procedure described in §8.4. Jet candidates must have $p_{\mathrm{T}} > 20$ GeV and $|\eta| < 2.8$ after the smearing.

Any electron candidate after smearing is required to have $p_{\mathrm{T}} > 10$ GeV and $|\eta| < 2.47$. Muon candidates must have $p_{\mathrm{T}} > 10$ GeV and $|\eta| < 2.4$. The amount of fake electrons coming from jets is estimated by the probability [327]:

$$\epsilon(p_{\mathrm{T}}) = 0.11 \times \exp(-0.033 \times p_{\mathrm{T}}). \tag{8.8}$$

The missing transverse energy is calculated from the non-interaction particles, such as neutrinos and the lightest SUSY particles.

8.5.1 Overlap removal

After objects are selected, any overlapping objects must be removed. We follow the same procedure as in chapter 5. Leptons and jets may be removed when overlapping with another object based on several criteria.

The overlap criteria are based on the simple geometric distance $\Delta R = \sqrt{(\Delta\phi)^2 + (\Delta\eta)^2}$. They are applied in the following order:

1. an electron and a jet within $\Delta R < 0.2$ are treated as an electron; the 'jet' is ignored;
2. a muon and jet within $\Delta R < 0.4$ are treated as a jet; the muon is ignored;
3. an electron and a jet within $0.2 < \Delta R < 0.4$ are identified as a jet; the electron is ignored.

Table 8.2 · Summary of selection requirements for 300 fb^{-1} and 3000 fb^{-1}. The 2j, 3j and 4jl regions, targeting squark-pair production, have two cuts on m_{eff}. The first is designed for scenarios where the gluino is decoupled, the other for the case in which the gluino mass is 4.5 TeV.

Selection	Channel									
	2jl	2jm	3j	4jl	4jm	4jt	5j	6jl	6jm	6jt
$p_{\text{T}}(j_1)$ [GeV] >	160									
$N_{\text{jets}}(p_{\text{T}} > 60\,\text{GeV}) \geq$	2		3	4			5	6		
$E_{\text{T}}^{\text{miss}}$ [GeV] >	160									
$\Delta\phi(j_i, E_{\text{T}}^{\text{miss}})_{\text{min}}$ [rad] >	0.4 (j_1, j_2, j_3), 0.2 (all $p_{\text{T}} > 40$ GeV jets)									
	$\langle\mu\rangle = 60$, 300 fb^{-1} scenario									
$E_{\text{T}}^{\text{miss}}/m_{\text{eff}}$ >	–	–	0.3	0.40	0.25	–	0.20	0.30	0.15	0.20
$E_{\text{T}}^{\text{miss}}/\sqrt{H_{\text{T}}}$ [GeV$^{1/2}$] >	8	15	–	–	–	10	–	–	–	–
m_{eff} [GeV] >	3600	3100, 4300	3600, 3000	3000, 2200	3200	3400	3000	2800	3400	3400
	$\langle\mu\rangle = 140$, 3000 fb^{-1} scenario									
$E_{\text{T}}^{\text{miss}}/m_{\text{eff}}$ >	–	–	0.3	0.35	0.25	–	0.25	0.25	0.35	0.15
$E_{\text{T}}^{\text{miss}}/\sqrt{H_{\text{T}}}$ [GeV$^{1/2}$] >	8	15	–	–	–	10	–	–	–	–
m_{eff} [GeV] >	4500, 5000	4500, 4900	4000	4000, 3800	4000	4500	4000	3400	3500	5000

8.6 Signal regions

The signal region selection is similar to the selection in [213]. Jets are selected with $p_{\text{T}} > 20$ GeV and $|\eta| < 2.8$. A minimum of two to six high-p_{T} jets is required, with no leptons present in the event. Jets are required to point in a different direction than $E_{\text{T}}^{\text{miss}}$ by requiring $\Delta\phi(\text{jet}, E_{\text{T}}^{\text{miss}})_{\text{min}}$ in order to suppress the multijets background [213]; without it, the assumption that its contribution is negligible no longer holds. Multiple signal regions have been optimised using requirements on the effective mass m_{eff}, $E_{\text{T}}^{\text{miss}}/m_{\text{eff}}$ and $E_{\text{T}}^{\text{miss}}/\sqrt{H_{\text{T}}}$. A summary of the signal regions is shown in table 8.2.

Harder selections on $E_{\text{T}}^{\text{miss}}$ and jet p_{T} would need to be made to satisfy the trigger thresholds for these signal regions. However, the results are expected to be the same due to the hard selections on m_{eff} and $E_{\text{T}}^{\text{miss}}/\sqrt{H_{\text{T}}}$.

Background distributions

Fig. 8.3 shows the m_{eff} distribution for the Standard Model background in several signal regions. Two SUSY signal points for each scenario are superimposed on the background. For squark-pair production, $m_{\tilde{q}} = 1050$ GeV and $m_{\tilde{\chi}_1^0} = 900$ GeV, and $m_{\tilde{q}} = 2250$ GeV and $m_{\tilde{\chi}_1^0} = 1$ GeV are shown. For gluino-pair production, the models shown are $m_{\tilde{g}} = 1950$ GeV and $m_{\tilde{\chi}_1^0} = 1$ GeV, and $m_{\tilde{g}} = 1425$ GeV and $m_{\tilde{\chi}_1^0} = 1400$ GeV. For the compressed scenarios, where the mass difference between the two masses is small, the signal distribution is similar in shape to the background and does not extend beyond the tail of the background at high m_{eff}. Compressed signals are difficult to detect due to this behaviour.

The number of expected events for the irreducible backgrounds and two benchmark signal points for each scenario is shown in tables 8.3 and 8.4. As in the 8 TeV case, the Z+jets background is dominant, with the contribution from the $t\bar{t}$ background increasing with jet multiplicity.

8.7 Interpretation

Limits are set using the significance-like variable Z_N [329], which takes into account the systematic uncertainties on the background. For discovery, $Z_N \geq 5$ is required; for exclusion, the one-sided 95 % confidence level $Z_N \geq 1.64$ is used.[1]

The most important sources of experimental systematic uncertainties are the energy resolution and scale uncertainty of jets, leptons and $E_{\text{T}}^{\text{miss}}$, and the pile-up. A flat systematic uncertainty of 10 % on the estimated sum of all backgrounds is assumed. Theoretical uncertainties on the signal yields due to the choice of renormalisation and factorisation scales and choice of PDF are evaluated following the prescription in [63]. Experimental uncertainties on the signal yields have not been considered.

Fig. 8.4 shows the expected exclusion and discovery contours.

8.7.1 Gluino-pair production

Gluinos can be discovered up to $m_{\tilde{g}} = 2000$ GeV for 300 fb^{-1}, and $m_{\tilde{g}} = 2350$ GeV for the 3000 fb^{-1} luminosity scenario. Depending on the gluino mass, a $\tilde{\chi}_1^0$ with a mass up to 900 GeV (1100 GeV) can be discovered for the 300 fb^{-1} (3000 fb^{-1}) luminosity scenario. Notably, these mass ranges lie outside any current 8 TeV exclusion limits. The theoretical uncertainty on the limit increases with gluino mass and is primarily due to uncertainties in the parton-density functions. For gluinos with a mass of approximately 3 TeV, the uncertainty on the limit reaches 400 GeV.

In the event of an absence of an excess over the Standard Model expectation, gluino masses up to 2350 GeV (2950 GeV) for the 300 fb^{-1} (3000 fb^{-1}) luminosity scenario are expected to be excluded, assuming a massless $\tilde{\chi}_1^0$. Depending on the gluino mass, a $\tilde{\chi}_1^0$ up to 1100 GeV (1500 GeV) can be excluded for the 300 fb^{-1} (3000 fb^{-1}) luminosity scenario. Such exclusion limits would extend well beyond the existing limits already set by ATLAS.

8.7.2 Squark-pair production

If the gluino is decoupled, squarks can be excluded up to a mass of about 2000 GeV for light neutralinos using 3000 fb^{-1} integrated luminosity. The limit is reduced to 1850 GeV if the integrated luminosity is 300 fb^{-1}. Squarks can be discovered up to 1400 GeV with 3000 fb^{-1}.

If the gluino is lighter, the squark reach is increased due to the higher cross-section. For squark-pair production in the case where $m_{\tilde{g}} = 4.5$ TeV, squarks can be discovered up to a mass of 2400 GeV for 300 fb^{-1} and 3100 GeV for 3000 fb^{-1}. Here, the exclusion reach for squarks reaches 3100 GeV for 300 fb^{-1} and 3500 GeV for 3000 fb^{-1} for very light neutralinos.

[1] The use of a dedicated 95 % CL exclusion test has been considered; it yields very similar results.

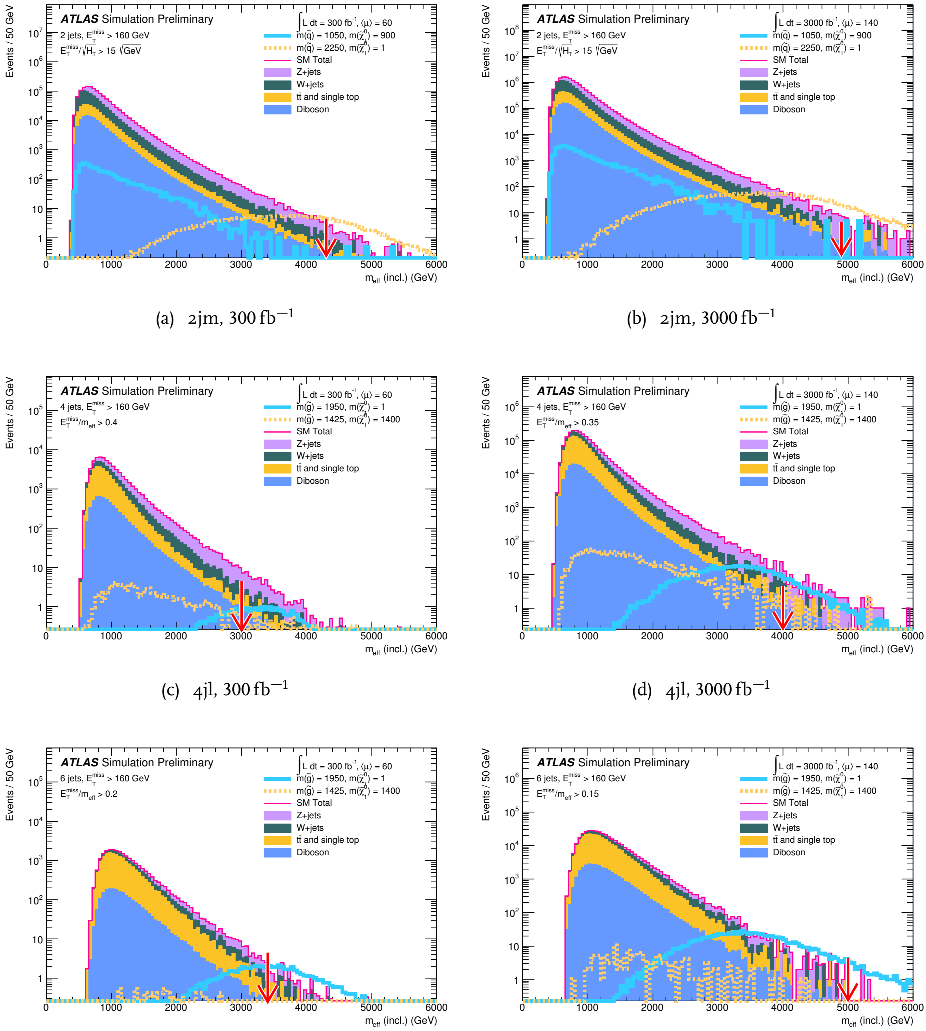

(a) 2jm, 300 fb^{-1} (b) 2jm, 3000 fb^{-1}

(c) 4jl, 300 fb^{-1} (d) 4jl, 3000 fb^{-1}

(e) 6jt, 300 fb^{-1} (f) 6jt, 3000 fb^{-1}

Fig. 8.3 · Distributions in m_{eff} for several benchmark signals models. The squark models (top) are $m_{\tilde{q}} = 1050$ GeV and $m_{\tilde{\chi}_1^0} = 900$ GeV, and $m_{\tilde{q}} = 2250$ GeV and $m_{\tilde{\chi}_1^0} = 1$ GeV. The gluino models (middle, bottom) are $m_{\tilde{g}} = 1950$ GeV and $m_{\tilde{\chi}_1^0} = 1$ GeV, and $m_{\tilde{g}} = 1425$ GeV and $m_{\tilde{\chi}_1^0} = 1400$ GeV. The signal regions shown are 2jm (top), 4jl (middle) and 6jt (bottom) for 300 fb^{-1} (left) and 3000 fb^{-1} (right). The arrows indicate the final cut on m_{eff} for the chosen signal regions.

Table 8.3 · Yields for the main backgrounds and selected signal points simulated with $\langle\mu\rangle = 60$, normalised to $\mathcal{L} = 300\,\mathrm{fb}^{-1}$. The signal samples for squark-pair production are normalised for the scenario with a gluino mass of 4.5 TeV.

Region	SR2jl	SR2jm	SR3j	SR4jl	SR4jm
W+jets	45.0 ± 3.5	2.7 ± 0.9	11.2 ± 1.8	11.8 ± 1.8	25.7 ± 2.7
Z+jets	104.4 ± 3.1	16.9 ± 1.2	43.0 ± 2.0	48.5 ± 2.1	75.9 ± 2.6
$t\bar{t}$	15.7 ± 1.8	1.6 ± 0.5	4.2 ± 0.8	5.1 ± 1.1	10.6 ± 1.5
Diboson	18.4 ± 1.7	2.4 ± 0.5	6.5 ± 0.9	7.3 ± 1.0	12.5 ± 1.3
Total background	183 ± 5	23.6 ± 1.7	64.9 ± 2.9	72.6 ± 3.1	125 ± 4
$m_{\tilde{g}} = 1950\,\mathrm{GeV}$, $m_{\tilde{\chi}_1^0} = 1\,\mathrm{GeV}$	68.8 ± 0.6	12.48 ± 0.27	35.4 ± 0.5	18.41 ± 0.33	70.6 ± 0.7
$m_{\tilde{g}} = 1425\,\mathrm{GeV}$, $m_{\tilde{\chi}_1^0} = 1400\,\mathrm{GeV}$	12.6 ± 1.2	3.7 ± 0.6	8.5 ± 1.0	7.5 ± 0.9	8.1 ± 0.9
$m_{\tilde{q}} = 1050\,\mathrm{GeV}$, $m_{\tilde{\chi}_1^0} = 900\,\mathrm{GeV}$	2.5 ± 1.1	1.5 ± 0.9	2.0 ± 1.0	3.5 ± 1.3	6.4 ± 1.8
$m_{\tilde{q}} = 2250\,\mathrm{GeV}$, $m_{\tilde{\chi}_1^0} = 1\,\mathrm{GeV}$	141.7 ± 0.9	60.1 ± 0.6	82.1 ± 0.7	39.2 ± 0.5	59.3 ± 0.6

Region	SR4jt	SR5j	SR6jl	SR6jm	SR6jt
W+jets	113 ± 6	30.4 ± 2.9	8.5 ± 1.5	6.3 ± 1.3	3.6 ± 1.0
Z+jets	111.1 ± 3.2	74.4 ± 2.6	20.7 ± 1.4	13.0 ± 1.1	10.0 ± 1.0
$t\bar{t}$	45.9 ± 3.4	19.3 ± 2.2	5.2 ± 1.1	6.0 ± 1.2	3.4 ± 0.9
Diboson	30.0 ± 2.4	13.8 ± 1.5	3.8 ± 0.8	2.8 ± 0.7	1.9 ± 0.5
Total background	300 ± 8	138 ± 5	38.3 ± 2.5	28.1 ± 2.2	18.8 ± 1.7
$m_{\tilde{g}} = 1950\,\mathrm{GeV}$, $m_{\tilde{\chi}_1^0} = 1\,\mathrm{GeV}$	102.4 ± 0.8	83.4 ± 0.7	25.6 ± 0.4	44.6 ± 0.5	35.4 ± 0.5
$m_{\tilde{g}} = 1425\,\mathrm{GeV}$, $m_{\tilde{\chi}_1^0} = 1400\,\mathrm{GeV}$	6.2 ± 0.8	4.7 ± 0.7	1.6 ± 0.4	1.05 ± 0.33	1.05 ± 0.33
$m_{\tilde{q}} = 1050\,\mathrm{GeV}$, $m_{\tilde{\chi}_1^0} = 900\,\mathrm{GeV}$	4.0 ± 1.4	7.4 ± 1.9	3.5 ± 1.3	1.5 ± 0.9	1.5 ± 0.9
$m_{\tilde{q}} = 2250\,\mathrm{GeV}$, $m_{\tilde{\chi}_1^0} = 1\,\mathrm{GeV}$	58.9 ± 0.6	28.4 ± 0.4	7.84 ± 0.21	8.00 ± 0.21	7.57 ± 0.20

Table 8.4 · Yields for the main backgrounds and selected signal points simulated with $\langle\mu\rangle = 140$, normalised to $\mathcal{L} = 3000\,\text{fb}^{-1}$. The signal samples for squark-pair production are normalised for the scenario with a gluino mass of 4.5 TeV. A dash indicates no events pass the selection criteria.

Region	SR2jl	SR2jm	SR3j	SR4jl	SR4jm
W+jets	8 ± 5	5 ± 4	38 ± 10	8 ± 5	14 ± 6
Z+jets	51 ± 7	51 ± 7	185 ± 13	78 ± 8	127 ± 11
$t\bar{t}$	9 ± 4	9 ± 4	20 ± 5	7.0 ± 3.1	18 ± 6
Diboson	7.6 ± 3.1	7.2 ± 2.9	27 ± 6	10.4 ± 3.4	18 ± 5
Total background	76 ± 10	72 ± 9	269 ± 18	104 ± 11	176 ± 14
$m_{\tilde{g}} = 1950$ GeV, $m_{\tilde{\chi}_1^0} = 1$ GeV	55.8 ± 1.8	43.4 ± 1.6	163.9 ± 3.1	75.2 ± 2.1	191.0 ± 3.4
$m_{\tilde{g}} = 1425$ GeV, $m_{\tilde{\chi}_1^0} = 1400$ GeV	10.5 ± 3.3	15 ± 4	48 ± 7	19 ± 4	23 ± 5
$m_{\tilde{q}} = 1050$ GeV, $m_{\tilde{\chi}_1^0} = 900$ GeV	5 ± 5	10 ± 7	15 ± 9	10 ± 7	15 ± 9
$m_{\tilde{q}} = 2250$ GeV, $m_{\tilde{\chi}_1^0} = 1$ GeV	186 ± 3	208.2 ± 3.4	558 ± 6	254 ± 4	320 ± 4

Region	SR4jt	SR5j	SR6jl	SR6jm	SR6jt
W+jets	101 ± 17	14 ± 6	25 ± 8	11 ± 5	– [a]
Z+jets	125 ± 11	65 ± 8	85 ± 9	29 ± 5	3.6 ± 1.8
$t\bar{t}$	37 ± 9	11 ± 4	17 ± 5	3.5 ± 2.1	1.4 ± 1.4
Diboson	29 ± 7	9.9 ± 3.5	14 ± 4	4.8 ± 2.6	0.6 ± 0.8
Total background	292 ± 23	99 ± 11	141 ± 14	48 ± 8	5.6 ± 2.4
$m_{\tilde{g}} = 1950$ GeV, $m_{\tilde{\chi}_1^0} = 1$ GeV	159.1 ± 3.1	152.7 ± 3.0	257 ± 4	73.4 ± 2.1	36.0 ± 1.5
$m_{\tilde{g}} = 1425$ GeV, $m_{\tilde{\chi}_1^0} = 1400$ GeV	8.4 ± 3.0	14 ± 4	7.4 ± 2.8	5.3 ± 2.4	– [a]
$m_{\tilde{q}} = 1050$ GeV, $m_{\tilde{\chi}_1^0} = 900$ GeV	15 ± 9	10 ± 7	25 ± 11	5 ± 5	5 ± 5
$m_{\tilde{q}} = 2250$ GeV, $m_{\tilde{\chi}_1^0} = 1$ GeV	182.6 ± 3.2	136.4 ± 2.7	75.2 ± 2.0	50.9 ± 1.7	13.6 ± 0.9

[a] An attempt could be made to estimate an upper limit on the value by assuming a Poisson distribution and determining the expectation for which $P(x = 0|\mu) \leq 0.05$ (i.e., $\mu \approx 2.99$) and then scaling it with the proper factor for the sample. However, this would be an extremely conservative approach: it does not take any information on the distribution below the selection into account. Moreover, such an approach would be inconsistent with one used to obtain the errors quoted for small non-zero event yields.

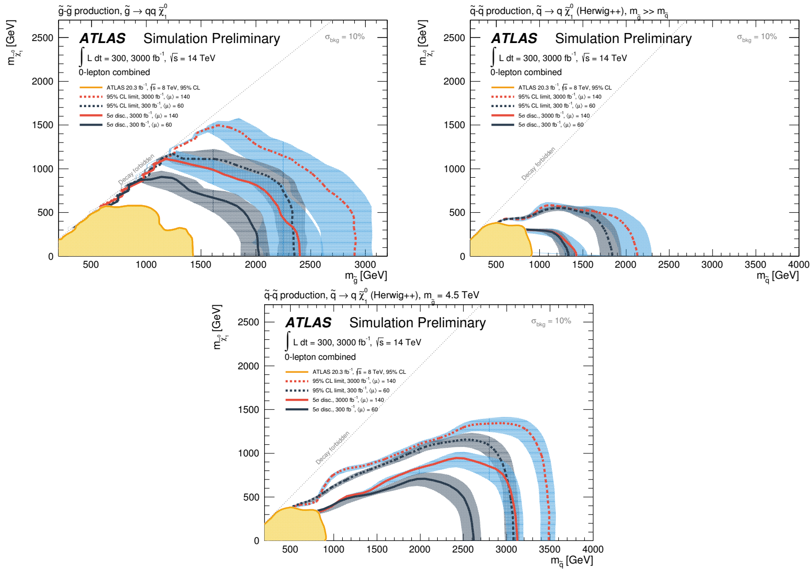

Fig. 8.4 · Expected 95 % CL exclusion contours (dashed) and 5σ discovery contours (solid) for $\mathcal{L}_{\text{int}} = 300\,\text{fb}^{-1}$ (black) and $3000\,\text{fb}^{-1}$ (red) for gluino and squark-pair production. For squark-pair production, the gluino mass is either decoupled or set to 4.5 TeV. The bands reflect the 1σ uncertainty on the production cross-section. The stepping along the diagonal in the top left figure is a non-physical effect caused by the granularity of the grid.

8.8 Conclusion

The obtained results for both gluino-pair and squark-pair production extend significantly beyond current limits set by ATLAS and by CMS. Notably, particles with masses not currently excluded at the LHC can be discovered at $\sqrt{s} = 14\,\text{TeV}$, an encouragement to continue SUSY searches at the HL-LHC. In the case of squark-pair production, t-channel production will need to be taken into account: completely decoupled gluinos are not realistic if squarks themselves are accessible. The relative importance of t-channel increases greatly from 8 TeV to 14 TeV: decoupled gluinos and heavy gluinos are no longer practically indistinguishable. Moreover, the existence of the channel allows for the setting of limits on the gluino mass independent of $m_{\tilde{q}}$.

CHAPTER NINE

HistFitter

DATA ANALYSIS OF large datasets is a complicated procedure that requires careful bookkeeping and well-functioning statistical tools. This chapter describes HistFitter, a software package authored within the ATLAS collaboration to perform analyses such as the one presented in chapter 5 easily. HistFitter has been developed by a small team of six people; the other developers are M. Baak, D. Côté, A. Koutsman, J. Lorenz and D. Short.

HistFitter is a programmable and flexible framework to build, book-keep, fit, interpret and present results of data models of nearly arbitrary complexity. Starting from an object-oriented configuration, the framework builds probability density functions that are automatically fitted to data and interpreted with statistical tests. Being capable of working with multiple data models at once, HistFitter introduces an additional level of abstraction that allows for easy bookkeeping, manipulation and testing of large collections of signal hypotheses. Finally, HistFitter provides a collection of tools to present results with publication-quality style through a simple command-line interface.

This chapter is based on [264], co-authored by all HistFitter developers.

9.1 Introduction

HistFitter is written in Python and C++, the former being used for configuration and the latter for CPU-intensive calculations. Internally, HistFitter uses the software packages HistFactory [265] and RooStats [267], which are based on RooFit [266] and ROOT [268, 269], to construct parametric models and perform statistical tests of the data. HistFitter extends these tools in four key areas:

1. **Programmable framework:** HistFitter is capable of performing complete statistical analyses of pre-formatted input data samples by putting together tools from several sources in a coherent and programmable framework.
2. **Analysis strategy:** HistFitter has built-in concepts of control, signal and validation regions, which are used to constrain, extrapolate and validate data model predictions across an analysis. The framework also introduces a rigorous treatment of validation regions.
3. **Bookkeeping:** HistFitter can keep track of numerous data models, including all generated input histograms, both before and after adjustment to measured data, and can perform statistical tests and model-parameter scans of all these models in an organised way. This

introduces a powerful additional level of abstraction, which aids the processing of large collections of signal hypothesis tests.

4. **Presentation and interpretation:** HistFitter provides a collection of methods to determine the statistical significance of signal hypotheses, estimate the quality of likelihood fits, and produce publication-quality tables and plots expressing these results.

9.2 Analysis concepts

Analyses of large datasets generally rely on external predictions for the various background and signal components in the data to aid the interpretation of observations, where the signal component describes the process of interest. In particle physics, these are simulated background processes and a process of interest, for example supersymmetry.

HistFitter configures and builds parametric models to describe the observed data, and provides tools to interpret the data in terms of these models. It uses the concepts of control, validation, and signal regions in the construction and handling of these models. A key innovation of HistFitter is to weave these concepts into its very fabric, and to treat them with statistically rigorous methods.

The concept of signal, control and validation regions is described in more detail in §5.1 and in the paper this chapter is based on. The background estimation through transfer factors has been discussed in §5.6.

9.3 HistFitter software framework

HistFitter provides a programmable framework to build and test a set of data models. To do so, HistFitter takes a configuration file as input, together with raw data. The HistFitter processing sequence then consists of three steps, illustrated in fig. 9.1. From left to right:

1. Based on the configuration, HistFitter automatically prepares initial histograms, using ROOT, from the provided input source(s) that model the physics processes in the data. (The configuration and histogram creation is discussed further below and in §A.1.)

2. According to each specified configuration, the generated histograms are combined by HistFactory to construct a corresponding PDF. At the end of this process, each PDF is stored in a `RooWorkspace` object together with the dataset and model configuration.

3. The constructed PDFs are used to perform fits of the data with RooFit, perform statistical tests with RooStats, and to produce plots and tables.

These steps all require a substantial bookkeeping and configuration machinery, which is provided by HistFitter. The following sub-sections summarise the central HistFitter configuration tool and the prominent features of the HistFactory and RooStats software tools that HistFitter utilises.

The various steps can be executed individually or consecutively in a single run, and are all controlled with a single (and simple) user-defined configuration file. For example, in early stages of an analysis a set of requirements may need to be determined, requiring frequent regeneration

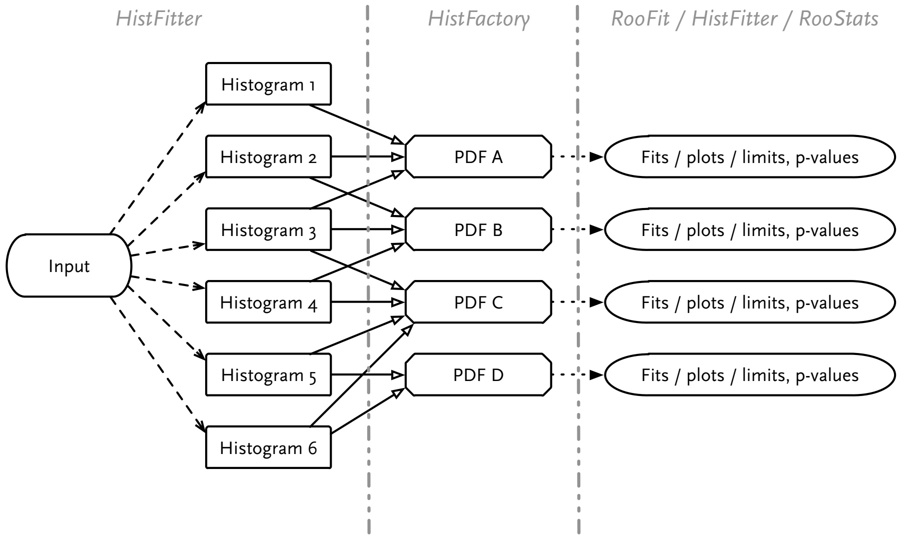

Fig. 9.1 · Overview of the HistFitter processing sequence.

of just the histograms that describe the data. In contrast, in the later stages of an analysis (such as limit setting) there is no need to repeat such low-level steps. The separation of the steps in the processing sequence can thus have quite a beneficial impact.

One of the key benefits of having a single configuration is to aid collaboration between the various members of an analysis group. Moreover, the process of combining existing analyses is made more efficient than if each group has to independently submit histograms to some third party for a statistical combination.

9.3.1 Configuration manager

The central HistFitter configuration and bookkeeping machinery is built around a configuration manager, `configManager`, implemented by two singleton objects: one in Python and one in C++. When executing HistFitter, users interact with the Python interface of the `configManager` to define a `fitConfig` object for each data model. The configuration manager can hold any number of `fitConfig` objects.

A `fitConfig` object contains a PDF describing the control, signal and validation region data belonging to the model, together with metadata required for the sequence of building, fitting, visualising and interpreting each configuration (i.e. one entire row in fig. 9.1) including the generation of relevant input histograms. The `fitConfig` class is described further in §A.1.1.

In terms of design patterns, the `configManager` can be seen as a factory of factories, since it generates the construction of `fitConfig` objects, which are themselves factories of PDF objects. By producing a *list* of data models, HistFitter introduces an additional level of abstraction which allows hypothesis tests to be performed over grids of signal models.

The construction of each data model typically requires the preparation of tens to hundreds of histograms. This can lead to memory exhaustion problems for long lists of models. However, while signal samples tend to be unique to each model, the background samples are often identical in most of the models. When preparing input histograms for each sample of each model, the `configManager` stores unique auto-generated names in a Python dictionary. The dictionary is used in turn to efficiently identify and re-use the histograms that can be shared between independent data models (see fig. 9.1), which significantly reduces the memory usage of the software. Additionally, the generated histograms are stored in an external file, allowing them to be directly loaded when rerunning HistFitter in the same configuration. This avoids the need for their usually time-consuming regeneration and helps in sharing workload between a collaboration.

HistFitter uses the HistFactory package to construct a parametric model describing the data, based on provided input histograms. This parametric model describes the nominal prediction and associated systematic variations of multiple signal and background processes in multiple regions, up to nearly arbitrary complexity. The input histograms can be generated by HistFitter, or can be provided externally by users.

As detailed in [265], the PDF constructed by HistFactory describes the parameter(s) of interest, such as the rate of a signal process, the normalisation factors for background processes (as estimated from data), and the so-called nuisance parameters that parametrise the impact of systematic uncertainties.

Each systematic uncertainty i is described with a nuisance parameter, θ_i, that continuously interpolates between the variation and nominal templates, e.g. $\theta_i = \pm 1$ for $\pm 1\,\sigma$ variations and $\theta_i = 0$ for the nominal template.

The general likelihood L of the analyses considered here is the product of Poisson distributions of event counts in the signal regions(s) and/or control region(s) and of additional distributions that implement the constraints on systematic uncertainties. It can be written as:

$$\begin{aligned} L(\boldsymbol{n}, \boldsymbol{\theta}^0 | \mu_{\text{sig}}, \boldsymbol{b}, \boldsymbol{\theta}) &= P_{\text{SR}} \times P_{\text{CR}} \times C_{\text{syst}} \\ &= P(n_S | \lambda_S(\mu_{\text{sig}}, \boldsymbol{b}, \boldsymbol{\theta})) \times \prod_{i \in \text{CR}} P(n_i | \lambda_i(\mu_{\text{sig}}, \boldsymbol{b}, \boldsymbol{\theta})) \times C_{\text{syst}}(\boldsymbol{\theta}^0, \boldsymbol{\theta}) \,. \end{aligned} \tag{9.1}$$

The first two terms in (9.1) reflect the Poisson measurements of n_S and n_i, the number of observed events in the signal region and each control region i. The Poisson expectations λ_S and λ_i are functions depending on the predictions $\boldsymbol{b}$ for various background sources, the nuisance parameters that parametrise systematic uncertainties, the normalisation factors for background processes, μ_{p}, and also the signal strength parameter μ_{sig}. For $\mu_{\text{sig}} = 0$ the signal component is turned off, and for $\mu_{\text{sig}} = 1$ the signal expectation equals the nominal value of the model under consideration.

The predictions for signal and background sources are forced to be positive in HistFactory for any values of the nuisance parameters and in any histogram bin.

Systematic uncertainties are included using the probability density function $C_{\text{syst}}(\boldsymbol{\theta}^0, \boldsymbol{\theta})$, where $\boldsymbol{\theta}^0$ are the central values of the auxiliary measurements around which $\boldsymbol{\theta}$ can be varied, for example when maximising the likelihood. The impact of changes in nuisance parameters on the expectation values are described completely by the functions predicting the amount of signal and background, λ_S and λ_i. For independent nuisance parameters, C_{syst} is simply a product of the probability distributions corresponding to the auxiliary measurements describing each of the systematic uncertainties, typically normal distributions G with unit width:

$$C_{\text{syst}}(\boldsymbol{\theta}^0, \boldsymbol{\theta}) = \prod_{j \in S} G(\theta_j^0 - \theta_j)\,, \tag{9.2}$$

where S is the full set of systematic uncertainties considered. The auxiliary measurements θ_j^0 are typically fixed to zero, but can be varied when generating pseudo experiments (see below).

Several interpolation (and extrapolation) algorithms are employed in HistFactory to describe the PDF for all values of nuisance parameters θ_j. Some details of these algorithms are discussed in §A.1.4, but for a complete overview the reader is referred to [265].

The execution of HistFactory results in a `RooWorkspace`, a persistent RooFit object containing the parametrised PDF, the dataset, and a helper object summarising the model configuration. As discussed in the next sub-section, these are used as input to perform statistical tests with the RooStats package.

9.3.2 RooStats

HistFitter is capable of performing a list of pre-configured statistical tests to one or several data-set(s) from a single command-line call. To do so, it interfaces with the RooStats package. These tests are:

1. hypothesis tests of signal models;
2. the construction of expected and observed confidence intervals on model parameters. For example, the 95 % confidence level upper limit on the rate of a signal process;
3. the significance determination of a potentially observed event excess.

A suite of statistical calculations can be performed, as configured by the user, ranging from Bayesian to Frequentist philosophies and using various test statistic quantities as input.[1] By default, HistFitter employs a Frequentist method to perform hypothesis tests and uses the profile likelihood ratio $q_{\mu_{\text{sig}}}$ as test statistic. The CL_s method [271] is used to test the exclusion of new physics hypotheses. Whenever appropriate, this method is approximated by asymptotic formulae [270] to speed up the evaluation process.

More details on hypothesis tests and how they are performed with HistFitter are given in [264].

[1] Supported test statistics are: a maximum likelihood estimate of the parameter of interest, a simple likelihood ratio $-2\log\left(L(\mu,\tilde{\theta})/L(0,\tilde{\theta})\right)$, as used by the LEP collaborations, a ratio of profile likelihoods $-2\log\left(L(\mu,\hat{\hat{\theta}})/L(0,\hat{\theta})\right)$, as used by the Tevatron collaborations, or a profile likelihood ratio $-2\log\left(L(\mu,\hat{\hat{\theta}})/L(\hat{\mu},\hat{\theta})\right)$, as used by the LHC collaborations. For the later case, the hypothesis tests can be evaluated as one- or two-sided. The sampling of the test statistics is done either with a Bayesian, Frequentist, or a hybrid calculator [267].

9.4 Using HistFitter

HistFitter allows the user to build probability density functions in an easy way using several classes in Python. These are further discussed in Appendix A.

9.4.1 Visualisation

HistFitter also contains an extensive array of user-friendly functions and scripts, which help with the understanding and detailing of the results obtained from the fits. These scripts and plotting functions are generalised, such that for every model built with HistFitter all of these features come without any need for further coding. All scripts and plotting functions can be called by single-line commands.

Two main presentation components are the visualisation of fit results and scripts for producing event yield and uncertainty tables. All tables and plots can be produced for any fit configuration of a defined model, as well as before and after the fit to data. Multiple details, such as the legends on plots or the set of regions to be processed for tables, can easily be set in the configuration file or from the command line.

All figures and tables in chapter 5 have been produced using these scripts.

9.4.2 Interpretation

HistFitter provides the functionality to perform hypothesis tests of the data through calls to the appropriate RooStats classes, and to interpret the corresponding results in the form of plots and tables. Four different statistical tests are available in HistFitter. Each of these depend on the various available fit setups. In all of these setups both the control and signal region(s) are part of the input to the fit.

In the absence of an observed excess of events in one or more signal region(s), exclusion limits can be set on specific signal models using the model-dependent signal fit configuration. The third approach obtains exclusion upper limits on any potential new physics signal, without model dependency. The fourth interpretation performs the significance determination of a potentially observed event excess. Both of these rely on the model-independent signal fit configuration.

These different statistical tests are discussed in further detail in the paper.

9.5 Public release

The HistFitter software package is publicly available through `http://cern.ch/histfitter` and requires ROOT release v5.34.20 or greater. The web-page contains a description of the source code, a tutorial on how to set up an analysis, and working examples of how to run HistFitter.

CHAPTER TEN

Conclusions and outlook

A search for squarks and gluinos in a channel with jets and missing energy was presented in chapter 5. The results were interpreted in mSUGRA/CMSSM and in several simplified models. Later chapters used similar results in global fits to a 15-parameter phenomenological MSSM and investigated prospects for such searches at a centre-of-mass energy of 14 TeV. All results are briefly discussed below and put in a wider context. A comparison with results from other experiments is also made.

10.1 Discussion

The non-observation of supersymmetrical particles in the 0-lepton analysis, if these indeed exist, can be due to several reasons. Supersymmetry has been searched for under a set of assumptions that may not necessarily be true. Possible reasons for the non-observation of any existing SUSY particles include:

compressed mass spectra with a small mass difference between the LSP and a squark or gluino are difficult to probe experimentally: their signal efficiency is low. Moreover, very compressed scenarios lead to a final state with only $E_{\mathrm{T}}^{\mathrm{miss}}$ that can be probed solely through ISR and FSR; such states would be easier to search for using e.g. a mono-jet analysis;

heavy LSP's are outside of the sensitivity of the analysis: depending on the exact model, the heaviest LSP that can be excluded is between 400 and 600 GeV;

longer cascade decays with leptons, due to intermediate particles (e.g. a chargino) decaying leptonically, lead to the events being vetoed. These types of decays are better probed in an analysis requiring leptons, and techniques to reconstruct W and Z bosons already used should be further developed. In addition, cascade decays with e.g. a Higgs boson may also be used to search for SUSY. However, the longer a cascade, the more difficult it is to probe;

squarks and gluinos are too heavy to have been produced at the LHC until now; electroweak production of SUSY might in fact have been the dominant mechanism;

squarks, not gluinos, are predominantly produced, which would be easier to investigate using different variables that better reconstruct such a simple decay topology: the suppression of additional jets for the Standard Model background processes does not benefit the typical 2- or 3-jet final state for this production mechanism, leading to larger backgrounds.

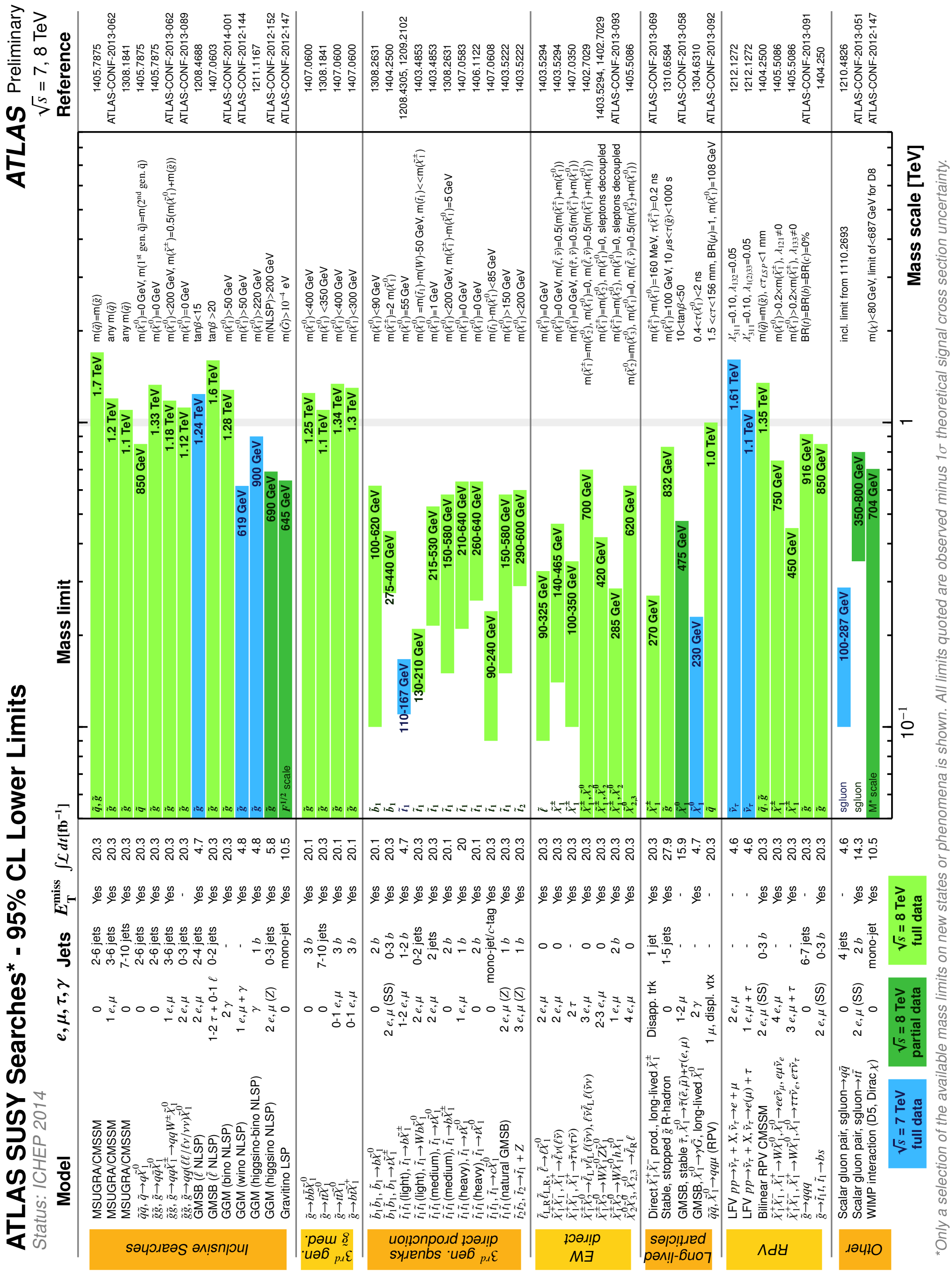

Fig. 10.1 · Mass reach of ATLAS searches for supersymmetry. Only a representative selection of the available results is shown.

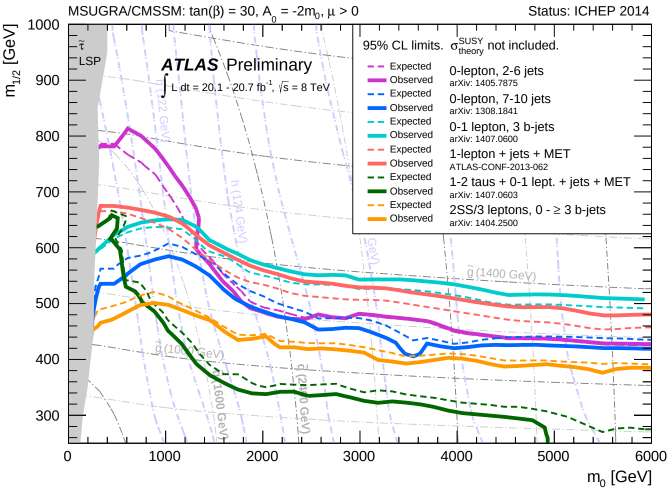

Fig. 10.2 · Exclusion limits at 95 % CL for 8 TeV analysis in the $(m_0, m_{1/2})$ plane for the MSUGRA/CMSSM model with the remaining parameters set to $\tan(\beta) = 30$, $A_0 = -2 \times m_0$ and $\mu > 0$. Part of the model plane accommodates a lightest neutral scalar Higgs boson mass of 125 GeV. Theoretical signal cross-section uncertainties are not included in the limits shown.

However, the 0-lepton analysis does not stand on its own. Within ATLAS, the various final states mentioned above are targeted in dedicated analyses. These results are best summed up in fig. 10.1, which shows the mass reach of a wide spectrum of analyses. These searches cover a large range of final states through signatures using jets, E_T^{miss}, electrons, muons, τ leptons, photons and b jets. None of these analyses point to a significant excess over the Standard Model expectation. Related searches by the CMS collaboration have lead to similar constraints on SUSY particle masses. Fig. 10.2 shows the status of MSUGRA/CMSSM after the ATLAS searches performed until now.

An obvious way to create a more generic analysis unbiased towards any particular SUSY model is to go back to each of the analyses and ensure its orthogonality to others. The combination performed in chapter 7 encountered difficulties in performing these combinations but shows the promise of performing a larger analysis. Slightly decreased results in individual analyses should be considered an acceptable trade-off if a combined analysis ultimately leads to a better sensitivity.

Several interesting things can be gleaned from CMS analyses targeting squark and gluino production. Four analyses overlap with the one presented in this thesis: a multijets search [330], a search using the variable α_T [278], a search using the Razor variables[1] [332] and a search using m_{T2} [333]. First, the use of the variable α_T does not yield improved results compared to other choices. The variable m_{T2} attempts to measure the mass of primary pair-produced particles; it might offer an interesting complement to m_{eff} for the production of squark pairs. The Razor variables appear to offer no tangible benefit over selections on easier kinematic variables: the exclusion limits are not better.

---

1 The *Razor* variables are a set of kinematic variables that exploit both transverse and longitudinal event information [331].

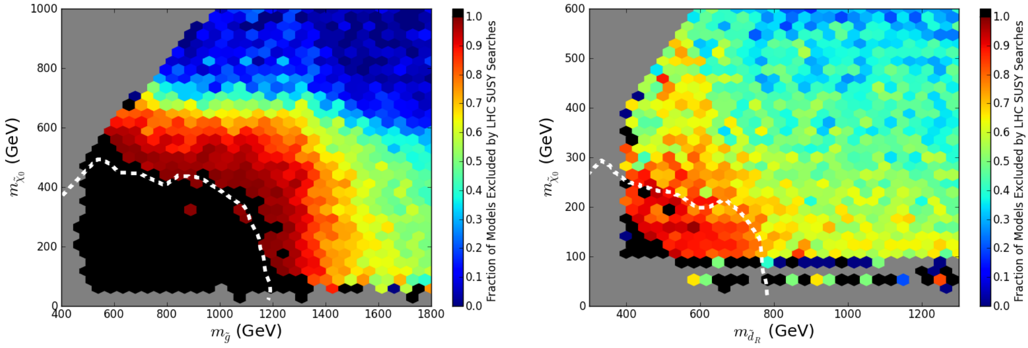

Fig. 10.3 · PMSSM models points projected on to a plane of $(m_{\tilde{g}}, m_{\tilde{\chi}_1^0})$ (left) and $(m_{\tilde{d}_R}, m_{\tilde{\chi}_1^0})$ (right). For each point, the excluded fraction of models is shown [334]. The white lines are the exclusion limits obtained in the 0-lepton analysis using 5.8 fb^{-1} [279].

The most interesting fundamental difference in approach comes to the fore when considering the CMS multijets analysis, which selects events with at least 3 jets. It categorises these according to the number of jets, the scalar sum of jet p_{T}'s and $E_{\mathrm{T}}^{\mathrm{miss}}$, leading to in total 36 orthogonal bins. In all these bins, a *simultaneous* fit is performed – an approach very different from the 15 single-bin fits performed in the ATLAS 0-lepton analysis, and one that is in principle better suited to aggressively exclude models of supersymmetry. However, it is not clear whether systematic uncertainties are properly dealt with, whether theoretical uncertainties on the background are taken into account correctly, whether any of these uncertainties are over-constrained and how such a complicated fit is validated. Nevertheless, it can be argued that the current approach of the 0-lepton analysis should at least be reconsidered and an analysis with orthogonal signal regions could be designed without necessarily resorting to an approach along the lines of the CMS multijets analysis.

10.2 Implications in larger models

As already discussed earlier, interpretations in models such as MSUGRA/CMSSM are limited in scope. The interpretation in simplified models alleviates some of these limitations, but still targets very specific scenarios. In addition to the global fits performed in chapter 6, the entire PMSSM may be scanned to yield information on unusual scenarios and to identify weaknesses of and overlaps between SUSY searches. Such an approach was followed in [334].

In that scan, millions of model points in the PMSSM's phase space are generated randomly and subjected to a set of constraints; 225 000 models with squarks and gluinos with a mass less than 4 TeV and $\tilde{\chi}_1^0$ as the LSP are studied in detail. These models are analysed using emulated versions of a set of ATLAS SUSY searches and a smaller set of searches by CMS, and constrained using $B_s \to \mu^+\mu^-$. In this way, the regions of phase space excluded by this wide range of searches are determined.

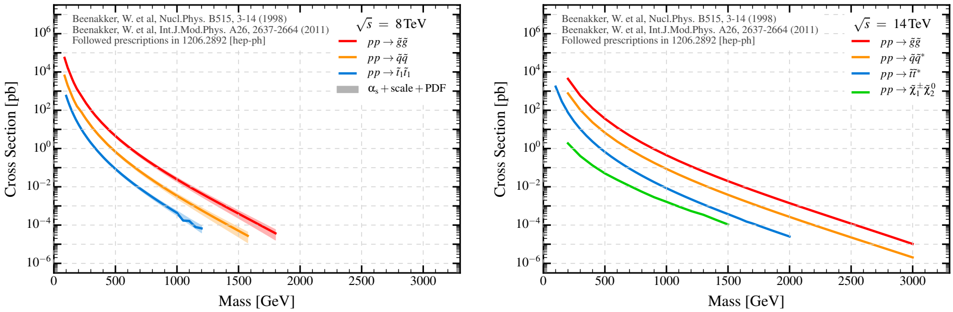

Fig. 10.4 · Production cross-sections for various supersymmetrical processes at 8 TeV (left) and 14 TeV (right). For each process shown, other sparticles are assumed to be decoupled.

Out of the models studied, 37 % are excluded by one or more of the LHC searches. An earlier version of the 0-lepton analysis discussed in chapter 5 using only 5.8 fb^{-1} and larger systematic uncertainties excludes the largest fraction of models: 27 % of them are excluded using this channel alone. The fraction of models excluded, projected on to two simplified-model planes, is shown in fig. 10.3. The superimposed white lines show the regions excluded by the ATLAS 0-lepton search.

The limits set on simplified models correlate well with the fraction of models excluded in the pMSSM. The right figure uses only a right-handed light-flavour squark, while the ATLAS exclusion line shown assumes degenerate light-flavour squarks, equivalent to a cross-section 8 times higher. The limit for non-degenerate squarks shown in fig. 5.20 again correlates well with the fraction of points that are excluded. This underscores the power of the 0-lepton search in exploring the MSSM.

A similar study on the pMSSM is currently being performed by the ATLAS collaboration and will be published soon. This study uses the latest results, employs a proper detector simulation and uses the full likelihood of each analysis.

10.3 Outlook

Strongly-produced supersymmetry is one of the most promising research avenues for the ATLAS collaboration at the increased centre-of-mass energy of 14 TeV. In particular the 0-lepton channel will offer interesting results with a very small dataset: 1 to 2 fb^{-1} is too small a dataset to discover squarks and gluinos, but would offer limits comparable to the current ones. The best-fit point obtained in chapter 6 corresponds to a squark mass of 2.3 TeV and a gluino mass of 2.1 TeV, which would be within the reach of this analysis within several years.

Several methods to improve the analysis should be pursued. First of all, a dedicated control region for the diboson background will be needed. In the current analysis, the theoretical error on this background leads to the largest uncertainty on the prediction; the increased datasets will allow for a dedicated region. Care must also be taken to improve the sensitivity of the analysis to compressed scenarios, which could be done using dedicated signal regions and/or variables.

While the last iterations of the analysis on the 8 TeV data were all optimised for exclusion, the upcoming analysis should both be able to discover supersymmetry and to set stringent limits in case again no excess over the Standard Model expectation would be observed. A two-prong approach can be considered: as in the current analysis, a set straightforward single-bin counting experiments can be used to reject the Standard Model, while binned fits can be used to exclude (simplified) models of supersymmetry.

Finally, care must be taken to ensure that the baseline strategies of the various strong-production channels are harmonised. Irrespective of possible minor improvements in each analysis, the same Monte Carlo generators should in principle be used and an agreement on the treatment of important systematic uncertainties should be made. Provided all these ingredients are in place, ATLAS will always be able to combine analyses in relatively short time-spans in case of an observed excess or to set more stringent limits. In order for the analysis to remain a favourite for reinterpretation by theorists in larger models, the publication of correlation matrices for such a combination should then be considered.

Nonetheless, neither experimentalists nor theorists should despair in case of non-observation in the first few years of data-taking. The study presented in chapter 8 shows that scenarios out of reach for smaller datasets can still be discovered at the high-luminosity LHC in 2022 and beyond. Moreover, the increased cross-sections for electroweak production of supersymmetry (see fig. 10.4) means that novel ways to search for SUSY that were previously impossible can be pursued: the claim that supersymmetry is dead after Run 1 of the LHC is misguided.

APPENDIX ONE

Using HistFitter

This appendix further discusses how to perform an analysis using HistFitter, the software described in chapter 9.

A.1 Programming of Probability Density Functions

HistFitter is designed to build and manipulate PDFS of nearly arbitrary complexity. In the terminology of HistFactory, the likelihood function in (9.1) has multiple *channels*, which need inputs in the form of *samples*, corresponding to the signal and background processes for that region. In turn, the various samples have systematic uncertainties, or *systematics*. A HistFactory "channel" is a synonym for a "region", generically referring to either control, signal or validation in this section. The systematic uncertainties can be either statistical, theoretical or experimental in nature. These HistFactory C++ classes are mirrored by HistFitter in Python, and extended by adding the flexibility to construct multiple PDFS from these building blocks in a programmable way, as discussed further in this section.

An example HistFitter configuration file, written in Python and demonstrating these components, is shown in Appendix B.

A.1.1 The fit configuration

HistFitter uses the `fitConfig` class to construct its PDFS. The design of this class allows for the creation of highly complex PDFS, describing highly non-trivial analysis setups, with only a few lines of intuitive code. It is configured by users as follows:

```
from configManager import configMgr
myFitConfig = configMgr.addFitConfig("myAnalysisName")
```

where `myFitConfig` is a reference to a new `fitConfig` object owned by the `configManager`. The `fitConfig` class logically corresponds to a PDF decorated with metadata about the properties of the contained channels (control, signal and validation regions), including visualisation, fitting and interpretation options.

During configuration, instances of channels, samples and systematics are put together by `fitConfig` objects, together with links to the corresponding input histograms. During execution, the `fitConfig` information is used to steer the HistFactory package's creation of a `RooSimultaneous` object modelling the actual PDF with RooFit.

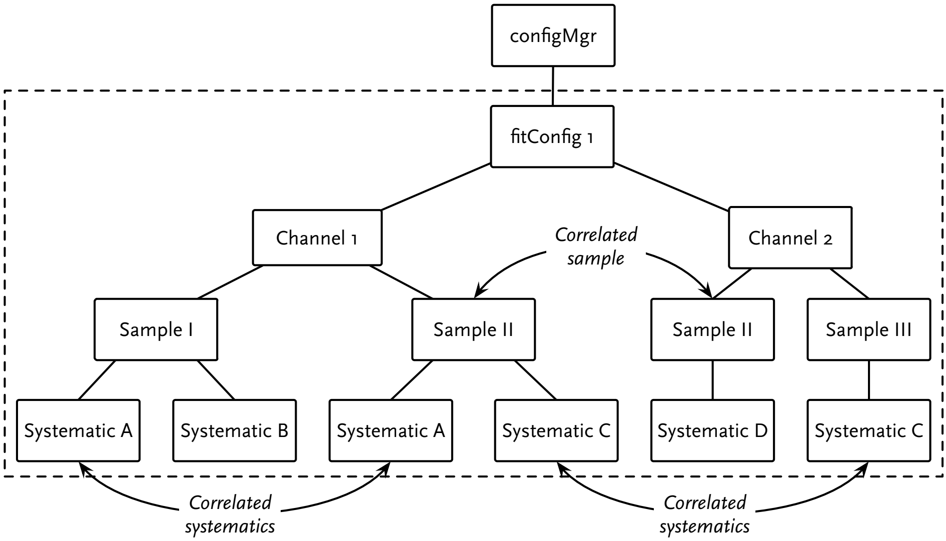

Fig. A.1 · Illustration of a fit configuration in HistFitter. Each `fitConfig` instance defines a PDF built from a list of channel (i.e. a control, signal or validation region), sample and systematic objects. Each channel owns a list of samples and each sample owns a list of systematic uncertainties. Correlated samples and systematics are declared by being given identical names. Otherwise they are treated as uncorrelated.

Fig. A.1 illustrates the modular design of a typical HistFitter fit configuration. The user interface provides the methods `addChannel()`, `addSample()` and `addSystematic()` to build up data models in an intuitive manner. For instance, samples and systematics can be efficiently added to multiple channels through a trickle-down mechanism, as illustrated by fig. A.2. This means that `fitConfig.addSample()` adds a sample to all the channels owned by the `fitConfig`, while `channel.addSample()` adds a sample to one specific channel. Similarly, `sample.addSystematic()` only adds a systematic to one specific sample while `channel.addSystematic()` adds a systematic to all the samples owned by the channel and `fitConfig.addSystematic()` adds a systematic to all the samples of all the channels owned by the `fitConfig`.

Since different channels often share the same samples (consider a background process in particle physics), and different samples often share the correlated systematic uncertainties, the trickle-down mechanism is in fact an extremely useful feature. It makes it so that complex configurations of PDFs can often be described with only a few lines of code.

A basic fit configuration can also be conveniently cloned and extended to specify new configurations, a feature which is frequently used to build data models corresponding to multiple signal hypotheses from a common background description.

A.1.2 Channels

The `Channel` objects contain data from a region of phase space defined by event selection criteria on the input dataset. Channels can represent either a simple event count (i.e. one bin), or the

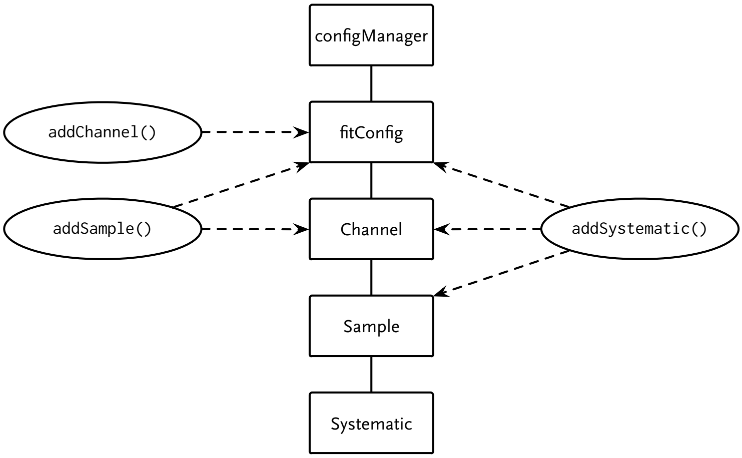

Fig. A.2 · The methods addChannel(), addSample() and addSystematic() are used to build complex PDFs in an intuitive way. The methods addSample() and addSystematic() implement a trickle-down mechanism, discussed in the text.

multi-binned distribution of a physical observable. New binned and unbinned channels can be added to a `fitConfig` by calling:

```
myChannel = myFitConfig.addChannel("myObs", ["mySelection"], nBins, varLow, varHigh)
myUnbinnedChannel = myFitConfig.addChannel("cuts", ["mySelection"], 1, 0.5, 1.5)
```

where `myObs` is the name of an element of the input dataset, `nBins`, `varLow` and `varHigh` indicate the number of bins and the range of values as for a one-dimensional histogram, and `mySelection` specifies the selection criteria of the considered region. For unbinned channels, `cuts` is a reserved keyword indicating that only the total number of events passing the selection criteria needs to be considered (a "cut-and-count" analysis).

A `Channel` object can represent a control, signal or validation region. This information is configured by users as follows:

```
myFitConfig.setBkgConstrainChannels(myChannel)
myFitConfig.setValidationChannels(myChannel)
myFitConfig.setSignalChannels(myChannel)
```

It is possible to add an arbitrary number of channels to a given `fitConfig` by simply calling `addChannel()` multiple times. Consequently, HistFitter automatically performs simultaneous fits constrained by the data of all `BkgConstrainChannels` (control regions) and `SignalChannels` (signal regions), but not by the `ValidationChannels` (validation regions). The data itself is described by a list of `Sample` objects owned by each channel, as discussed in the next sub-section.

A.1.3 Samples

The `Sample` class logically corresponds to a component of a RooFit PDF decorated with HistFitter metadata. In a typical particle physics analysis, each sample corresponds to a specific physics process and several samples are needed to model a complete dataset.

In HistFitter, samples can be defined in a specific channel or defined simultaneously in multiple channels. The `Sample` class also owns a list of objects representing its systematic uncertainties. Importantly, samples provide the link between PDF components and raw input data. Three types of inputs are supported:

1. **TTree:** a ROOT data structure, stored in a `TFile`, in which a list of *events* is mapped to a list of key-value pairs characterising the properties of each event;
2. **float:** floating-point numbers provided by users through the Python interface of HistFitter;
3. **histogram:** pre-made histograms using the ROOT `TH1` structure, stored in a `TFile`.

The most commonly used type of input is `TTree`, which provides maximal flexibility and most features, but requires the largest amount of processing power and disk I/O. Float inputs tend to be used for quick tests and simple processes. Histogram inputs can be used for compatibility with external frameworks, and also allow the user to conveniently skip the `TTree`-to-histogram processing when re-building PDFs. In all cases, the raw input is transformed into histograms as specified by `Sample` objects, before being saved to a temporary file and passed to HistFactory to build the RooFit PDFs (see §A.1.1).

A basic sample can be created and configured by users as follows:

```
mySample = Sample("SampleName",myColor)
myChannel.addSample(mySample)
```

which constructs a sample object owned by `myChannel` and displayed with `myColor` color by the visualisation tools. In this example, HistFitter takes inputs from a `TTree` object named `SampleName` in the default ROOT file specified at the configManager level. To construct the sample, HistFitter uses the event selection criteria of the parent channel and applies a default sample weight.

The default settings can be overwritten by users to achieve specific goals. For instance, a sample can be built from Float input with:

```
mySample.buildHisto([100,34,220], "region", "observable")
```

where the list `[100,34,220]` specifies the values of three bins in an histogram. The default sample weight and path to the input data can also be overwritten as follows:

```
mySample.setWeight(("weight1","weight2"))
mySample.setFileList(["File1.root","File2.root"])
mySample.setTreeName("ArbitraryName")
mySample.setHistoName("ArbitraryName")
```

Weights are passed as a string to also allow the easy use of weights stored in a ROOT `TTree`. In addition, the `Sample` class has methods to configure its corresponding RooFit PDF, such as:

```
mySample.setStatConfig(False)
mySample.setNormFactor("my_Norm", 1.0, 0.0, 10.0)
```

resulting in the deactivation of the built-in Poisson statistical uncertainties that are by default activated, and in the creation of a fit normalisation factor `my_Norm` with initial value 1.0 and allowed range 0.0 to 10.0, respectively.

Last but not least, HistFitter provides many features for modelling the systematic uncertainties associated to each sample, as discussed in the next sub-section.

A.1.4 Systematic uncertainties

For each model component, a nominal distribution representing the best available prediction is typically provided to the physics analysis as a histogram owned by a `Sample` object. These components typically have systematic uncertainties whose impact gets quantified in dedicated studies. These are often modelled as variations of one standard deviation around the nominal prediction, provided to the physics analysis as sets of two additional histograms. These systematic uncertainties are parametrised in the PDF with nuisance parameters, as in (9.1).

In HistFitter, systematic uncertainties are implemented with a dedicated `Systematic` class with several options. In a typical analysis, several `Systematic` objects are built and owned by a parent `Sample`. Through the trickle-down mechanism described in §A.1, systematics can be defined for a specific sample or defined simultaneously for multiple samples and/or channels.

A `Systematic` object can be conceived as a doublet of samples specifying up and down variations around the parent `Sample`. Hence `Systematic` objects can be constructed from the same types of inputs as `Samples`: `TTree`, floating-point numbers and histogram.

When using `TTree` inputs, two methods can be used to compute the up/down variations of a systematic: weight-based or tree-based. In the weight-based method, histograms are always built from the same `TTree`, using three different sets of weights: up, nominal and down. In the tree-based method, histograms are built from three different `TTrees` using the same set of weights. If only one variation is available, users can either build a one-sided uncertainty or symmetrise the variation as $\frac{\text{nominal}\pm(\text{up}-\text{nominal})}{\text{nominal}}$.

`Systematic` objects can be created by users as follows:

```
mySys = Systematic("myTreeSys", "ASample", "ASample_UP", "ASample_DOWN", "tree",
                   "myMethods")
mySys = Systematic("myWeightSys", ["nominalWeights"], ["upWeights"], ["downWeights"],
                   "weight", "myMethods")
mySys = Systematic("myUserSys", ["nominalWeights"], 1.1, 0.8, "user", "myMethods")
```

where `myTreeSys` and `myWeightSys` rely on the tree-based and weight-based methods. `myUserSys` relies on the floating-point input discussed above, and, in this example, has asymmetric up and down input uncertainty values of 10 % and 20 %. The last argument `myMethods` is discussed below. Systematic objects are then associated to `Sample` or `Channel` objects with:

```
mySample.addSystematic(mySys)
myChannel.addSystematic(mySys)
```

As illustrated in fig. A.1, correlated systematic uncertainties are declared simply by giving them identical names in the corresponding `Samples`. Otherwise, they are treated as uncorrelated.

When turning the above into nuisance parameters, additional input is required to specify the interpolation (extrapolation) algorithm and constraint parametrisation for each systematic uncertainty. This is done with the argument `myMethods` above. Several possible analysis strategies can be envisaged, requiring a detailed discussion, case by case. To address this, HistFitter does not enforce a specific strategy but provides users with as many methods as possible to cover all reasonable possibilities.

Table A.1 · Sub-set of the systematic methods available in HistFitter. The methods are specified by a string argument containing a combination of basic HistFactory methods and optional HistFitter keywords: `norm`, `OneSide` and/or `Sym`. Systematic objects can be built with tree-based, weight-based, floating-point or histogram input methods in all cases.

Basic systematic methods in HistFactory	
`overallSys`	uncertainty of the global normalisation, not affecting the shape
`histoSys`	correlated uncertainty of shape and normalisation
`shapeSys`	uncertainty of statistical nature applied to a sum of samples, bin by bin
Additional systematic methods in HistFitter	
`overallNormSys`	`overallSys` constrained to conserve total event count in a list of region(s)
`normHistoSys`	`histoSys` constrained to conserve total event count in a list of region(s)
`normHistoSysOneSide`	one-sided `normHistoSys` uncertainty built from tree- or weight-based inputs
`normHistoSysOneSideSym`	symmetrised `normHistoSysOneSide`
`overallHistoSys`	factorised normalisation shape and uncertainty, described with `overallSys` and `histoSys` respectively
`overallNormHistoSys`	`overallHistoSys` in which the shape uncertainty is modelled with a `normHistoSys` and the global normalisation uncertainty is modelled with an `overallSys`
`shapeStat`	`shapeSys` applied to an individual sample

The basic methods for systematic uncertainties defined in HistFactory are called: `overallSys`, `histoSys` and `shapeSys`, and are listed in the top half of table A.1. Further details about these types are given in [264].

To respond to various use cases encountered during real-life analysis of ATLAS Run 1 data, HistFitter provides additional systematic methods derived from the basic HistFactory methods. A sub-set of the systematic methods available in HistFitter is listed in the bottom half of table A.1.

These methods can be specified with combinations of the `norm`, `OneSide` and `Sym` keywords. The `norm` keyword indicates that the total event count is required to remain invariant in a user-specified list of normalisation region(s) when constructing up/down variations and describes uncertainties of the shape only. Such a systematic uncertainty is transformed from an uncertainty on event counts in each region into a systematic uncertainty on the transfer factors. The `OneSide` and `Sym` keywords indicate that a one-sided or a symmetrised uncertainty should be constructed when using tree-based or weight-based inputs.

A.2 Extrapolation of fit results and error propagation

This section discusses the extrapolation of coherently normalised background estimates from the control region(s) to each signal or validation region, as obtained from the background-only fit[1]. The basic strategy behind the background extrapolation approach is to share the background parameters of the PDF in all the different regions.

[1] The various fits have been discussed already in chapter 5.

As discussed in §9.3.1, a likelihood function is built from both the parametric model and the observed data. In other words, a background-only fit to the control regions technically requires a PDF modelling only these regions. On the other hand, the extrapolation of the normalised background processes from the control regions to the signal and validation regions, which uses the background-only fit result, requires a *different* PDF containing all these regions.

In HistFitter, the technical construction of these various PDFS proceeds as follows. First a total PDF describing *all* regions is constructed using HistFactory. This PDF is not used to fit the data, as the likelihood is unaware of the concept of different region types. HistFitter has dedicated functions to deconstruct and reconstruct PDFS, based on the various channel types.

To perform the background-only fit, the total PDF is deconstructed and then reconstructed describing only the control regions. The result of the background-only fit is stored, containing the values, the errors and the covariance matrix corresponding to all fit parameters. After this fit, the normalised backgrounds are extrapolated to the signal regions (or validation regions). For this HistFitter deconstructs and reconstructs the total PDF, now describing the control regions and the signal regions (or validation regions). The background-only fit result is then incorporated into this PDF to obtain the extrapolated background prediction b in any signal or validation region.

Once the background-only fit to data has been performed and the total PDF been reconstructed, an estimate of the uncertainty on an extrapolated background prediction $\sigma_{b,\,\mathrm{tot}}$ can be calculated. The determination of this error requires the uncertainties and correlations from the stored fit result. The total error on b is calculated using the error propagation formula

$$\sigma^2_{b,\,\mathrm{tot}} = \sum_i^n \left(\frac{\partial b}{\partial \eta_i}\right)^2 \sigma^2_{\eta_i} + \sum_i^n \sum_{j \neq i}^n \rho_{ij} \left(\frac{\partial b}{\partial \eta_i}\right)\left(\frac{\partial b}{\partial \eta_j}\right) \sigma_{\eta_i} \sigma_{\eta_j}\,, \tag{A.1}$$

where η_i are the fit parameters, consisting of normalisation factors μ_k and nuisance parameters θ_l, ρ_{ij} is the correlation coefficient, between η_i and η_j, and σ_{η_i} is the standard deviation of η_i. Any partial derivatives to b are evaluated on-the-fly.

The after-fit parameter values, uncertainties and correlations are saved in the class `RooFitResult`. As an example, consider a background-only fit result (from control regions only) that needs to be extrapolated to a signal region. The total PDF (consisting of control and signal regions) contains a set of parameters that can be subdivided as follows:

1. a large set of parameters shared between control regions and the signal region, $\boldsymbol{\eta}_{\mathrm{shared}}$, for example the background normalisation factors and most systematic uncertainties;
2. a subset of parameters connected only to the control regions, $\boldsymbol{\eta}_{\mathrm{CR}}$, for example the uncertainties due to limited Monte Carlo statistics in the control regions;
3. another subset of parameters connected only to the signal region, $\boldsymbol{\eta}_{\mathrm{SR}}$.

When the fit is performed with the (deconstructed) control-regions-only PDF, only the parameters $\boldsymbol{\eta}_{\mathrm{shared}}$ and $\boldsymbol{\eta}_{\mathrm{CR}}$ are evaluated and saved in the fit result.

Hence when this fit result is propagated to the signal region, the estimated error only contains the parameters that are shared between the control regions and the signal region, and thus is

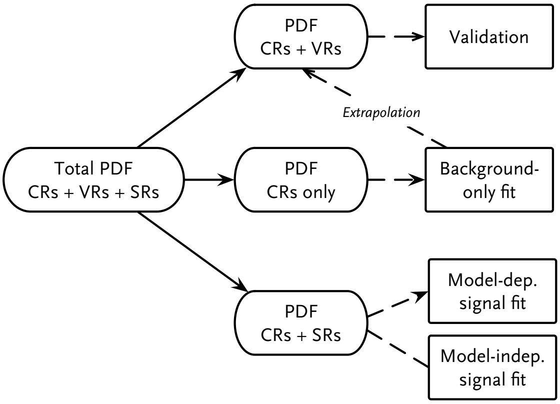

Fig. A.3 · An overview of the various PDFS HistFitter uses internally, together with their typical use. The large PDF for all regions is automatically deconstructed into separate, smaller ones defined on those subsets of regions depending on the fit and/or statistical test performed. The PDFS are indicated as rounded squares, and the fit configurations as squares.

incomplete. The uncertainties corresponding to η_{SR} are not picked up in (A.1), as these are not contained in the fit result.

HistFitter uses the class `RooExpandedFitResult`, an expanded version of the `RooFitResult` class that contains all of the nuisance parameters of all regions in the extrapolation PDF, even if these are not used in the background-only fit configuration. This expansion makes it possible to extrapolate all of the shared parameters while keeping the unshared parameters, such that a complete error can be calculated in any region. In the expanded fit result, the correlations between the shared and unshared parameters are set to zero. Using the `RooExpandedFitResult` class the validation regions can now provide a rigorous statistical cross check. If the background-only fit to the control regions finds that changing the background normalisation and/or shape parameters of a kinematic distribution gives a better description of the data, this will be reflected automatically in the validation regions. Likewise, if the uncertainty on these parameters has a strong impact, and is reduced by the fit, the effect will be readily propagated.

In HistFitter, the before-fit parameter values, errors and correlations are stored in an expanded fit result object as well. The before- and after-fit background value and uncertainty predictions can thus be easily compared. A few assumptions are made to construct this before-fit object. First, all correlations are set to zero prior to the fit, effectively taking out the second term of (A.1). Second, the errors on the normalisation factors of the background processes are unknown prior to the fit, and hence set to zero.

The various fit strategies are illustrated in fig. A.3, together with the PDF restructuring detailed in this section. The various constructed PDFS are indicated as rounded squares and the fit configurations as squares on the right-hand side.

APPENDIX TWO

Example HistFitter configuration

An example configuration file for HistFitter is shown here, using the programmable components of §A.1. The example configuration illustrates a single-bin counting experiment. In short, a single channel SR is defined, containing two background samples A and B, besides the data sample Data. Two systematic uncertainties are defined, treeSys and weightSys, where the latter is only applied to sample A. There is also a luminosity uncertainty, applied to both samples.

Two fit configuration objects are created, one for a discovery hypothesis test, which is labelled Discovery, and one for a model-dependent exclusion fit, labelled Exclusion. These contain a (dummy) signal sample (predicting 1 signal event) and a specific signal sample, called Signal, respectively. Several additional options and comments are given in-line.

```
from configManager import configMgr
from ROOT import kBlack, kGreen, kAzure, kMagenta, kPink
from configWriter import fitConfig, Measurement, Channel, Sample
from systematic import Systematic

# Parameters for hypothesis test and upper limit
configMgr.calculatorType = 2 # Asymptotic
configMgr.testStatType = 3 # Frequentist
configMgr.nPoints = 20 # #points to use in UL scan

# Now we start to build the data model
configMgr.analysisName = "MyOneBinExample"
configMgr.histCacheFile = "data/"+configMgr.analysisName+".root"
configMgr.outputFileName = "results/"+configMgr.analysisName+"_Output.root"

# Scaling calculated by outputLumi / inputLumi
configMgr.inputLumi = 0.001 # Luminosity of input after weighting
configMgr.outputLumi = 4.713 # Luminosity required for output histograms
configMgr.setLumiUnits("fb-1")
configMgr.blindSR = False
configMgr.useSignalInBlindedData = False

# Set the files to read from, use the intermediate cache file if not reading trees
bgdFiles = []
if configMgr.readFromTree:
    bgdFiles.append("fileA.root")
    bgdFiles.append("fileB.root")
else:
    bgdFiles = [configMgr.histCacheFile]
    pass
configMgr.setFileList(bgdFiles)

```

```
# Dictionary of cuts to place on input trees
configMgr.cutsDict["SR"] = "leptonPt > 20 && ( (met > 160 && met/meff > 0.2) || met > 1000)"

# Tuples of nominal weights
configMgr.weights = ("genWeight", "eventWeight", "leptonWeight", "triggerWeight")

# Weight-based systematics: provide up and down weights, and a systematic type
highWeights = ("eventWeight", "weightUp")
lowWeights = ("eventWeight", "weightDown")
weightSys = Systematic("KtScaleTop", configMgr.weights, highWeights, lowWeights, "weight", "
     overallSys")

# Tree-based: provide name, plus 3 suffixes for nominal, up and down, and a systematic type
treeSys = Systematic("SYS", "_NoSys", "_SYS_up", "_SYS_down", "tree", "overallSys")
configMgr.nomName = "_NoSys"

# List of samples and their plotting colours
aSample = Sample("A", kGreen)
bSample = Sample("B", kAzure)
dataSample = Sample("Data", kBlack)
dataSample.setData()

# Signal model independent fit config (aka Discovery fit)
discoveryFitConfig = configMgr.addFitConfig("Discovery")
meas = discoveryFitConfig.addMeasurement(name="NormalMeasurement", lumi=1.0, lumiErr=0.039)
meas.addPOI("mu_SIG")

discoveryFitConfig.addSamples([aSample, bSample, dataSample]) # Add samples

# Systematics: add weightSys to one sample, treeSys to all
discoveryFitConfig.getSample("A").addSystematic(weightSys)
discoveryFitConfig.addSystematic(treeSys)

SR = discoveryFitConfig.addChannel("cuts", ["SR"], 1, 0.5, 1.5)
discoveryFitConfig.setSignalChannels([SR])
SR.addDiscoverySamples(["SIG"], [1.], [0.], [100.], [kMagenta]) # Dummy sample of 1

# Signal model dependent fit config (aka Exclusion fit)
exclusionFitConfig = configMgr.addFitConfig("Exclusion")
meas = exclusionFitConfig.addMeasurement(name="NormalMeasurement", lumi=1.0, lumiErr=0.039)
meas.addPOI("mu_SIG")

exclusionFitConfig.addSamples([aSample, bSample, dataSample])
exclusionFitConfig.getSample("A").addSystematic(weightSys)
exclusionFitConfig.addSystematic(treeSys)
SR = exclusionFitConfig.addChannel("cuts", ["SR"], 1, 0.5, 1.5)
exclusionFitConfig.setSignalChannels([SR])

sigSample = Sample("Signal", kPink)
sigSample.setFileList(["signal.root"]) # Signal sample to test
sigSample.setNormByTheory()
sigSample.setNormFactor("mu_SIG", 1., 0., 5.)
exclusionFitConfig.addSamples(sigSample)
exclusionFitConfig.setSignalSample(sigSample)
```

Listing B.1 · MyOneBinExample.py

Bibliography

[1] J. Thomson, *Cathode Rays*, Phil. Mag. **44** (1897) 293–316. (Cited on page 3.)

[2] E. Rutherford, *The scattering of alpha and beta particles by matter and the structure of the atom*, Phil. Mag. **21** (1911) 669–688. (Cited on page 3.)

[3] P. Dirac, *The Quantum Theory of the Electron*, Proc. Roy. Soc. A **117** (1928) 610–624. (Cited on page 3.)

[4] P. Dirac, *A Theory of Electrons and Protons*, Proc. Roy. Soc. A **126** (1930) 360–365. (Cited on page 3.)

[5] C. D. Anderson, *The Positive Electron*, Phys. Rev. **43** (1933) 491–494. (Cited on page 3.)

[6] J. Chadwick, *Possible Existence of a Neutron*, Nature **129** (1932) 312. (Cited on page 3.)

[7] S. H. Neddermeyer and C. D. Anderson, *Note on the Nature of Cosmic-Ray Particles*, Phys. Rev. **51** (1937) 884–886. (Cited on page 3.)

[8] E. Fermi, *Versuch einer Theorie der β-Strahlen*, Z. Phys. **88** (1934) 161–177. (Cited on page 3.)

[9] M. Gell-Mann, *A Schematic Model of Baryons and Mesons*, Phys. Lett. **8** (1964) 214–215. (Cited on page 3.)

[10] G. Zweig, *An $SU(3)$ model for strong interaction symmetry and its breaking*, Tech. Rep. CERN-TH-401, CERN, Geneva, 1964. (Cited on page 3.)

[11] V. E. Barnes et al., *Observation of a Hyperon with Strangeness Minus Three*, Phys. Rev. Lett. **12** (1964) 204–206. (Cited on page 3.)

[12] S. Weinberg, *A Model of Leptons*, Phys. Rev. Lett. **19** (1967) 1264–1266. (Cited on page 3.)

[13] A. Salam, *Weak and Electromagnetic Interactions*, Conf. Proc. **C680519** (1968) 367–377. (Cited on page 3.)

[14] R. P. Feynman, *Mathematical Formulation of the Quantum Theory of Electromagnetic Interaction*, Phys. Rev. **80** (1950) 440–457. (Cited on page 3.)

[15] J. Schwinger, *Quantum Electrodynamics. I. A Covariant Formulation*, Phys. Rev. **74** (1948) 1439–1461. (Cited on page 3.)

[16] S. Tomonaga, *On a Relativistically Invariant Formulation of the Quantum Theory of Wave Fields*, Prog. Theor. Phys. **1** (1946) 27–42. (Cited on page 3.)

[17] S. Glashow, *Partial Symmetries of Weak Interactions*, Nucl. Phys. **22** (1961) 579–588. (Cited on page 3.)

[18] P. W. Anderson, *Plasmons, Gauge Invariance, and Mass*, Phys. Rev. **130** (1963) 439–442. (Cited on pages 3 and 6.)

[19] P. W. Higgs, *Broken Symmetries and the Masses of Gauge Bosons*, Phys. Rev. Lett. **13** (1964) 508–509. (Cited on pages 3 and 6.)

[20] F. Englert and R. Brout, *Broken Symmetry and the Mass of Gauge Vector Mesons*, Phys. Rev. Lett. **13** (1964) 321–323. (Cited on pages 3 and 6.)

[21] G. S. Guralnik, C. R. Hagen, and T. W. B. Kibble, *Global Conservation Laws and Massless Particles*, Phys. Rev. Lett. **13** (1964) 585–587. (Cited on pages 3 and 6.)

[22] G. 't Hooft and M. Veltman, *Regularization and renormalization of gauge fields*, Nucl. Phys. **B 44** (1972) 189–213. (Cited on pages 3 and 9.)

[23] UA1 Collaboration, *Experimental observation of isolated large transverse energy electrons with associated missing energy at* $\sqrt{s}$ *540 GeV*, Phys. Lett. **B 122** (1983) 103–116. (Cited on page 3.)

[24] UA2 Collaboration, *Observation of single isolated electrons of high transverse momentum in events with missing transverse energy at the CERN* $\bar{p}p$ *collider*, Phys. Lett. **B 122** (1983) 476–485. (Cited on page 3.)

[25] UA1 Collaboration, *Experimental observation of lepton pairs of invariant mass around 95 GeV/c*^{2} *at the CERN SPS collider*, Phys. Lett. **B 126** (1985) 398–410. (Cited on page 3.)

[26] UA2 Collaboration, *Evidence for* $Z^0 \to e^+e^-$ *at the CERN* $\bar{p}p$ *collider*, Phys. Lett. **B 129** (1983) 130–140. (Cited on page 3.)

[27] H. Fritzsch, M. Gell-Mann, and H. Leutwyler, *Advantages of the color octet gluon picture*, Phys. Lett. **B 47** (1973) 365–368. (Cited on page 3.)

[28] D. J. Gross and F. Wilczek, *Ultraviolet Behavior of Non-Abelian Gauge Theories*, Phys. Rev. Lett. **30** (1973) 1343–1346. (Cited on pages 3 and 8.)

[29] H. D. Politzer, *Reliable Perturbative Results for Strong Interactions?*, Phys. Rev. Lett. **30** (1973) 1346–1349. (Cited on pages 3 and 8.)

[30] TASSO Collaboration, *Evidence for planar events in e+e- annihilation at high energies*, Phys. Lett. **B 86** (1979) 243–249. (Cited on page 3.)

[31] H1 and ZEUS Collaboration, *Combined Measurement and QCD Analysis of the Inclusive e+- p Scattering Cross Sections at HERA*, JHEP **1001** (2010) 109, `arXiv:0911.0884 [hep-ex]`. (Cited on pages 3 and 9.)

[32] ATLAS Collaboration, *Observation of a new particle in the search for the Standard Model Higgs boson with the ATLAS detector at the LHC*, Phys. Lett. **B 716** (2012) 1–29, `arXiv:1207.7214 [hep-ex]`. (Cited on page 3.)

[33] CMS Collaboration, *Observation of a new boson at a mass of 125 GeV with the CMS experiment at the LHC*, Phys. Lett. **B 716** (2012) 30–61, `arXiv:1207.7235 [hep-ex]`. (Cited on page 3.)

[34] ATLAS Collaboration, *Measurement of the Higgs boson mass from the* $H \to \gamma\gamma$ *and* $H \to ZZ^* \to 4\ell$ *channels with the ATLAS detector using 25 fb*$^{-1}$ *of pp collision data*, Phys. Rev. **D 90** (2014) 052004, `arXiv:1406.3827 [hep-ex]`. (Cited on page 3.)

[35] CMS Collaboration, *Precise determination of the mass of the Higgs boson and studies of the compatibility of its couplings with the standard model*, Tech. Rep. CMS-PAS-HIG-14-009, CERN, Geneva, 2014. (Cited on page 3.)

[36] H. W. Baer and X. Tata, *Weak scale supersymmetry: from superfields to scattering events*. Cambridge Univ. Press, Cambridge, 2006. (Cited on pages 4, 12, 15, 18, 19, and 22.)

[37] S. P. Martin, *A Supersymmetry primer*, Adv. Ser. Direct. High Energy Phys. **21** (2010) 1–153, `arXiv:hep-ph/9709356 [hep-ph]`. (Cited on pages 4, 15, 16, 17, 18, and 19.)

[38] I. J. Aitchison, *Supersymmetry and the MSSM: An Elementary introduction*, `arXiv:hep-ph/0505105 [hep-ph]`. (Cited on pages 4 and 15.)

[39] A. Einstein, *Zur Elektrodynamik bewegter Körper*, Ann. Phys. **322** (1905) 891–921. (Cited on page 4.)

[40] E. Schrödinger, *Quantisierung als Eigenwertproblem*, Ann. Phys. **385** (1926) 437–490. (Cited on page 4.)

[41] W. Heisenberg, *Über quantentheoretische Umdeutung kinematischer und mechanischer Beziehungen*, Z. Phys. **33** (1925) 879–893. (Cited on page 4.)

[42] F. Halzen and A. D. Martin, *Quarks and Leptons: An Introductory Course In Modern Particle Physics*. John Wiley & Sons, New York, 1984. (Cited on page 4.)

[43] M. E. Peskin and D. V. Schroeder, *An Introduction to Quantum Field Theory*. Westview Press, Boulder, 1995. (Cited on pages 4 and 9.)

[44] W. Cottingham and D. Greenwood, *An Introduction to the Standard Model of Particle Physics*. Cambridge Univ. Press, Cambridge, 2007. (Cited on page 4.)

[45] N. Cabibbo, *Unitary Symmetry and Leptonic Decays*, Phys. Rev. Lett. **10** (1963) 531–533. (Cited on page 8.)

[46] M. Kobayashi and T. Maskawa, *CP-Violation in the Renormalizable Theory of Weak Interaction*, Prog. Theor. Phys. **49** (1973) 652–657. (Cited on page 8.)

[47] H1 Collaboration, *Measurement of inclusive jet production in deep-inelastic scattering at high Q^2 and determination of the strong coupling*, Phys. Lett. **B 653** (2007) 134–144, arXiv:0706.3722 [hep-ex]. (Cited on page 9.)

[48] ZEUS Collaboration, *Inclusive-jet and dijet cross-sections in deep inelastic scattering at HERA*, Nucl. Phys. **B 765** (2007) 1–30, arXiv:hep-ex/0608048 [hep-ex]. (Cited on page 9.)

[49] ZEUS Collaboration, *Inclusive jet cross-sections in the Breit frame in neutral current deep inelastic scattering at HERA and determination of α_s*, Phys. Lett. **B 547** (2002) 164–180, arXiv:hep-ex/0208037 [hep-ex]. (Cited on page 9.)

[50] DØ Collaboration, *Measurement of the inclusive jet cross-section in $p\bar{p}$ collisions at $\sqrt{s} = 1.96$ TeV*, Phys. Rev. Lett. **101** (2008) 062001, arXiv:0802.2400 [hep-ex]. (Cited on page 9.)

[51] CDF Collaboration, *Measurement of the Inclusive Jet Cross Section using the k_T algorithm in $p\bar{p}$ Collisions at $\sqrt{s} = 1.96$ TeV with the CDF II Detector*, Phys. Rev. **D 75** (2007) 092006, arXiv:hep-ex/0701051 [hep-ex]. (Cited on page 9.)

[52] CDF Collaboration, *Measurement of the forward-backward charge asymmetry from $W \to e\nu$ production in $p\bar{p}$ collisions at $\sqrt{s} = 1.96$ TeV*, Phys. Rev. **D 71** (2005) 051104, arXiv:hep-ex/0501023 [hep-ex]. (Cited on page 9.)

[53] DØ Collaboration, *Measurement of the shape of the boson rapidity distribution for $p\bar{p} \to Z/\gamma^* \to e^+e^- + X$ events produced at $\sqrt{s}$ of 1.96 TeV*, Phys. Rev. **D 76** (2007) 012003, arXiv:hep-ex/0702025 [hep-ex]. (Cited on page 9.)

[54] Y. L. Dokshitzer, *Calculation of the Structure Functions for Deep Inelastic Scattering and $e^+ e^-$ Annihilation by Perturbation Theory in Quantum Chromodynamics.*, Sov. Phys. JETP **46** (1977) 641–653. (Cited on page 9.)

[55] V. Gribov and L. Lipatov, *$e^+ e^-$ pair annihilation and deep inelastic e p scattering in perturbation theory*, Sov. J. Nucl. Phys. **15** (1972) 675–684. (Cited on page 9.)

[56] V. Gribov and L. Lipatov, *Deep inelastic e p scattering in perturbation theory*, Sov. J. Nucl. Phys. **15** (1972) 438–450. (Cited on page 9.)

[57] G. Altarelli and G. Parisi, *Asymptotic Freedom in Parton Language*, Nucl. Phys. **B 126** (1977) 298. (Cited on page 9.)

[58] A. Martin, W. Stirling, R. Thorne, and G. Watt, *Parton distributions for the LHC*, Eur. Phys. J. **C 63** (2009) 189–285, arXiv:0901.0002 [hep-ph]. (Cited on pages 9, 38, and 61.)

[59] P. M. Nadolsky, H.-L. Lai, Q.-H. Cao, J. Huston, J. Pumplin, et al., *Implications of CTEQ global analysis for collider observables*, Phys. Rev. **D 78** (2008) 013004, arXiv:0802.0007 [hep-ph]. (Cited on pages 9, 38, 61, and 132.)

[60] R. D. Ball, L. Del Debbio, S. Forte, A. Guffanti, J. I. Latorre, et al., *A first unbiased global NLO determination of parton distributions and their uncertainties*, Nucl. Phys. **B 838** (2010) 136–206, arXiv:1002.4407 [hep-ph]. (Cited on page 9.)

[61] J. C. Collins, D. E. Soper, and G. F. Sterman, *Factorization of Hard Processes in QCD*, Adv. Ser. Direct. High Energy Phys. **5** (1988) 1–91, arXiv:hep-ph/0409313 [hep-ph]. (Cited on page 9.)

[62] S. Weinberg, *The quantum theory of fields. Vol. 2: Modern applications*. Cambridge Univ. Press, Cambridge, 1996. (Cited on page 9.)

[63] M. Kramer, A. Kulesza, R. van der Leeuw, M. Mangano, S. Padhi, et al., *Supersymmetry production cross sections in pp collisions at $\sqrt{s} = 7$ TeV*, arXiv:1206.2892 [hep-ph]. (Cited on pages 9, 64, and 138.)

[64] G. Degrassi, S. Di Vita, J. Elias-Miro, J. R. Espinosa, G. F. Giudice, et al., *Higgs mass and vacuum stability in the Standard Model at NNLO*, JHEP **1208** (2012) 098, arXiv:1205.6497 [hep-ph]. (Cited on page 12.)

[65] M. Shaposhnikov and D. Zenhausern, *Quantum scale invariance, cosmological constant and hierarchy problem*, Phys. Lett. **B 671** (2009) 162–166, arXiv:0809.3406 [hep-th]. (Cited on page 11.)

[66] A. Boyarsky, O. Ruchayskiy, and M. Shaposhnikov, *The Role of sterile neutrinos in cosmology and astrophysics*, Ann. Rev. Nucl. Part. Sci. **59** (2009) 191–214, arXiv:0901.0011 [hep-ph]. (Cited on page 11.)

[67] L. D. Landau in *Niels Bohr and the Development of Physics*, W. Pauli, L. Rosenfeld, and V. Weisskopf, eds. Pergamon Press, London, 1955. (Cited on page 11.)

[68] H. Gies and J. Jaeckel, *Renormalization flow of QED*, Phys. Rev. Lett. **93** (2004) 110405, arXiv:hep-ph/0405183 [hep-ph]. (Cited on page 11.)

[69] K. Lane, *Two lectures on technicolor*, arXiv:hep-ph/0202255 [hep-ph]. (Cited on page 12.)

[70] J. L. Hewett and M. Spiropulu, *Particle physics probes of extra space-time dimensions*, Ann. Rev. Nucl. Part. Sci. **52** (2002) 397–424, arXiv:hep-ph/0205106 [hep-ph]. (Cited on page 12.)

[71] F. Zwicky, *Die Rotverschiebung von extragalaktischen Nebeln*, Helv. Phys. Acta **6** (1933) 110–127. (Cited on page 12.)

[72] V. Rubin, N. Thonnard, and W.K. Ford Jr., *Rotational properties of 21 SC galaxies with a large range of luminosities and radii, from NGC 4605 (R = 4kpc) to UGC 2885 (R = 122 kpc)*, Astrophys. J. **238** (1980) 471. (Cited on page 12.)

[73] T. van Albada, J. N. Bahcall, K. Begeman, and R. Sancisi, *The Distribution of Dark Matter in the Spiral Galaxy NGC-3198*, Astrophys. J. **295** (1985) 305–313. (Cited on pages 12, 189, and 201.)

[74] Planck Collaboration, *Planck 2013 results – XVI. Cosmological parameters*, Astron. Astrophys. **571** (2014) A16, arXiv:1303.5076 [astro-ph.CO]. (Cited on pages 12, 22, and 113.)

[75] S. Coleman and J. Mandula, *All Possible Symmetries of the S Matrix*, Phys. Rev. **159** (1967) 1251–1256. (Cited on page 13.)

[76] R. Haag, J. T. Łopuszański, and M. Sohnius, *All possible generators of supersymmetries of the S-matrix*, Nucl. Phys. **B 88** (1975) 257–274. (Cited on page 13.)

[77] J. Wess and B. Zumino, *Supergauge transformations in four dimensions*, Nucl. Phys. **B 70** (1974) 39–50. (Cited on page 13.)

[78] Super-Kamiokande Collaboration, *Search for proton decay via $p \to \nu K^+$ using 260 kiloton year data of Super-Kamiokande*, Phys. Rev. **D 90** (2014) 072005. (Cited on page 17.)

[79] A. Salam and J. Strathdee, *Superfields and Fermi-Bose symmetry*, Phys. Rev. **D 11** (1975) 1521–1535. (Cited on page 17.)

[80] E. Cremmer, P. Fayet, and L. Girardello, *Gravity Induced Supersymmetry Breaking and Low-Energy Mass Spectrum*, Phys. Lett. **B 122** (1983) 41. (Cited on page 17.)

[81] G. Giudice and R. Rattazzi, *Theories with gauge mediated supersymmetry breaking*, Phys. Rept. **322** (1999) 419–499, arXiv:hep-ph/9801271 [hep-ph]. (Cited on page 17.)

[82] J. L. Feng and T. Moroi, *Supernatural supersymmetry: Phenomenological implications of anomaly mediated supersymmetry breaking*, Phys. Rev. **D 61** (2000) 095004, arXiv:hep-ph/9907319 [hep-ph]. (Cited on page 17.)

[83] R. Barbieri and G. Giudice, *Upper Bounds on Supersymmetric Particle Masses*, Nucl. Phys. **B 306** (1988) 63. (Cited on page 18.)

[84] A. H. Chamseddine, R. Arnowitt, and P. Nath, *Locally Supersymmetric Grand Unification*, Phys. Rev. Lett. **49** (1982) 970–974. (Cited on page 19.)

[85] G. L. Kane, C. Kolda, L. Roszkowski, and J. D. Wells, *Study of constrained minimal supersymmetry*, Phys. Rev. **D 49** (1994) 6173–6210. (Cited on page 19.)

[86] D. Alves et al., *Simplified Models for LHC New Physics Searches*, J. Phys. **G 39** (2012) 105005, arXiv:1105.2838 [hep-ph]. (Cited on page 20.)

[87] J. Alwall, P. Schuster, and N. Toro, *Simplified Models for a First Characterization of New Physics at the LHC*, Phys. Rev. **D 79** (2009) 075020, arXiv:0810.3921 [hep-ph]. (Cited on page 20.)

[88] N. Arkani-Hamed and S. Dimopoulos, *Supersymmetric unification without low energy supersymmetry and signatures for fine-tuning at the LHC*, JHEP **0506** (2005) 073, arXiv:hep-th/0405159 [hep-th]. (Cited on page 20.)

[89] R. M. Barnett, J. F. Gunion, and H. E. Haber, *Gluino Decay Patterns and Signatures*, Phys. Rev. **D 37** (1988) 1892. (Cited on page 20.)

[90] W. Kilian, T. Plehn, P. Richardson, and E. Schmidt, *Split supersymmetry at colliders*, Eur. Phys. J. **C 39** (2005) 229–243, arXiv:hep-ph/0408088 [hep-ph]. (Cited on page 20.)

[91] C. Gutschow and Z. Marshall, *Setting limits on supersymmetry using simplified models*, arXiv:1202.2662 [hep-ex]. (Cited on page 20.)

[92] D. S. Alves, E. Izaguirre, and J. G. Wacker, *Where the Sidewalk Ends: Jets and Missing Energy Search Strategies for the 7 TeV LHC*, JHEP **1110** (2011) 012, arXiv:1102.5338 [hep-ph]. (Cited on pages 21 and 123.)

[93] CDF Collaboration, *Inclusive Search for Squark and Gluino Production in $p\bar{p}$ Collisions at $\sqrt{s} = 1.96$ TeV*, Phys. Rev. Lett. **102** (2009) 121801. (Cited on page 21.)

[94] DØ Collaboration, *Search for squarks and gluinos in events with jets and missing transverse energy using 2.1 fb^{-1} of $p\bar{p}$ collision data at $\sqrt{s} = 1.96$ TeV*, Phys. Lett. **B 660** (2008) 449–457, arXiv:0712.3805 [hep-ex]. (Cited on page 21.)

[95] LEP2 SUSY Working group, *Combined LEP Chargino Results, up to 208 GeV for large m_0*, Tech. Rep. LEPSUSYWG/01-03.1, CERN, Geneva, 2001. (Cited on page 21.)

[96] LEP2 SUSY Working group, *Combined LEP Chargino Results, up to 208 GeV for low DM*, Tech. Rep. LEPSUSYWG/02-04.1, CERN, Geneva, 2002. (Cited on page 21.)

[97] DELPHI Collaboration, *Searches for supersymmetric particles in $e^+ e^-$ collisions up to 208 GeV and interpretation of the results within the MSSM*, Eur. Phys. J. **C 31** (2003) 421–479, arXiv:hep-ex/0311019 [hep-ex]. (Cited on page 21.)

[98] ALEPH Collaboration, *Absolute lower limits on the masses of selectrons and sneutrinos in the MSSM*, Phys. Lett. **B 544** (2002) 73–88, arXiv:hep-ex/0207056 [hep-ex]. (Cited on page 21.)

[99] H. K. Dreiner, S. Heinemeyer, O. Kittel, U. Langenfeld, A. M. Weber, et al., *Mass Bounds on a Very Light Neutralino*, Eur. Phys. J. **C 62** (2009) 547–572, arXiv:0901.3485 [hep-ph]. (Cited on page 21.)

[100] DAMA Collaboration, *First results from DAMA/LIBRA and the combined results with DAMA/NaI*, Eur. Phys. J. **C 56** (2008) 333–355, arXiv:0804.2741 [astro-ph]. (Cited on page 21.)

[101] C. E. Aalseth et al., *Search for an Annual Modulation in a p-Type Point Contact Germanium Dark Matter Detector*, Phys. Rev. Lett. **107** (2011) 141301, arXiv:1106.0650 [astro-ph.CO]. (Cited on page 21.)

[102] O. Adriani et al., *Cosmic-Ray Positron Energy Spectrum Measured by PAMELA*, Phys. Rev. Lett. **111** (2013) 081102. (Cited on page 21.)

[103] AMS Collaboration, *Electron and Positron Fluxes in Primary Cosmic Rays Measured with the Alpha Magnetic Spectrometer on the International Space Station*, Phys. Rev. Lett. **113** (2014) 121102. (Cited on page 21.)

[104] AMS Collaboration, *High Statistics Measurement of the Positron Fraction in Primary Cosmic Rays of 0.5–500 GeV with the Alpha Magnetic Spectrometer on the International Space Station*, Phys. Rev. Lett. **113** (2014) 121101. (Cited on page 21.)

[105] XENON100 Collaboration, *Dark Matter Results from 225 Live Days of XENON100 Data*, Phys. Rev. Lett. **109** (2012) 181301, arXiv:1207.5988 [astro-ph.CO]. (Cited on pages 21, 109, and 113.)

[106] LUX Collaboration, *First results from the LUX dark matter experiment at the Sanford Underground Research Facility*, Phys. Rev. Lett. **112** (2014) 091303, arXiv:1310.8214 [astro-ph.CO]. (Cited on pages 21 and 109.)

[107] WMAP Collaboration, *Nine-Year Wilkinson Microwave Anisotropy Probe (WMAP) Observations: Cosmological Parameter Results*, Astrophys. J. Suppl. **208** (2013) 19, arXiv:1212.5226 [astro-ph.CO]. (Cited on page 22.)

[108] C. Beskidt, W. de Boer, T. Hanisch, E. Ziebarth, V. Zhukov, et al., *Constraints on Supersymmetry from Relic Density compared with future Higgs Searches at the LHC*, Phys. Lett. **B 695** (2011) 143–148, arXiv:1008.2150 [hep-ph]. (Cited on page 22.)

[109] Particle Data Group Collaboration, J. Beringer et al., *Review of Particle Physics (RPP)*, Phys. Rev. **D 86** (2012) 010001. (Cited on pages 22, 47, 60, and 113.)

[110] Y. Amhis et al., *Averages of B-Hadron, C-Hadron, and tau-lepton properties as of early 2012*, arXiv:1207.1158 [hep-ex]. (Cited on pages 22 and 113.)

[111] LHCb Collaboration, *Measurement of the $B_s^0 \to \mu^+\mu^-$ branching fraction and search for $B^0 \to \mu^+\mu^-$ decays at the LHCb experiment*, Phys. Rev. Lett. **111** (2013) 101805, arXiv:1307.5024 [hep-ex]. (Cited on page 22.)

[112] CMS and LHCb Collaborations, *Combination of results on the rare decays $B^0_{(s)} \to \mu^+\mu^-$ from the CMS and LHCb experiments*, Tech. Rep. CMS-PAS-BPH-13-007, CERN-LHCb-CONF-2013-012, CERN, Geneva, Jun, 2014. (Cited on page 22.)

[113] A. Arbey, M. Battaglia, F. Mahmoudi, and D. Martinez Santos, *Supersymmetry confronts $B_s \to \mu^+\mu^-$: Present and future status*, Phys. Rev. **D 87** (2013) 035026, arXiv:1212.4887 [hep-ph]. (Cited on page 22.)

[114] BaBar Collaboration, *Evidence for an excess of $\bar{B} \to D^{(*)}\tau^-\bar{\nu}_\tau$ decays*, Phys. Rev. Lett. **109** (2012) 101802, arXiv:1205.5442 [hep-ex]. (Cited on page 22.)

[115] Muon G-2 Collaboration, *Final Report of the Muon E821 Anomalous Magnetic Moment Measurement at BNL*, Phys. Rev. **D 73** (2006) 072003, arXiv:hep-ex/0602035 [hep-ex]. (Cited on page 22.)

[116] M. Davier, A. Hoecker, B. Malaescu, and Z. Zhang, *Reevaluation of the Hadronic Contributions to the Muon g−2 and to $\alpha(M_Z^2)$*, Eur. Phys. J. **C 71** (2011) 1515, arXiv:1010.4180 [hep-ph]. (Cited on pages 22 and 113.)

[117] J. L. Feng and K. T. Matchev, *Supersymmetry and the anomalous magnetic moment of the muon*, Phys. Rev. Lett. **86** (2001) 3480–3483, arXiv:hep-ph/0102146 [hep-ph]. (Cited on page 22.)

[118] M. S. Carena and H. E. Haber, *Higgs boson theory and phenomenology*, Prog. Part. Nucl. Phys. **50** (2003) 63–152, arXiv:hep-ph/0208209 [hep-ph]. (Cited on page 22.)

[119] J. Cao, Z. Heng, J. M. Yang, and J. Zhu, *Status of low energy SUSY models confronted with the LHC 125 GeV Higgs data*, JHEP **1210** (2012) 079, arXiv:1207.3698 [hep-ph]. (Cited on page 22.)

[120] L. Evans and P. Bryant, *LHC Machine*, JINST **3** (2008) S08001. (Cited on page 23.)

[121] *LEP design report*. CERN, Geneva, 1984. (Cited on page 23.)

[122] ATLAS Collaboration, *The ATLAS Experiment at the CERN Large Hadron Collider*, JINST **3** (2008) S08003. (Cited on pages 24, 27, 28, 31, 34, and 35.)

[123] CMS Collaboration, *The CMS experiment at the CERN LHC*, JINST **3** (2008) S08004. (Cited on page 24.)

[124] LHCb Collaboration, *The LHCb Detector at the LHC*, JINST **3** (2008) S08005. (Cited on page 24.)

[125] ALICE Collaboration, *The ALICE experiment at the CERN LHC*, JINST **3** (2008) S08002. (Cited on page 24.)

[126] LHCf Collaboration, *The LHCf detector at the CERN Large Hadron Collider*, JINST **3** (2008) S08006. (Cited on page 24.)

[127] MoEDAL Collaboration, *Technical Design Report of the MoEDAL Experiment*, Tech. Rep. CERN-LHCC-2009-006, CERN, Geneva, Jun, 2009. (Cited on page 24.)

[128] TOTEM Collaboration, *The TOTEM Experiment at the CERN Large Hadron Collider*, JINST **3** (2008) S08007. (Cited on page 24.)

[129] C. Lefevre, *LHC: the guide*, https://cds.cern.ch/record/1165534, Jan, 2008. (Cited on page 24.)

[130] P. Lefèvre and D. Möhl, *A low energy accumulation ring of ions for LHC (a feasibility study)*, Tech. Rep. CERN-PS-93-62, CERN, Geneva, Dec, 1993. (Cited on page 25.)

[131] J. Pequenao, *Computer generated image of the whole ATLAS detector*, https://cds.cern.ch/record/1095924, Mar, 2008. (Cited on page 29.)

[132] J. Pequenao and P. Schaffner, *A computer generated image representing how ATLAS detects particles*, https://cds.cern.ch/record/1505342, Jan, 2013. (Cited on page 30.)

[133] ATLAS Collaboration, *ATLAS magnet system: Technical Design Report, 1*. No. ATLAS-TDR-6 in Technical Design Report ATLAS. CERN, Geneva, 1997. (Cited on page 30.)

[134] ATLAS Collaboration, *ATLAS inner detector: Technical Design Report, 1*. No. ATLAS-TDR-4 in Technical Design Report ATLAS. CERN, Geneva, 1997. (Cited on page 31.)

[135] ATLAS Collaboration, *ATLAS inner detector: Technical Design Report, 2*. No. ATLAS-TDR-5 in Technical Design Report ATLAS. CERN, Geneva, 1997. (Cited on page 31.)

[136] J. Pequenao, *Computer generated image of the ATLAS inner detector*, http://cds.cern.ch/record/1095926, Mar, 2008. (Cited on page 32.)

[137] ATLAS Collaboration, *ATLAS pixel detector: Technical Design Report*. No. ATLAS-TDR-11 in Technical Design Report ATLAS. CERN, Geneva, 1998. (Cited on page 31.)

[138] A. Abdesselam et al., *The barrel modules of the ATLAS semiconductor tracker*, Nucl. Instrum. Meth. **A 568** (2006) 642–671. (Cited on page 31.)

[139] A. Abdesselam et al., *The ATLAS semiconductor tracker end-cap module*, Nucl. Instrum. Meth. **A 575** (2007) 353–389. (Cited on page 31.)

[140] ATLAS TRT Collaboration, *The ATLAS TRT Barrel Detector*, JINST **3** (2008) P02014. (Cited on page 32.)

[141] ATLAS TRT Collaboration, *The ATLAS TRT end-cap detectors*, JINST **3** (2008) P10003. (Cited on page 32.)

[142] J. Pequenao, *Computer Generated image of the ATLAS calorimeter*, http://cds.cern.ch/record/1095927, Mar, 2008. (Cited on page 33.)

[143] ATLAS Collaboration, *ATLAS liquid-argon calorimeter: Technical Design Report*. No. ATLAS-TDR-2 in Technical Design Report ATLAS. CERN, Geneva, 1996. (Cited on page 33.)

[144] ATLAS Collaboration, *ATLAS tile calorimeter: Technical Design Report*. No. ATLAS-TDR-3 in Technical Design Report ATLAS. CERN, Geneva, 1996. (Cited on page 34.)

[145] ATLAS Collaboration, *ATLAS detector and physics performance: Technical Design Report, 1*. No. ATLAS-TDR-14 in Technical Design Report ATLAS. CERN, Geneva, 1999. (Cited on page 37.)

[146] ATLAS Collaboration, *ATLAS detector and physics performance: Technical Design Report, 2*. No. ATLAS-TDR-15 in Technical Design Report ATLAS. CERN, Geneva, 1999. (Cited on page 37.)

[147] R. Achenbach et al., *The ATLAS Level-1 Calorimeter Trigger*, JINST **3** (2008) P03001. (Cited on page 37.)

[148] T. Gleisberg, S. Hoeche, F. Krauss, M. Schonherr, S. Schumann, et al., *Event generation with SHERPA 1.1*, JHEP **0902** (2009) 007, arXiv:0811.4622 [hep-ph]. (Cited on pages 39, 61, and 132.)

[149] M. Bahr et al., *Herwig++ Physics and Manual*, Eur. Phys. J. **C 58** (2008) 639–707, arXiv:0803.0883 [hep-ph]. (Cited on pages 39 and 132.)

[150] T. Sjostrand, S. Mrenna, and P. Z. Skands, *PYTHIA 6.4 physics and manual*, JHEP **0605** (2006) 026, arXiv:0603175 [hep-ph]. (Cited on pages 39, 62, and 115.)

[151] T. Sjostrand, S. Mrenna, and P. Z. Skands, *A Brief Introduction to PYTHIA 8.1*, Comput. Phys. Commun. **178** (2008) 852–867, arXiv:0710.3820 [hep-ph]. (Cited on pages 39 and 61.)

[152] J. Alwall, M. Herquet, F. Maltoni, O. Mattelaer, and T. Stelzer, *MadGraph 5 : Going Beyond*, JHEP **1106** (2011) 128, arXiv:1106.0522 [hep-ph]. (Cited on pages 39 and 62.)

[153] M. L. Mangano, M. Moretti, F. Piccinini, R. Pittau, and A. D. Polosa, *ALPGEN, a generator for hard multiparton processes in hadronic collisions*, JHEP **0307** (2003) 001, arXiv:hep-ph/0206293. (Cited on pages 39 and 61.)

[154] S. Frixione and B. R. Webber, *Matching NLO QCD computations and parton shower simulations*, JHEP **0206** (2002) 029, arXiv:0204244 [hep-ph]. (Cited on page 39.)

[155] S. Alioli, P. Nason, C. Oleari, and E. Re, *A general framework for implementing NLO calculations in shower Monte Carlo programs: the POWHEG BOX*, JHEP **1006** (2010) 043, arXiv:1002.2581 [hep-ph]. (Cited on pages 39 and 62.)

[156] S. Agostinelli et al., *GEANT 4, a simulation toolkit*, Nucl. Instrum. Meth. **A 506** (2003) 250. (Cited on page 39.)

[157] J. L. Henning, *SPEC CPU2000: Measuring CPU Performance in the New Millennium*, Computer **33** (2000) 28–35. (Cited on page 39.)

[158] T. Yamanaka and the ATLAS Collaboration, *The ATLAS calorimeter simulation FastCaloSim*, J. Phys. Conf. Ser. **331** (2011) 032053. (Cited on page 39.)

[159] ATLAS Collaboration, *The ATLAS Simulation Infrastructure*, Eur. Phys. J. **C 70** (2010) 823–874, arXiv:1005.4568 [physics.ins-det]. (Cited on page 39.)

[160] ATLAS Collaboration, *ATLAS Computing: Technical Design Report*. No. ATLAS-TDR-17 in Technical Design Report ATLAS. CERN, Geneva, 2005. (Cited on page 41.)

[161] G. Barrand, I. Belyaev, P. Binko, M. Cattaneo, R. Chytracek, et al., *GAUDI - A software architecture and framework for building HEP data processing applications*, Comput. Phys. Commun. **140** (2001) 45–55. (Cited on page 41.)

[162] T. Cornelissen, M. Elsing, S. Fleischmann, W. Liebig, E. Moyse, and A. Salzburger, *Concepts, Design and Implementation of the ATLAS New Tracking (NEWT)*, Tech. Rep. ATL-SOFT-PUB-2007-007, CERN,

Geneva, Mar, 2007. (Cited on page 41.)

[163] ATLAS Collaboration, *Performance of the ATLAS Inner Detector Track and Vertex Reconstruction in the High Pile-Up LHC Environment*, Tech. Rep. ATLAS-CONF-2012-042, CERN, Geneva, Mar, 2012. (Cited on pages 41, 42, and 43.)

[164] R. E. Kalman, *A New Approach to Linear Filtering and Prediction Problems*, Trans. ASME J. Basic Eng. **D 82** (1960) 35–45. (Cited on page 41.)

[165] ATLAS Collaboration, *Performance of primary vertex reconstruction in proton-proton collisions at $\sqrt{s} = 7$ TeV in the ATLAS experiment*, Tech. Rep. ATLAS-CONF-2010-069, CERN, Geneva, Jul, 2010. (Cited on page 42.)

[166] ATLAS Collaboration, *Characterization of Interaction-Point Beam Parameters Using the pp Event-Vertex Distribution Reconstructed in the ATLAS Detector at the LHC*, Tech. Rep. ATLAS-CONF-2010-027, CERN, Geneva, May, 2010. (Cited on page 42.)

[167] W. Waltenberger, R. Frühwirth, and P. Vanlaer, *Adaptive vertex fitting*, J. Phys. **G 34** (2007) N343. (Cited on page 43.)

[168] ATLAS Collaboration, *Vertex reconstruction plots*, `http://atlas.web.cern.ch/Atlas/GROUPS/PHYSICS/IDTRACKING/PublicPlots/ATL-COM-PHYS-2012-474/`. (Cited on page 43.)

[169] ATLAS Collaboration, *Expected electron performance in the ATLAS experiment*, Tech. Rep. ATL-PHYS-PUB-2011-006, CERN, Geneva, Apr, 2011. (Cited on page 43.)

[170] ATLAS Collaboration, *Electron and photon energy calibration with the ATLAS detector using LHC Run 1 data*, Eur. Phys. J. **C 74** (2014) 3071, `arXiv:1407.5063 [hep-ex]`. (Cited on page 43.)

[171] W. Lampl, S. Laplace, D. Lelas, P. Loch, H. Ma, et al., *Calorimeter Clustering Algorithms: Description and Performance*, Tech. Rep. ATL-LARG-PUB-2008-002, CERN, Geneva, Apr, 2008. (Cited on pages 43, 48, and 50.)

[172] ATLAS Collaboration, *Improved electron reconstruction in ATLAS using the Gaussian Sum Filter-based model for bremsstrahlung*, Tech. Rep. ATLAS-CONF-2012-047, CERN, Geneva, May, 2012. (Cited on page 44.)

[173] ATLAS Collaboration, *Electron efficiency measurements with the ATLAS detector using the 2012 LHC proton-proton collision data*, Tech. Rep. ATLAS-CONF-2014-032, CERN, Geneva, Jun, 2014. (Cited on pages 44 and 45.)

[174] ATLAS Collaboration, *Electron reconstruction and identification efficiency measurements with the ATLAS detector using the 2011 LHC proton-proton collision data*, Eur. Phys. J. **C 74** (2014) 2941, `arXiv:1404.2240 [hep-ex]`. (Cited on page 44.)

[175] ATLAS Collaboration, *Performance of the ATLAS Electron and Photon Trigger in p-p Collisions at $\sqrt{s} = 7$ TeV in 2011*, Tech. Rep. ATLAS-CONF-2012-048, CERN, Geneva, May, 2012. (Cited on page 45.)

[176] ATLAS Collaboration, *Muon Reconstruction Performance*, Tech. Rep. ATLAS-CONF-2010-064, CERN, Geneva, Jul, 2010. (Cited on page 45.)

[177] ATLAS Collaboration, *Muon Performance in Minimum Bias pp Collision Data at $\sqrt{s} = 7$ TeV with ATLAS*, Tech. Rep. ATLAS-CONF-2010-036, CERN, Geneva, Jul, 2010. (Cited on page 46.)

[178] S. Hassani, L. Chevalier, E. Lançon, J.-F. Laporte, R. Nicolaidou, and A. Ouraou, *A muon identification and combined reconstruction procedure for the ATLAS detector at the LHC using the (MUONBOY, STACO, MuTag) reconstruction packages*, Nucl. Instrum. Meth. **A 572** (2007) 77–79. (Cited on pages 46 and 65.)

[179] T. Lagouri, D. Adams, K. Assamagan, M. Biglietti, G. Carlino, et al., *A muon identification and combined reconstruction procedure for the ATLAS detector at the LHC at CERN*, IEEE Trans. Nucl. Sci. **51** (2004) 3030–3033. (Cited on page 46.)

[180] ATLAS Collaboration, *Measurement of the muon reconstruction performance of the ATLAS detector using 2011 and 2012 LHC proton-proton collision data*, arXiv:1407.3935 [hep-ex]. (Cited on pages 46 and 47.)

[181] ATLAS Collaboration, *Performance of the ATLAS Muon Trigger in p-p collisions at $\sqrt{s} = 7$ TeV*, Tech. Rep. ATLAS-CONF-2010-095, CERN, Geneva, Oct, 2010. (Cited on page 47.)

[182] ATLAS Collaboration, *Performance of the ATLAS muon trigger in 2011*, Tech. Rep. ATLAS-CONF-2012-099, CERN, Geneva, Jul, 2012. (Cited on page 47.)

[183] ATLAS Collaboration, *Expected performance of the ATLAS experiment: detector, trigger and physics*, Tech. Rep. CERN-OPEN-2008-020, CERN, Geneva, 2009. (Cited on pages 48 and 54.)

[184] M. Cacciari, G. P. Salam, and G. Soyez, *Anti-k_t jet clustering algorithm*, JHEP **0804** (2008) 063, arXiv:0802.1189 [hep-ph]. (Cited on pages 48 and 51.)

[185] ATLAS Collaboration, T. Barillari et al., *Local Hadronic Calibration*, Tech. Rep. ATL-LARG-PUB-2009-001-2, CERN, Geneva, Jun, 2008. (Cited on page 48.)

[186] ATLAS Collaboration, *Performance of the Reconstruction and Identification of Hadronic Tau Decays with ATLAS*, Tech. Rep. ATLAS-CONF-2011-152, CERN, Geneva, Nov, 2011. (Cited on page 48.)

[187] ATLAS Collaboration, *Performance of the Reconstruction and Identification of Hadronic Tau Decays in ATLAS with 2011 Data*, Tech. Rep. ATLAS-CONF-2012-142, CERN, Geneva, Oct, 2012. (Cited on pages 48 and 49.)

[188] ATLAS Collaboration, *Identification of the Hadronic Decays of Tau Leptons in 2012 Data with the ATLAS Detector*, Tech. Rep. ATLAS-CONF-2013-064, CERN, Geneva, Jul, 2013. (Cited on pages 48 and 49.)

[189] ATLAS Collaboration, *Expected photon performance in the ATLAS experiment*, Tech. Rep. ATL-PHYS-PUB-2011-007, CERN, Geneva, Apr, 2011. (Cited on page 49.)

[190] ATLAS Collaboration, *Measurements of the photon identification efficiency with the ATLAS detector using 4.9 fb^{-1} of pp collision data collected in 2011*, Tech. Rep. ATLAS-CONF-2012-123, CERN, Geneva, Aug, 2012. (Cited on page 49.)

[191] ATLAS Collaboration, *Measurements of the photon identification efficiencies using 20.3 fb^{-1} of pp collisions collected by ATLAS at $\sqrt{s} = 8$ TeV in 2012*, https://atlas.web.cern.ch/Atlas/GROUPS/PHYSICS/EGAMMA/PublicPlots/20140611/ATL-COM-PHYS-2014-542/. (Cited on page 50.)

[192] M. Cacciari and G. P. Salam, *Dispelling the N^3 myth for the k_t jet-finder*, Phys. Lett. **B641** (2006) 57–61, arXiv:hep-ph/0512210 [hep-ph]. (Cited on page 51.)

[193] S. D. Ellis and D. E. Soper, *Successive combination jet algorithm for hadron collisions*, Phys. Rev. **D 48** (1993) 3160–3166, arXiv:hep-ph/9305266 [hep-ph]. (Cited on page 51.)

[194] Y. L. Dokshitzer, G. Leder, S. Moretti, and B. Webber, *Better jet clustering algorithms*, JHEP **9708** (1997) 001, arXiv:hep-ph/9707323 [hep-ph]. (Cited on page 51.)

[195] M. Cacciari, G. P. Salam, and G. Soyez, *FastJet User Manual*, Eur. Phys. J. **C 72** (2012) 1896, arXiv:1111.6097 [hep-ph]. (Cited on page 51.)

[196] ATLAS Collaboration, *Jet energy measurement with the ATLAS detector in proton-proton collisions at $\sqrt{s} = 7$ TeV*, Eur. Phys. J. **C 73** (2013) 2304, arXiv:1112.6426 [hep-ex]. (Cited on page 51.)

[197] ATLAS Collaboration, *Approved 2012 jet energy scale uncertainty*, https://twiki.cern.ch/twiki/bin/view/AtlasPublic/JetEtmissApproved2013JESUncertainty. (Cited on page 52.)

[198] ATLAS Collaboration, *Jet energy measurement and its systematic uncertainty in proton-proton collisions at $\sqrt{s} = 7$ TeV with the ATLAS detector*, arXiv:1406.0076 [hep-ex]. (Cited on page 52.)

[199] ATLAS Collaboration, *Pile-up subtraction and suppression for jets in ATLAS*, Tech. Rep. ATLAS-CONF-2013-083, CERN, Geneva, Aug, 2013. (Cited on page 52.)

[200] ATLAS Collaboration, *Calibrating the b-Tag Efficiency and Mistag Rate in 35 pb^{-1} of Data with the ATLAS Detector*, Tech. Rep. ATLAS-CONF-2011-089, CERN, Geneva, Jun, 2011. (Cited on page 53.)

[201] ATLAS Collaboration, *Commissioning of the ATLAS high-performance b-tagging algorithms in the 7 TeV collision data*, Tech. Rep. ATLAS-CONF-2011-102, CERN, Geneva, Jul, 2011. (Cited on page 53.)

[202] ATLAS Collaboration, *Measurement of the b-tag Efficiency in a Sample of Jets Containing Muons with 5 fb^{-1} of data from the ATLAS Detector*, Tech. Rep. ATLAS-CONF-2012-043, CERN, Geneva, Mar, 2012. (Cited on page 53.)

[203] ATLAS Collaboration, *Calibration of b-tagging using dileptonic top pair events in a combinatorial likelihood approach with the ATLAS experiment*, Tech. Rep. ATLAS-CONF-2014-004, CERN, Geneva, Feb, 2014. (Cited on page 53.)

[204] ATLAS Collaboration, *Calibration of the performance of b-tagging for c and light-flavour jets in the 2012 ATLAS data*, Tech. Rep. ATLAS-CONF-2014-046, CERN, Geneva, Jul, 2014. (Cited on page 53.)

[205] ATLAS Collaboration, *Performance of Missing Transverse Momentum Reconstruction in ATLAS studied in Proton-Proton Collisions recorded in 2012 at 8 TeV*, Tech. Rep. ATLAS-CONF-2013-082, CERN, Geneva, Aug, 2013. (Cited on pages 54 and 55.)

[206] ATLAS Collaboration, *Determination of the tau energy scale and the associated systematic uncertainty in proton-proton collisions at $\sqrt{s} = 8$ TeV with the ATLAS detector at the LHC in 2012*, Tech. Rep. ATLAS-CONF-2013-044, CERN, Geneva, Apr, 2013. (Cited on page 54.)

[207] ATLAS Collaboration, *Pile-up Suppression in Missing Transverse Momentum Reconstruction in the ATLAS Experiment in Proton-Proton Collisions at $\sqrt{s} = 8$ TeV*, Tech. Rep. ATLAS-CONF-2014-019, CERN, Geneva, May, 2014. (Cited on page 54.)

[208] P. Fayet, *Supersymmetry and Weak, Electromagnetic and Strong Interactions*, Phys. Lett. **B 64** (1976) 159. (Cited on page 57.)

[209] P. Fayet, *Spontaneously Broken Supersymmetric Theories of Weak, Electromagnetic and Strong Interactions*, Phys. Lett. **B 69** (1977) 489. (Cited on page 57.)

[210] G. R. Farrar and P. Fayet, *Phenomenology of the Production, Decay, and Detection of New Hadronic States Associated with Supersymmetry*, Phys. Lett. **B 76** (1978) 575–579. (Cited on page 57.)

[211] P. Fayet, *Relations Between the Masses of the Superpartners of Leptons and Quarks, the Goldstino Couplings and the Neutral Currents*, Phys. Lett. **B 84** (1979) 416. (Cited on page 57.)

[212] S. Dimopoulos and H. Georgi, *Softly Broken Supersymmetry and $SU(5)$*, Nucl. Phys. **B 193** (1981) 150. (Cited on page 57.)

[213] ATLAS Collaboration, *Search for squarks and gluinos with the ATLAS detector in final states with jets and missing transverse momentum using $\sqrt{s} = 8$ TeV proton–proton collision data*, JHEP **1409** (2014) 176, arXiv:1405.7875 [hep-ex]. (Cited on pages 57, 132, and 137.)

[214] ATLAS Collaboration, *Search for squarks and gluinos with the ATLAS detector in final states with jets and missing transverse momentum and 20.3 fb^{-1} of $\sqrt{s} = 8$ TeV proton-proton collision data*, Tech. Rep. ATLAS-CONF-2013-047, CERN, Geneva, May, 2013. (Cited on pages 57, 76, 102, 103, and 107.)

[215] ATLAS Collaboration, *Search for squarks and gluinos with the ATLAS detector using final states with jets and missing transverse momentum and 5.8 fb^{-1} of $\sqrt{s} = 8$ TeV proton-proton collision data*, Tech. Rep. ATLAS-CONF-2012-109, CERN, Geneva, Aug, 2012. (Cited on page 57.)

[216] ATLAS Collaboration, *Search for squarks and gluinos with the ATLAS detector in final states with jets and missing transverse momentum using 4.7 fb^{-1} of $\sqrt{s} = 7$ TeV proton-proton collision data*, Phys. Rev. **D 87** (2013) 012008, arXiv:1208.0949 [hep-ex]. (Cited on pages 57, 109, 112, 113, and 114.)

[217] ATLAS Collaboration, *Search for squarks and gluinos using final states with jets and missing transverse momentum with the ATLAS detector in $\sqrt{s} = 7$ TeV proton-proton collisions*, Phys. Lett. **B 710** (2012) 67–85, arXiv:1109.6572 [hep-ex]. (Cited on page 57.)

[218] ATLAS Collaboration, *Search for squarks and gluinos using final states with jets and missing transverse momentum with the ATLAS detector in $\sqrt{s} = 7$ TeV proton-proton collisions*, Phys. Lett. **B 701** (2011) 186–203, arXiv:1102.5290 [hep-ex]. (Cited on page 57.)

[219] ATLAS Collaboration, *Improved luminosity determination in pp collisions at $\sqrt{s} = 7$ TeV using the ATLAS detector at the LHC*, Eur. Phys. J. **C 73** (2013) 2518, arXiv:1302.4393 [hep-ex]. (Cited on page 60.)

[220] ATLAS Collaboration, *Further ATLAS tunes of PYTHIA6 and Pythia 8*, Tech. Rep. ATL-PHYS-PUB-2011-014, CERN, Geneva, Nov, 2011. (Cited on page 61.)

[221] S. Catani, F. Krauss, R. Kuhn, and B. Webber, *QCD matrix elements + parton showers*, JHEP **0111** (2001) 063, arXiv:hep-ph/0109231. (Cited on page 61.)

[222] F. Krauss, *Matrix elements and parton showers in hadronic interactions*, JHEP **0208** (2002) 015, arXiv:hep-ph/0205283. (Cited on page 61.)

[223] S. Hoeche, F. Krauss, S. Schumann, and F. Siegert, *QCD matrix elements and truncated showers*, JHEP **0905** (2009) 053, arXiv:0903.1219 [hep-ph]. (Cited on page 61.)

[224] J. Alwall, S. Hoche, F. Krauss, N. Lavesson, L. Lonnblad, et al., *Comparative study of various algorithms for the merging of parton showers and matrix elements in hadronic collisions*, Eur. Phys. J. **C 53** (2008) 473–500, arXiv:0706.2569 [hep-ph]. (Cited on page 61.)

[225] H.-L. Lai, M. Guzzi, J. Huston, Z. Li, P. M. Nadolsky, et al., *New parton distributions for collider physics*, Phys. Rev. **D 82** (2010) 074024, arXiv:1007.2241 [hep-ph]. (Cited on pages 61 and 132.)

[226] G. Corcella, I. Knowles, G. Marchesini, S. Moretti, K. Odagiri, et al., *HERWIG 6: An Event generator for hadron emission reactions with interfering gluons (including supersymmetric processes)*, JHEP **0101** (2001) 010, arXiv:hep-ph/0011363. (Cited on page 61.)

[227] J. M. Butterworth, J. R. Forshaw, and M. H. Seymour, *Multiparton interactions in photoproduction at HERA*, Z. Phys. **C 72** (1996) 637–646, arXiv:hep-ph/9601371. (Cited on page 61.)

[228] S. Catani, L. Cieri, G. Ferrera, D. de Florian, and M. Grazzini, *Vector boson production at hadron colliders: A Fully exclusive QCD calculation at NNLO*, Phys. Rev. Lett. **103** (2009) 082001, arXiv:0903.2120 [hep-ph]. (Cited on page 61.)

[229] P. Nason, *A New method for combining NLO QCD with shower Monte Carlo algorithms*, JHEP **0411** (2004) 040, arXiv:hep-ph/0409146. (Cited on page 62.)

[230] S. Frixione, P. Nason, and C. Oleari, *Matching NLO QCD computations with parton shower simulations: the POWHEG method*, JHEP **0711** (2007) 070, arXiv:0709.2092 [hep-ph]. (Cited on page 62.)

[231] B. Cooper, J. Katzy, M. Mangano, A. Messina, L. Mijovic, et al., *Monte Carlo tuning in the presence of Matching*, Eur. Phys. J. **C 72** (2012) 2078, arXiv:1109.5295 [hep-ph]. (Cited on page 62.)

[232] P. Z. Skands, *Tuning Monte Carlo Generators: The Perugia Tunes*, Phys. Rev. **D 82** (2010) 074018, arXiv:1005.3457 [hep-ph]. (Cited on page 62.)

[233] ATLAS Collaboration, *Measurement of top-quark pair differential cross-sections in the ℓ+jets channel in pp collisions at $\sqrt{s} = 7$ TeV using the ATLAS detector*, Tech. Rep. ATLAS-CONF-2013-099, CERN, Geneva, Sep, 2013. (Cited on page 62.)

[234] M. Cacciari, M. Czakon, M. Mangano, A. Mitov, and P. Nason, *Top-pair production at hadron colliders with next-to-next-to-leading logarithmic soft-gluon resummation*, Phys. Lett. **B 710** (2012) 612–622, arXiv:1111.5869 [hep-ph]. (Cited on page 62.)

[235] P. Bärnreuther, M. Czakon, and A. Mitov, *Percent Level Precision Physics at the Tevatron: First Genuine NNLO QCD Corrections to $q\bar{q} \to t\bar{t} + X$*, Phys. Rev. Lett. **109** (2012) 132001, arXiv:1204.5201

[hep-ph]. (Cited on page 62.)

[236] M. Czakon and A. Mitov, *NNLO corrections to top-pair production at hadron colliders: the all-fermionic scattering channels*, JHEP **1212** (2012) 054, arXiv:1207.0236 [hep-ph]. (Cited on page 62.)

[237] M. Czakon and A. Mitov, *NNLO corrections to top pair production at hadron colliders: the quark-gluon reaction*, JHEP **1301** (2013) 080, arXiv:1210.6832 [hep-ph]. (Cited on page 62.)

[238] M. Czakon, P. Fiedler, and A. Mitov, *Total Top-Quark Pair-Production Cross Section at Hadron Colliders Through $\mathcal{O}(\alpha_S^4)$*, Phys. Rev. Lett. **110** (2013) 252004, arXiv:1303.6254 [hep-ph]. (Cited on page 62.)

[239] M. Czakon and A. Mitov, *Top++: A Program for the Calculation of the Top-Pair Cross-Section at Hadron Colliders*, Comput. Phys. Commun. **185** (2014) 2930, arXiv:1112.5675 [hep-ph]. (Cited on page 62.)

[240] B. P. Kersevan and E. Richter-Was, *The Monte Carlo event generator AcerMC versions 2.0 to 3.8 with interfaces to PYTHIA 6.4, HERWIG 6.5 and ARIADNE 4.1*, Comput. Phys. Commun. **184** (2013) 919–985, arXiv:hep-ph/0405247. (Cited on page 62.)

[241] N. Kidonakis, *NNLL resummation for s-channel single top quark production*, Phys. Rev. **D 81** (2010) 054028, arXiv:1001.5034 [hep-ph]. (Cited on page 62.)

[242] N. Kidonakis, *Next-to-next-to-leading-order collinear and soft gluon corrections for t-channel single top quark production*, Phys. Rev. **D 83** (2011) 091503, arXiv:1103.2792 [hep-ph]. (Cited on page 62.)

[243] N. Kidonakis, *Two-loop soft anomalous dimensions for single top quark associated production with a W- or H-*, Phys. Rev. **D 82** (2010) 054018, arXiv:1005.4451 [hep-ph]. (Cited on page 62.)

[244] J. M. Campbell and R. K. Ellis, *An Update on vector boson pair production at hadron colliders*, Phys. Rev. **D 60** (1999) 113006, arXiv:hep-ph/9905386. (Cited on page 63.)

[245] J. M. Campbell, R. K. Ellis, and C. Williams, *Vector boson pair production at the LHC*, JHEP **1107** (2011) 018, arXiv:1105.0020 [hep-ph]. (Cited on page 63.)

[246] *Summary of ATLAS Pythia 8 tunes*, Tech. Rep. ATL-PHYS-PUB-2012-003, CERN, Geneva, Aug, 2012. (Cited on page 63.)

[247] A. Djouadi, M. Muhlleitner, and M. Spira, *Decays of supersymmetric particles: The Program SUSY-HIT (SUspect-SdecaY-Hdecay-InTerface)*, Acta Phys. Polon. **B 38** (2007) 635–644, arXiv:hep-ph/0609292. (Cited on page 63.)

[248] B. Allanach, *SOFTSUSY: a program for calculating supersymmetric spectra*, Comput. Phys. Commun. **143** (2002) 305–331, arXiv:hep-ph/0104145. (Cited on page 63.)

[249] S. Gieseke, C. Rohr, and A. Siodmok, *Colour reconnections in Herwig++*, Eur. Phys. J. **C 72** (2012) 2225, arXiv:1206.0041 [hep-ph]. (Cited on page 63.)

[250] W. Beenakker, R. Hopker, M. Spira, and P. M. Zerwas, *Squark and gluino production at hadron colliders*, Nucl. Phys. **B 492** (1997) 51–103, arXiv:hep-ph/9610490. (Cited on pages 64 and 115.)

[251] A. Kulesza and L. Motyka, *Threshold resummation for squark-antisquark and gluino-pair production at the LHC*, Phys. Rev. Lett. **102** (2009) 111802, arXiv:0807.2405 [hep-ph]. (Cited on pages 64 and 115.)

[252] A. Kulesza and L. Motyka, *Soft gluon resummation for the production of gluino-gluino and squark-antisquark pairs at the LHC*, Phys. Rev. **D 80** (2009) 095004, arXiv:0905.4749 [hep-ph]. (Cited on pages 64 and 115.)

[253] W. Beenakker, S. Brensing, M. Kramer, A. Kulesza, E. Laenen, et al., *Soft-gluon resummation for squark and gluino hadroproduction*, JHEP **0912** (2009) 041, arXiv:0909.4418 [hep-ph]. (Cited on pages 64 and 115.)

[254] W. Beenakker, S. Brensing, M. Kramer, A. Kulesza, E. Laenen, et al., *Squark and gluino hadroproduction*, Int. J. Mod. Phys. **A 26** (2011) 2637–2664, arXiv:1105.1110 [hep-ph]. (Cited on pages 64 and 115.)

[255] ATLAS Collaboration, *Selection of jets produced in proton-proton collisions with the ATLAS detector using 2011 data*, Tech. Rep. ATLAS-CONF-2012-020, CERN, Geneva, Mar, 2012. (Cited on page 67.)

[256] I. Hinchliffe, F. Paige, M. Shapiro, J. Soderqvist, and W. Yao, *Precision SUSY measurements at CERN LHC*, Phys. Rev. **D 55** (1997) 5520–5540, arXiv:hep-ph/9610544. (Cited on page 69.)

[257] D. Tovey, *Measuring the SUSY mass scale at the LHC*, Phys. Lett. **B 498** (2001) 1–10, arXiv:hep-ph/0006276. (Cited on page 69.)

[258] S. Owen, *Data-driven estimation of the QCD multijet background to SUSY searches with jets and missing transverse momentum at ATLAS using jet smearing*, Tech. Rep. ATL-PHYS-INT-2012-008, CERN, Geneva, Feb, 2012. (Cited on page 79.)

[259] ATLAS Collaboration, *Measurement of the cross-section for W boson production in association with b-jets in pp collisions at $\sqrt{s} = 7$ TeV with the ATLAS detector*, JHEP **1306** (2013) 084, arXiv:1302.2929 [hep-ex]. (Cited on page 82.)

[260] ATLAS Collaboration, *Measurement of the inclusive isolated prompt photon cross section in pp collisions at $\sqrt{s} = 7$ TeV with the ATLAS detector using 4.6 fb^{-1}*, Phys. Rev. **D 89** (2014) 052004, arXiv:1311.1440 [hep-ex]. (Cited on page 82.)

[261] ATLAS Collaboration, *Search for pair-produced top squarks decaying into a charm quark and the lightest neutralinos with 20.3 fb^{-1} of pp collisions at $\sqrt{s} = 8$ TeV with the ATLAS detector at the LHC*, Tech. Rep. ATLAS-CONF-2013-068, CERN, Geneva, Jul, 2013. (Cited on page 83.)

[262] ATLAS Collaboration, *Search for pair-produced third-generation squarks decaying via charm quarks or in compressed supersymmetric scenarios in pp collisions at $\sqrt{s} = 8$ TeV with the ATLAS detector*, Phys. Rev. **D 90** (2014) 052008, arXiv:1407.0608 [hep-ex]. (Cited on page 83.)

[263] J. Neyman and E. S. Pearson, *On the Problem of the Most Efficient Tests of Statistical Hypotheses*, Phil. Trans. R. Soc. B **231** (1933) 289–337. (Cited on page 84.)

[264] M. Baak, G. J. Besjes, D. Cote, A. Koutsman, J. Lorenz, et al., *HistFitter software framework for statistical data analysis*, arXiv:1410.1280 [hep-ex]. (Cited on pages 87, 124, 143, 147, and 160.)

[265] ROOT Collaboration, K. Cranmer, G. Lewis, L. Moneta, A. Shibata, and W. Verkerke, *HistFactory: A tool for creating statistical models for use with RooFit and RooStats*, Tech. Rep. CERN-OPEN-2012-016, CERN, Geneva, Jan, 2012. (Cited on pages 87, 143, 146, and 147.)

[266] W. Verkerke and D. P. Kirkby, *The RooFit toolkit for data modeling*, eConf **C0303241** (2003) MOLT007, arXiv:physics/0306116. (Cited on pages 87 and 143.)

[267] L. Moneta, K. Belasco, K. S. Cranmer, S. Kreiss, A. Lazzaro, et al., *The RooStats Project*, PoS **ACAT2010** (2010) 057, arXiv:1009.1003 [physics.data-an]. (Cited on pages 87, 143, and 147.)

[268] R. Brun and F. Rademakers, *ROOT: An object oriented data analysis framework*, Nucl. Instrum. Meth. **A 389** (1997) 81–86. (Cited on pages 87 and 143.)

[269] I. Antcheva, M. Ballintijn, B. Bellenot, M. Biskup, R. Brun, et al., *ROOT: A C++ framework for petabyte data storage, statistical analysis and visualization*, Comput. Phys. Commun. **182** (2011) 1384–1385. (Cited on pages 87 and 143.)

[270] G. Cowan, K. Cranmer, E. Gross, and O. Vitells, *Asymptotic formulae for likelihood-based tests of new physics*, Eur. Phys. J. **C 71** (2011) 1554, arXiv:1007.1727 [physics.data-an]. (Cited on pages 88 and 147.)

[271] A. L. Read, *Presentation of search results: the CL_s technique*, J. Phys. **G 28** (2002) 2693. (Cited on pages 88 and 147.)

[272] T. J. LeCompte and S. P. Martin, *Large Hadron Collider reach for supersymmetric models with compressed mass spectra*, Phys. Rev. **D 84** (2011) 015004, arXiv:1105.4304 [hep-ph]. (Cited on page 97.)

[273] T. J. LeCompte and S. P. Martin, *Compressed supersymmetry after 1/fb at the Large Hadron Collider*, Phys. Rev. **D 85** (2012) 035023, arXiv:1111.6897 [hep-ph]. (Cited on page 97.)

[274] R. Mahbubani, M. Papucci, G. Perez, J. T. Ruderman, and A. Weiler, *Light Nondegenerate Squarks at the LHC*, Phys. Rev. Lett. **110** (2013) 151804, arXiv:1212.3328 [hep-ph]. (Cited on page 97.)

[275] W. S. Cho, J. E. Kim, and J.-H. Kim, *Amplification of endpoint structure for new particle mass measurement at the LHC*, Phys. Rev. **D 81** (2010) 095010, arXiv:0912.2354 [hep-ph]. (Cited on page 102.)

[276] D. R. Tovey, *On measuring the masses of pair-produced semi-invisibly decaying particles at hadron colliders*, JHEP **0804** (2008) 034, arXiv:0802.2879 [hep-ph]. (Cited on page 102.)

[277] L. Randall and D. Tucker-Smith, *Dijet Searches for Supersymmetry at the LHC*, Phys. Rev. Lett. **101** (2008) 221803, arXiv:0806.1049 [hep-ph]. (Cited on page 102.)

[278] CMS Collaboration, *Search for supersymmetry in hadronic final states with missing transverse energy using the variables α_T and b-quark multiplicity in pp collisions at $\sqrt{s} = 8$ TeV*, Eur. Phys. J. **C 73** (2013) 2568, arXiv:1303.2985 [hep-ex]. (Cited on pages 102 and 151.)

[279] ATLAS Collaboration, *Search for squarks and gluinos with the ATLAS detector using final states with jets and missing transverse momentum and 5.8 fb^{-1} of $\sqrt{s} = 8$ TeV proton-proton collision data*, Tech. Rep. ATLAS-CONF-2012-109, CERN, Geneva, Aug, 2012. (Cited on pages 103 and 152.)

[280] C. Strege, G. Bertone, G. J. Besjes, S. Caron, R. Ruiz de Austri, et al., *Profile likelihood maps of a 15-dimensional MSSM*, JHEP **1409** (2014) 081, arXiv:1405.0622 [hep-ph]. (Cited on pages 109, 115, 117, and 118.)

[281] ATLAS Collaboration, *Search for direct production of charginos and neutralinos in events with three leptons and missing transverse momentum in $\sqrt{s} = 7$ TeV pp collisions with the ATLAS detector*, Phys. Lett. **B 718** (2013) 841–859, arXiv:1208.3144 [hep-ex]. (Cited on pages 109, 112, 113, and 114.)

[282] MSSM Working Group Collaboration, A. Djouadi et al., *The Minimal supersymmetric standard model: Group summary report*, arXiv:hep-ph/9901246 [hep-ph]. (Cited on page 110.)

[283] C. F. Berger, J. S. Gainer, J. L. Hewett, and T. G. Rizzo, *Supersymmetry Without Prejudice*, JHEP **0902** (2009) 023, arXiv:0812.0980 [hep-ph]. (Cited on page 110.)

[284] A. Arbey, M. Battaglia, and F. Mahmoudi, *Implications of LHC Searches on SUSY Particle Spectra: The pMSSM Parameter Space with Neutralino Dark Matter*, Eur. Phys. J. **C 72** (2012) 1847, arXiv:1110.3726 [hep-ph]. (Cited on page 110.)

[285] M. Cahill-Rowley, R. Cotta, A. Drlica-Wagner, S. Funk, J. Hewett, et al., *Complementarity and Searches for Dark Matter in the pMSSM*, arXiv:1305.6921 [hep-ph]. (Cited on page 110.)

[286] E. A. Baltz, M. Battaglia, M. E. Peskin, and T. Wizansky, *Determination of dark matter properties at high-energy colliders*, Phys. Rev. **D 74** (2006) 103521, arXiv:hep-ph/0602187 [hep-ph]. (Cited on page 110.)

[287] S. S. AbdusSalam, B. C. Allanach, F. Quevedo, F. Feroz, and M. Hobson, *Fitting the Phenomenological MSSM*, Phys. Rev. **D 81** (2010) 095012, arXiv:0904.2548 [hep-ph]. (Cited on page 110.)

[288] S. S. AbdusSalam, *LHC-7 supersymmetry search interpretation within the phenomenological MSSM*, Phys. Rev. **D 87** (2013) 115012, arXiv:1211.0999 [hep-ph]. (Cited on page 110.)

[289] C. Boehm, P. S. B. Dev, A. Mazumdar, and E. Pukartas, *Naturalness of Light Neutralino Dark Matter in pMSSM after LHC, XENON100 and Planck Data*, JHEP **1306** (2013) 113, arXiv:1303.5386 [hep-ph]. (Cited on page 110.)

[290] S. S. Wilks, *The Large-Sample Distribution of the Likelihood Ratio for Testing Composite Hypotheses*, Ann. Math. Statist. **9** (1938) 60–62. (Cited on page 111.)

[291] F. Feroz, K. Cranmer, M. Hobson, R. Ruiz de Austri, and R. Trotta, *Challenges of Profile Likelihood Evaluation in Multi-Dimensional SUSY Scans*, JHEP **1106** (2011) 042, arXiv:1101.3296 [hep-ph].

(Cited on page 111.)

[292] F. Feroz and M. Hobson, *Multimodal nested sampling: an efficient and robust alternative to MCMC methods for astronomical data analysis*, Mon. Not. Roy. Astron. Soc. **384** (2008) 449, arXiv:0704.3704 [astro-ph]. (Cited on page 111.)

[293] F. Feroz, M. Hobson, and M. Bridges, *MultiNest: an efficient and robust Bayesian inference tool for cosmology and particle physics*, Mon. Not. Roy. Astron. Soc. **398** (2009) 1601–1614, arXiv:0809.3437 [astro-ph]. (Cited on page 111.)

[294] R. R. de Austri, R. Trotta, and L. Roszkowski, *A Markov chain Monte Carlo analysis of the CMSSM*, JHEP **0605** (2006) 002, arXiv:hep-ph/0602028 [hep-ph]. (Cited on pages 112 and 113.)

[295] D. C. Tevatron Electroweak Working Group, CDF Collaboration, *Combination of CDF and DØ results on the mass of the top quark using up to 8.7 fb^{-1} at the Tevatron*, arXiv:1305.3929 [hep-ex]. (Cited on page 113.)

[296] BaBar Collaboration, *Observation of the semileptonic decays $B \to D^*\tau^-\bar{\nu}_\tau$ and evidence for $B \to D\tau^-\bar{\nu}_\tau$*, Phys. Rev. Lett. **100** (2008) 021801, arXiv:0709.1698 [hep-ex]. (Cited on page 113.)

[297] LEP Electroweak Working Group. http://lepewwg.web.cern.ch/LEPEWWG/. (Cited on page 113.)

[298] M. Antonelli, V. Cirigliano, G. Isidori, F. Mescia, M. Moulson, et al., *An Evaluation of $|V_{us}|$ and precise tests of the Standard Model from world data on leptonic and semileptonic kaon decays*, Eur. Phys. J. **C 69** (2010) 399–424, arXiv:1005.2323 [hep-ph]. (Cited on page 113.)

[299] F. Mahmoudi, S. Neshatpour, and J. Orloff, *Supersymmetric constraints from $B_s \to \mu^+\mu^-$ and $B \to K^*\mu^+\mu^-$ observables*, JHEP **1208** (2012) 092, arXiv:1205.1845 [hep-ph]. (Cited on page 113.)

[300] LHCb Collaboration, *First Evidence for the Decay $B_s^0 \to \mu^+\mu^-$*, Phys. Rev. Lett. **110** (2013) 021801, arXiv:1211.2674 [hep-ex]. (Cited on page 113.)

[301] ATLAS Collaboration, *Physics at a High-Luminosity LHC with ATLAS*, Tech. Rep. ATL-PHYS-PUB-2012-001, CERN, Geneva, Aug, 2012. (Cited on page 113.)

[302] CMS Collaboration, *Combination of standard model Higgs boson searches and measurements of the properties of the new boson with a mass near 125 GeV*, Tech. Rep. CMS-PAS-HIG-12-045, CERN, Geneva, 2012. (Cited on page 113.)

[303] CMS Collaboration, *Updated measurements of the Higgs boson at 125 GeV in the two photon decay channel*, Tech. Rep. CMS-PAS-HIG-13-001, CERN, Geneva, 2013. (Cited on page 113.)

[304] CMS Collaboration, *Evidence for a particle decaying to W^+W^- in the fully leptonic final state in a standard model Higgs boson search in pp collisions at the LHC*, Tech. Rep. CMS-PAS-HIG-13-003, CERN, Geneva, 2013. (Cited on page 113.)

[305] CMS Collaboration, *Properties of the Higgs-like boson in the decay H to ZZ to 4l in pp collisions at $\sqrt{s} = 7$ and 8 TeV*, Tech. Rep. CMS-PAS-HIG-13-002, CERN, Geneva, 2013. (Cited on page 113.)

[306] CMS Collaboration, *Search for the standard model Higgs boson produced in association with W or Z bosons, and decaying to bottom quarks for HCP 2012*, Tech. Rep. CMS-PAS-HIG-12-044, CERN, Geneva, 2012. (Cited on page 113.)

[307] CMS Collaboration, *Search for the Standard-Model Higgs boson decaying to tau pairs in proton-proton collisions at $\sqrt(s) = 7$ and 8 TeV*, Tech. Rep. CMS-PAS-HIG-13-004, CERN, Geneva, 2013. (Cited on page 113.)

[308] CDF Collaboration, *Observation of $B_s^0 - \bar{B}_s^0$ Oscillations*, Phys. Rev. Lett. **97** (2006) 242003, arXiv:hep-ex/0609040 [hep-ex]. (Cited on page 113.)

[309] LHCb Collaboration, *Measurement of the $B_s^0 - \bar{B}_s^0$ oscillation frequency Δm_s in $B_s^0 \to D_s^-(3)\pi$ decays*, Phys. Lett. **B 709** (2012) 177–184, arXiv:1112.4311 [hep-ex]. (Cited on page 113.)

[310] BELLE Collaboration, *Measurement of the $B \to K^*$ gamma branching fractions and asymmetries*, Phys. Rev. **D 69** (2004) 112001, arXiv:hep-ex/0402042 [hep-ex]. (Cited on page 113.)

[311] BaBar Collaboration, *Measurement of Branching Fractions and CP and Isospin Asymmetries in $B \to K^*\gamma$*, arXiv:0808.1915 [hep-ex]. (Cited on page 113.)

[312] W. Beenakker, M. Klasen, M. Kramer, T. Plehn, M. Spira, et al., *The Production of charginos / neutralinos and sleptons at hadron colliders*, Phys. Rev. Lett. **83** (1999) 3780–3783, arXiv:hep-ph/9906298 [hep-ph]. (Cited on page 115.)

[313] ATLAS Collaboration, *ATLAS Monte Carlo tunes for MC09*, Tech. Rep. ATL-PHYS-PUB-2010-002, CERN, Geneva, Mar, 2010. (Cited on page 115.)

[314] DELPHES 3 Collaboration, J. de Favereau et al., *DELPHES 3, A modular framework for fast simulation of a generic collider experiment*, JHEP **1402** (2014) 057, arXiv:1307.6346 [hep-ex]. (Cited on page 115.)

[315] ATLAS Collaboration, *Summary of the inclusive searches for squarks and gluinos with Run I LHC data at ATLAS*. ATLAS-SUSY-2014-06. In preparation. (Cited on page 121.)

[316] ATLAS Collaboration, *Search for squarks and gluinos in events with isolated leptons, jets and missing transverse momentum at $\sqrt{s} = 8$ TeV with the ATLAS detector*, arXiv:1501.03555 [hep-ex]. (Cited on page 121.)

[317] ATLAS Collaboration, *Search for Supersymmetry at the high luminosity LHC with the ATLAS experiment*, Tech. Rep. ATL-PHYS-PUB-2014-010, CERN, Geneva, Jul, 2014. (Cited on page 131.)

[318] ATLAS Collaboration, *Letter of Intent for the Phase-I Upgrade of the ATLAS Experiment*, Tech. Rep. CERN-LHCC-2011-012, LHCC-I-020, CERN, Geneva, Nov, 2011. (Cited on page 132.)

[319] L. Rossi and O. Brüning, *High Luminosity Large Hadron Collider, a description for the European Strategy Preparatory Group*, Tech. Rep. CERN-ATS-2012-236, CERN, Geneva, Aug, 2012. (Cited on page 132.)

[320] ATLAS Collaboration, *Letter of Intent for the Phase-II Upgrade of the ATLAS Experiment*, Tech. Rep. CERN-LHCC-2012-022, LHCC-I-023, CERN, Geneva, Dec, 2012. (Cited on pages 132 and 135.)

[321] *Expected pileup values at the HL-LHC*, Tech. Rep. ATL-UPGRADE-PUB-2013-014, CERN, Geneva, Sep, 2013. (Cited on page 132.)

[322] TOTEM Collaboration, *Luminosity-independent measurements of total, elastic and inelastic cross-sections at $\sqrt{s} = 7$ TeV*, Europhys. Lett. **101** (2013) 21004. (Cited on page 132.)

[323] J. Alwall et al., *MadGraph/MadEvent v4: The new web generation*, JHEP **0709** (2007) 028, arXiv:0706.2334 [hep-ph]. (Cited on page 132.)

[324] M. Aliev, H. Lacker, U. Langenfeld, S. Moch, P. Uwer, et al., *HATHOR: HAdronic Top and Heavy quarks crOss section calculatoR*, Comput. Phys. Commun. **182** (2011) 1034–1046, arXiv:1007.1327 [hep-ph]. (Cited on page 132.)

[325] K. Melnikov and F. Petriello, *Electroweak gauge boson production at hadron colliders through $\mathcal{O}(\alpha_s^2)$*, Phys. Rev. **D 74** (2006) 114017, arXiv:hep-ph/0609070. (Cited on page 132.)

[326] C. Anastasiou, L. J. Dixon, K. Melnikov, and F. Petriello, *High precision QCD at hadron colliders: Electroweak gauge boson rapidity distributions at NNLO*, Phys. Rev. **D 69** (2004) 094008, arXiv:hep-ph/0312266. (Cited on page 132.)

[327] ATLAS Collaboration, *Performance assumptions for an upgraded ATLAS detector at a High-Luminosity LHC*, Tech. Rep. ATL-PHYS-PUB-2013-004, CERN, Geneva, Mar, 2013. (Cited on pages 134 and 136.)

[328] ATLAS Collaboration, *Performance assumptions based on full simulation for an upgraded ATLAS detector at a High-Luminosity LHC*, Tech. Rep. ATL-PHYS-PUB-2013-009, CERN, Geneva, Sep, 2013. (Cited on pages 134, 135, and 136.)

[329] J. T. Linnemann, *Measures of Significance in HEP and Astrophysics*, arXiv:physics/0312059. (Cited on page 138.)

[330] CMS Collaboration, *Search for new physics in the multijet and missing transverse momentum final state in proton-proton collisions at $\sqrt{s} = 8$ TeV*, JHEP **1406** (2014) 055, arXiv:1402.4770 [hep-ex]. (Cited on page 151.)

[331] C. Rogan, *Kinematical variables towards new dynamics at the LHC*, arXiv:1006.2727 [hep-ph]. (Cited on page 151.)

[332] CMS Collaboration, *Exclusion limits on gluino and top-squark pair production in natural SUSY scenarios with inclusive razor and exclusive single-lepton searches at 8 TeV*, Tech. Rep. CMS-PAS-SUS-14-011, CERN, Geneva, 2014. (Cited on page 151.)

[333] CMS Collaboration, *Search for supersymmetry in hadronic final states using m_{T2} with the CMS detector at $\sqrt{s} = 8$ TeV*, Tech. Rep. CMS-PAS-SUS-13-019, CERN, Geneva, 2014. (Cited on page 151.)

[334] M. Cahill-Rowley, J. Hewett, A. Ismail, and T. Rizzo, *pMSSM Studies at the 7, 8 and 14 TeV LHC*, arXiv:1307.8444 [hep-ph]. (Cited on page 152.)

Summary

In this thesis, a search for new elementary particles predicted by a theory called supersymmetry (SUSY), which attempts to address shortcomings in our current description of particle physics, the Standard Model, was presented. No events incompatible with the Standard Model were observed. The results obtained in this search were used in fits to a larger supersymmetric model, and combined with different analyses to obtain improved limits on simplified models. In addition, prospects for a similar search at the proposed high-luminosity LHC were discussed. Finally, HistFitter was presented, a program developed to perform searches in high-energy physics.

Searches for supersymmetry are motivated by the fact that the Standard Model of particle physics is incomplete. Astronomical observations indicate that a mere 4.9 % of the universe consists of matter as described by the Standard Model. The remaining part consists of dark matter (26.8 %) and dark energy (68.3 %) that cannot be explained without more encompassing theories. Moreover, the Standard Model suffers from a fine-tuning problem: loop corrections to the Higgs mass lead to enormous corrections on the mass parameter m_H. Supersymmetry addresses the Standard Model's shortcomings by introducing an additional symmetry on the model, leading to each particle obtaining a *superpartner* that differs in spin by ½. As a result, the large corrections to the Higgs mass automatically cancel. Moreover, the lightest supersymmetrical particle is a candidate for dark matter if R-parity is conserved.

Accelerators may be used to study subatomic particles by colliding them at high energy. The equivalence of mass and energy ensures that, provided the collision is energetic enough, heavy particles with a short lifetime may be produced and their properties studied. The decay products can be measured in a dedicated detector. The ATLAS detector at the Large Hadron Collider at CERN is such an apparatus, and is used in the work in this thesis. The event reconstruction and detector performance are also discussed.

Supersymmetry is searched for in this thesis in a decay channel with 2–6 jets, missing energy, and no leptons in the final state. The analysis targets the production of squarks and gluinos, which would be the most predominantly produced SUSY particles at the LHC. Their coupling to the strong force leads to a final state with many jets, in which the lightest supersymmetric particle produced in the cascade decay escapes the detector unseen. The analysis is designed using 15 signal regions, with varying selections on the *effective mass* of the collision. These signal regions were optimised for exclusion on simplified models. For each of the signal regions, four control regions are used to estimate the main backgrounds in a semi-data-driven way through a combined likelihood fit: W+jets, Z+jets, $t\bar{t}$ and QCD multijet events. No significant excess over the Standard Model expectation is observed in any of the signal regions.

The results of the analysis are interpreted in several SUSY models. Large swaths of the theoretically well-motivated MSUGRA/CMSSM model's parameter space are ruled out after Run I of the LHC. Various simplified models are also used for interpretation. These target a very specific production mechanism and decay chain, and can also be used to reinterpret results in larger, more encompassing models. In the case of massless neutralinos, pair-produced gluinos that decay directly into quarks and the lighest SUSY particle are ruled out up to 1330 GeV. Pair-produced degenerate light-flavour squarks that decay directly into quarks and the lightest SUSY particle are ruled out up to 850 GeV. In the case of non-degenerate squarks, the latter limit is relaxed to 440 GeV. The results are also interpreted in several other (simplified) models.

Other experimental results can also be used to shed further light on supersymmetry. Data from B- and D-physics experiments, LEP and Tevatron results and astrophysical observations can be combined with LHC limits and Higgs measurements to explore the phase space of supersymmetrical models. The model used in this thesis is a 15-parameter version of the phenomenological MSSM; the number of parameters is reduced to 15 by assumptions that retain the most relevant phenomenological aspects of the pMSSM in terms of collider and dark matter searches. The best-fit point obtained corresponds to a squark mass of 2.3 TeV, a gluino mass of 2.1 TeV and a 130 GeV neutralino with a spin-independent cross-section of 2.4×10^{-10} pb, which is within the reach of future multi-ton scale direct detection experiments and of the next LHC run.

Combinations of data as in the fits described above cannot leverage correlations between uncertainties easily. They have to rely on uncorrelated parameters, which is a conservative approach in the case one uses multiple results from the same experiment. Using the full likelihood descriptions of these analyses, which are not publicly available, better limits in various models can be obtained by correlating identical nuisance parameters. A combination of the 0-lepton channel with analyses selecting leptons leads to stronger constraints on MSUGRA/CMSSM and on simplified models squarks and gluinos that decay via 1 or 2 intermediate particles.

In most of the work done in this thesis, the software tool HistFitter was relied upon to produce histograms and likelihoods, and for the interpretation of the results. It builds on commonly used existing software tools in high energy physics, but was specifically developed to be more user-friendly in its configuration. An entire analysis may be written out in a single Python script, an additional level of abstraction that allows for easy bookkeeping, manipulation and testing of large collections of signal hypotheses.

The negative results obtained in supersymmetry searches so far do not mean that it is no longer a viable theory. The production cross-section of supersymmetrical particles may be too low for them to have been produced at the energies colliders have operated at until now. For the proposed high-luminosity LHC, which will collect a dataset 150 times larger than the one currently available at twice the current centre-of-mass enery, the prospects for SUSY searches remain excellent. Even in simplified models of squark and gluino production, models that can be discovered lie outside the range currently excluded by searches at the LHC. Moreover, the increased sensitivity to electroweak production of supersymmetry ensures new avenues to pursue this type of physics beyond the Standard Model remain open during at least the coming decade.

List of publications

Geert Jan Besjes is a member of the ATLAS collaboration and co-author of 237 papers (as of 3 February 2015). He made significant contributions to the following results.

Publications

[1] ATLAS Collaboration, *Summary of the inclusive searches for squarks and gluinos with Run I LHC data at ATLAS*. ATLAS-SUSY-2014-06. In preparation.

[2] M. Baak, G.J. Besjes, D. Côté, A. Koutsman, J. Lorenz and D. Short, *HistFitter software framework for statistical data analysis*. arXiv:1410.1280 [hep-ex]. Submitted to Eur. Phys. J. **C**.

[3] ATLAS Collaboration, *Search for squarks and gluinos with the ATLAS detector in final states with jets and missing transverse momentum using $\sqrt{s} = 8$ TeV proton–proton collision data*, arXiv:1405.7875 [hep-ex]. JHEP **1409** (2014) 176

[4] C. Strege, G. Bertone, G.J. Besjes, S. Caron, R. Ruiz de Austri, et al., *Profile likelihood maps of a 15-dimensional MSSM*, arXiv:1405.0622 [hep-ph]. JHEP **1409** (2014) 081

[5] G.J. Besjes, P. de Jong, and R. van der Leeuw, *In ATLAS speuren naar fysica voorbij het Standaardmodel*, Ned. T. Nat. **79** (2013) 200. (In Dutch)

[6] ATLAS Collaboration, *Search for squarks and gluinos with the ATLAS detector in final states with jets and missing transverse momentum using 4.7 fb^{-1} of $\sqrt{s} = 7$ TeV proton-proton collision data*, Phys. Rev. **D 87** (2013) 012008.

Conference and public notes

[1] ATLAS Collaboration, *Search for supersymmetry at the high luminosity LHC with the ATLAS experiment*, Tech. Rep. ATL-PHYS-PUB-2014-010, CERN, Geneva, July, 2014.

[2] ATLAS Collaboration, *Search for squarks and gluinos with the ATLAS detector in final states with jets and missing transverse momentum and 20.3 fb^{-1} of $\sqrt{s} = 8$ TeV proton-proton collision data*, Tech. Rep. ATLAS-CONF-2013-047, CERN, Geneva, May, 2013.

[3] ATLAS Collaboration, *Search for squarks and gluinos with the ATLAS detector using final states with jets and missing transverse momentum and 5.8 fb^{-1} of $\sqrt{s} = 8$ TeV proton-proton collision data*, Tech. Rep. ATLAS-CONF-2012-109, CERN, Geneva, Aug, 2012.

Popular scientific summary

What is everything around us made of? How does it fit together? Can we explain the processes in nature that we see happening around us? These are the kinds of questions physics tries to answer, and this thesis forms part of the ongoing search for answers to these questions.

Our curiosity has led us to a very refined model of subatomic physics, called the *Standard Model of particle physics*. The building blocks of the universe – the particles described by the model – and their properties can be studied in a laboratory by creating short-lived particles in a controlled environment. One such laboratory is CERN, the European Organisation for Nuclear Research, located near Geneva. It operates the Large Hadron Collider (LHC), a particle accelerator used to collide protons at very high energies in order to study the fundamental questions of nature.

At the LHC, four dedicated experiments continuously measure the result of the collisions of protons. One of these experiments is the ATLAS detector. The results from ATLAS are used to not only study the properties of particles predicted by the Standard Model, but also to search for evidence of the existence of any new particles predicted by extensions of the model. These extensions attempt to address several shortcomings in the Standard Model.

This thesis focuses on a very popular model that addresses the Standard Model's problems, known as *supersymmetry*. It predicts the existence of new, heavy particles that we might be able to produce at the LHC. Such new particles would lead to particular signatures in the detectors. In the large haystack of data collected, these signatures are the needles we attempt to find.

In this summary, the theoretical background behind the Standard Model and supersymmetry, the Large Hadron Collider and ATLAS detector, and a search for supersymmetry are described. A statistical intermezzo may safely be skipped for those familiar with elementary statistical concepts such as null and alternative hypotheses, and how to reject them using p-values. The outlook for future supersymmetry searches is also briefly discussed.

Theoretical background: the Standard Model of particle physics

Imagine you had an uncannily good microscope that could zoom in on any object step by step to an extremely fine level. First, you would encounter the molecules of the material the object is made of. Next, you would be able to see the that these molecules are built out of atoms. An atom, in turn, consists of a nucleus with (possibly many) electrons around it. Going yet one level deeper, the nucleus consist of protons and neutrons that both are made of three particles, which are called *quarks*. As far as we know, electrons and quarks are not composite particles, no matter how hard you try to look. This is the realm of particle physics, which describes the building blocks

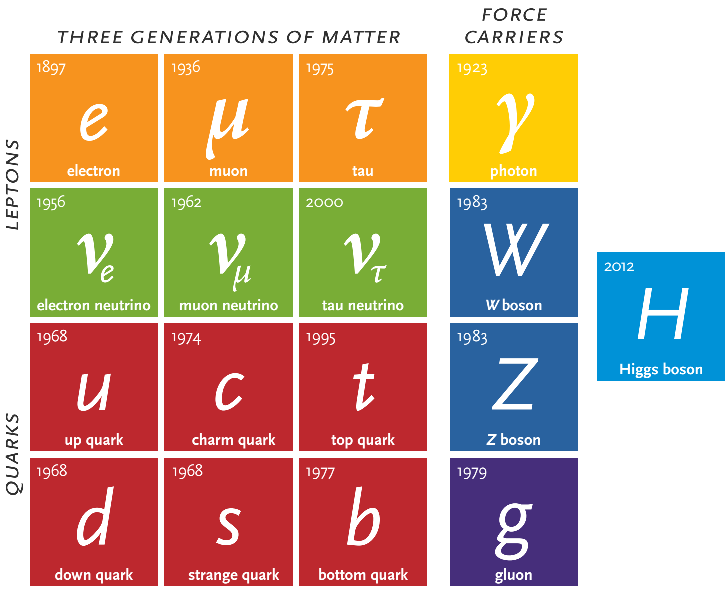

Fig. S1.1 · Particles in the Standard Model and their year of discovery. Matter particles (leptons and quarks) come in three generations; each force has an accompanying particle. The Higgs boson is a consequence of the Higgs mechanism, which gives mass to the W and Z bosons.

of matter around us. These can also interact, through forces working between the elementary particles. The fundamental description of matter in the universe at the smallest scale and how this matter interacts is called the *Standard Model of particle physics*.

All particles are described by fields that have a value at each point in space and time.[1] These fields cannot obtain every possible value, but are *quantised*[2]: the Standard Model is thus a so-called *quantum field theory*. The forces between particles are mathematically described as interactions between the corresponding fields; i.e., how the fields link between each other.

Luckily for us, the matter in the universe does not idly float around: the Standard Model is a dynamical theory, with interactions. The heart of the Standard Model is a function that describes these dynamics (its *Lagrangian*). Interactions between the fields arise from the fact that the Standard Model is symmetric under various operations, for example a simple rotation, called *symmetries*.[3] That rotation in fact describes the interaction of light and matter (electromagnetism), while more complex mathematical symmetries describe two other forces: the *weak nuclear force*, which describes radioactive decays, and the *strong nuclear force*, which is responsible for keeping together the particles in the proton.

All particles described by the Standard Model are shown in fig. S1.1. Matter particles are *fermions* and divided between leptons and quarks. Both come in three *generations*: each charged

[1] A field has a value at every coordinate, can vary in time and may have a direction: think of a magnetic field.
[2] The fields only take on discrete values: something akin to half an electron does not exist.
[3] For example, a beer bottle, *sans* labels, is also invariant under this kind of rotation.

lepton (the electron e, the muon μ and the τ lepton) is accompanied by a *neutrino* ν. Quarks are also described in pairs: *up* and *down*, *charm* and *strange*, and *top* and *bottom*. All matter around us is built up only using the first generation: electrons, protons (uud) and neutrons (udd).

The three forces are each governed by their own particles (called *bosons*): the photon for electromagnetism, the W and Z bosons for the weak nuclear force and the gluon for the strong nuclear force. All these particles must be massless: introducing the masses for these particles would break the mathematical symmetries, which is forbidden. However, this is incompatible with the observation that the W and Z bosons have mass; clearly, the symmetry must be broken.

Here, the final piece of the Standard Model's puzzle is needed: the Higgs boson. The Higgs boson is the consequence of the introduction of an *extra* field that leads to *spontaneous symmetry breaking*. In other words, the presence of the Higgs field elegantly explains why the W and Z bosons have mass (the *Higgs mechanism*), and as a result of its introduction a new particle must exist.[1] The Standard Model does not predict the mass of the Higgs boson; it was discovered in 2012 after a decades-long search.

Shortcomings of the Standard Model and SUSY to the rescue

Despite its accuracy, the Standard Model cannot be a complete theory of nature at an elementary level. First of all, and most obvious, gravity is not described in the model. Several considerations, both experimental and theoretical, point in the direction of some *new physics* and the need of a bigger model, even excluding the problem of gravity.

For this summary, we will constrain ourselves to two of these. First of all, astrophysical observations indicate the presence of *dark matter* in the universe. The behaviour of (clusters of) galaxies can not be explained in a satisfying way, unless extra matter is present, as shown in fig. S1.2. However, this invisible matter can only interact via gravity, or other phenomena would appear. Moreover, the Standard Model lacks a building block to describe dark matter: there is no candidate particle for it. Secondly, the Standard Model suffers from a theoretical problem known as *fine-tuning*: the observed Higgs mass (125 GeV) is the difference of two huge numbers (of the order 10^{17} GeV), which need to cancel to give exactly the observed value. This compels theorists to develop theories without such shortcomings.

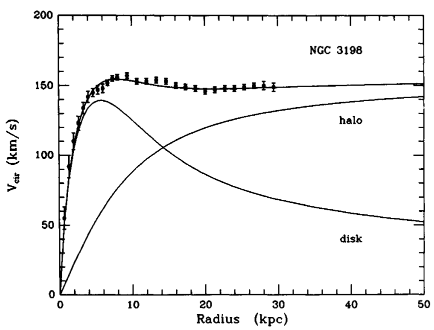

Fig. S1.2 · Measured rotation speed as a function of the distance to the centre of a galaxy [73]. The "disk" line is the contribution from visible matter, which cannot explain the measured values.

[1] Think back of the beer bottle: an analogy would be a situation where it is forbidden to manufacture the bottle with a special place for a label, as this would break the symmetry before the label is applied. Once a label is placed on the bottle, a preferred direction is automatically chosen – which direction that is was not preordained, however.

Supersymmetry (SUSY), as the name suggests, introduces an *additional* symmetry on top of the Standard Model, motivated by the fact that particle physics can be so well described by imposing symmetries. It gives partner particles with identical properties to the existing ones; only their spin is different.[1] For reasons not discussed here, supersymmetry predicts the existence of not one, but five Higgs bosons. The new particles are indicated with a tilde above the symbol and called *sleptons* ($\tilde{\ell}$, $\tilde{\nu}$), *squarks* ($\tilde{q}$), *higgsinos* and *gauginos*. The gauginos are the *bino*, *wino* and *gluino* $\tilde{g}$.[2] Of these particles, the charged higgsinos and gauginos mix to form four *charginos* $\tilde{\chi}_1^{\pm}$ and $\tilde{\chi}_2^{\pm}$, while the neutral ones mix to form the *neutralinos* $\tilde{\chi}^0_{1,2,3,4}$.

It is important to note that this proposed new symmetry of nature can not be exact: in that case, the new particles would be as heavy as the Standard Model particles and would already have been observed. Similar to the Higgs mechanism, SUSY is broken at a higher energy scale[3], which leads to heavy partner particles.

An additional feature of supersymmetry is that the *lightest* neutralino (called $\tilde{\chi}_1^0$) can be a stable particle that cannot decay into Standard Model particles: it is a perfect candidate for dark matter. A downside to supersymmetry is that, in its most general form, it has 124 free parameters. The existence of SUSY can manifest itself in many different ways, depending on its parameters. Some of these ways are harder to detect than others, and simplifying assumptions are often made.

Measuring elementary particles: the LHC and the ATLAS detector

In order to study the particles described by the Standard Model and to be able to discover new particles by supersymmetry, an experimental setup is needed. Particle physics relies on the equivalence between mass and energy to produce particles: by smashing known particles together at (very) high energies, other elementary particles can be created and studied. As most of the created particles have a very short lifetime, they decay and are never observed directly.[4] Instead, a detector such as ATLAS is used to measure all the debris and reconstruct the initial particles that were created.

The Large Hadron Collider is a 27 km long circular particle accelerator used to collide protons at an energy of 4 TeV per proton, which corresponds to 99.999 999 1 % of the speed of light – or the same energy per beam as an aircraft carrier cruising at 5.6 knots. Protons are charged particles, which follow a curved trajectory in a magnetic field: most of the accelerator is in fact built of 1232 superconducting magnetic dipoles used only to keep the protons on their circular trajectory. At only one location along the ring, an electric field is used to accelerate the beams. The protons are made to collide at four points: at these places, detectors are placed to measure the result of the collisions and record the resulting *events*. An aereal view of the accelerator is shown in fig. S1.3.

1 Spin is a fundamental property of a particle, just as its electric charge is. It is the quantum mechanical equivalent to angular momentum.

2 The reason why a *bino* and not a *zino* exists is that the Standard Model Z boson and the photon are a mix of two fields: the photon field B and the field W^3. The $W^{\pm}$ bosons are a mix of $W^{1,2}$. These fields have superpartners, not the particles.

3 There is no consensus on the exact SUSY breaking mechanism.

4 These lifetimes range from the relatively long 2.2 µs (two millionths of a second) for the muon to the extremely short 5×10^{-25} s (half a millionth of a billionth of a billionth of a second) predicted for the top quark.

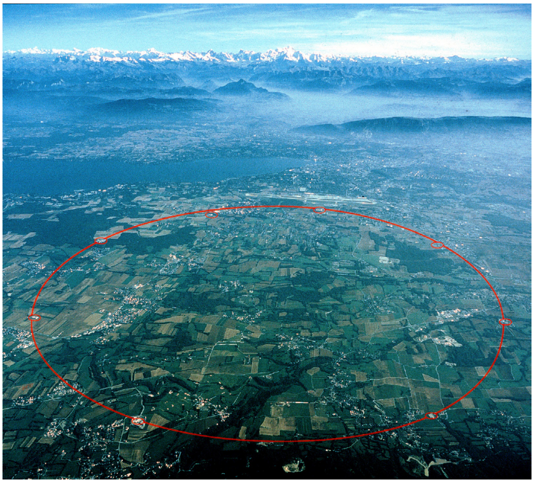

Fig. S1.3 · The scale of the Large Hadron Collider, with Lake Geneva and the city visible. Mont Blanc can be seen in the top of the image. ATLAS is located at the 2 o'clock position along the ring.

A particle detector must be able to precisely measure all the debris from the collision. As such, ATLAS is built as a cylinder so that anything that happens inside the detector volume can be recorded. Its length is approximately 44 m and height 25 m: such a large machine is needed to research subatomic particles because of the enormous amount of debris created in the collisions.

To make sure that each kind of particle that lives long enough to reach the detector is measured accurately, ATLAS is not one type of apparatus, but a set of machines all built around each other. A schematic view of how particles are measured is shown in fig. S1.4. Very close to the collision, charged particles are measured by a *tracking system*: from the measurements, dedicated algorithms later reconstruct the flight path of these particles. Around the tracker, two detectors measure the energy of all particles except muons. Energetic muons are measured by a special muon spectrometer that surrounds the rest of the detectors.

Finally, when a quark or gluon is produced, a tight cone of particles (jets) is formed due to a phenomenon known as confinement: free quarks do not exist. A jet is not a particle, but a cone of a certain size: special jet reconstruction algorithms are used to recognise these objects.

This allows us to measure any *visible* particle. Invisible particles, such as the neutralino, and neutrinos cannot be detected directly. Their presence must be inferred from *missing transverse momentum* (also called missing transverse energy): if the transverse momentum of all other objects is added together, it may not add up to zero.[1]

Reconstruction all objects for every single collision is impossible. Inside the ATLAS detector, 40 million collisions occur every second. All these collisions must be measured, but only interesting events have to be stored. Storing every collision would lead to 65 TB of data *per second*, which is far too much to be properly stored and analysed. A system of *triggers* is used that bring down the data

[1] By construction this must be the case: the incoming protons have momentum in the direction of the beam, not perpendicular to it! Any missing transverse momentum is attributed to invisible particles.

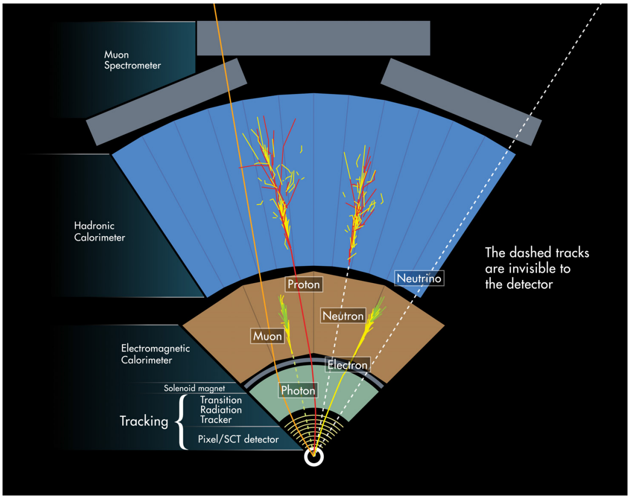

Fig. S1.4 · An illustration of the way different particles are detected in ATLAS.

rate to around 200 events per second, mostly limited by the data size of each event. These triggers operate using requirements that the event contains a certain interesting object, for example an electron with enough energy.

After objects and the event have been reconstructed, an enormous dataset is obtained. Statistical methods are used to determine whether new particles have been seen, or to determine the properties of known particles.

Statistical intermezzo

Having obtained a dataset of events, the question must be answered whether any signs of *new*, yet undiscovered particles were observed. The answer to such a question is given much in the same way as one would answer the question “is this die loaded?”: by quantifying the *probability of the observation*. In other words: if a die is thrown 120 times and we see 22 sixes, we must ask ourselves how (un)likely we consider such a measurement. Depending on an agreed upon level of how unlikely a measurement must be, one concludes the die is loaded or not. Intuitively, one could argue that 22 times a six is in the ballpark of what is expected (20), whereas 60 times a six would surely be called suspect.

In a more quantified approach, the question asked is “what is the probability of obtaining a result of 22 *or more* times a six?”: this is the so-called *p-value*.[1] It quantifies how (un)likely an observation is under the expected value, which in the case of our die is 20, given a certain uncertainty: exactly 20 sixes is not seen every single time this experiment is done. The expectation is therefore denoted as 20 ± 4.5.[2]

[1] Note that the p-value for obtaining exactly the expected 20 times a six is by construction 0.5: half of the probability distribution lies above, half below.
[2] The number 4.5 gives the range around 20 in which 68 % of all measurements should occur, a *confidence interval*.

To determine whether or not a die is loaded, an agreed upon p-value must be used. In particle physics, the p-value that constitutes a *discovery* 3×10^{-7}, or 0.00003 %.[1] Practically speaking, this means we expect that the experiment (120 throws) should be repeated 3.3 million times for such an unlikely scenario to spuriously occur if the die is not loaded. In this case, the value is 50.3. Rounding off, it means that an observation of 51 or more sixes would lead to the conclusion the die must be loaded.[2,3]

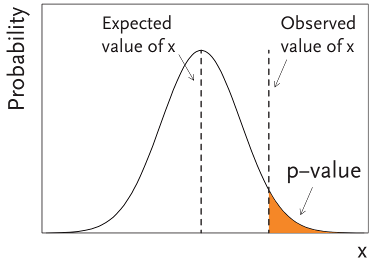

Fig. S1.5 · Illustration of a p-value.

However, what if we measure less than 51 sixes and cannot conclude the die is loaded at the agreed-upon confidence level? An attempt to determine *how* loaded the die can then still be can be made: that is, one is interested what loaded die would never give only the observed 22 *or less* times a six and attempts to reject these alternative hypotheses.[4] For this, a p-value of 0.05 is used. In the example, this corresponds to a loaded die that would yield an expected 30 sixes. In other words, in case only 22 sixes are observed, we can conclude that all types of die that have an expectation value of at least 30 times a six are ruled out at 95 % confidence level. [5]

Two important observations must be made about a statistical procedure as used for the die:

- a smaller uncertainty on the expected value makes it easier to obtain significant results (e.g. determining whether a die is loaded): measuring 27 when 20 ± 4.5 is expected is *not* significant, while measuring the same value *is* significant when 20 ± 0.05 is expected;
- as a consequence, the larger the dataset, the easier it becomes to make a significant observation: the relative uncertainty typically decreases as $\sqrt{N}$. Taking the same example, a dataset 10 000 bigger (270 000 measured when $200\,000 \pm 450$ is expected) does allow for a significant result.

The take-home message for the aspiring particle physicist is thus: ensure you have a dataset with as much expected *signal* (for example, events due to supersymmetry) on top of the expected *background* (all the known processes), while keeping the uncertainty on the background sufficiently small. If *selections* are made on the dataset that reject (much) more background than hypothetical signal, these are useful to increase the power of an analysis. An ideal selection would be one that decreases the background by a (very) large factor and does not reject any signal. In practice, trade-offs are made as no selection is ideal, and the *ratio* of signal over background is optimised.

1 This corresponds to five standard deviations of the normal distribution, or $5\,\sigma$.

2 The more common confidence level of 95 % can also be used, which corresponds to 27.9: only 28 sixes would be sufficient to conclude the die is loaded.

3 The confidence intervals used in both examples are one-sided. For argument's sake we do not assume an attempt to load a die would lead to *less* signals – such a clumsy attempt at cheating at a game of chance would be rather pathetic. This corresponds to what happens in particle physics: new hypothetical particles lead to *more* events, never less.

4 Note that this uses the left tail of a probability distribution, instead of the right. We are now attempting to reject an alternative hypothesis, rather than the null hypothesis.

5 An interesting question arises in case one would observe (much) less than the expected value, e.g. 5. In this case, both the null (20) and the alternative hypothesis (30) would be rejected. One then is forced to conclude that this is a scenario in which the statistical test has no power; see §5.9.2 for a more detailed discussion.

Searching for supersymmetry

Having obtained a dataset of events from our detector, and knowing how to find evidence of new particles by statistical means, we can perform a search for supersymmetry. If SUSY exists, the particles it predicts are all produced at different rates and all interact in different ways. Any analysis therefore focuses on a particular set of particles that are produced, and that subsequently decay in a certain way. In this thesis, we have focused on squarks and gluinos, the partner particles of the quarks and the gluon. If SUSY exists, these are the most abundantly produced SUSY particles at the LHC.

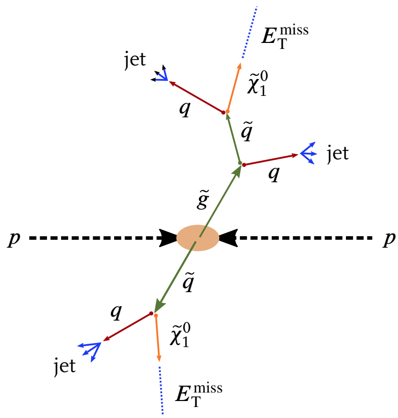

Fig. S1.6 · Schematic view of squark–gluino production at the LHC. A squark $\tilde{q}$ and gluino $\tilde{g}$ are produced that each decay directly to quarks, which form jets, and neutralinos, which cannot be seen.

In chapter 5 a search using events without a lepton, with several jets and with missing energy was presented. The choice for this final state is motivated by the fact that it is the most sensitive to direct decays of squarks and gluinos, which are shown in fig. S1.6. These decays occur in many complicated supersymmetrical models. In direct decays, a squark decays to a quark and missing energy and a gluino to two quarks and missing energy. In scenarios where squarks and gluinos are produced in pairs, direct decays thus lead to an event that contains 2 to 4 quarks, which lead to jets, and several particles that escape the detector unseen and thus lead to missing energy. The analysis uses events with 2 to 6 jets to also be sensitive to less common decay mechanisms, which all lead to extra jets.

To select interesting events, we require that they have 2 to 6 jets and that all these jets have a high momentum (at least 60 GeV). In addition, one of the jets must have a very high momentum (at least 130 GeV) and the event should have high missing transverse energy (at least 160 GeV). These requirements ensure plenty of SUSY events are selected, and that known processes are suppressed: they are less likely to lead to such events.

Events are also required to contain no electron or muon. This suppresses background processes further, as the direct decays of squarks and the gluino do not lead to such a particle. Standard Model processes which give the same kind of event, but with an electron or muon, are suppressed in this way. [1]

However, we are unable to reject *all* Standard Model backgrounds. For example, the production of a Z boson in association with jets can also to exactly the same kind of event as the

[1] We are therefore less sensitive to decays of squarks and gluinos via a W boson, and even less sensitive to decay mechanisms where 2 leptons are produced. Dedicated analyses that focus on events with exactly 1 lepton and events with two or more leptons also exist.

production of SUSY particles.[1] Moreover, the measurements performed by ATLAS are not perfect: e.g. an event containing only jets will also mimic interesting events in the case a jet is misidentified, which leads to *fake missing transverse energy* (fake E_T^{miss}). All background processes must therefore be estimated correctly and as precisely as possible.

To discriminate between interesting events and events likely to come from background, further selections are used. The final *signal regions* used select and reject events using the *effective mass*: the sum of all the jet momenta and the missing transverse energy. Studies have shown that this quantity correlates well with the mass of the original SUSY particle. As these particles are predicted to be heavier than Standard Model particles, we can thus select events with high effective mass to reject background while signal events are kept.

The remaining number of Standard Model background events after all selections is estimated using four dedicated *control regions*: one for each background process. These regions have almost the same selections as the corresponding signal regions, but with one or two selections reversed or changed to predominantly select events from one particular process, e.g. Z+jets events. Measurements in the control regions can be used to correct the backgrounds obtained from simulation: if 100 Z+jets events are observed but 90 were predicted from computer simulations, the prediction for that background as obtained from simulation will be scaled by 1.11. All backgrounds are scaled *simultaneously* in all regions, so that cross-contaminations in the control regions are taken into account correctly.[2]

After this complicated fitting procedure, we are left with an improved prediction of the remaining Standard Model background in the signal region. The signal regions are then unblinded[3] and the amount of expected events is compared to the amount of measured events: at this stage, the procedure proceeds exactly as for the die in the previous section.

No statistically significant excess over the background is observed in the signal regions: the measurements are compatible with the Standard Model predictions. A discovery of supersymmetry can not be claimed.

Interpreting and using the results

With no significant excesses found, we can set *upper limits* for each of the signal regions. The number of extra events allowed in each region is determined, which can be used by theorists to test their own models against the analyses: any model that predicts more than the allowed number of events would be impossible. These limits are thus *model-independent*. A large set of specific SUSY signal models is also tested: if these models predict too many extra events (i.e., the number of observations is much less than the model predicts), they are ruled out.

Limits for particular models can be set by varying the parameters of the model. In the case of a simplified model of gluino-pair production, the only two parameters are the mass of the

[1] The Z boson can decay into two neutrinos, which also escape the detector unseen.

[2] The entire fitting procedure, as well as the limit setting, is implemented using the program HistFitter that is described in chapter 9. HistFitter is also used for most analysis in the SUSY working group of the ATLAS experiment.

[3] A blinded region is one where the *measured* amount of data is not looked at yet, in order to avoid any bias in designing the analysis. After unblinding, measurements in that region are used.

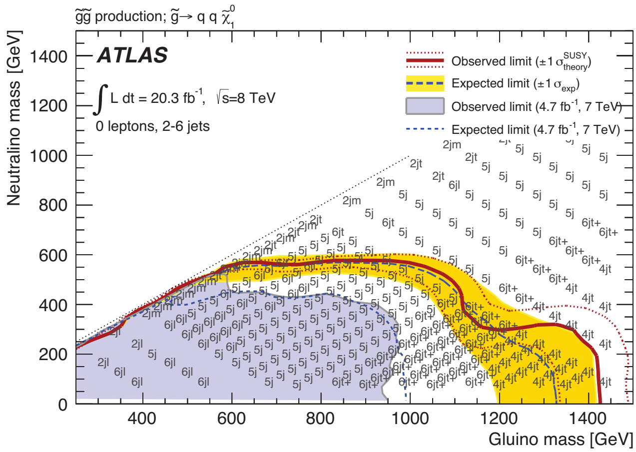

Fig. S1.7 · Exclusion limits for direct production of gluino pairs with decoupled squarks. The grey labels indicate the signal region that was used to exclude a particular model. The blue dashed line is the *expected* exclusion: the set of models that we would exclude if we measure exactly the Standard Model expectation. Due to less events observed than were expected in signal region 4jt, we were able to exclude more models than expected in the lower right-hand corner.

gluino and the mass of the neutralino that it decays into. By testing a large set of combinations of these two masses, we can determine the limit in this simple model's parameter space through interpolation.[1] An example for gluino-pair production is shown in fig. S1.7.

To improve such limits, the results from other analyses can be used. The analysis described so far uses events without leptons. A different analysis that relies on an entirely separate dataset can be combined with the obtained result. In this way, a smaller total uncertainty can be gained. As several experimental uncertainties are the same between the analysis, a naïve combination of the result would overestimate the uncertainty, and lead to worse results than possible. Instead, the uncertainty can be correlated between the two analyses, leading to the best possible combined limit. Such an approach is followed in chapter 7, where results are combined with results from the 1- and 2-lepton analyses.

The results obtained can also be used to explore more complicated models of supersymmetry. A simplified model of gluino-pair production is not a very realistic manifestation of supersymmetry: it would be very strange to be able to produce only gluinos and neutralinos. In chapter 6 a scan over a *phenomenological Minimal Supersymmetric Standard Model* (pMSSM) with 15 free parameters is performed. Such models reduce the number of parameters of the most general form of supersymmetry, but retain the most important parameters for collider physics.

By not only incorporating results from the LHC, but also many other limits and measurements[2], the most likely parameters can be sampled using scanning techniques. These rely on

[1] This procedure is easier than it sounds: the interpolation at 95 % confidence level can be compared to lines on a hiking map or isobaric lines on a weather chart.

[2] These include results from previous accelerator experiments and from direct dark matter detection experiments, and precise measurements of processes involving bottom and down quarks that would be heavily influenced if SUSY particles exist.

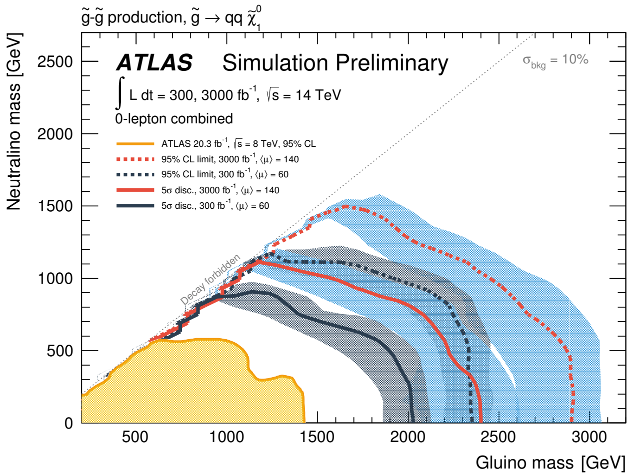

Fig. S1.8 · Prospects for direct production of gluino pairs with decoupled squarks using datasets 15 and 150 times larger than the one currently available. The models excluded already are shown in yellow. Models under the solid lines can be discovered, while models under dashed lines can be excluded. The bands reflect the uncertainty on the theoretical prediction.

Bayesian *priors*[1] of the parameters and explore the parameter space to obtain the *posterior* distributions given the constraints. The best-fit point is then the most probable in light of all measurements performed worldwide until now. After inclusion of all data it corresponds to a squark mass of 2.3 TeV, a gluino mass of 2.1 TeV and a 130 GeV neutralino with a spin-independent cross-section of 2.4×10^{-10} pb, which is within the reach of future multi-tonne scale direct dark matter detection experiments and of the upcoming LHC run.

What's next for supersymmetry?

The negative results obtained in supersymmetry searches so far do not mean that it is no longer a viable theory. The production rate of supersymmetrical particles may be too low for them to have been produced in sufficient amounts at the energies colliders have operated at until now. For a proposed upgrade LHC, which will collide more protons per second and collect a dataset 150 times larger than the one currently available at twice the LHC's current centre-of-mass energy, the prospects for SUSY searches remain excellent. Even in simplified models of squark and gluino production, the models that can be discovered lie outside the range currently excluded by searches at the LHC as shown in fig. S1.8 and chapter 8. Moreover, the increased sensitivity to (much) rarer production mechanisms of supersymmetry, such as the direct production of neutralinos and charginos, ensures new avenues to pursue this type of physics beyond the Standard Model remain open during at least the coming decade.

[1] A prior is the a priori likelihood of a parameter having a certain value. A flat prior means all values in a certain range are considered equally likely. Secretly we all employ Bayesian priors in life: try thinking of the probability distribution of how well your favourite football team will do in the Champions League next year. (Hint: it's definitely not uniform and the chance of winning probably close to zero, unless of course you're Spanish or from Bavaria.)

In the immediate future, the years 2015–2017 will be an interesting time for high energy physics. After a two-year hiatus in data taking, the LHC will return with a vengeance and collide protons at its design energy of 14 TeV. It might not seem an enormous improvement over the current 8 TeV, but the production rate for e.g. gluino production will increase by a factor 40 to 100, depending on the mass. Both ATLAS and its competing sister experiment CMS will thus be able to surpass their results obtained until now rapidly, and likely start venturing into unknown territory shortly after summer 2015. The increased energy will also allow the properties of the Higgs boson to be measured more precisely and in new decay channels, which can shed more light on supersymmetry. New and larger direct dark matter detection experiments will be able to probe even rarer processes. Whether the Standard Model starts to show cracks soon or only after several years' worth of data-taking will remain to be seen, but bearing in mind that it took 48 years from the Higgs boson's conception to its discovery there is no need to despair (yet?).

Populair-wetenschappelijke samenvatting

Waar bestaat de wereld om ons heen uit? Hoe werken de fysische processen die we in de natuur om ons heen waarnemen? Op dergelijke vragen probeert de natuurkunde antwoorden te geven, en dit proefschrift vormt een onderdeel van de altijd gaande zoektocht daarnaar.

Onze nieuwsgierigheid heeft ons tot een verfijnd model van de subatomaire natuurkunde gebracht, het *Standaardmodel* van de deeltjesfysica. De bouwstenen van het universum – de deeltjes beschreven door het model – en hun eigenschappen kunnen in een laboratorium bestudeerd worden door ze door middel van een versneller te produceren. CERN, de Europese organisatie voor kernonderzoek in de buurt van Genève, is een dergelijk lab. De door CERN gebouwde Large Hadron Collider (LHC) is een deeltjesversneller waar protonen op hoge snelheid met elkaar in botsing gebracht worden om zo fundamentele vragen over de natuur te kunnen beantwoorden.

Vier experimenten bij de LHC meten continu de resultaten van de protonbotsingen. De ATLAS-detector is één van deze vier experimenten. Niet alleen worden bij de LHC de eigenschappen van Standaardmodeldeeltjes bestudeerd, maar ook wordt gezocht naar het bestaan van deeltjes die voorspeld worden door uitbreidingen van de theorie. Dergelijke uitbreidingen proberen (een aantal) tekortkomingen van het Standaardmodel op te lossen.

In dit proefschrift ligt de focus op een erg populaire uitbreiding bekend staat als *supersymmetrie*. Die uitbreiding voorspelt veel nieuwe, zware deeltjes die we mogelijk bij de LHC kunnen produceren om daarna bepaalde specifieke signalen in de detectoren te meten. In de grote hooiberg aan data die opgeslagen wordt, zijn die specifieke signalen de naalden waarnaar we op zoek zijn.

De theoretische achtergrond van het Standaardmodel en supersymmetrie, de werking van de LHC en de ATLAS-detector en een zoektocht naar supersymmetrische deeltjes worden in deze samenvatting kort besproken. In een kort statistisch intermezzo wordt uitgelegd hoe nulhypothesen, alternatieve hypothesen en p-waarden gebruikt worden. Aan het einde worden de vooruitzichten voor toekomstige zoektochten ook kort besproken.

Theoretische achtergrond: het Standaardmodel

Stel dat we de beschikking hadden over een waanzinnig goede microscoop die op elk object tot een willekeurig niveau zou kunnen inzoomen. Al inzoomend zouden eerst de moleculen van het materiaal waaruit het object bestaat zichtbaar worden. Daarna zou duidelijk worden dat de moleculen bestaan uit verschillende atomen, die op hun beurt weer bestaan uit een kern

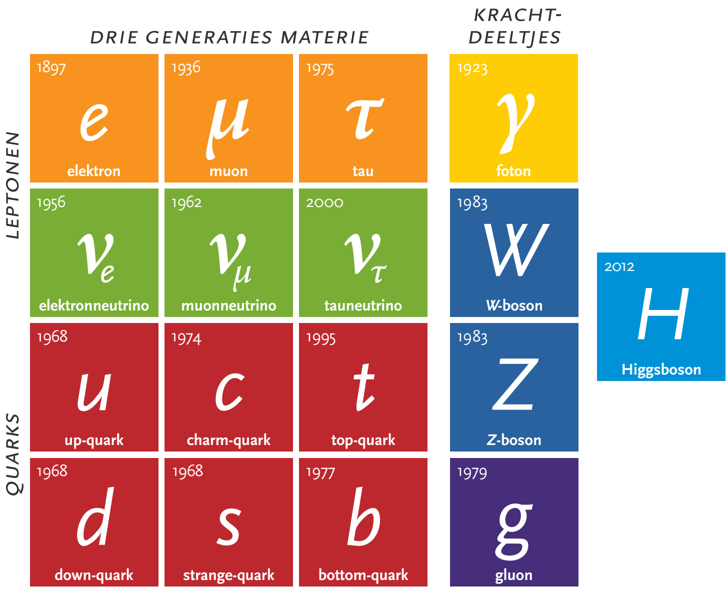

Fig. S2.1 · Deeltjes in het Standaardmodel en het jaar van hun ontdekking. Materie (leptonen en quarks) bestaat in drie generaties; elke kracht heeft een bijbehorend deeltje. Het Higgsboson is een gevolg van het Higgsmechanisme, dat massa aan de W- en Z-bosonen geeft.

met een wolk van (mogelijk veel) elektronen. Nog een niveau lager zouden we zien dat een atoomkern is gemaakt van protonen en neutronen. Protonen en neutronen bestaan uit drie *quarks*. Daar bereiken we het kleinst mogelijke niveau: voor zover bekend zijn quarks en elektronen geen samengestelde deeltjes. Dit is het terrein van de deeltjesfysica, die de bouwstenen van de materie om ons heen en hun interacties beschrijft. Het model waarmee dat gedaan wordt heet het *Standaardmodel* van de deeltjesfysica.

Alle deeltjes worden beschreven door *velden* die een waarde op elke plaats in de ruimte en tijd hebben.[1] Deze velden kunnen geen willekeurige waarden aannemen en zijn *gekwantiseerd*:[2] het Standaardmodel heet daarom technisch een *kwantumveldentheorie*.

Gelukkig voor ons bestaan is het niet zo dat de materiedeeltjes rondzweven in het universum zonder iets te doen. Het Standaardmodel is een dynamische theorie die ook interacties beschrijft. De krachten tussen deeltjes worden wiskundig beschreven als interacties tussen de corresponderende velden: dat wil zeggen, hoe de velden elkaars aanwezigheid merken.

Ten grondslag aan het model ligt een wiskundige functie die deze dynamica beschrijft (de *Lagrangiaan*). Interacties tussen velden komen voort uit het feit dat het Standaardmodel symmetrisch is onder bepaalde operaties, zoals een rotatie.[3] Een eenvoudige rotatie beschrijft de interactie tussen licht en materie (elektromagnetisme). De andere twee krachten, de *zwakke kernkracht*, die

[1] Een veld is een object dat op elk punt een waarde die met de tijd kan variëren heeft en dat een richting kan hebben: denk bijvoorbeeld aan een magnetisch veld.
[2] De veldwaarden zijn discreet: er bestaat niet zoiets als een half elektron.
[3] Een bierflesje, zonder labels, is ook symmetrisch onder een dergelijke rotatie rond zijn lengte-as.

bijvoorbeeld radioactief verval beschrijft, en de *sterke kernkracht*, die ervoor zorgt dat de quarks in het proton bijeen gehouden worden, worden beschreven door ingewikkelder symmetrieën.

Alle deeltjes in het Standaardmodel zijn weergegeven in fig. S2.1. Materiedeeltjes zijn zogenaamde *fermionen* en onderverdeeld in leptonen en quarks. Beide komen in drie *generaties* voor: drie geladen leptonen (het elektron e, het muon μ en het τ-lepton), elk vergezeld door een *neutrino* ν. Quarks worden ook in paren beschreven: *up* en *down*, *charm* en *strange*, en *top* en *bottom*. Alle materie om ons heen bestaat slechts uit deeltjes uit de eerste generatie: elektronen, protonen (uud) en neutronen (udd).

De drie krachten worden elk geregeerd door hun eigen deeltjes (*bosonen*): het foton voor elektromagnetisme, de W- en Z-bosonen voor de zwakke kernkracht en het gluon voor de sterke kernkracht. Deze krachtdeeltjes moeten a priori massaloos zijn; een term die massa geeft in het model stoppen is verboden omdat hij de wiskundige symmetrieën zou breken, wat op theoretische gronden niet is toegestaan. Dat is echter problematisch: de W- en de Z-bosonen hebben wel degelijk massa. De symmetrie kan daarom niet exact zijn, maar moet *gebroken* zijn.

Daarvoor is het laatste stukje van het Standaardmodel nodig: het Higgsboson. Het Higgsboson is het gevolg van het toevoegen van een *extra* veld dat tot *spontane symmetriebreking* leidt. Het bestaan van het Higgsveld verklaart op een elegante manier waarom de W- en de Z-bosonen toch massa hebben (het *Higgsmechanisme*), en als gevolg bestaat er een extra deeltje.[1] Na een zoektocht van enkele decennia werd het Higgsboson in 2012 ontdekt.

Tekortkomingen van het Standaardmodel en SUSY als redder in nood

Ondanks al zijn nauwkeurige voorspellingen kan het Standaardmodel niet een volledige theorie van de natuur op haar fundamenteelste niveau zijn. Bovenal wordt de zwaartekracht niet door het model beschreven. Nog los daarvan geven verschillende overwegingen, zowel experimenteel als theoretisch van aard, suggesties voor *nieuwe fysica* en een groter, omvattender model.

In deze samenvatting beperken we ons tot twee van deze overwegingen. Allereerst geven sterrenkundige waarnemingen aan dat er *donkere materie* in het universum moet bestaan. Het gedrag van (clusters van) sterrenstelsels kan zonder deze donkere materie niet verklaard worden, zoals getoond in fig. S2.2. Donkere materie kan echter alleen indirect door zijn aantrekking via de zwaartekracht worden gezien: als dat niet het geval was, waren

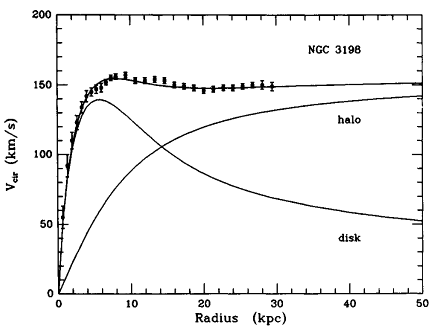

Fig. S2.2 · Rotatiesnelheid als een functie van de afstand tot het centrum van een sterrenstelsel [73]. De lijn met "disk" is de bijdrage van zichtbare materie en kan de metingen niet verklaren; er is een halo van donkere materie nodig om dat wel te doen.

[1] Denk even terug aan het bierflesje: het flesje zo produceren dat er een voorbestemde plaats is voor een label is niet toegestaan. Echter, zodra een label wordt geplaatst is automatisch ("spontaan") een voorkeursrichting bepaald. Het cruciale punt is dat die richting niet vooraf lag vastgelegd: elke plek was goed geweest, maar zodra het label ergens zit bepaalt dit de speciale richting.

fenomenen voorgekomen waardoor het toch direct waargenomen had kunnen worden. Het Standaardmodel ontbeert echter een deeltje waaruit donkere materie opgebouwd zou kunnen zijn. Ten tweede heeft het Standaardmodel last van een theoretisch probleem dat bekend staat als *fine-tuning*. De waargenomen massa van het Higgsdeeltje (125 GeV) is het verschil van twee enorme getallen (van de orde 10^{17} GeV) die elkaar precies net niet moeten opheffen om de gemeten waarde te krijgen. Dat spoort theoretici aan modellen *zonder* dergelijke tekortkomingen te ontwikkelen.

Supersymmetrie (SUSY) introduceert, zoals de naam al suggereert, een *extra* symmetrie bovenop het Standaardmodel, gemotiveerd door het feit dat deeltjesfysica zo goed beschreven kan worden door symmetrieën. SUSY geeft partnerdeeltjes met identieke eigenschappen aan elk bestaand deeltje; slechts hun spin verschilt.[1] Om redenen waarop we hier niet verder ingaan worden door SUSY niet één maar vijf Higgsbosonen voorspeld. De overige nieuwe deeltjes worden aangegeven met een tilde boven het symbool en *sleptonen* ($\tilde{\ell}$, $\tilde{\nu}$), *squarks* ($\tilde{q}$), *higgsino's* en *gaugino's* genoemd. De gaugino's zijn het *bino*, *wino* en *gluino*.[2] De geladen higgsino's en gaugino's mengen tot vier *chargino's* $\tilde{\chi}_1^{\pm}$ en $\tilde{\chi}_2^{\pm}$; de neutrale tot de *neutralino's* $\tilde{\chi}_{1,2,3,4}^0$.

Het is belangrijk op te merken dat deze nieuwe voorgestelde symmetrie niet exact kan zijn: in dat geval zouden partnerdeeltjes precies dezelfde massa hebben als bekende deeltjes en daarom al gemeten zijn. Op een manier vergelijkbaar met het Higgsmechanisme moet SUSY gebroken worden bij een bepaalde hogere energieschaal,[3] hetgeen leidt tot zware partnerdeeltjes.

Een bijkomende eigenschap van supersymmetrie is dat het *lichtste* neutralino (aangegeven met $\tilde{\chi}_1^0$) een stabiel deeltje kan zijn dat niet vervalt naar Standaardmodeldeeltjes. Daarmee is het een perfecte kandidaat voor donkere materie. De keerzijde is daarentegen dat in zijn meest algemene vorm supersymmetrie 124 vrije parameters heeft. Afhankelijk van de waarden van die parameters kan het bestaan van supersymmetrische deeltjes veel mogelijke consequenties hebben. Dat maakt de theorie niet makkelijk de bevestigen of te verwerpen. Meestal wordt, al dan niet noodgedwongen, gebruik gemaakt van vereenvoudigende aannames.

Productie en detectie van elementaire deeltjes: de LHC en de ATLAS-detector

Om de deeltjes beschreven in het Standaardmodel te bestuderen en om nieuwe deeltjes voorspeld door supersymmetrie te ontdekken is een experimentele opstelling nodig. De deeltjesfysica maakt gebruik van het equivalent tussen massa en energie (de beroemde formule $E = mc^2$) om deeltjes te produceren. Door bekende deeltjes met (heel) hoge energieën op elkaar te laten botsen kunnen andere elementaire deeltjes geproduceerd en bestudeerd worden. De meeste van deze deeltjes hebben een levensduur die zo kort is dat ze vervallen voordat ze direct gemeten kunnen worden.[4] Er wordt daarom gebruik gemaakt van een detector zoals ATLAS om alle vervalsproducten die bij een botsing geproduceerd worden te meten en zo de oorspronkelijke deeltjes te reconstrueren.

1 *Spin* is een fundamentele eigenschap van een deeltje, net zoals bijvoorbeeld zijn lading dat is. Het is het kwantummechanisch equivalent van draaiimpuls.

2 De reden dat er een *bino* en geen *zino* bestaat is dat het Z-boson en het foton een menging van twee velden zijn: het fotonveld $\boldsymbol{B}$ en het veld W^3. De $W^{\pm}$-bosonen zijn een menging van $W^{1,2}$. Deze velden hebben superpartners, niet de deeltjes.

3 Er bestaat geen consensus over de wijze waarop deze symmetrie van SUSY gebroken wordt.

4 De levensduren lopen uiteen van relatief lang voor het muon (2,2 µs, of tweemiljoenste van een seconde) tot extreem kort voor het top-quark (5×10^{-25} s, of een halfmiljoenste van een miljardste van een miljardste van een seconde).

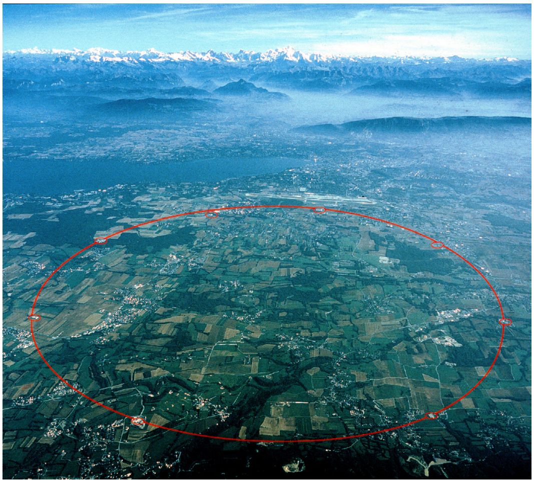

Fig. S2.3 · De schaal van de Large Hadron Collider, met het meer van Genève en de stad. De Mont Blanc is zichtbaar in het midden van het beeld. ATLAS is gebouwd bij de 2-uur-positie langs de ring.

De Large Hadron Collider is een 27 km lange ronde ondergrondse deeltjesversneller die protonen met een energie van 4 TeV op elkaar botst, wat correspondeert met 99,999 999 1 % van de lichtsnelheid – of dezelfde energie per bundel als een vliegdekschip met een kruissnelheid van 5,6 knopen. Omdat protonen een lading hebben kunnen ze worden afgebogen in een magnetisch veld. Het grootste deel van de versneller is daarom gemaakt van 1232 supergeleidende magneten die alleen gebruikt worden om de protonen in hun cirkelvormige baan te houden. Op slechts één punt langs de ring wordt een elektrisch veld gebruikt om de bundels te versnellen. De protonbundels kruisen elkaar op vier punten; op deze plekken zijn detectoren geplaatst om het resultaat van de botsingen te meten en deze *events* op te slaan. Een luchtweergave staat in fig. S2.3.

Een deeltjesdetector moet in staat zijn de in een botsing produceerde deeltjes precies te meten. ATLAS is daarom cilindervormig gebouwd om de plek van de botsingen heen, zodat alles binnen het detectorvolume geregistreerd kan worden. Het experiment is ongeveer 44 m lang en 25 m hoog. Een dergelijk grote machine is nodig om subatomaire deeltjes te onderzoeken vanwege de grote hoeveelheid hoogenergetische deeltjes die bij elke botsing geproduceerd worden.

Om te zorgen dat elk soort vervalsproduct goed gemeten wordt is ATLAS niet één groot apparaat, maar bestaat het uit meerdere subdetectoren die om elkaar heen gebouwd zijn. Een schematische weergave van de wijze waarop deeltjes gedetecteerd worden staat in fig. S2.4. Dichtbij de plaats waar de botsingen plaatsvinden worden geladen deeltjes gemeten door *tracking*-detectoren. Uit de metingen worden door middel van algoritmen later de sporen van deeltjes gereconstrueerd. Rondom de tracker meten twee detectoren de energie van alle deeltjes. Behalve muonen worden alle deeltjes door deze *calorimeters* gestopt. Energetische muonen worden gemeten door een speciale muondetector die de rest van de subdetectoren omvat.

Wanneer een quark of een gluon wordt gemaakt, ontstaat een lawine van deeltjes (een *jet*) dankzij een fenomeen dat *confinement* heet: quarks kunnen niet vrij bestaan. Een jet is geen

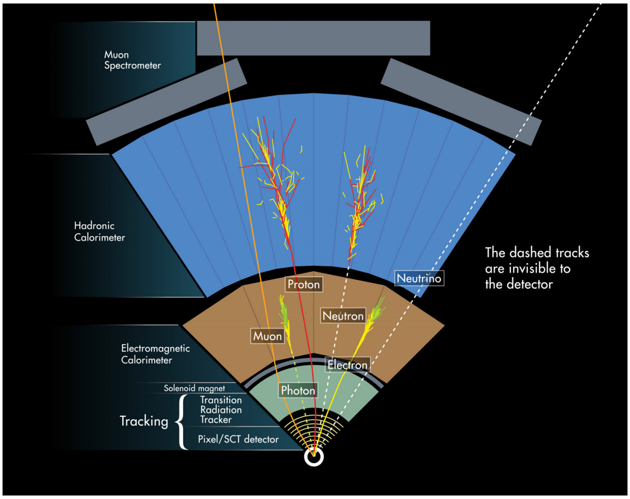

Fig. S2.4 · Een weergave van de wijze waarop verschillende deeltjes worden gedetecteerd.

deeltje, maar een kegel van deeltjes met een bepaalde straal. Speciale algoritmen worden gebruikt om deze objecten te herkennen.

Op deze manier kunnen alle *zichtbare* deeltjes gemeten worden. Onzichtbare deeltjes, zoals het neutralino, en neutrino's kunnen niet direct gedetecteerd worden. Hun aanwezigheid wordt afgeleid uit *ontbrekende transversale impuls* (ook wel ontbrekende transversale energie genoemd): als de transversale impulsen van alle andere deeltjes opgeteld worden hoeft de som niet nul te zijn.[1] Het verschil wordt toegekend aan onzichtbare deeltjes.

Om alle objecten voor elke botsing helemaal te reconstrueren is onmogelijk. Binnen de detector vinden 40 miljoen botsingen per seconde plaats. Al deze botsingen moeten gemeten worden. Het opslaan van elke botsing zou echter tot 65 TB aan data *per seconde* leiden, wat veel te veel is om volledig te verwerken. Een systeem van *triggers* wordt daarom gebruikt om de hoeveelheid opgeslagen botsingen (of events) terug te brengen tot ongeveer 200 per seconde, wat vooral bepaald is door de datagrootte van elk event. Deze triggers eisen dat een event iets interessants bevat, bijvoorbeeld een hoogenergetisch elektron of een jet.

Nadat alle objecten in elk event zijn gereconstrueerd in deze enorme dataset van events met behulp van statistische methoden gezocht worden naar bewijs van nieuwe deeltjes.

Statistisch intermezzo

De vraag of in een bepaalde dataset bewijs van supersymmetrie aanwezig is, is heel vergelijkbaar met de wijze waarop we bepalen of bijvoorbeeld een dobbelsteen verzwaard is. Door de *waarschijnlijkheid van de observatie* te kwantificeren. Met andere woorden, als we een dobbelsteen 120 keer werpen en 22 maal zien we zes ogen, hoe (on)waarschijnlijk vinden we dat resultaat? Afhankelijk van een vooraf afgesproken mate van (on)waarschijnlijkheid kan dan geconcludeerd worden of

[1] Dat moet automatisch het geval zijn: de protonen die botsen hebben impuls in de richting van de bundel, niet loodrecht erop!

de dobbelsteen verzwaard is of niet. Intuïtief zouden we al zeggen dat 22 zessen niet zo vreemd is (we verwachten er immers 20), maar dat 60 zessen bijzonder verdacht is.

Kwantitatief stellen we daarom onszelf de vraag "hoe waarschijnlijk is het om 22 *of meer* zessen te zien?": dit is de zogenaamde p-waarde.[1] Een p-waarde kwantificeert hoe (on)verwacht een observatie is gegeven een verwachting, die in het geval van de dobbelsteen 20 zessen is. We verwachten echter nooit elke keer precies 20 zessen te zien, maar een verdeling rond die waarde: de verwachting wordt daarom weergegeven met $20 \pm 4{,}5$.[2]

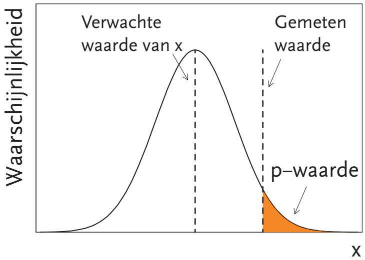

Fig. S2.5 · Illustratie van een p-waarde.

Om te bepalen of een dobbelsteen verzwaard is moet vooraf een p-waarde afgesproken worden. In de deeltjesfysica is de p-waarde die voor een *ontdekking* gebruikt wordt 3×10^{-7}, of 0,00003 %.[3] Met andere woorden, we verwachten dat een dergelijk scenario wanneer we ons experiment (120 worpen) herhalen gemiddeld slechts eens op de 3,3 miljoen keer per toeval zou voorkomen. In het geval van de dobbelsteen is de grens 50,3: we zouden dus 51 of meer keer zes ogen moeten zien om te concluderen dat onze dobbelsteen verzwaard is.[4,5]

Wat nu als we minder dan 51 maal zes ogen werpen, bijvoorbeeld 22? In dat geval kunnen we niet concluderen dat de dobbelsteen verzwaard was, maar wel kan een limiet geplaatst worden op *hoe* verzwaard de dobbelsteen dan nog kan zijn. Met andere woorden, onze vraag wordt nu welke dobbelsteen nooit 22 *of minder* zessen zou geven; we proberen nu deze *alternatieve hypothese* te verwerpen.[6] In dit geval wordt een p-waarde van 0.05 gebruikt. In het voorbeeld correspondeert dat met een dobbelsteen waar 30 zessen verwacht worden. We zeggen dus dat wanneer 22 maal zes ogen gemeten wordt, elke dobbelsteen die 30 of meer zessen had voorspeld uitgesloten is bij een betrouwbaarheidsinterval van 95 %. [7]

Twee belangrijke conclusies over een statistische procedure zoals voor de dobbelsteen kunnen getrokken worden:

- een kleinere onzekerheid op de verwachte waarde maakt het makkelijker significante resultaten te verkrijgen. Het meten van 27 zessen waar $20 \pm 4{,}5$ verwacht werd is *niet* significant, terwijl het *wel* significant is als de verwachtingswaarde $20 \pm 0{,}05$ is;

1 Merk op dat de p-waarde om de verwachte 20 zessen te zien 0,5 is: de helft van de kansverdeling ligt erboven, de helft eronder.
2 Het getal 4,5 geeft het bereik aan waarbinnen 68 % van de verwachte resultaten ligt: een *betrouwbaarheidsinterval*.
3 Dit correspondeert met vijf standaarddeviaties van de normaalverdeling, of $5\,\sigma$.
4 Een meer gebruikelijke grens van 95 % kan ook gebruikt worden: in dat geval zouden 28 zessen afdoende zijn.
5 In beide gevallen zijn eenzijdige betrouwbaarheidsintervallen gebruikt: we nemen voor het gemak aan dat een gemanipuleerde dobbelsteen meer en niet minder zessen zou geven, aangezien dat laatste vermoedelijk niet bijzonder veel zou helpen met valsspelen tijdens kansspelen. Dit is ook het geval in de deeltjesfysica: voorspelde nieuwe deeltjes geven aanleiding tot meer events, nooit minder.
6 In dit geval wordt de linkerstaart van de kansverdeling gebruikt, in plaats van de rechter.
7 Een interessant scenario is wanneer we (veel) minder meten dan verwacht wordt voor een onverzwaarde dobbelsteen, bijvoorbeeld 5 zessen. In dat geval zouden zowel de nulhypothese (20) als de alternatieve hypothese (30) verworpen worden. In dit scenario heeft de statistische test geen onderscheidend vermogen meer; zie §5.9.2 voor de discussie hierover.

- hoe groter de dataset, hoe makkelijker het wordt een ontdekking te doen: de relatieve onzekerheid neemt typisch af met $\sqrt{N}$. In hetzelfde voorbeeld is een 10 000 keer grotere dataset (270 000 gemeten waar 200 000 ± 450 verwacht werd) ook afdoende.

Een deeltjesfysicus in spé is dus gebaat bij een dataset met zoveel mogelijk verwacht *signaal* (bijvoorbeeld supersymmetrische events) bovenop de verwachte *achtergrond* (alle bekende processen), met een zo klein mogelijke onzekerheid op de achtergrondvoorspelling. Door *selecties* te maken op de dataset die (veel) meer achtergrond dan hypothetisch signaal weggooien, kunnen we een analyse krachtiger maken. Een ideale selectie zou de achtergrond met een (erg) grote factor reduceren en geen enkel signaal weggooien. In de praktijk moeten compromissen gemaakt worden: de verhouding tussen verwacht signaal en achtergrond wordt geoptimaliseerd.

Zoeken naar supersymmetrie

Gewapend met onze statistische procedure en een grote dataset kunnen we gaan zoeken naar bewijs voor het bestaan van supersymmetrie. Als SUSY bestaat worden de verschillende deeltjes voorspeld door de theorie allemaal in verschillende hoeveelheden geproduceerd en gaan ze verschillende interacties aan. Elke analyse focust zich daarom op een bepaald deel van de door supersymmetrie voorspelde deeltjes, die vervolgens op een bepaalde manier vervallen. In dit proefschrift is gezocht naar het bestaan van squarks en gluino's, de partnerdeeltjes van het quark en het gluon. Indien supersymmetrie bestaat zijn dit de SUSY-deeltjes die naar verwachting het vaakst geproduceerd worden bij de LHC.

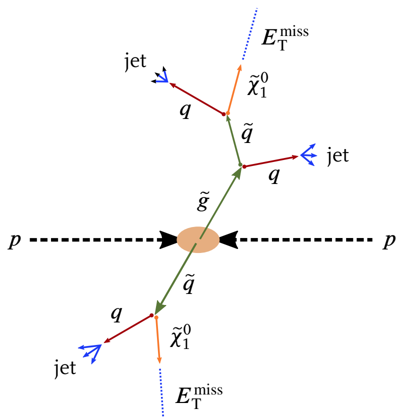

Fig. S2.6 · Schematische weergave van squark–gluino-productie bij de LHC. Een squark $\tilde{q}$ en gluino $\tilde{g}$ worden geproduceerd en vervallen elk direct naar quarks, die jets vormen, en neutralino's, die niet direct gemeten kunnen worden.

In hoofdstuk 5 is een zoektocht naar supersymmetrie die gebruik maakt van events zonder elektron of muon, met een aantal jets en met ontbrekende energie gepresenteerd. Onze keuze hiervoor is bepaald door het feit dat dit het vaakst voorkomt in het geval van direct verval van squarks en gluino's, zoals weergegeven in fig. S2.6. Deze simpele vervallen komen veel voor in gecompliceerde supersymmetrische modellen en zijn daarom interessant. In directe vervallen vervalt een squark naar een quark en ontbrekende energie; een gluino vervalt naar twee quarks en ontbrekende energie. Voor paarproductie van deze deeltjes verwachten we derhalve events met 2 tot 4 quarks, die tot jets leiden, en een aantal deeltjes die uit de detector ontsnappen en daarmee aanleiding geven tot ontbrekende energie. We gebruiken events met 2 tot 6 jets om ook te kunnen zoeken naar gecompliceerdere vervallen van squarks en gluino's (via extra tussenstappen), die altijd tot extra jets leiden.

Om interessante events te selecteren, eisen we dat ze 2 tot 6 jets bevatten en dat al deze jets veel impuls hebben (minstens 60 GeV). Een van de jets moet bovendien een heel hoge impuls hebben (minstens 130 GeV) en het event moet veel ontbrekende energie bevatten (minstens 160 GeV). Deze eisen zorgen ervoor dat veel SUSY-events geselecteerd worden, terwijl bekende processen onderdrukt worden omdat deze minder vaak tot dergelijke vingerafdrukken leiden. Ook eisen we dat events geen elektron of muon bevatten. Dit onderdrukt de achtergrondprocessen nog meer, aangezien de directe vervallen van squarks en het gluino nooit tot dergelijke deeltjes leiden.[1]

We kunnen echter niet *alle* achtergrond onderdrukken. Zo kan de productie van een Z-boson met jets bijvoorbeeld tot exact hetzelfde soort event als de productie van SUSY-deeltjes leiden.[2] Ook zijn de metingen van de detector niet perfect: zo kan een event met alleen maar jets kan niet goed gemeten zijn, waardoor er sprake is van *foutief gemeten ontbrekende energie* ("fake $E_{\mathrm{T}}^{\mathrm{miss}}$"). We moeten daarom alle achtergrondprocessen zo goed en precies mogelijk bepalen.

Om in de overgebleven events onderscheid te maken tussen achtergrond en signaal worden verdere selecties gebruikt. We selecteren events voor onze uiteindelijke *signaalgebieden* op basis van hun *effectieve massa*: de som van de impulsen van alle jets en de ontbrekende energie. Studies hebben aangetoond dat die grootheid goed correleert met de massa van de oorspronkelijke deeltjes. Omdat SUSY-deeltjes zwaarder zijn dan bekende deeltjes selecteren we events met hoge effectieve massa, om zo achtergrond weg te gooien en zoveel mogelijk signaal over te houden.

De dan nog overgebleven achtergrond bepalen we door middel van vier *controlegebieden*: één voor elk achtergrondproces. Deze gebieden hebben bijna dezelfde selecties als de signaalgebieden, met een of twee omgedraaid of veranderd om juist zoveel mogelijk events afkomstig van een bepaald achtergrondproces te selecteren, bijvoorbeeld Z+jets events. We gebruiken metingen in de controlegebieden om de voorspelling van onze simulaties te corrigeren: wanneer we 100 Z+jets events meten waar er 90 verwacht werden, wordt de voorspelling overal met 1.11 geschaald. Dit schalen gebeurt *tegelijkertijd* voor alle achtergrondprocessen, zodat cross-contaminaties in de verschillende controlegebieden correct worden meegenomen.[3]

Dankzij deze gecompliceerde procedure hebben we een verbeterde voorspelling voor de Standaardmodelachtergrond in de signaalgebieden. Die worden dan ongeblindeerd[4] en we vergelijken de gemeten hoeveelheid events met de verwachting: de procedure verloopt vanaf hier precies hetzelfde als voor de dobbelsteen.

We meten helaas geen significant overschot aan events boven de verwachte achtergrond in de signaalgebieden: de metingen zijn compatibel met het Standaardmodel. Er is derhalve geen bewijs voor supersymmetrie gevonden.

---

1 De consequentie is dat we minder gevoelig zijn voor bepaalde vervallen van squarks en gluino's via een of meer W- of Z-bosonen: deze kunnen leiden tot leptonen in het event. Er zijn ook analyses die zich specifiek op eindtoestanden met 1 lepton en met 2 of meer leptonen richten.

2 Het Z-boson kan vervallen naar twee neutrino's, die net als de neutralino's de detector ongemerkt verlaten.

3 De gehele procedure, en de manier waarop limieten bepaald zijn, is geïmplementeerd gebruikmakende van HistFitter, een softwareprogramma beschreven in hoofdstuk 9. HistFitter wordt ook gebruikt voor de meeste andere analyses in de SUSY-werkgroep van het ATLAS-experiment.

4 In een geblindeerd signaalgebied wordt nog niet naar de *gemeten* hoeveelheid events gekeken, om statistische bias tijdens het ontwerpen van de analyse te voorkomen.

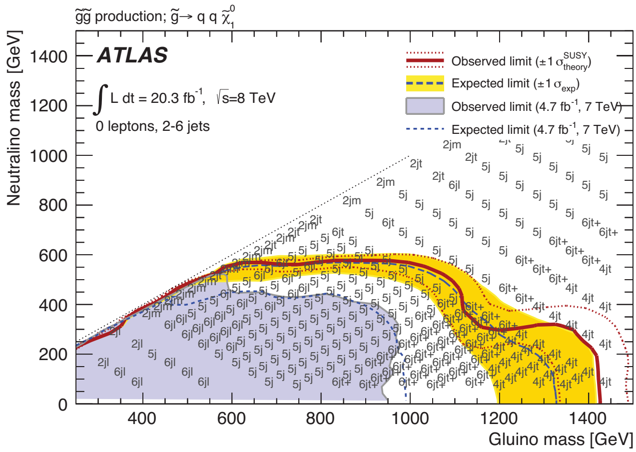

Fig. S2.7 · Uitgesloten modellen voor gluino-paarproductie. De grijze labels geven aan welk signaalgebied een modelpunt het beste uitsloot. De dikke onderbroken blauwe lijn is de *verwachte* limiet en geeft die modellen aan die we zouden uitsluiten als precies de Standaardmodelverwachting gemeten zou worden. Omdat in signaalgebied 4jt minder events dan verwacht gemeten zijn, zijn we in staat meer modellen dan verwacht uit te sluiten in de hoek rechtsonder.

Interpretatie en gebruik van de resultaten

Bij gebrek aan significant overschot aan events kunnen we *bovenlimieten* bepalen voor elk van de signaalgebieden. Het maximum aantal toegestane extra events in elk gebied is bepaald, zodat de resultaten ook gebruikt kunnen worden om andere modellen te toetsen. Elk model dat meer dan het toegestane aantal voorspelt is uitgesloten. De limieten zijn daarom *modelonafhankelijk*. We toetsen ook een grote hoeveelheid specifieke SUSY-modellen. Als deze teveel extra events voorspellen (dat wil zeggen, het gemeten aantal is significant lager dan de modelvoorspelling), zijn ze uitgesloten.

Voor deze specifieke modellen kunnen we limieten bepalen door de parameters te variëren. Voor een vereenvoudigd model van paarproductie van gluino's zijn de enige twee parameters de gluinomassa en de massa van het neutralino waarnaar het gluino vervalt. Door verschillende combinaties van de parameters te simuleren en te vergelijken met de metingen verkrijgen we een limiet in de parameterruimte van het model door middel van interpolatie.[1] Het voorbeeld voor gluino-paarproductie is weergegeven in fig. S2.7.

De limieten voor dergelijke modellen kunnen we verbeteren door het resultaat te combineren met andere analyses die een compleet onafhankelijke dataset gebruikt hebben, bijvoorbeeld gebruik makende van events *met* een elektron of muon. Omdat verschillende experimentele onzekerheden tussen deze analyses gecorreleerd zijn, vinden we een kleinere onzekerheid op de achtergrondvoorspellingen en kunnen we zo een betere limiet bepalen. Een eenvoudige combinatie zou dergelijke onzekerheden als onafhankelijk beschouwen en in feite dubbel meenemen, en

1 Deze procedure is eenvoudiger dan hij klinkt: een interpolatie bij 95 % betrouwbaarheidsinterval is vergelijkbaar met het bepalen van hoogtelijnen op een wandelkaart of isobaren op een weerkaart.

zo de totale onzekerheid overschatten. In hoofdstuk 7 zijn de resultaten voor een aantal modellen gecombineerd met de resultaten van de 1- en 2-lepton analyses.

In het algemeen kunnen we de gevonden resultaten ook gebruiken om gecompliceerde modellen te toetsen. Een model waar alleen paren gluino's geproduceerd worden is namelijk geen realistische manifestatie van supersymmetrie: het zou merkwaardig zijn om alleen gluino's en neutralino's te kunnen produceren. In hoofdstuk 6 gebruiken we de resultaten om het *phenomenological Minimal Supersymmetric Standard Model* met 15 vrije parameters te onderzoeken. Dit model reduceert het aantal vrije parameters van de meeste algemene vorm van supersymmetrie, maar behoudt de belangrijkste die het gedrag bij de versnellers beïnvloeden.

Door niet alleen resultaten van de LHC maar ook veel andere limieten en metingen[1] te gebruiken kunnen we de waarschijnlijkste waardes van de parameters door middel van scantechnieken bepalen. Dergelijke technieken maken gebruik van Bayesiaanse *priors*[2] voor de parameters en verkennen de parameterruimte om de a-posteriori waarschijnlijkheden te bepalen gegeven alle metingen en limieten. Op die manier wordt ook het waarschijnlijkste model gevonden, dat het beste past bij alle data. Na alle data, inclusief resultaten van de LHC, meegenomen te hebben is een squarkmassa van 2,3 TeV, een gluinomassa van 2,1 TeV en een neutralino met een massa van 130 GeV en een spinonafhankelijke botsingsdoorsnede van $2{,}4 \times 10^{-10}$ pb het waarschijnlijkst. Die waarden liggen binnen bereik van de LHC en toekomstige experimenten voor de directe detectie van donkere materie; dit model zal dus aangetoond of uitgesloten kunnen worden.

Wat nu voor supersymmetrie?

De tot dusver gevonden negatieve resultaten bij zoektochten naar supersymmetrie betekenen niet dat de theorie niet langer levensvatbaar is. De mate waarin supersymmetrische deeltjes geproduceerd worden kan simpelweg te laag zijn geweest om ze in voldoende hoeveelheden bij de huidige energiën te hebben gemaakt. Voor een voorgestelde upgrade van de LHC, die meer protonen per seconde zal botsen en een dataset 150 keer groter dan de huidige zal meten en bij bijna tweemaal zo hoge energie, zijn de vooruitzichten voor zoektochten naar SUSY prima. Zelfs voor vereenvoudigde modellen van squark- en gluino-paarproductie liggen de modellen die ontdekt kunnen worden buiten de tot nu toe bij de LHC uitgesloten gebieden, zoals beschreven in hoofdstuk 8. In fig. S2.8 staat een voorbeeld voor gluino-paarproductie weergegeven. Bovendien zal de hogere energie ervoor zorgen dat (veel) zeldzamer productiemechanismen voor supersymmetrische deeltjes, zoals de productie van paren neutralino's en chargino's, bestudeerd kunnen worden bij de LHC. Er zijn al met al voldoende wegen te bewandelen in het komende decennium om supersymmetrie aan te tonen of verder uit te sluiten.

---

[1] Zoals resultaten van vorige experimenten bij versnellers, experimenten die donkere materie direct proberen te detecteren, en precisiemetingen van processen met bottom- en down-quarks die erg beïnvloed zouden worden indien SUSY-deeltjes bestaan.

[2] Een *prior* is de a-priori waarschijnlijkheid dat een parameter een bepaalde waarde heeft. Een vlakke verdeling betekent dat elke waarde even waarschijnlijk is. In het dagelijks leven maken we veel gebruik van dergelijke priors: probeer bijvoorbeeld eens na te denken over de kansverdeling hoe goed je favoriete voetbalclub het volgend jaar in de Champions League zal doen. (Hint: die verdeling is bepaald niet uniform en de winkans nagenoeg nul, tenzij je natuurlijk Spaans bent of uit Beieren komt.).

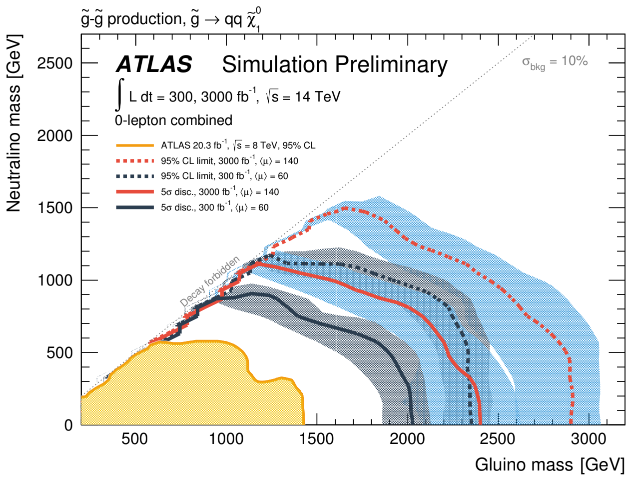

Fig. S2.8 · Vooruitzichten voor paarproductie van gluino's voor datasets 15 en 150 keer groter dan de huidig gemeten dataset van de LHC. Al uitgesloten modellen zijn weergegeven in geel. Modellen onder de ononderbroken lijnen zijn te ontdekken; die onder de gestippelde lijnen kunnen worden uitgesloten. De banden geven de onzekerheden op de theoretische voorspellingen aan.

In de nabijere toekomst zullen de jaren 2015–2017 een bijzonder interessante periode voor de hoge-energiefysica zijn. Na een pauze van twee jaar zullen bij de LHC vanaf het voorjaar van 2015 weer botsingen plaatsvinden, ditmaal met een energie van 14 TeV. Dat lijkt wellicht geen grote verbetering ten opzichte van de huidige 8 TeV, maar bijvoorbeeld de hoeveelheid gluino's die geproduceerd kan worden neemt, afhankelijk van de gluinomassa, met een factor 40 tot 100 toe. Zowel ATLAS als het concurrerende experiment CMS zullen met een veel kleinere dataset dan tot nu toe gemeten de huidige resultaten al kunnen verbeteren en na de zomer van 2015 in onontgonnen gebied belanden. De hogere energie zorgt er ook voor dat de eigenschappen van het nieuwe ontdekte Higgsdeeltje nauwkeuriger en in nieuwe vervalskanalen gemeten kunnen worden, wat op indirecte wijze ons ook veel over supersymmetrie kan leren. Nieuwe, grotere experimenten die donkere materie direct hopen te detecteren zullen nog zeldzamere processen kunnen onderzoeken. Of het Standaardmodel binnenkort of pas na enkele jaren metingen scheurtjes zal gaan vertonen zal de tijd moeten leren, maar in het achterhoofd houdende dat het 48 jaar duurde om het Higgsdeeltje te ontdekken is er (nog?) geen reden om in paniek te raken.

Curriculum vitae

Geert-Jan Besjes was born in Utrecht on 29 August 1987. After graduating from the Lorentz College in Arnhem in 2003, he enrolled in the bachelor programme in Physics and Astronomy at Radboud University Nijmegen. After completing his degree in 2007, he continued in the MSc programme in Physics and Astromony at the same university, specialising in high energy physics. He spent the summer of 2008 at CERN working as a summer student under Dr Wolfgang Liebig. In 2010 he obtained his degree *cum laude*, after completing a thesis *Linear Sigma Models on the Lattice* in Theoretical High Energy Physics under supervision of Prof. Ronald Kleiss.

During his studies, the author was active in student organisations and politics: from 2004–2006 he was a board member and vice-chairman of the physics' students association *Marie Curie*, from 2005–2006 secretary and chairman of the board of the faculty-wide umbrella organisation *Olympus* and in 2008–2009 chairman of the national umbrella organisation *Studenten Physica in Nederland* and a board member of the Dutch Physical Society. He was elected to the Faculty Student Council in 2005–2006, twice to the Physics and Astronomy curriculum QA committee (*opleidingscommissie*) in 2006–2008 and a member of the University Student Council in 2007–2008. In addition, he participated in several Model United Nations conferences as part of the *United Netherlands* delegation, winning the award for Best Delegate at Harvard National Model United Nations 2008.

In December 2010, he started as a graduate student at the department of Experimental High Energy Physics under supervison of Prof. Nicolo de Groot and Dr Sascha Caron. The work done as a graduate student led to this thesis. Part of it was performed during a stay at CERN from January 2012 to April 2013. The results were presented at conferences in Veldhoven, Marseille, Barcelona and San Francisco and a summer school at Stanford. As a graduate student, he taught courses in programming, complex analysis, subatomic physics and quantum field theory. He was also part of the supervisory board of the United Netherlands foundation from 2012 to 2014.

Acknowledgements

OOK AL STAAT mijn naam op de kaft van dit proefschrift is werk binnen de hoge-energiefysica geen eenpersoonsproject. Mijn dank gaat allereerst uit naar mijn promotor Nicolo de Groot, voor het aannemen van alweer een overgelopen theoriestudent, alle geboden vrijheid en de mogelijkheid een aantal maanden langer op CERN te blijven, en naar mijn copromotor Sascha Caron: je enthousiasme voor supersymmetrie werkte dermate aanstekelijk dat een promovendus zich weinig betere dagelijkse begeleiding kan wensen en wanneer er eens een hobbel voor de analyse gladgestreken moest worden kon ik altijd op je rekenen. Over het optimale puntensysteem voor een WK-pool zullen we het echter denk ik nooit eens worden.

Gelukkig bestaat de afdeling hoge-energiefysica uit meer dan een losse groep samenwerkende mensen. Mijn hartelijke dank gaat uit naar Annelies, Gemma en Marjo voor de levendige sfeer. Sharing an office throughout the years with Thijs, Melvin, Magda, Folkert, Marcel, Antonio, Antonia, Vince, Cristina, Luca and Valerio was always a pleasure. Next to them, a big thank you to Stefan, Irene, Stefan, Guus, Harm, José, Harm, Yiannis, Marie, Gijs, Antje, Lucian, Snezana and Jari for making the department the great place that it is. Mijn excuses voor alle compleet nutteloze nieuwsberichten en feiten die jullie soms van me moesten aanhoren, en mijn dank voor alle uiteenlopende (al dan niet nutteloze) discussies door de jaren heen. Ik hoop van harte dat de HEF-skitrips nog meer lustra dan het behaalde eerste zullen meemaken.

Leendertjan en Bernard wil ik bedanken voor alle lol over koppen koffie en glazen bier door de jaren heen. Ik hoop dat we er na al onze promoties nog mee mogen doorgaan. Frank en Crispijn, in het bijzonder bedankt voor alle (on)regelmatige potjes tennissen. Met Tom en Jord naar Europese voetbalwedstrijden gaan was bij tijd en wijle tandenknarsen, maar dat lag zeker niet aan het gezelschap. Floris, ik hoop dat ik niet alleen op bezoek mag blijven komen om een plafond in je huis te slopen.

Most of this thesis is on supersymmetry without leptons. The small group from Nikhef working on it was a great team to be a part of: thank you, Robin, Marija and Ingrid. I'm grateful to Michael Rammensee for introducing me to the limit setting procedures and getting things moving early on. Renaud and Nikola, thank you for the excellent cooperation. Working on HistFitter with Max, Jeanette, David and Alex also proved an very enjoyable and valuable collaboration.

Working in the Nikhef ATLAS group was often fun. In no particular order, I would like to mention Stefan, Rogier, Jörn, Rosemarie, Priscilla, Lucie, Pier-Olivier, Koen, Pierfrancesco, Daniël, Duc and Antonio, and outside ATLAS Lisa, Roel, Rose, Veerle, Serena, Suvayu, Jeroen and Maurizio.

Het toezicht proberen te houden op een stichting was een leuke uitdaging en afwisseling naast het dagelijkse werk van een promotie. Vanaf het eerste smsje "gefeliciteerd met je eerste commissariaat, let wel even op de code-Tabaksblat" tot de laatste stukken die samenvielen met het schrijven van dit proefschrift, mijn dank aan Iris, Mark, Joost, Wouter, Annalise, René en Anoep voor de plezierige samenwerking. Ik hoop dat we elkaar nog tegen zullen komen.

Before this thesis was sent to be scrutinised by my supervisors, several people read parts beforehand. I'm grateful to Cristina, Antonio, Antonia and Ingrid for reading (rough) drafts of various chapters. Leendertjan, Bernard en Melvin, bedankt voor het stevig op de pijnbank leggen van de introductie en de populair-wetenschappelijke samenvatting.

Dit proefschrift had er nooit zo mooit uitgezien zonder de omslag, die ik nooit zelf had kunnen bedenken laat staan vervaardigen. Merel Brouns wil ik bedanken voor het prachtige ontwerp.

Being stationed at CERN for a year served for a pleasant change of scenery. Plenty of things were always available to do outside office hours (although at times those hours were not many); especially the CERN skiing club and the footballing antics with the CERN football team, *Le Club Zapata* and *Zapatilla* proved a welcome distraction.

Als laatste gaat mijn diepe dank uit naar Maarten en mijn ouders. Maarten, in het bijzonder het jaar dat ik in Genève woonde was door omstandigheden bepaald niet makkelijk; laten we hopen dat zoiets niet weer voorkomt. Wedstrijden Ajax–Vitesse lijken me alleen niet zo'n succes om te blijven bezoeken, zeker niet met veel te veel idioten in het geel-zwart in de buurt. Bedankt dat je een van mijn paranimfen wilde zijn. Aan mijn ouders ben ik de meeste dank verschuldigd. Zonder hen had ik hier niet kunnen staan.

Nijmegen, februari 2015